AN IMAGE-BASED APPROACH TO THREE-DIMENSIONAL COMPUTER GRAPHICS

by

Leonard McMillan Jr.

A dissertation submitted to the faculty of the University of North Carolina at Chapel Hill in partial fulfillment of the requirements for the degree of Doctor of Philosophy in the Department of Computer Science.

Chapel Hill

1997

Approved by:

_____

Advisor: Gary Bishop

_____

Reader: Anselmo Lastra

_____

Reader: Stephen Pizer

ABSTRACT

Leonard McMillan Jr.

An Image-Based Approach to Three-Dimensional Computer Graphics

(Under the direction of Gary Bishop)

The conventional approach to three-dimensional computer graphics produces images from geometric scene descriptions by simulating the interaction of light with matter. My research explores an alternative approach that replaces the geometric scene description with perspective images and replaces the simulation process with data interpolation.

I derive an image-warping equation that maps the visible points in a reference image to their correct positions in any desired view. This mapping from reference image to desired image is determined by the center-of-projection and pinhole-camera model of the two images and by a *generalized disparity* value associated with each point in the reference image. This generalized disparity value, which represents the structure of the scene, can be determined from point correspondences between multiple reference images.

The image-warping equation alone is insufficient to synthesize desired images because multiple reference-image points may map to a single point. I derive a new visibility algorithm that determines a drawing order for the image warp. This algorithm results in correct visibility for the desired image independent of the reference image's contents.

The utility of the image-based approach can be enhanced with a more general pinhole-camera model. I provide several generalizations of the warping equation's pinhole-camera model and discuss how to build an image-based representation when information about the reference image's center-of-projection and camera model is unavailable.

ACKNOWLEDGMENTS

I owe tremendous debts of gratitude to the following:

- My advisor and long time friend Gary Bishop who first challenged me to return to graduate school and has subsequently served as both teacher and advocate during the entire process.

- My committee members, Fred Brooks, James Coggins, Henry Fuchs, Anselmo Lastra, Steve Pizer, and Turner Whitted who have been endless sources of wisdom, enthusiasm, and inspiration.

- The department research faculty, in particular Vern Chi for his advice on limiting cases; and John Poulton, Nick England, and Mary Whitton for their enthusiasm and support.

- My department colleagues and fellow students, in particular Bill Mark for his collaborations and willingness to endure my ramblings.

- My parents Leonard McMillan Sr. and Joan McMillan for nurturing, encouragement, and their willingness to allow me to take things apart, while knowing that I might not succeed in putting them back together. Also, my brother John McMillan whose belongings I so often dismantled.

I wish both to thank and to dedicate this dissertation to my wife Donna for all of the love that she brings to my life, and to my daughter Cassie for all of the joy that she brings.

TABLE OF CONTENTS

LIST OF FIGURES

LIST OF EQUATIONS

Chapter 1

INTRODUCTION

> *"Computer graphics concerns the pictorial synthesis of real or imaginary objects from their computer-based models, whereas the related field of image processing treats the converse process: the analysis of scenes, or the reconstruction of models of 2D or 3D objects from their pictures."*
>
> **— Foley, van Dam, Feiner, and Hughes**

The field of three-dimensional computer graphics has long focused on the problem of synthesizing images from geometric models. These geometric models, in combination with surface descriptions characterizing the reflective properties of each geometric element, represent a desired scene that is to be rendered by the computer graphics system. Computationally, the computer-graphics image synthesis process is a simulation problem in which light's interactions with the supplied scene description are computed.

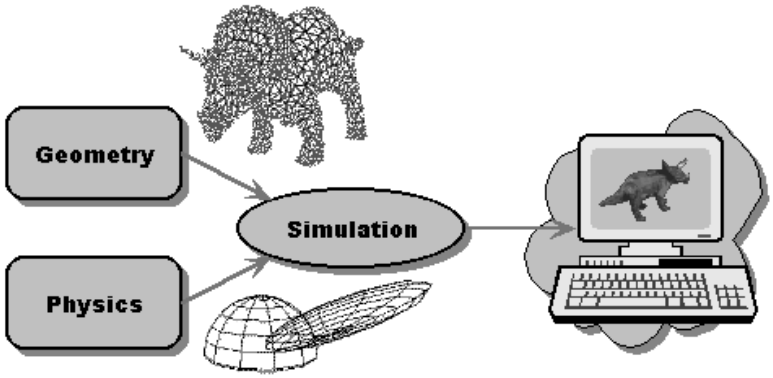

Figure 1-1: Traditional approach to three-dimensional computer graphics

Conventional computer vision considers the opposite problem of synthesizing geometric models from images. In addition to images, computer-vision systems depend on accurate camera models and estimates of a camera's position and orientation in order to synthesize the desired geometric models. Often a simple reflectance model of the observed scene's surfaces is another integral part of a computer-vision system. The image-processing methods employed in

computer vision include the identification of image features and filtering to remove noise and to resample the source images at desired scales. In addition to image processing, geometric computations are required to map the identified image features to their positions in a three-dimensional space.

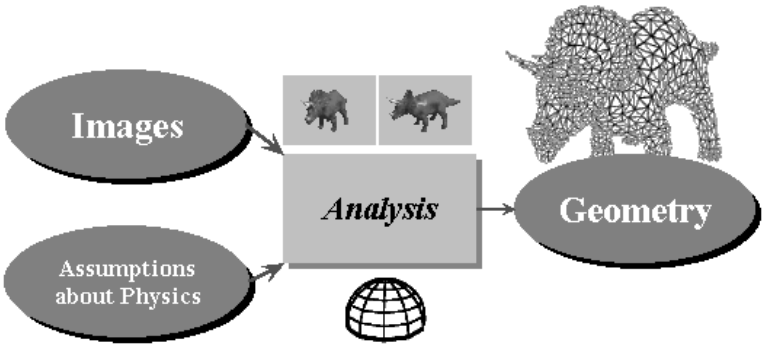

Figure 1-2: Traditional approach to computer vision

The efforts of computer graphics and computer vision are generally perceived as complementary because the results of one field can frequently serve as an input to the other. Computer graphics often looks to the field of computer vision for the generation of complex geometric models, whereas computer vision relies on computer graphics both for the generation of reference images and for viewing results. Three-dimensional geometry has been the fundamental interface between the fields of computer vision and computer graphics since their inception. Seldom has the appropriateness of this link been challenged.

The research presented in this dissertation suggests an alternative interface between the image analysis of computer vision and the image synthesis of computer graphics. In this work I describe methods for synthesizing images, comparable to those produced by conventional three-dimensional computer graphics methods, directly from other images without a three-dimensional geometric representation. I will demonstrate that the computations used in this image-based approach are fundamentally different from the simulation techniques used by traditional three-dimensional computer graphics.

In this chapter, I first discuss the various model representations commonly used in computer graphics today, and how all of these modeling approaches stem from a common geometric heritage. Then I will propose an image-based alternative to three-dimensional graphics, and discuss why one is needed. I will finally consider previous research in which images have served as computer graphics models.

1.1 Conventional Computer Graphics Models

Since its inception, a primary goal of computer graphics has been the synthesis of images from models. It is standard for images to be represented as two-dimensional arrays of pixels stored in the frame buffer of the computer. Model descriptions, however, are much more varied.

One modeling technique represents the boundaries between objects as a series of two-dimensional surfaces embedded within a three-dimensional space. This approach is called a *boundary representation*. Boundary representations can be further broken down according to the degree of the surface description. A first-degree description might consist entirely of polygonal facets specified by the coordinates of their vertices. A higher-degree description might describe a curved surface patch whose three-dimensional shape is defined in terms of a series of three-dimensional control points.

Another representation commonly used to describe three-dimensional models is the Boolean combinations of solids. In this method the primitive descriptions enclose a volume, rather than specify a surface. There are two popular variants of this approach: constructive solid geometry (CSG) and binary spatial partitioning (BSP). In constructive solid geometry the desired shape is specified in terms of a tree of elementary solids that are combined using simple set operations. The BSP approach is a special case of CSG in which the only modeling primitive used is a region of space, called a half-space, that is bounded on one side by a plane. The only operation allowed in a BSP model's tree representation is the intersection of the child node's half-space with the space enclosed by its parent.

Enumerated space representations are a third popular modeling description. The distinguishing attribute of enumerated space models is that they represent objects as a set of discrete volume elements. An example is volumetric modeling in which the spatial relationships between elements are encoded implicitly within a three-dimensional data structure.

A common attribute of all these popular modeling paradigms is that they describe shape in three spatial dimensions. In addition, an orthogonal set of axes and a unit of measure are usually assumed. Models of this type, regardless of whether they represent surface boundaries, solids, or discrete volumes, describe entities from a three-dimensional *Euclidean geometry*.

Using Euclidean geometry as a basis for describing models has many practical advantages. Euclidean geometry is the geometry of our everyday experience. Our common notions of length, area, and volume are all deeply rooted within a Euclidean description. Unfortunately, the extraction of Euclidean information from two-dimensional images is known to be a difficult problem [Kanatani89]. This is because Euclidean geometry is an unnatural choice for describing the relationships between images and image points. A better choice is *projective geometry*. The value of Euclidean geometric models for image synthesis has been established. But, the question still remains—how might images be synthesized based on projective relationships?

1.2 Thesis Statement and Contributions

This research presents an alternative modeling paradigm in which the underlying representation is a set of two-dimensional images rather than a collection of three-dimensional geometric primitives. The resulting visualization process involves a systematic projective mapping of the points from one image to their correct position in another image. Correctness will be defined as being consistent with the equivalent projections of a static three-dimensional Euclidean geometry. In short, I propose to generate valid views of a three-dimensional scene by synthesizing images from images without an explicit Euclidean representation.

The central thesis of this research is that

> *Three-dimensional computer graphics can be synthesized using only images and information derivable from them. The resulting computation process is a signal reconstruction problem rather than a simulation as in traditional three-dimensional computer graphics.*

Three central problems must be addressed in order to synthesize three-dimensional computer graphics from images. The first problem is the determination of mapping functions that move the points of a source image to new positions in a desired image. This mapping is constrained to be consistent with reprojections of the three-dimensional scene depicted in the source. In Chapter 3 I derive this family of warping functions. The second problem of image-based computer graphics is the accurate determination of the subset of source points that are visible from other viewpoints in the absence of a geometric description. Chapter 3 presents an algorithm for computing such a visibility solution for the case of planar projections. This result is expanded and generalized to other viewing surfaces in Chapter 6. The third issue that must be resolved in order to build viable image-based computer graphics systems is the

reconstruction of continuous models from sampled image representations. Discretely sampled images are a common form of data representation that are amenable to computation, and the classical approaches to two-dimensional image reconstruction are not directly extensible to the nonlinear behaviors induced by projection and changes in visibility. In Chapter 3, I will address many of the issues of this reconstruction and make the argument that, in the absence of additional information, the problem is essentially ambiguous. I then propose two alternative approaches to the reconstruction problem based on two extreme assumptions about the three-dimensional space depicted by a scene.

This dissertation contributes to the field of computer science a family of algorithms useful for rendering image-based computer graphics. Included among these are

- an image-warping equation for transforming the points of one image to their appropriate position in another image as seen from a different viewing point
- a visibility algorithm that determines which points from one image can be seen from another viewing point without any knowledge of the shapes represented in the original image
- a method for approximating the continuous shapes of the visible figures in an image when given only a sampled image representation

Furthermore, this research establishes new links between the synthesis techniques of computer graphics and the analysis methods of computer vision. This work also compares and contrasts the image-based and geometry-based approaches to computer graphics.

I will provide substantial evidence supporting the following assertions:

- three-dimensional computer graphics can be synthesized using only images and information derivable from them
- image-based computer graphics is a signal reconstruction problem rather than a simulation problem like traditional computer graphics
- given known viewing parameters, an image-to-image mapping function can be established that is consistent with arbitrary projections of a static three-dimensional Euclidean geometry from the same view
- even with unknown viewing parameters, under a reasonable set of constraints, an image-to-image mapping function can be established that is consistent with arbitrary projections of a static three-dimensional Euclidean geometry from the same view

- the visibility ordering of a reprojected-perspective image can be established without explicit knowledge of the geometry represented in the original projection
- images synthesized using image-based methods can be generated using fewer operations than geometry-based methods applied to an equivalent Euclidean representation
- the images synthesized from image-based methods are at least as realistic as those images synthesized from geometric models using simulation methods
- the model acquisition process in image-based rendering is at least as easy as extracting Euclidean geometric information from images

Having provided this short overview of the problem addressed by my research, I will now explain why a solution to this problem is important.

1.3 Motivation

While geometry-based rendering technology has made significant strides towards achieving photorealism, the process of creating accurate models is still nearly as difficult as it was twenty-five years ago. Technological advances in three-dimensional scanning methods provide some promise for simplifying the process of model building. However, these automated model acquisition methods also verify our worst suspicions—the geometry of the real-world is exceedingly complex.

Ironically, one of the primary subjective measures of image quality used in geometry-based computer graphics is the degree to which a rendered image is indistinguishable from a photograph. Consider, though, the advantages of using photographs (images) as the underlying scene representation. Photographs, unlike geometric models, are both plentiful and easily acquired, and needless to say, photorealistic. Images are capable of representing both the geometric complexity and photometric realism of a scene in a way that is currently beyond our modeling capabilities.

Throughout the three-dimensional computer graphics community, researchers, users, and hardware developers alike, have realized the significant advantages of incorporating images, in the form of texture maps, into traditional three-dimensional models. Texture maps are commonly used to add fine photometric details as well as to substitute for small-scale geometric variations. Texture mapping can rightfully be viewed as the precursor to image-

based computer graphics methods. In fact, the image-based approach discussed in this thesis can be viewed as an extension of texture-mapping algorithms commonly used today. However, unlike a purely image-based approach, an underlying three-dimensional model still plays a crucial role with traditional texture maps.

In order to define an image-based computer graphics method, we need a principled process for transforming a finite set of known images, which I will henceforth refer to as *reference images*, into new images as they would be seen from arbitrary viewpoints. I will call these synthesized images, *desired images*.

Techniques for deriving new images based on a series of reference images or drawings are not new. A skilled architect, artist, draftsman, or illustrator can, with relative ease, generate accurate new renderings of an object based on surprisingly few reference images. These reference images are, frequently, illustrations made from certain cardinal views, but it is not uncommon for them to be actual photographs of the desired scene taken from a different point-of-view. One goal of this research is to emulate the finely honed skills of these artisans by using computational powers.

While image-based computer graphics has come many centuries after the discovery of perspective illustration techniques by artists, its history is still nearly as long as that of geometry-based computer graphics. Progress in the field of image-based computer graphics can be traced through at least three different scientific disciplines. In *photogrammetry* the problems of distortion correction, image registration, and photometrics have progressed toward the synthesis of desired images through the composition of reference images. Likewise, in *computer vision*, problems such as navigation, discrimination, and image understanding have naturally led in the same direction. In *computer graphics*, as discussed previously, the progression toward image-based rendering systems was initially motivated by the desire to increase the visual realism of the approximate geometric descriptions. Most recently, methods have been introduced in which the images alone constitute the overall scene description. The remainder of this introduction discusses previous works in image-based computer graphics and their relationship to this work.

1.4 Previous Work

In recent years, images have supplemented the image generation process in several different capacities. Images have been used to represent approximations of the geometric

contents of a scene. Collections of images have been employed as databases from which views of a desired environment are queried. And, most recently, images have been employed as full-fledged scene models from which desired views are synthesized. In this section, I will give an overview of the previous work in image-based computer graphics partitioned along these three lines.

1.4.1 Images as approximations

Images, mapped onto simplified geometry, are often used as an approximate representation of visual environments. Texture mapping is perhaps the most obvious example of this use. Another more subtle approximation involves the assumption that all, or most, of the geometric content of a scene is located so far away from the viewer that its actual shape is inconsequential.

Much of the pioneering work in texture mapping is attributable to the classic work of Catmull, Blinn, and Newell. The flexibility of image textures as three-dimensional computer graphics primitives has since been extended to include small perturbations in surface orientation (bump maps) [Blinn76] and approximations to global illumination (environment and shadow mapping) [Blinn76] [Greene86] [Segal92]. Recent developments in texture mapping have concentrated on the use of visually rich textures mapped onto very approximate geometric descriptions [Shade96] [Aliaga96][Schaufler96].

Texture mapping techniques rely on mapping functions to specify the relationship of the texture's image-space coordinates to their corresponding position on a three-dimensional model. A comprehensive discussion of these mapping techniques was undertaken in [Heckbert86]. In practice the specification of this mapping is both difficult and time consuming, and often requires considerable human intervention. As a result, the most commonly used mapping methods are restricted to very simple geometric descriptions, such as polygonal facets, spheres and cylinders.

During the rendering process, these texture-to-model mapping functions undergo another mapping associated with the perspective-projection process. This second mapping is from the three-dimensional space of the scene's representation to the coordinate space of the desired image. In actual rendering systems, one or both of these mapping processes occurs in the opposite or inverse order. For instance, when ray tracing, the mapping of the desired image's coordinates to the three-dimensional coordinates in the space of the visible object occurs

first. Then, the mapping from the three-dimensional object's coordinates to the texture's image-space coordinates is found. Likewise, in z-buffering based methods, the mapping from the image-space coordinate to texture's image-space occurs during the rasterization process. These inverse methods are known to be subject to aliasing and reconstruction artifacts. Many techniques, including mip-maps [Williams83] and summed-area tables [Crow84] [Glassner86], have been suggested to address these problems with texture mapping.

Another fundamental limitation of texture maps is that they rely solely on the geometry of the underlying three-dimensional model to specify the object's shape[1]. The precise representation of three-dimensional shape using primitives suitable for the traditional approach to computer graphics is, in itself, a difficult problem which has long been an active topic in computer graphics research. When the difficulties of representing three-dimensional shape are combined with the issues of associating a texture coordinate to each point on the surface (not to mention the difficulties of acquiring suitable textures in the first place), the problem becomes even more difficult.

It is conceivable that, given a series of photographs, a three-dimensional computer model could be assembled. And, from those same photographs, various figures might be identified, cropped, and the perspective distortions removed so that a texture might be extracted. Then, using traditional three-dimensional computer graphics methods, renderings of any desired image could be computed. While the process outlined is credible, it is both tedious and prone to errors. The image-based approach to computer graphics described in this thesis attempts to sidestep many of these intermediate steps by defining mapping functions from the image-space of one or more reference images directly to the image-space of a desired image.

A new class of scene approximation results when an image is mapped onto the specific geometric figure of the set of points at infinity. The mapping is accomplished in exactly the same way that texture maps are applied to spheres, since each point on a sphere can be directly associated with another point located an infinite distance from the sphere's center. This observation is also the basis of the environment maps mentioned previously. Environments maps were, however, designed to be observed indirectly as either reflections within other objects or as representations of a scene's illumination environment. When such an image

[1] Displacement maps [Upstill90] and, to a lesser extent, bump maps are exceptions to this limitation.

mapping is intended for direct viewing, a new type of scene representation results. This is characteristic of the work by Regan and Pose and the QuickTimeVR system.

Regan and Pose [Regan94] have described a *hybrid system* in which panoramic reference images are generated using traditional geometry-based rendering systems at available rendering rates, and interactive rendering is provided by the image-based subsystem. Their work demonstrates some of the practical advantages of image-based computer graphics over traditional geometric approaches. Among these are higher performance and reduced latency. In Regan and Pose's system, at any instant a user interacts with just a single reference image. Their approach allows the user to make unconstrained changes in orientation about a fixed viewing point, using a technique called *address recalculation*. Regan and Pose also discuss a strategy for rendering nearby scene elements and integrating these results with the address recalculation results. This approximation amounts to treating most scene elements as being placed at infinity.

The image recalculation process of Regan and Pose is a special case of my image-based rendering method, called *reprojection*. Reprojection, like address recalculation, allows for the generation of arbitrary desired views where all of the points in the scene are considered to be an infinite distance from the observer. This restriction results in a loss of both kinetic and stereoscopic depth effects. However, with a very small modification, the same reprojection method can be extended to allow objects to appear any distance from the viewer. In [Mark97] the image-based methods described here have been applied to a hybrid rendering system similar to the one described by Regan and Pose. Mark's system demonstrates significant advantages over address recalculation, and, by employing more than one reference image, he shows how the need for rendering nearby scene elements can be eliminated.

A commercially available image-based computer graphics system, called QuickTimeVR [Chen95], has been developed by Apple Computer Incorporated. In QuickTimeVR, the underlying scene is represented by a set of cylindrical images. The system is able to synthesize new planar views in response to a user's input by warping one of these cylindrical images. This is accomplished at highly interactive rates (greater than 20 frames per second) and is done entirely in software. The system adapts both the resolution and reconstruction filter quality based on the rate of the interaction. QuickTimeVR must be credited with exposing to a wide audience the vast potential of image-based computer graphics. In particular, because of its

ability to use a series of stitched photographs as a reference image, it has enabled many new computer graphics applications.

The QuickTimeVR system is also a reprojection method much like the address-recalculation method described by Regan and Pose. Therefore, it is only capable of describing image variations due to changes in viewing orientation. Translations of the viewing position can only be approximated by selecting the cylindrical image whose center-of-projection is closest to the current viewing position.

The panoramic representation afforded by the cylindrical image description provides many practical advantages. It provides for the immersion of the user within the visual environment, and it eliminates the need to consider the viewing angle when determining which reference image is closest to a desired view. However, several normal photographs are required to create a single cylindrical projection. These images must be properly registered and then reprojected to construct the cylindrical reference image.

QuickTimeVR's image-based approach has significant similarity to the approach described here. Its rendering process is a special case of the cylinder-to-plane warping equation (described in Chapter 4) in the case where all image points are computed as if they were an infinite distance from the observer. However, the more general warping equation presented in this thesis allows for the proper reprojection of points at any depth.

1.4.2 Images as databases

The movie-map system by Lippman [Lippman80] was one of the earliest attempts at constructing a purely image-based computer graphics system. In a movie-map, many thousands of reference images were stored on interactive video laser disks. These images could be accessed randomly, according to the current viewpoint of the user. The system could also accommodate simple panning, tilting, or zooming about these fixed viewing positions. The movie-map approach to image-based computer graphics can also be interpreted as a table-based approach, where the rendering process is replaced by a database query into a vast set of reference images. This database-like structure is common to many image-based computer graphics systems.

Movie-maps were unable to reconstruct all possible desired views. Even with the vast storage capacities currently available on media such as laser disks, and the rapid development

of even higher capacity storage media, the space of all possible desired images appears so large that any purely database-oriented approach will continue to be impractical in the near future. Also, the very subtle differences between images observed from nearby points under similar viewing conditions brings into question the overall efficiency of this approach. The image-based rendering approach described in this thesis could be viewed as a reasonable compression method for movie maps.

Levoy and Hanrahan [Levoy96] have described another database approach to computer graphics in which the underlying modeling primitives are rays rather than images. The key innovation of this technique, called *light-field rendering*, is the recognition that all of the rays that pass through a slab of empty space which is enclosed between two planes can be described using only four parameters (a two-dimensional coordinate on each plane) rather than the five dimensions required for the typical specifications of a ray (a three-dimensional coordinate for the ray's origin and two angles to specify its direction.) This assumes that all of the rays will enter the slab at one plane and exit through the other. They also describe an efficient technique for generating the ray parameters needed to construct any arbitrary view.

The subset of rays originating from a single point on a light field's entrance plane can be considered as an image corresponding to what would have been seen at that point. Thus, the entire two-parameter family of ray subsets originating from points on the entrance plane can be considered as a set of reference images.

During the rendering process, the three-dimensional entrance and exit planes are projected onto the desired viewing plane. The final image is constructed by determining the image-space coordinates of the two points visible at a specified pixel coordinate (one coordinate from the projected image of the entrance plane, and the second from the image of the exiting plane). The desired ray can be looked up in the light field's database of rays using these four parameter values.

Image generation using light fields is inherently a database query process, much like the movie map image-based process. The storage requirements for a light-field's database of rays can be very large. Levoy and Hanrahan discuss a lossy method for compressing light fields that attempts to minimize some of the redundancy in the light-field representation.

The lumigraph [Gortler96] is another ray-database query algorithm closely related to the light-field. It also uses a four-dimensional parameterization of the rays passing through a pair of planes with fixed orientations. The primary differences in the two algorithms are the acquisition methods used and the final reconstruction process. The lumigraph, unlike the light field, considers the geometry of the underlying models when reconstructing desired views. This geometric information is derived from image segmentations based on the silhouettes of image features. The preparation of the ray database represented in a lumigraph requires considerable preprocessing when compared to the light field. This is a result of the arbitrary camera poses that are used to construct the database of visible rays. In a light-field, though, the reference images are acquired by scanning a camera along a plane using a motion platform.

The lumigraph reconstruction process involves projecting each of the reference images as they would have appeared when mapped onto the exit plane. The exit plane is then viewed through an aperture on the entrance plane surrounding the center-of-projection of the reference image. When both the image of the aperture on the entrance plane and the reference image on the exit plane are projected as they would be seen from the desired view, the region of the reference image visible through the aperture can be drawn into the desired image. The process is repeated for each reference image. The lumigraph's approach to image-based three-dimensional graphics uses geometric information to control the blending of the image fragments visible through these apertures.

Like the light-field, the lumigraph is a data intensive rendering process. The image-based approach to computer graphics discussed in this research attempts to reconstruct desired views based on far less information. First, the reference image nearest the desired view is used to compute as much of the desired view as possible. Regions of the desired image that cannot be reconstructed based on the original reference image are subsequently filled in from other reference images.

The image-based approach proposed in this thesis can also be considered as a compression method for both light fields and lumigraphs. Redundancy of the database representation is reduced by considering the projective constraints induced by small variations in the viewing configuration. Thus, an image point, along with its associated mapping function, can be used to represent rays in many different images from which the same point is visible.

1.4.3 Images as models

Computer graphics methods have been developed where images serve as the underlying representation. These methods handle the geometric relationships between image points very differently. In the case of *image morphing*, the appearance of a dynamic Euclidean geometry is often a desired effect. Another method, known as *view interpolation* relies on an approximation to a true projective treatment in order to compute the mapping from reference images to desired images. Also, additional Euclidean geometric information is required to determine correct visibility. A third method, proposed by Laveau and Faugeras, is based on an entirely projective approach to image synthesis and, therefore, is closely related to my work. However, they have chosen to make a far more restrictive set of assumptions in their model, which allows for an ambiguous Euclidean interpretation.

Image morphing is a popular image-based computer graphics technique [Beier92], [Sietz96], [Wolberg90]. Generally, morphing describes a series of images representing a transition between two reference images. These reference images can be considered as endpoints along some path through time and/or space. An interpolation process is used to reconstruct intermediate images along the path's trajectory. Image morphing techniques have been used to approximate dynamic changes in camera pose [Sietz96], dynamic changes in scene geometry [Wolberg90], and combinations of these effects. In addition to reference images, the morphing process requires that some number of points in each reference be associated with corresponding points in the other. This association of points between images is called a *correspondence*. This extra information is usually hand crafted by an animator. Most image-morphing techniques make the assumption that the transition between these corresponding points occurs at a constant rate along the entire path, thus amounting to a linear approximation. Also, a graduated blending function is often used to combine the reference images after they are mapped from their initial configuration to the desired point on the path. This blending function is usually some linear combination of the two images based on what percentage of the path's length has been traversed. The flexibility of image-morphing methods, combined with the fluidity and realism of the image transitions generated, have made a dramatic impact on the field of computer graphics, especially when considering how recently they have been developed.

A subset of image morphing, called *view morphing*, is a special case of image-based computer graphics. In view morphing the scene geometry is fixed, and the pose of the desired views lies on a locus connecting the centers-of-projection of the reference images. With the

notable exception of the work done by Seitz, general image morphing makes no attempt to constrain the trajectory of this locus, the characteristics of the viewing configurations, or the shapes of the objects represented in the reference images. In this thesis, I will propose image mapping functions which will allow desired images to be specified from any viewing point, including those off the locus. Furthermore, these mapping functions, like those of Sietz, are subject to constraints that are consistent with prescribed viewing conditions and the static Euclidean shape of the objects represented in the reference images.

Chen and Williams [Chen93] have presented a *view interpolation* method for three-dimensional computer graphics. It uses several reference images along with image correspondence information to reconstruct desired views. Dense correspondence[2] between the pixels in reference images is established by a geometry-based rendering preprocess. During the reconstruction process, linear interpolation between corresponding points is used to map the reference images to the desired viewpoints, as in image morphing. In general, this interpolation scheme gives a reasonable approximation to an exact reprojection as long as the change in viewing position is slight. Indeed, as the authors point out, in some viewing configurations this interpolation is exact.

Chen and Williams acknowledge, and provide a solution for, one of the key problems of image-based rendering—visible surface determination. Chen and Williams presort a quadtree compressed flow-field[3] in a back-to-front order according to the scene's depth values. This approach works only when all of the partial sample images share a common gaze direction and the synthesized viewpoints are restricted to stay within 90 degrees of this gaze angle. The underlying problem is that correspondence information alone (i.e., without depth values) still allows for many ambiguous visibility solutions unless we restrict ourselves to special flow fields that cannot fold (such as rubber-sheet local spline warps or thin-plate global spline warps). This problem must be considered in any general-purpose image-based rendering system, and ideally, it should be accomplished without an appeal to a geometric scene description.

Establishing the dense correspondence information needed for a view interpolation system can also be problematic. Using pre-rendered synthetic images, Chen and Williams were

---

[2] Dense correspondence refers to the case when nearly all points of one image are associated with points in a second.

[3] A flow-field represents correspondences as a vector field. A vector is defined at each image point indicating the change in image coordinates between reference images.

able to determine the association of points by using the depth values stored in a z-buffer. In the absence of a geometric model, they suggest that approximate correspondence information can be established for all points using correlation methods[4].

The image-based approach to three-dimensional computer graphics described in this research has a great deal in common with the view interpolation method. For instance, both methods require dense correspondence information in order to generate the desired image, and both methods define image-space to image-space mapping functions. In the case of view interpolation, the correspondence information is established on a pairwise basis between reference images. As a result the storage requirements for the correspondence data associating N reference images is $\boldsymbol{O}(N^2)$. My approach is able to decouple the correspondence information from the difference in viewing geometries. This allows a single flow field to be associated with each image, requiring only $\boldsymbol{O}(N)$ storage. Furthermore, the approach to visibility used in my method does not rely on any auxiliary geometric information, such as the presorted image regions based on the z-values, used in view interpolation.

Laveau's and Faugeras' [Laveau94] image-based computer-graphics system takes advantage of many recent results from computer vision. They consider how a particular projective geometric structure called an *epipolar geometry* can be used to constrain the potential reprojections of a reference image. They explain how the projective shape of a scene can be described by a fundamental matrix with scalar values defined at each image point. They also provide a two-dimensional ray-tracing-like solution to the visibility problem which does not require an underlying geometric description. Yet, it might require several images to assure an unambiguous visibility solution. Laveau and Faugeras also discuss combining information from several views, though primarily for the purpose of resolving visibility as mentioned before. By relating the reference views and the desired views by the homogenous transformations between their projections, Laveau and Faugeras can compute exact perspective depth solutions.

However, the solutions generated using Laveau and Faugeras' techniques do not reflect an unambiguous Euclidean environment. Their solution is consistent with an entire family of affine coordinate frames. They have pointed out elsewhere [Faugeraus92b] that when additional constraints are applied, such as the addition of more reference images and the requirement that a fixed camera model be used for all references images, then a unique Euclidean solution can be assured.

---

[4] Assuming that all points are mutually visible in both reference images.

The methods described by Laveau and Faugeras are very similar to the image-based approach to computer graphics described here. In Chapter 5, the relationship of an epipolar geometry and the fundamental matrix to the proposed rendering methods are discussed in detail. The major difference in my approach is that I assume that more information is available than simply the epipolar geometries between reference images. This subject is also discussed in detail in Chapter 5. Other significant differences are that the forward-mapping approach described here has fewer restrictions on the desired viewing position, and I provide a simpler solution to the visibility problem.

1.5 Discussion

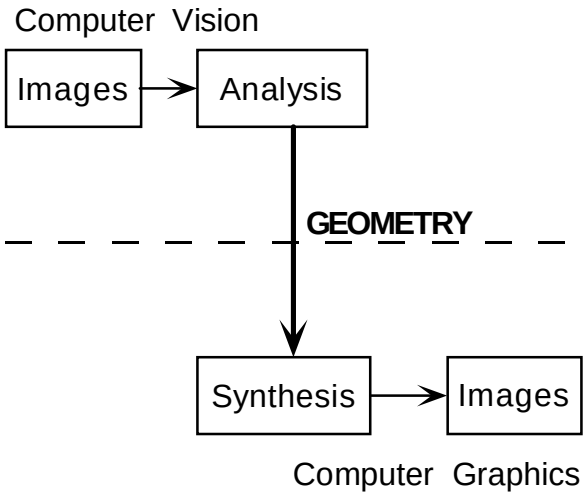

Figure 1-3: Conventional partitioning of computer vision and computer graphics

The delineation between computer graphics and computer vision has always been at the point of a geometric description. In this research I intend to draw the lines somewhat differently. Rather than beginning the image synthesis task with a geometric description, I plan to begin with images. In this chapter I presented a summary of the various geometry-based modeling methods frequently used today and explained how all of these models stem from a common approach to geometry. I suggested an image-based approach using projective geometry instead.

Images have already begun to take on increasingly significant roles in the field of computer graphics. They have been successfully used to enhance the apparent visual complexity of relatively simple geometric screen descriptions. The discussion of previous work

showed how the role of images has progressed from approximations, to databases, to actual scene descriptions.

In this thesis I will present an approach to three-dimensional computer graphics in which the underlying scene representation is composed of a set of reference images. I will present algorithms that describe the mapping of image-space points in these reference images to their image-space coordinates in any desired image. All information concerning the three-dimensional shape of the objects seen in the reference images will be represented implicitly using a scalar value that is defined for each point on the reference image plane. This value can be established using point correspondences between reference images. I will also present an approach for computing this mapping from image-space to image-space with correct visibility, independent of the scene's geometry.

Chapter 2

THE PLENOPTIC MODEL

One of the advantages of the geometry-based approach to computer graphics is that it has a well established computational model rooted in simulation. In this chapter, I describe an analogous computational model for image-based computer graphics. This model is based on the *plenoptic function,* which describes all possible images of an environment. I begin by defining a projective image. Then I present the plenoptic function and explore relevant geometric structures in its parameter space. Finally, I consider the problem of adequately sampling an environment with images.

The fundamental computation of traditional geometry-based computer graphics is the simulation of light's interaction with objects in a scene. The geometric structure and material properties of the objects, along with descriptions of the light sources and the viewing parameters, constitute a problem specification. The rendering process itself is but a simulation, however approximate, of a photographer's camera.

The field of computer graphics is built on this foundation. For instance, many previous advances can be categorized as the inclusion of a more accurate simulation model in which previously ignored effects were accounted for. These roots in simulation also enable us to recognize correct results and dismiss errors. These are advantages of a clear and concise problem statement.

The development of image-based computer graphics requires that we understand how the images comprising our model relate to the environment that they depict. Once the nature of this problem is understood, then we can set out to develop a computational model to serve as a foundation for image-based computer graphics.

I begin by refining the notion of an image. Any function that is defined over two or more independent variables can be considered as an image. For many disciplines, such as image processing, this definition is entirely adequate, but for our purposes, a more precise definition is required. In the approach to computer graphics discussed here, images will be defined as a field of measurements over two dimensions. Points within an image can be identified with a coordinate pair, (u,v). These measurements at a given point in an image might have multiple values, which is represented by a measurement vector, $\overline{\mu}(u,v)$. Each measurement is indicative of a scene element that is located along an infinite half line, or ray, which passes through the image point where the measurement is recorded. The crucial geometric entities that are represented by an image are the set of rays that it describes. Thus, any point on an image is completely characterized by both its measurements and its ray. In general, all of the rays for a particular image will be considered to originate from a common origin, called the *center-of-projection*. This class of two-dimensional images is sometimes called *perspective-projected images*.

In classical image processing, the only geometric relationships considered are those relating the two-dimensional neighborhoods defined in the image's own (u,v) parameter space. Image-based computer graphics considers a more global three-dimensional geometric neighborhood. Given this larger geometric context, it is possible to discuss an entire space of potential images and to identify geometric relationships between the points represented in these different images. In this chapter, I will formalize the notion of a space containing all possible images of a given environment, and then I will discuss various geometric structures in this space.

2.1 The Plenoptic Function

Adelson and Bergen [Adelson91] assigned the name *plenoptic function* (from the latin root plenus, meaning complete or full, and optic pertaining to vision) to the set of rays visible from any point in space, at any time, and over any range of wavelengths. They used this function to develop a complete taxonomy for evaluating models of low-level human vision. The plenoptic function, therefore, describes all of the radiant energy received at the point-of-view of an observer rather than the point-of-view of an object or an illumination source. They postulate

> *"… all the basic visual measurements can be considered to characterize local change along one or two dimensions of a single function that describes the structure of the information in the light impinging on an observer."*

Adelson and Bergen further formalized this functional description by providing a parameter space over which the plenoptic function is defined. Imagine an idealized eye that can be freely positioned at any point in space (V_x, V_y, V_z). From there, a viewing direction can be selected by choosing an azimuth and an elevation angle (θ, ϕ), as well as a band of wavelengths, λ, from which measurements will be taken. In the case of a dynamic scene, we can additionally choose the time, *t*, at which we wish to evaluate the function. This results in the following form for the plenoptic function:

$$\mu = Plenoptic(\theta, \phi, \lambda, V_x, V_y, V_z, t)$$

Equation 2-1: Plenoptic Function

Ideally, the plenoptic function is continuous over the range of parameters for which it is defined. The following figure depicts the geometric elements of this relationship.

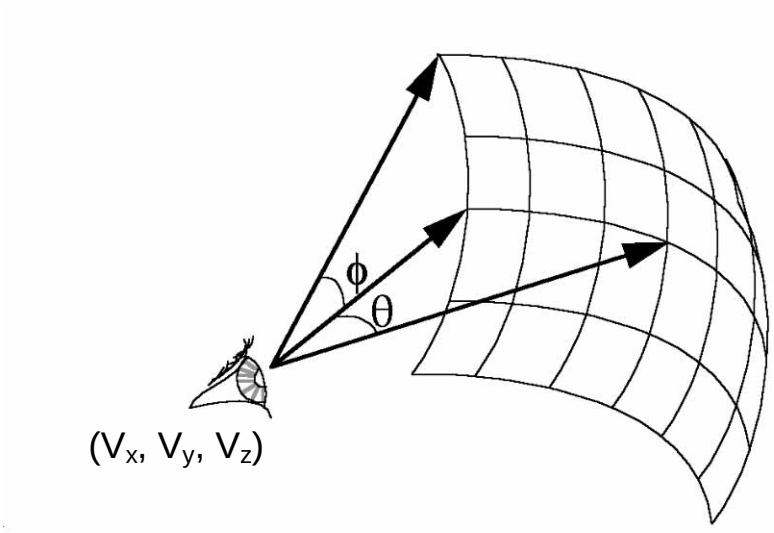

Figure 2-1: Parameters of the plenoptic function

In traditional computer-graphics terms, the plenoptic function can be considered as the set of all possible environment maps that can be defined for a given scene. For the purposes of visualization, one can consider the plenoptic function as both a scene representation and a rendering method. The process of generating a desired image of a scene from a plenoptic function requires an appropriate value for a viewing point, (V_x, V_y, V_z), the selection of a viewing time, t, and the specification of a desired field-of-view as a range of (θ, ϕ). Once these parameters are specified, the desired image is synthesized by integrating over the range of

wavelengths, λ, associated with the photometric measurements. Unfortunately, the plenoptic function for a given scene is seldom available.

However, any perspective-projected image is a subset of an environment's plenoptic function. Its center-of-projection defines a viewing point, and its field-of-view defines a solid angle over which values of θ and ϕ are defined. The photometric measurements represented in the image indicate known values of the plenoptic function. Thus, any set of reference images from an environment represents a sparse set of samples from that scene's plenoptic function. Given enough of these sparse samples, it might be possible to reconstruct a suitable approximation of the entire function over some range of input parameters. Using this derived approximation, the rendering process can proceed as before.

Given a sparse subset of a plenoptic function, the underlying problem of image-based computer graphics is how to best reconstruct a continuous approximation of the entire plenoptic function over the desired domain. From this approximation, the process of generating desired images is straightforward. This computational approach of image-based computer graphics is quite different from that of geometry-based methods. Whereas the rendering process used for geometry-based representations is inherently simulation, the rendering process used for image-based representations is fundamentally a function-approximation or signal-reconstruction problem.

Many reconstruction processes are subject to additional external constraints that affect the approximation. The geometric relationships between sample points of the sparse set are often used to constrain function-approximation methods. For instance, when using global-spline reconstruction methods, it is common to select basis functions whose weighting values are determined by the pair-wise Euclidean distances between all available samples [Franke82]. Local-spline reconstruction methods limit the influence of each known sample point to some local neighborhood surrounding it, where the neighborhood is defined by some geometric relationship. Because these two examples are defined in Euclidean space, we can use Euclidean metrics as geometric constraints. However, alternate metrics are required when considering the geometries of non-Euclidean spaces. In the remainder of this section I will discuss several of the geometric structures defined within the five-dimensional non-Euclidean parameter space of the plenoptic function.

2.2 Geometric Structures in Plenoptic Space

The first significant geometric structure of the plenoptic function is the three-dimensional Euclidean subspace of possible viewpoints as defined by the coordinates (V_x, V_y, V_z). A point in this three dimensional subspace will be denoted as $\dot{X}$. Unless stated otherwise, it can be assumed that this space is Euclidean[5].

Another interesting structure, called a *bundle*, describes a two-dimensional subspace of the rays sharing a common origin [Coxeter74]. The geometric structure of this subspace is equivalent to the surface of a unit sphere. Usually, both reference and desired images will represent some portion of such a bundle. Often it will be useful to specify an element from this two-dimensional space of rays relative to the coordinate bases of viewing points, rather than the two angle parameters (θ, ϕ). In this three-dimensional space, the rays are overspecified. Therefore, all of the ray coordinates that are related by a positive scale factor will be considered as equivalent.

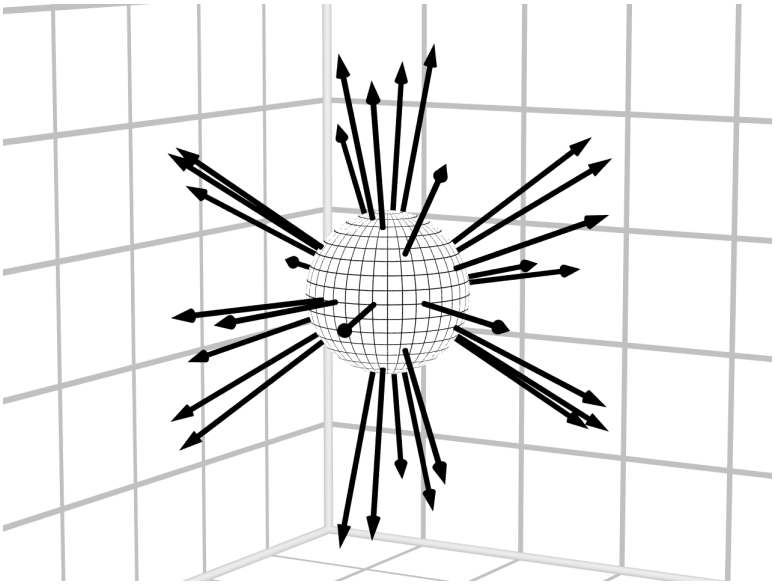

Figure 2-2: A bundle of rays

A third geometric structure, a planar subspace, can be specified in several ways. The standard Euclidean specification via three points from the viewing subspace can be used. Also, two viewing points and a ray, as well as one viewing point and a line through the bundle subspace at that point, identify a plane. There are subtle differences in these three specifications. In addition to identifying a plane, the three points also identify a convex region. Two viewing

[5] The basis vectors are mutually orthogonal and of unit length.

points and a ray divide the plane into two bounded regions, whereas, a viewing point and a line simply identify an infinite plane.

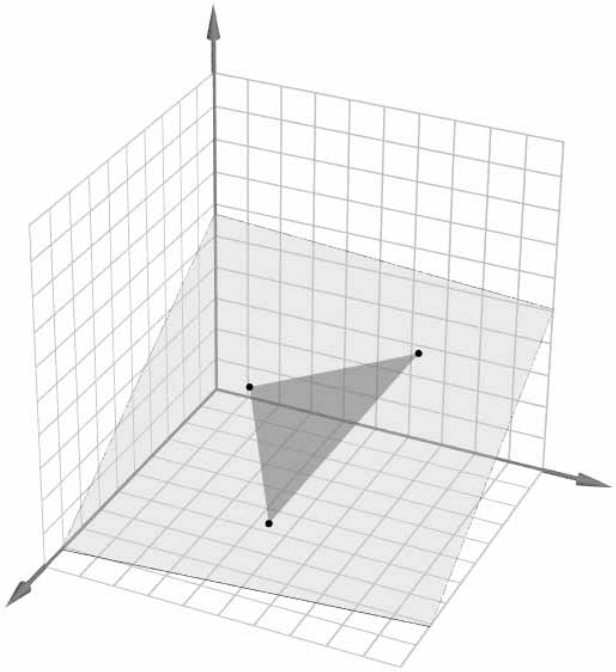

Figure 2-3: A plane and convex region specified by three points

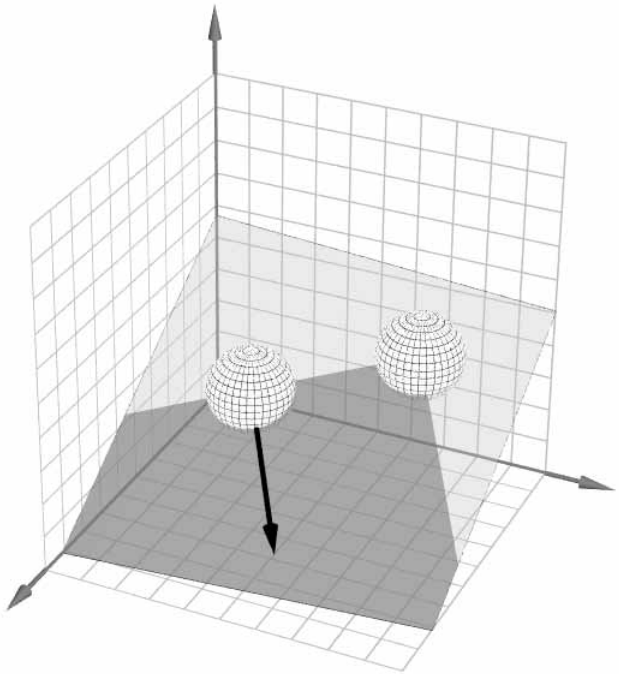

Figure 2-4: A plane and planar subspace specified by two viewing points and a ray

The darkened region of Figure 2-4 a planar region that is bounded by two edges having a common vertex at one of the two viewpoints. Any point within this bounded region might interact with those points along the specified ray. points

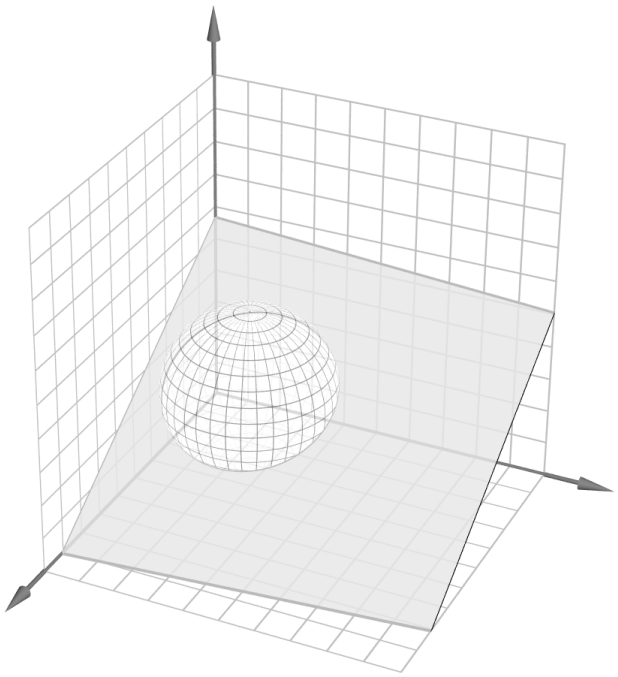

Figure 2-5: A plane specified by a viewing point and a great circle

A *correspondence* is a geometric structure defined by two rays originating from different viewpoints that intersect at a common point. Any two such rays will lie in a common plane. Therefore, a correspondence identifies three points, a plane, and a convex region.

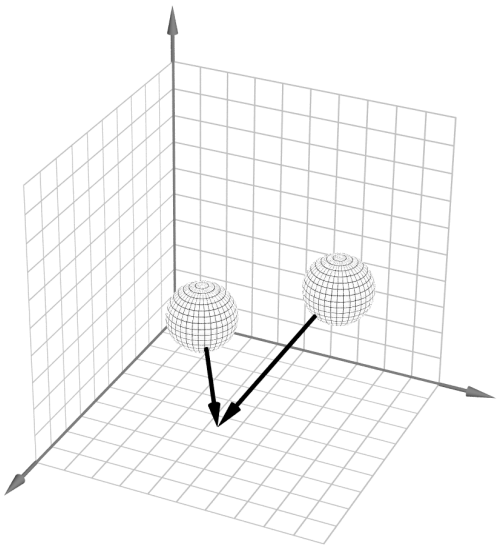

Figure 2-6: A correspondence

2.3 Alternative Models

The plenoptic function is a representation of a set of photometric measurements taken along a space of rays with significant similarities to the light-field [Levoy96] and the lumigraph [Gortler96]. The plenoptic function, though, employs five spatial dimensions, V_x, V_y, V_z, θ, and ϕ. Four dimensions, u, v, s and t are used by the light-field and lumigraph methods.

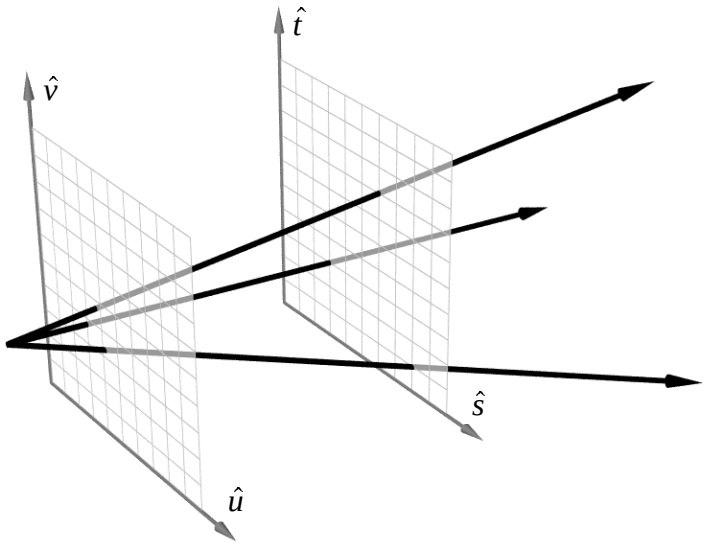

Figure 2-7: The parameterization of rays used in both light-fields and lumigraphs

The addition of this extra spatial dimension overcomes some of the limitations inherent in the light-field and lumigraph representations. These include the directed nature of the rays from the entrance plane to the exit plane, and the requirement that the bounded region of space be empty for viewing points inside of the bounded region. However, the additional spatial dimension used in the plenoptic function entails a dramatic increase in model size if a database-query approach is used.

2.4 Sampling an Environment

The single most difficult aspect of using an approximation method is determining whether a given sparse set of sample data is sufficient to represent the desired function. A general solution to this problem might require constraints on both the sampling density and the function being represented.

Consider Shannon's sampling theorem as an example. In order to guarantee a proper reconstruction, Shannon's theorem requires that the parameter space of the function be

Euclidean and that the sampling density be uniform along each spatial dimension. In addition, the function being represented is constrained to have no sinusoidal component[6] whose period is smaller or equal to the space separating two sample points.

In the traditional approach to three-dimensional computer graphics, it is expected that there should be few geometric restrictions on the environment being represented. Therefore, we have come to accept that the entire burden of proper reconstruction should fall on the rendering method. There are reasonable arguments against this approach. The purely mathematical formulations of geometry that are commonly used as scene elements are themselves only approximations to the real objects that they represent. While these models might be based on actual measurements taken from the real-world, they do not typically represent the accuracy or scale of these measurements. Even when models result from computer design methods, they are still not accurate reflections of realizable objects, unless manufacturing and tooling tolerances are incorporated into their representation.

A general sampling theorem for plenoptic functions is an interesting topic for future research in image-based computer graphics. It appears likely that such a solution will place some geometric requirements on the scene being represented. Alternatively, it might also be possible to define a heuristic method for identifying a sufficient plenoptic function sampling that is scene dependent. Such a method might be based on some minimal geometric constraints on the scene, such as a minimal scales for both localizing points and resolving those points when projected.

In the absence of a general solution, there are still several useful results that can be stated relating to the reconstruction of an accurate function approximation. These results can be expressed in terms of the geometric structures of the plenoptic parameter space that have already been identified.

First, in order to accurately reconstruct a point in the viewing space, the image of that point must appear in at least one reference image, and the origin of that reference image, its center-of-projection, must be identified. And, if we depend solely on correspondences to identify points in the viewing space then the image of each point must appear in at least two reference images, whose centers-of projection are identified.

---

[6] When transformed into an equivalent Fourier representation.

Second, the ability to localize a point in a viewing space depends on the accuracy to which the image of that point can be resolved in the reference image. Thus, the exactness of a plenoptic function's approximation depends on the resolution and solid angle of the reference images.

Other classes of interesting reconstruction possibilities arise when the centers-of-projection cannot be identified. For instance, with relative knowledge of two of the positions of one or more reference images, it is possible to identify the relative position of a point in the same viewing space. Even when the absolute distance separating two centers-of-projection is not known, a correspondence can identify the position of a point relative to this unknown separation.

Suppose that the two correspondences can be identified in two reference images, each with two distinct viewing positions, and the correspondences can be shown not to lie in a common plane with the viewing positions. Then these four unknown points, the two viewing positions and the two identified points, constitute a basis for assigning coordinates to all other points in the viewing space relative to their positions. A similar configuration arises when a correspondence can be established for a single point in all combinations of three reference images.

2.5 Summary

The plenoptic function, introduced here, will provide a foundation for computing new images based on other reference images. This function is defined over five spatial dimensions, and it uniquely identifies any ray within an environment. Any projective image is a subset of a plenoptic space. Various geometric structures can be identified in a plenoptic space that can be used to establish relationships between images. These relationships will allow us to reconstruct new representations of the environment from which the reference images were taken.

The image-based computer graphics method described in this thesis will construct an approximation of the plenoptic function for use as a visualization model. By evaluating this function at various points in the parameter space, desired images can be rendered. The initial plenoptic-function approximation will use the photometric information from a single reference image. Geometric information from the scene can be used to identify the visible reference-image points. In the absence of such geometric information, other reference images can be used to establish the correspondences needed to identify these points. However, once this

correspondence information has been established, its redundancy is eliminated from the approximation model. The definition of plenoptic-function approximations based on a single reference image is not only an interesting limiting case, but it is also of surprising utility.

Chapter 3

A WARPING EQUATION

In this chapter, I will present a complete image-based computer graphics system. This includes a function for mapping points from a reference image to a desired image, a method for determining which reference points are visible in the desired image, and a method for reconstructing the desired image from these mapped reference points. All of these methods consider the special case when the plenoptic-function approximation is based on a single reference image.

The plenoptic-function approximation describes a *mapping* of the points represented in the reference image to coordinates in a desired image according to the selected viewing parameters. These mappings from one image to another are called *image warps.* The warping functions derived here make specific assumptions concerning the geometry of the reference image. These assumptions, however, cover a wide range of useful applications, and in Chapters 4 and 5 many of these results will be further generalized.

However, the derived warping function is not a one-to-one mapping. Therefore, a method to resolve visibility at each point is required. I will describe a simple method for determining the visible reference image points. This method does not rely on any geometric information from the scene, but only on the change in pose between the reference and viewing positions.

Since images are usually represented as two-dimensional arrays of discrete samples, a reconstruction method is required so that the transformed points of the reference image will appear continuous in the desired image. I will describe two methods for this reconstruction. The first method assumes that the environment is sparsely populated with points, while the second assumes that it is densely populated.

3.1 From Images to Rays

The plenoptic function describes all of the rays visible from any viewing position over a range of wavelengths. For the moment I will consider the time, the viewing position, and the range of wavelengths to be fixed. The remaining parameters of the plenoptic function describe the geometric relationship of the rays originating from this fixed viewpoint.

In the formulation of the plenoptic function given in Chapter 2, the specification of any particular ray is determined by two angles on a unit sphere. While this parameterization sufficiently describes the full range and dimension of the set of rays, it is not a very convenient representation for analysis or computation. Here I will consider an alternative parameterization of rays based on a general *planar-pinhole camera model*. This is the same planar-pinhole camera model that is commonly used in traditional three-dimensional computer graphics and computer vision. In Chapter 4 I will discuss several alternate formulations of a pinhole camera, and I will explain the physical significance and applications of these different parameterizations.

3.2 A General Planar-Pinhole Model

The planar-pinhole camera is an idealized device for collecting luminous intensities along rays passing through a single point in space, called the *center-of-projection*, and contained within some solid angle defined by a bounded planar section, called the *image plane*. The solid angle defined by the pinhole camera is well defined as long as the center-of-projection does not lie on the extended image plane. As the bounds of the image plane are extended indefinitely, the solid angle approaches 2π steradians, exactly half of the visual sphere used in the plenoptic function.

Consider the rays emanating from the origin of a three-dimensional Euclidean space with basis vectors $(\hat{i},\hat{j},\hat{k})$. Suppose also, that a second two-dimensional coordinate system is defined in the image plane, allowing each point on it to be identified by an image coordinate, (u,v), where *u* and *v* are scalar multiples of the two basis vectors, $(\hat{s},\hat{t})$, defined in the image plane. Points on this image-plane can be given coordinates that are specified relative to this coordinate system. These points, along with their assigned coordinates, are referred to as *image-space points*. Without loss of generality, we assume that the origin of image space lies at one of the corners of the bounded image plane.

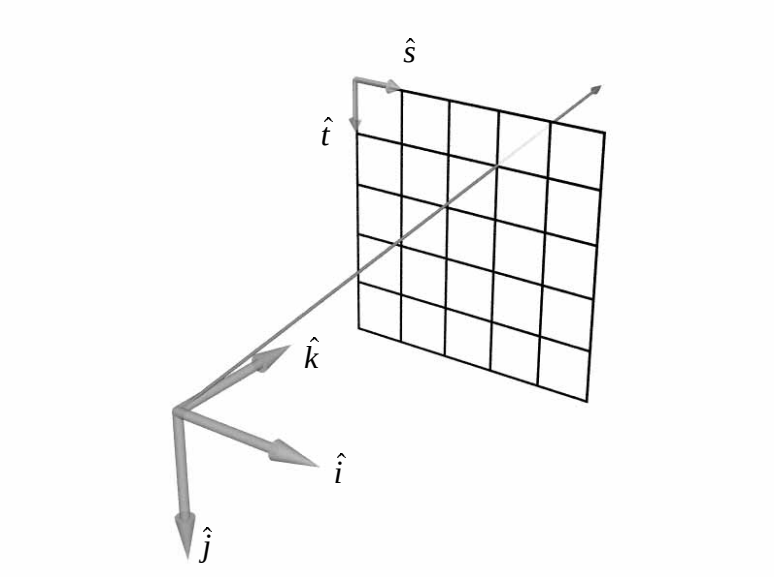

Figure 3-1: Mapping image-space point to rays

Each image-space point can be placed into one-to-one correspondence with a ray that originates from the Euclidean-space origin. This mapping function from image-space coordinates to rays can be described with a linear system:

$$\bar{d} = \begin{bmatrix} d_i \\ d_j \\ d_k \end{bmatrix} = \begin{bmatrix} a_i & b_i & c_i \\ a_j & b_j & c_j \\ a_k & b_k & c_k \end{bmatrix} \begin{bmatrix} u \\ v \\ 1 \end{bmatrix} = \mathbf{P} \begin{bmatrix} u \\ v \\ 1 \end{bmatrix}$$

Equation 3-1: Planar mapping function

where the coordinate of the image-space point is specified by the coordinate (u, v), and the resulting vector $\bar{d}$ represents the corresponding ray's direction. The entries of the mapping matrix, $\mathbf{P}$, can be easily understood by considering each column as a vector, $\bar{a}$, $\bar{b}$, and $\bar{c}$ in the same coordinate system as $\bar{d}$. This relationship is shown in Figure 3-2, where $\bar{a}$ and $\bar{b}$ are images of the $\hat{s}$ and $\hat{t}$ basis vectors in the $(\hat{i}, \hat{j}, \hat{k})$ coordinate system, and $\bar{c}$ is a vector from the ray origin to the origin of the image plane. Thus, while this parameterization is general, it still has a reasonable physical interpretation.

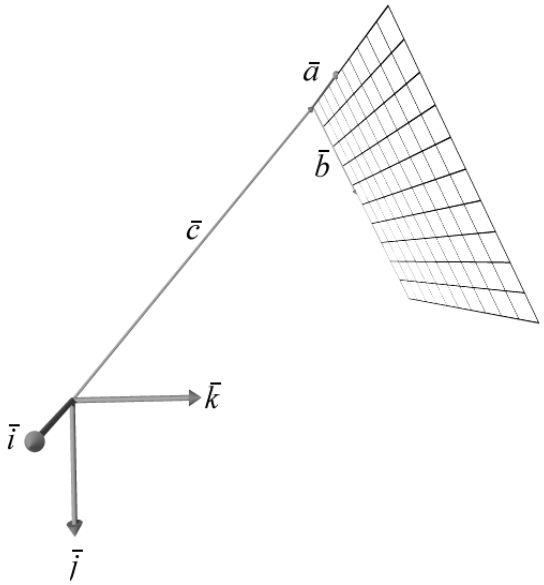

Figure 3-2: Relationship of the image-space basis vectors to the ray origin

The mapping function from image coordinates to rays is not uniquely defined. Any scalar multiple of the **P** matrix will also yield an equivalent set of image-space point-to-ray correspondences. This independence of scale is a consequence of the fact that the space of possible directions from any point in a three-dimensional space can be described using only two parameters (i.e., two angles). Thus, any representation of rays that uses unconstrained three-dimensional vectors will allow for multiple representations of the same ray.

3.3 A Warping Equation for Synthesizing Projections of a Scene

Equipped with only the simple planar-pinhole-camera model described in the previous section, an image-warping equation, which remaps those rays visible from a given viewpoint to any arbitrary viewing position, can be derived. As before, I will refer to the source image, or domain, of the warp as the *reference image*, and the resulting image, after the mapping is applied, as the *desired image*. For the moment, I will assume that both the pinhole-camera parameters of the desired and reference views are known. In addition, I will also assume that a single scalar value, called *generalized disparity* or *projective depth*, is known for all points of the reference image. The precise nature of this quantity will be discussed in more detail later in this section. For the moment it is sufficient to say that this quantity can be determined from a set of correspondences specified between images.

Throughout this section I will adopt an image-space-centered point of view for describing both the relationships and geometry of points, rather than the classic Euclidean three-space view. At first, this approach might seem awkward. However, in Chapter 5 we will see that a strict Euclidean interpretation of correspondences is but a special case of a more general result.

Consider the implications of the same point, $\dot{X}$, being sighted along rays from two different centers-of-projection, $\dot{C}_1$ and $\dot{C}_2$, specified relative to their pinhole camera models. The following diagram illustrates this configuration.

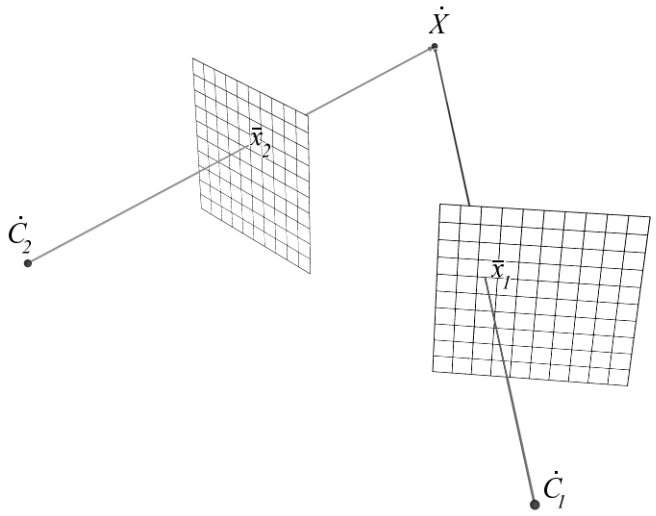

Figure 3-3: A point in three-dimensional space as seen from two pinhole cameras

The image coordinate, $\bar{x}_1$, in the first image determines a ray via the pinhole camera mapping $\bar{d}_1 = P_1\bar{x}_1$ with an origin of $\dot{C}_1$. Likewise, the image coordinate, $\bar{x}_2$, in the second image determines a ray, $\bar{d}_2 = P_2\bar{x}_2$, with origin $\dot{C}_2$. The coordinate of the point $\dot{X}$ can, therefore, be expressed using either of the following:

$$\dot{X} = \dot{C}_1 + t_1\mathbf{P}_1\bar{x}_1 = \dot{C}_2 + t_2\mathbf{P}_2\bar{x}_2$$

Equation 3-2: Specification of a 3D point in terms of pinhole-camera parameters

where t_1 and t_2 are the unknown scaling factors for the vector from the origin to the viewing plane which make it coincident with the point $\dot{X}$. This expression can be reorganized to give

$$\frac{t_2}{t_1}\mathbf{P}_2\bar{x}_2 = \frac{1}{t_1}\left(\dot{C}_1 - \dot{C}_2\right) + \mathbf{P}_1\bar{x}_1$$

Equation 3-3: Transformation of a ray in one camera to its corresponding ray in another

The left-hand side of Equation 3-3 is now a ray, as is the second term on the right hand side. If we relax our definition of equivalence to mean "equal down to some non-zero scale factor" (which is consistent with the notion that rays having the same direction are equivalent regardless of the length of the three-space vector specifying this direction[7]), then the t_2/t_1 factor can be eliminated. I will use the symbol, $\doteq$, to represent this equivalence relationship. Alternatively, we could take advantage of the property that both $\mathbf{P}_1$ and $\mathbf{P}_2$ are defined independent of scale, and absorb the scalar quantity, t_2/t_1, into the matrix $\mathbf{P}_2$. Substituting the *generalized disparity* term $\delta(\bar{x})$ for $\frac{1}{t_1}$ gives

$$\mathbf{P}_2\bar{x}_2 \doteq \delta(\bar{x}_1)\left(\dot{C}_1 - \dot{C}_2\right) + \mathbf{P}_1\bar{x}_1$$

Equation 3-4: Simplified planar ray-to-ray mapping

The name *generalized disparity* is derived from the stereo disparity quantity used in depth-from-stereo computations. In the normal depth-from-stereo case, the cameras are assumed to have a particular geometric configuration, as shown below.

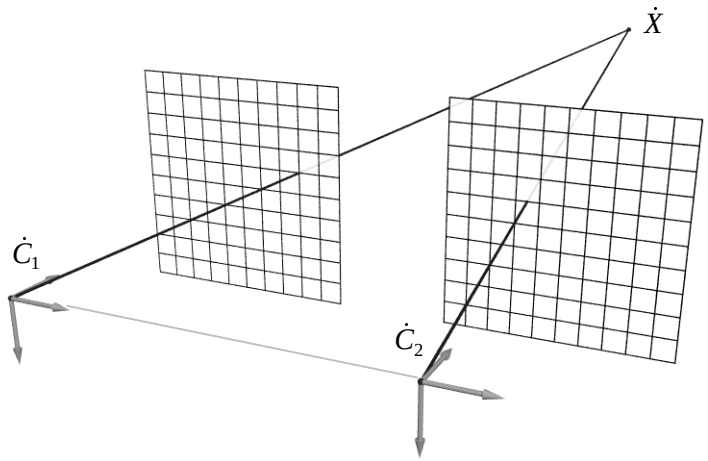

Figure 3-4: The depth-from-stereo camera configuration

[7] It is at precisely this point that we depart from a Euclidean geometry to a projective one. The relation of the warping equation to projective geometry will be pursued in greater detail later. But, for the moment, we can avoid dealing with these subtle differences.

Both image planes have the same pinhole-camera model, the vector connecting the centers-of-projection is parallel to both image planes, and the coordinate system is selected so that the $\hat{i}$ basis vector of the camera space is parallel to the $\hat{s}$ basis vector of the image planes. This configuration can be accomplished either by accurate alignments of the cameras or by a post-processing rectification (using re-projection see Equation 3-13) of the acquired data. Under these conditions the planar ray-to-ray mapping equation simplifies to

$$\mathbf{P}_1\bar{x}_2 \doteq \delta(\bar{x}_1)\left(\begin{bmatrix} C_{1x} \\ C_{1y} \\ C_{1z} \end{bmatrix} - \begin{bmatrix} C_{2x} \\ C_{2y} \\ C_{2z} \end{bmatrix}\right) + \mathbf{P}_1\bar{x}_1 = \delta(\bar{x}_1)\begin{bmatrix} C_{1x} - C_{2x} \\ 0 \\ 0 \end{bmatrix} + \mathbf{P}_1\bar{x}_1$$

Equation 3-5: Simplified planar mapping equation

Multiplying both sides by the inverse of the pixel-to-ray mapping gives the following normalized form:

$$\bar{x}_2 \doteq \delta(\bar{x}_1)\mathbf{P}_1^{-1}\begin{bmatrix} C_{1x} - C_{2x} \\ 0 \\ 0 \end{bmatrix} + \bar{x}_1$$

Equation 3-6: Normalized planar mapping equation

The alignment constraint on the camera-space and image-space basis vectors (that the $\hat{i}$ basis vector of the camera space is parallel to the $\hat{s}$ basis vector) implies that a unit step in image space produces a unit step in camera space. This is equivalent to

$$\mathbf{P}_1 = \begin{bmatrix} 1 & p_{12} & p_{13} \\ 0 & p_{22} & p_{23} \\ 0 & p_{23} & p_{33} \end{bmatrix} \quad \text{so} \quad \mathbf{P}_1^{-1} = \begin{bmatrix} 1 & q_{12} & q_{13} \\ 0 & q_{22} & q_{23} \\ 0 & q_{23} & q_{33} \end{bmatrix}$$

Equation 3-7: Aligned image-space mapping

After multiplying through and reorganizing terms we get the following:

$$\bar{x}_2 - \bar{x}_1 = \begin{bmatrix} u_2 \\ v_2 \\ 1 \end{bmatrix} - \begin{bmatrix} u_1 \\ v_1 \\ 1 \end{bmatrix} = \delta(\bar{x}_1)\begin{bmatrix} C_{1x} - C_{2x} \\ 0 \\ 0 \end{bmatrix}$$

Equation 3-8: Difference between image coordinates for stereo camera configuration

Thus, when camera geometries satisfy the depth-from-stereo requirement, the image-space coordinates of corresponding points differ only along a single dimension in the images. The size of this change is proportional to both the distance between the centers-of-projection, which is often called the stereo baseline, and the generalized disparity quantity, which has units of pixels per unit length. Therefore, generalized disparity, $\delta(\bar{x})$, is equivalent to stereo disparity, $u_2 - u_1$, when normalized by dividing through by the length of the baseline.

$$\delta_{stereo}(\bar{x}) = \frac{u_2 - u_1}{C_{1x} - C_{2x}}$$

Equation 3-9: Stereo disparity

The name *projective depth* comes from the inverse relationship between the range function and the term $\frac{1}{t_1}$. It should be noted that the units of t_1 depend on the distance from the center-of-projection to the viewing plane in the particular ray direction. While this measure of depth is useful for establishing relative depth between points along the same ray, it is not useful for the metric comparison of depths between rays unless the distance from the ray to the viewing plane is considered. Thus, $\delta(\bar{x}_1)$, is only inversely related to depth (or more precisely range) by a scale factor that varies from point to point on the viewing plane.

Let us consider further the generalized-disparity term, $\delta(\bar{x}_1)$. We can construct the following diagram of Equation 3-4 in the plane containing the three points $\dot{C}_1$, $\dot{C}_2$, and a visible point $\dot{X}$.

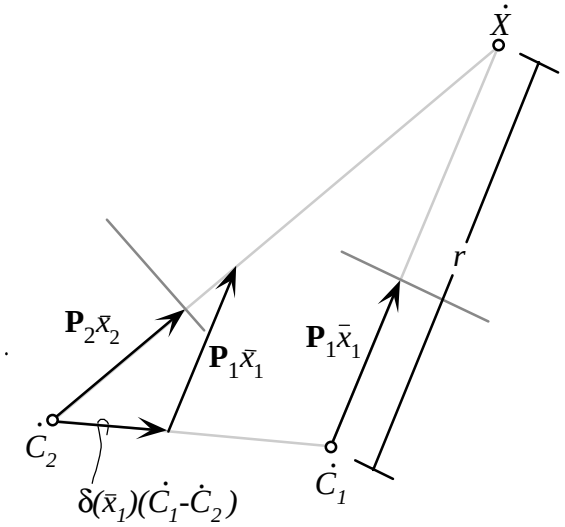

Figure 3-5: Vector diagram of planar warping equation

Using similar triangles it can be shown that

$$\frac{r}{\left|\dot{C}_1 - \dot{C}_2\right|} = \frac{\left|\mathbf{P}_1 \bar{x}_1\right|}{\delta(\bar{x}_1)\left|\dot{C}_1 - \dot{C}_2\right|}$$

Solving for generalized disparity gives the following expression:

$$\delta(\bar{x}_1) = \frac{\left|\mathbf{P}_1 \bar{x}_1\right|}{r}$$

Thus, the generalized disparity depends only on the distance from the center-of-projection to the position on the image plane where the point is observed and the range value of the actual point. The image-space coordinate in the second image of the actual point can be found using the following transformation:

$$\bar{x}_2 \doteq \delta(\bar{x}_1)\mathbf{P}_2^{-1}\left(\dot{C}_1 - \dot{C}_2\right) + \mathbf{P}_2^{-1}\mathbf{P}_1 \bar{x}_1$$

Equation 3-10: Planar image-warping equation

Since the generalized-disparity term, $\delta(\bar{x}_1)$, is independent of both the desired center-of-projection, $\dot{C}_2$, and the desired pinhole viewing parameters, $\mathbf{P}_2$, Equation 3-10 can also be used to determine the image-space coordinate of the observed point on any other viewing plane. This is accomplished by simply substituting the desired center-of-projection and pinhole-camera model into Equation 3-10.

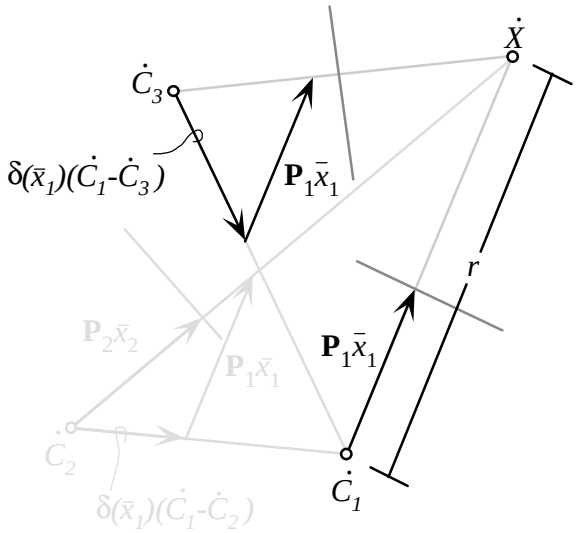

Figure 3-6: A third view of the point $\dot{\mathbf{X}}$

Figure 3-6 illustrates how the planar warping equation (Equation 3-10) can be used to synthesize arbitrary views. The third viewing position, $\dot{C}_3$, need not be in the same plane as $\dot{C}_1$, $\dot{C}_2$ and $\dot{X}$. Figure 3-6 also depicts how generalized disparity is an invariant fraction of the baseline vector. This fraction of the baseline vector applies to all potential views, and therefore, it can be used to align corresponding rays of a given reference image to their direction in any desired image. In addition, the resulting projection will be consistent to a fixed three-dimensional point. Generalized disparity is a scalar quantity that determines how a translation of the center-of-projection affects the coordinates of points in image space. The remaining matrix quantity, $\mathbf{P}_2^{-1}\mathbf{P}_1$, determines how changes in the pinhole-camera model, independent of translation, affect the coordinates of points in image space. A further explanation of this last claim will be presented in the next section.

The warping equation can be used to synthesize arbitrary views of a given reference image via the following procedure. Given a reference image, the matrix describing its planar-pinhole projection model, $\mathbf{P}_1$, its center-of-projection, $\dot{C}_1$, a generalized-disparity value, $\delta(\bar{x}_1)$, for each pixel, and the center-of-projection of the desired image, $\dot{C}_2$, and its projection model, the mapping of the reference image to a desired image can be computed. Using the vectors described in the generalized pinhole-camera model, the warping equation can be rewritten as

$$\alpha\begin{bmatrix} u_2 \\ v_2 \\ 1 \end{bmatrix} = \begin{bmatrix} \bar{a}_2 & \bar{b}_2 & \bar{c}_2 \end{bmatrix}^{-1}\left(\dot{C}_1 - \dot{C}_2\right)\delta(u_1, v_1) + \begin{bmatrix} \bar{a}_2 & \bar{b}_2 & \bar{c}_2 \end{bmatrix}^{-1}\begin{bmatrix} \bar{a}_1 & \bar{b}_1 & \bar{c}_1 \end{bmatrix}\begin{bmatrix} u_1 \\ v_1 \\ 1 \end{bmatrix}$$

where α is an arbitrary scale factor. This matrix sum can be rewritten as shown below:

$$\alpha\begin{bmatrix} u_2 \\ v_2 \\ 1 \end{bmatrix} = \begin{bmatrix} \bar{a}_2 & \bar{b}_2 & \bar{c}_2 \end{bmatrix}^{-1}\begin{bmatrix} \bar{a}_1 & \bar{b}_1 & \bar{c}_1 & \left(\dot{C}_1 - \dot{C}_2\right) \end{bmatrix}\begin{bmatrix} u_1 \\ v_1 \\ 1 \\ \delta(u_1, v_1) \end{bmatrix}$$

Multiplying both sides by the determinant of $\mathbf{P}_2$ and substituting for its inverse gives the following 4×3 matrix equation:

$$\alpha\left(\bar{c}_2 \cdot \left(\bar{a}_2 \times \bar{b}_2\right)\right)\begin{bmatrix} u_2 \\ v_2 \\ 1 \end{bmatrix} = \begin{bmatrix} \bar{a}_1 \cdot \left(\bar{b}_2 \times \bar{c}_2\right) & \bar{b}_1 \cdot \left(\bar{b}_2 \times \bar{c}_2\right) & \bar{c}_1 \cdot \left(\bar{b}_2 \times \bar{c}_2\right) & \left(\dot{C}_1 - \dot{C}_2\right) \cdot \left(\bar{b}_2 \times \bar{c}_2\right) \\ \bar{a}_1 \cdot \left(\bar{c}_2 \times \bar{a}_2\right) & \bar{b}_1 \cdot \left(\bar{c}_2 \times \bar{a}_2\right) & \bar{c}_1 \cdot \left(\bar{c}_2 \times \bar{a}_2\right) & \left(\dot{C}_1 - \dot{C}_2\right) \cdot \left(\bar{c}_2 \times \bar{a}_2\right) \\ \bar{a}_1 \cdot \left(\bar{a}_2 \times \bar{b}_2\right) & \bar{b}_1 \cdot \left(\bar{a}_2 \times \bar{b}_2\right) & \bar{c}_1 \cdot \left(\bar{a}_2 \times \bar{b}_2\right) & \left(\dot{C}_1 - \dot{C}_2\right) \cdot \left(\bar{a}_2 \times \bar{b}_2\right) \end{bmatrix}\begin{bmatrix} u_1 \\ v_1 \\ 1 \\ \delta\left(u_1, v_1\right) \end{bmatrix}$$

Equation 3-11: 4×3 matrix formulation of warping equation

This results in the following rational expressions for computing the reprojection of pixel coordinates from a reference image to the coordinates of a desired image:

$$u_2 = \frac{\bar{a}_1 \cdot \left(\bar{b}_2 \times \bar{c}_2\right) u_1 + \bar{b}_1 \cdot \left(\bar{b}_2 \times \bar{c}_2\right) v_1 + \bar{c}_1 \cdot \left(\bar{b}_2 \times \bar{c}_2\right) + \left(\dot{C}_1 - \dot{C}_2\right) \cdot \left(\bar{b}_2 \times \bar{c}_2\right) \delta\left(u_1, v_1\right)}{\bar{a}_1 \cdot \left(\bar{a}_2 \times \bar{b}_2\right) u_1 + \bar{b}_1 \cdot \left(\bar{a}_2 \times \bar{b}_2\right) v_1 + \bar{c}_1 \cdot \left(\bar{a}_2 \times \bar{b}_2\right) + \left(\dot{C}_1 - \dot{C}_2\right) \cdot \left(\bar{a}_2 \times \bar{b}_2\right) \delta\left(u_1, v_1\right)}$$

$$v_2 = \frac{\bar{a}_1 \cdot \left(\bar{c}_2 \times \bar{a}_2\right) u_1 + \bar{b}_1 \cdot \left(\bar{c}_2 \times \bar{a}_2\right) v_1 + \bar{c}_1 \cdot \left(\bar{c}_2 \times \bar{a}_2\right) + \left(\dot{C}_1 - \dot{C}_2\right) \cdot \left(\bar{c}_2 \times \bar{a}_2\right) \delta\left(u_1, v_1\right)}{\bar{a}_1 \cdot \left(\bar{a}_2 \times \bar{b}_2\right) u_1 + \bar{b}_1 \cdot \left(\bar{a}_2 \times \bar{b}_2\right) v_1 + \bar{c}_1 \cdot \left(\bar{a}_2 \times \bar{b}_2\right) + \left(\dot{C}_1 - \dot{C}_2\right) \cdot \left(\bar{a}_2 \times \bar{b}_2\right) \delta\left(u_1, v_1\right)}$$

Since the centers-of-projection and the planar-pinhole camera models for the reference and desired images are fixed for a given mapping, the warping equation simplifies to a pair of constant-coefficient linear rational expressions of the form

$$r(u_1, v_1, \delta(u_1, v_1)) = w_{11} u_1 + w_{12} v_1 + w_{13} + w_{14} \delta(u_1, v_1)$$

$$s(u_1, v_1, \delta(u_1, v_1)) = w_{21} u_1 + w_{21} v_1 + w_{23} + w_{24} \delta(u_1, v_1)$$

$$t(u_1, v_1, \delta(u_1, v_1)) = w_{31} u_1 + w_{32} v_1 + w_{33} + w_{34} \delta(u_1, v_1)$$

$$u_2 = \frac{r(u_1, v_1, \delta(u_1, v_1))}{t(u_1, v_1, \delta(u_1, v_1))}$$

$$v_2 = \frac{s(u_1, v_1, \delta(u_1, v_1))}{t(u_1, v_1, \delta(u_1, v_1))}$$

Equation 3-12: Warping equation as rational expressions

The mapping of a point in the reference image to its corresponding point in the desired image can be computed using nine adds, eleven multiplies, and one inverse calculation. When points of the reference image are processed sequentially, the number of adds is reduced to six, and the number of multiplies is reduced to five. Additional tests for a positive denominator, $t(u_1, v_1, \delta(u_1, v_1))$, and a valid range of the numerator can avoid two multiplies and the inverse calculation. This operation is the equivalent of screen-space clipping in traditional three-dimensional computer graphics (See discussion in Chapter 7).

3.4 Relation to Previous Results

Results similar to the warping equation described here have been reported by other researchers [Szeliski96] [Faugeras92b] for determining the projective coordinates of points between a pair of images. In these applications the image-space coordinates of the points $\bar{x}_1$ and $\bar{x}_2$ were given, and the projective depth, $\delta(\bar{x})$, was the quantity solved for. When this equation is used for image warping, coordinates of image points in the desired view, $\bar{x}_2$, are computed from points in the reference image, $\bar{x}_1$, and their projective depths.

This warping equation is also closely related to several other well-known results from computer graphics, image-warping, and projective geometry. Consider the situation where the reference image and the desired view share a common center-of-projection. In this case the planar-warping equation simplifies to

$$\bar{x}_2 \doteq \mathbf{P}_2^{-1}\mathbf{P}_1\bar{x}_1$$

Equation 3-13: Image reprojection

This illustrates the well known result that images defined on planar viewing surfaces sharing a common center-of-projection are related by a *projective transformation* or *planar homography*.

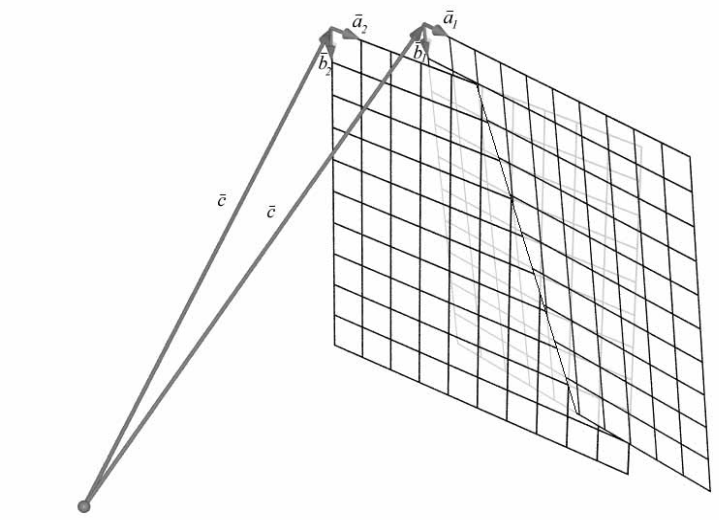

Figure 3-7: Reprojection of an image with the same center-of-projection

This projective transformation is merely the composition of the reference image's viewing matrix with the inverse of the desired image's viewing matrix, $\mathbf{H}_{reproject} = \mathbf{P}_2^{-1}\mathbf{P}_1$. This is indicative of the fact that, ignoring the clipping that occurs at the boundaries of the view

plane, a change of viewing surface does not change the set of rays visible from the center-of-projection. It only changes their spatial distribution on the viewing surface. I will refer to mappings of this sort as reprojections.

A second well known result from the fields of computer graphics and projective geometry is that all images of a common planar surface seen in planar projection are also related by a projective transform as long as the plane does not project to a line. This result is the underlying basis for the texture mapping of images onto planar surfaces. It allows for the rasterization of textured planar primitives in screen space using a rational linear expression (an alternate formulation for a projective transform). The figure below illustrates the projection of a planar region onto several viewing planes and the resulting image.

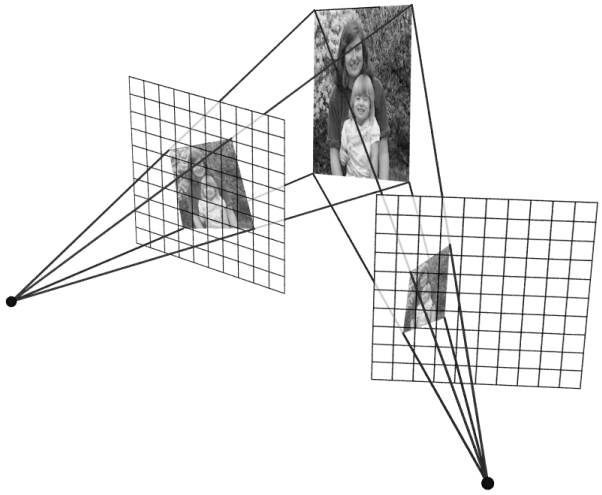

Figure 3-8: A planar region seen from multiple viewpoints

The mapping function that describes the possible views of a three-dimensional planar surface can be derived as a special case of the planar image-warping equation (Equation 3-10) by the following progression. The equation of a plane in the coordinate system having the reference image's center-of-projection as its origin is given by

$$\begin{bmatrix} A & B & C \end{bmatrix} \begin{bmatrix} x \\ y \\ z \end{bmatrix} = D$$

Equation 3-14: Equation of a plane

where the scalars *A*, *B*, *C*, and *D* are four parameters defining the plane, and x, y, and z are the coordinates of a point in space. These three-space coordinates can be re-expressed in terms of image coordinates by using a planar-pinhole model image-to-ray mapping function as follows:

$$\begin{bmatrix} A & B & C \end{bmatrix} t(u,v) \mathbf{P}_1 \begin{bmatrix} u \\ v \\ 1 \end{bmatrix} = D$$

where $t(u,v)$ is a multiple of the distance from the center-of-projection to the viewing plane for the ray. Dividing both sides by the scalar quantities appearing on opposite sides gives

$$\delta(u,v) = \frac{1}{t(u,v)} = \begin{bmatrix} \frac{A}{D} & \frac{B}{D} & \frac{C}{D} \end{bmatrix} \mathbf{P}_1 \begin{bmatrix} u \\ v \\ 1 \end{bmatrix}$$

The inverse of $t(u,v)$ is equivalent to the generalized-disparity term discussed in Equation 3-3. When the generalized-disparity value from above is substituted into the warping equation (Equation 3-10), the following expression results:

$$\bar{x}_2 \doteq \mathbf{P}_2^{-1}\left(\dot{C}_1 - \dot{C}_2\right)\begin{bmatrix} \frac{A}{D} & \frac{B}{D} & \frac{C}{D} \end{bmatrix} \mathbf{P}_1 \bar{x}_1 + \mathbf{P}_2^{-1} \mathbf{P}_1 \bar{x}_1 = \mathbf{P}_2^{-1}\left(\left(\dot{C}_1 - \dot{C}_2\right)\begin{bmatrix} \frac{A}{D} & \frac{B}{D} & \frac{C}{D} \end{bmatrix} + I\right) \mathbf{P}_1 \bar{x}_1$$

Equation 3-15: Mapping of a common plane seen at two centers-of-projection

The planar homography, $\mathbf{H}_{plane} = \mathbf{P}_2^{-1}\left(\left(\dot{C}_1 - \dot{C}_2\right)\begin{bmatrix} \frac{A}{D} & \frac{B}{D} & \frac{C}{D} \end{bmatrix} + I\right)\mathbf{P}_1$, is a projective mapping of the reference-image points on the plane to their coordinates in the desired image. When the reference and desired images share a common center-of-projection, the projective mapping reduces to the reprojection given in Equation 3-13 as expected.

The image plane of a reference image is but a plane in three-space. Therefore, its image in any reprojection is related by a projective mapping. The equation of the three-dimensional image plane of a given pinhole-camera model is given by

$$\left(\bar{a}_1 \times \bar{b}_1\right)^T \begin{bmatrix} x \\ y \\ z \end{bmatrix} = \bar{c}_1 \cdot \left(\bar{a}_1 \times \bar{b}_1\right)$$

Substitution into Equation 3-15, gives

$$\bar{x}_2 \doteq \mathbf{P}_2^{-1}\left(\left(\dot{C}_1 - \dot{C}_2\right)\frac{1}{\bar{c}_1\cdot\left(\bar{a}_1\times\bar{b}_1\right)}\left(\bar{a}_1\times\bar{b}_1\right)^T + I\right)\mathbf{P}_1\bar{x}_1 = \mathbf{P}_2^{-1}\left(\left(\dot{C}_1 - \dot{C}_2\right)\begin{bmatrix}0 & 0 & 1\end{bmatrix} + \mathbf{P}_1\right)\bar{x}_1$$

which simplifies to

$$\bar{x}_2 \doteq \left(\begin{bmatrix}\bar{0} & \bar{0} & \mathbf{P}_2^{-1}\left(\dot{C}_1 - \dot{C}_2\right)\end{bmatrix} + \mathbf{P}_2^{-1}\mathbf{P}_1\right)\bar{x}_1$$

Equation 3-16: Projection of the reference image plane in the desired image

The projective mapping, $H_{viewplane} = \begin{bmatrix}\bar{0} & \bar{0} & \mathbf{P}_2^{-1}\left(\dot{C}_1 - \dot{C}_2\right)\end{bmatrix} + \mathbf{P}_2^{-1}\mathbf{P}_1$, describes the projection of the reference image's viewing plane in the desired image. The significance of this result will be considered in Chapter 5.

3.5 Resolving visibility

The mapping function described by the planar image warping equation (Equation 3-10) is not one-to-one. The locus of potential points in three-space, $\dot{X}(t)$, that project to the same image coordinate, $\bar{x} = (u, v)$, is described by the center-of-projection and a planar pinhole-camera model using the following equation:

$$\dot{X}(t) = \dot{C} + t\mathbf{P}\bar{x}$$

Equation 3-17: Locus of three-space points along a ray

The parameter *t* identifies specific three-dimensional points that project to a given image-space coordinate. A policy of selecting the smallest of all positive *t* values for a given screen-space point can be used to determine visibility for opaque objects. This candidate *t* value is analogous to the z values stored in a z-buffer [Catmull74], or the ray-length maintained by a ray-casting algorithm [Appel68]. While the *t* parameter is an essential element of the reprojection process, (via its relationship to $\delta(\bar{x}_1)$) it is, surprisingly, not required to establish the visibility of a warped image.

In this section, an algorithm is presented for computing the visible surface at each image-space point of a desired image as it is being derived from a reference image via a warping equation. This is accomplished by establishing a warping order that guarantees a correct visibility solution. This ordering is established independently of the image contents. Only the centers-of-projection of the desired and reference images, as well as the pinhole-camera model for the reference image, are needed.

In order to simplify the following discussion, the reference image is assumed to be stored as a two-dimensional array whose entries represent uniformly spaced image samples. This simplification is not required for the algorithm to operate correctly, but it allows for a concise statement of the algorithm, and it is representative of many typical applications. Later, in Chapter 6, a more detailed discussion of the visibility algorithm will be presented along with a proof of the algorithm's correctness and extensions to non-planar viewing surfaces.

3.5.1 Visibility Algorithm

The approach of this visibility algorithm is to specify an ordering, or enumeration, of points from the reference image which guarantees that any scene element that is hidden by some other scene element in the desired image will always be drawn prior to its eventual occluder. This type of ordering is commonly called back-to-front. A simple painter's algorithm [Rogers85] can be used to display any collection of scene elements with correct visibility when a back-to-front ordering can be established.

Given the reference image's center-of-projection, $\dot{C}_1$, and ray-mapping function, $\mathbf{P}_1$, and the desired center-of-projection, $\dot{C}_2$, the projection of $\dot{C}_2$ onto the reference image is first computed as follows:

$$\begin{bmatrix} e_x \\ e_y \\ e_z \end{bmatrix} = \mathbf{P}_1^{-1}\left(\dot{C}_2 - \dot{C}_1\right)$$

Equation 3-18: Projection of desired center-of-projection onto reference image

An example of this projection is illustrated in Figure 3-9.

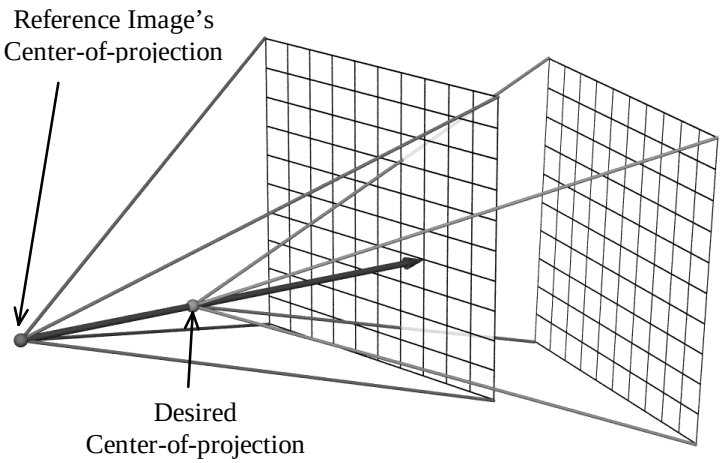

Figure 3-9: A desired center-of-projection projected onto the reference image

The image coordinate of $\dot{C}_2$ on the reference image is given by $\bar{e} = (e_x/e_z, e_y/e_z)$. It will fall into one of nine regions relative to the reference image shown below:

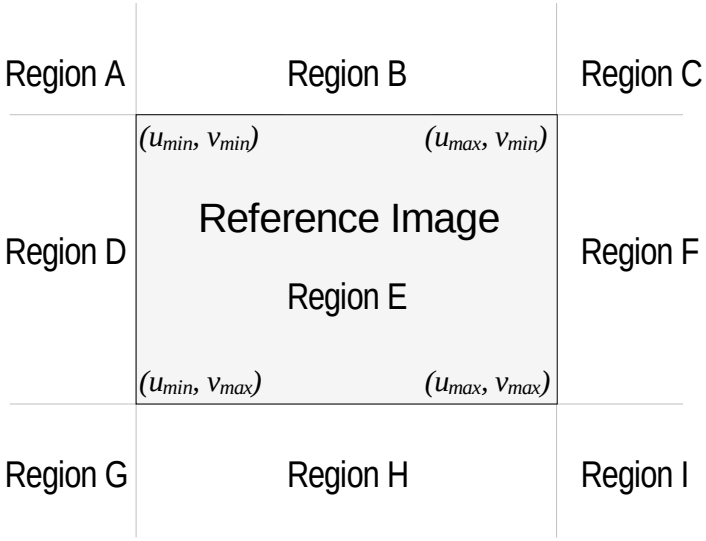

Figure 3-10:Figure of nine regions

Next, the reference image is subdivided into sheets that can be processed independently. Any set of orthogonal image-space basis vectors can be used to partition each sheet, but it is simplest to choose a coordinate basis aligned with the image's sampling grid. The reference image is partitioned into 1, 2, or 4 sheets depending on the image-space coordinates of

the projected point, $\bar{e}$. When $\bar{e}$ projects within the domain of the reference image, the image is divided into four sections separated along the row and column of $\bar{e}$.

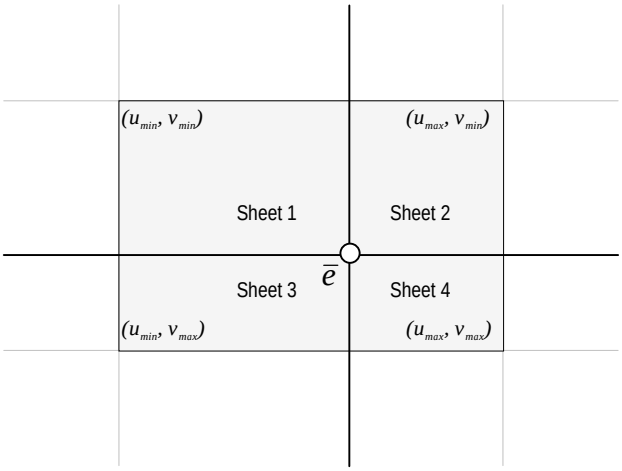

Figure 3-11: A desired center-of-projection that divides the reference image into 4 sheets

When only one coordinate of $\bar{e}$ falls within the reference image, (i.e., when $\bar{e}$ falls into regions B, D, F, and H) the image is subdivided into two sheets whose boundary is determined by either the row or column of the one coordinate that lies within the domain.

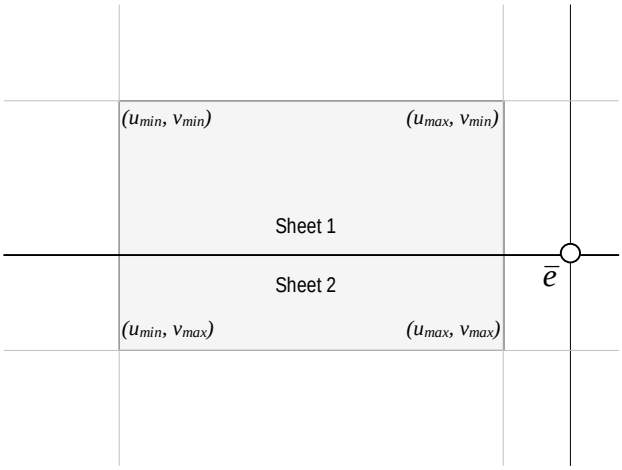

Figure 3-12: A desired center-of-projection that divides the reference image into 2 sheets

If neither component of $\bar{e}$ falls within the reference image's domain, (when $\bar{e}$ projects into regions A, C, H or J) then the entire image is treated as a single sheet.

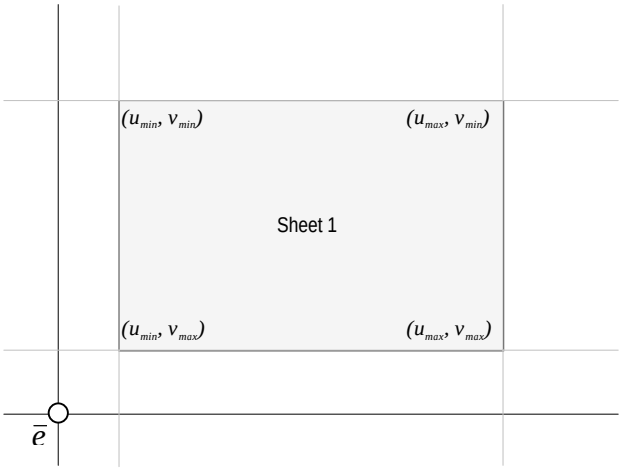

Figure 3-13: A desired center-of-projection that divides the reference image into 1 sheet

Once the reference image's domain is subdivided according to the projected position of the desired center-of-projection, the warping order for each sheet can be determined as follows. The enumeration direction is determined by the sign of the e_z component from Equation 3-18. When e_z is non-negative the warping order of each sheet progresses toward the point $\bar{e}$, otherwise the warping progresses away from $\bar{e}$, as shown in the figure below. The case where e_z is zero indicates that the desired viewing position has no proper projection onto the reference image, because the vector $\dot{C}_1 - \dot{C}_2$ is parallel to the reference image's viewing plane. In this case, only one sheet will be enumerated, and the warping order progresses in the direction determined by the quadrant indicated by the signs of the remaining two vector components, e_x and e_y.

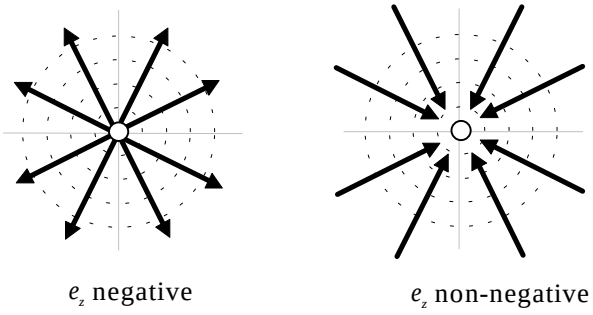

Figure 3-14: Enumeration direction

During the warp, each radial line originating from the projected image of the desired center-of-projection can be traversed independently. Alternatively, the warp can progress along either rows or columns of the sheets so long as the image of the desired center-of-projection, $\overline{e}$, is drawn at the appropriate time (i.e., p is drawn first when e_z is negative, and last otherwise), allowing either a row major or column major traversal. The advantage of the latter approach is that it allows the reference image's traversal to take maximum advantage of the access coherence of most memory systems.

The entire visibility algorithm involves three simple steps. First, the three-dimensional coordinate of the desired center-of-projection, $\dot{C}_2$, is projected on the reference image's viewing plane. Second, the image-plane is divided into sheets determined by the image-space coordinate of the projected center-of-projection, $\overline{e}$, and whose boundaries are aligned with the image-space coordinate axes[8]. Computing this coordinate involves a projective normalization. Finally, the traversal of the reference image is determined by the sign of the planar normalizing element of the projective coordinate[9].

The algorithm presented here is similar to Anderson's algorithm for bivariate functions [Anderson82] with the exceptions that his visibility algorithm was defined for a different class of surfaces (i.e., a height field, or Monge patch, rather than a projective surface), and his algorithm enumerates the facets in a front-to-back occlusion order. Anderson's choice of a front-to-back order requires that some representation of the grid perimeter be maintained to aid in deciding what parts or edges of subsequent facets need to be rendered. Representing this perimeter requires auxiliary storage and extra clipping computations. This list must then be queried before each new facet's edge is displayed, and the display must be updated if any part of the facet is visible. In contrast, a back-to-front ordering requires no additional storage because the proper occlusion is handled by the drawing order using the painter's algorithm.

3.6 Reconstruction Issues

The planar-warping equation describes a mapping of the image-space points on a reference viewing plane to image-space points on a desired viewing plane. The underlying assumption is that both the reference and desired images are continuous over their domains. This is not generally the case for typical images. Usually, images are represented by a two-

[8] Along the rows and columns of a discretely sampled image array.

[9] This is often called the homogeneous element of the projective coordinate.

dimensional array of discrete samples. There are many subtle implications of warping sampled images rather than continuous ones. While the warping equation can easily be applied to the discrete coordinates of a sampled image, the likelihood that any sample will map exactly onto a sampling-grid point of the desired image is negligible. In addition to warping to locations off the sampling grid, the points of a reference image will also distribute unevenly over the desired image. The desired image must then be synthesized from this irregular distribution of sampled and reprojected image points.

The process of mapping a sampled image from one image-space to another is called *image resampling*. Conceptually, image resampling constructs a continuous representation of a reference image which is then mapped onto the desired viewing plane using the warping function and resampled to form the final discrete image. When the three-dimensional points represented in the reference image lie on a common plane, as shown in Figure 3-8, and the scene contents are appropriately band limited, reconstructing a continuous representation is a straightforward application of signal processing theory [Wolberg90]. The same situation occurs when three-dimensional points are constrained to lie along the same rays of different viewing planes, as when reprojecting an arbitrary set of points from the same center-of-projection as shown in Figure 3-7. The ideal continuous reconstruction of these surfaces is the summation of two-dimensional sinc functions centered at each sample-grid point and scaled by the sample's intensity. Since the sinc function has an infinite extent, local polynomial approximations are often used instead [Mitchell88]. However, when the three-dimensional points visible in an image are not constrained to lie in a plane or share a center-of-projection, the reconstruction of a continuous reference image representation is more involved.

Three-dimensional surfaces can be built up from discrete sub-surfaces, called *surface patches*. The composite of a group of surface patches can represent the reconstruction of a three-dimensional point set. One measure of the continuity of a composite set of surface patches, called *derivative continuity*, is the number of matching terms in the Taylor series expansions at abutting surface patches. When only the first terms of the composite surfaces' Taylor series expansions match along their common boundaries, the surface patches will have the same three-dimensional coordinate values along their abutting regions, and the overall surface has C^0 continuity. When both the first and second terms of the expansion agree, the tangent spaces of the abutting surfaces coincide, and the composite surface will have C^1 continuity.

One approach to reconstructing a continuous function from a sampled reference image is to consider each sample as specifying a surface patch. The basis for these surface patch definitions are typically polynomial. However, this is not a requirement for defining a continuous reconstruction. All that is necessary is that the basis functions are sufficiently differentiable. For instance, a sinc or a Gaussian basis are both valid representations of surface patches[10].

I will next describe two different methods for constructing a continuous representation of a reference image for use in image warping based on C^0 continuity models that use different surface patch bases. Recent work by Mark [Mark97] has extended these methods to include a model in which C^0 and C^1 continuity alternates throughout the domain. His approach requires a local estimate of the tangent space at each sample point. This requirement can be easily satisfied when the reference images are synthesized using traditional computer graphics techniques, but it is more difficult for acquired reference images. However, there is some promise in this area. It appears that many shape-from-shading [Horn89] and photometric-ratio-based correspondence methods [Wolff94] can be adapted to estimate a surface normal at each image-space point.

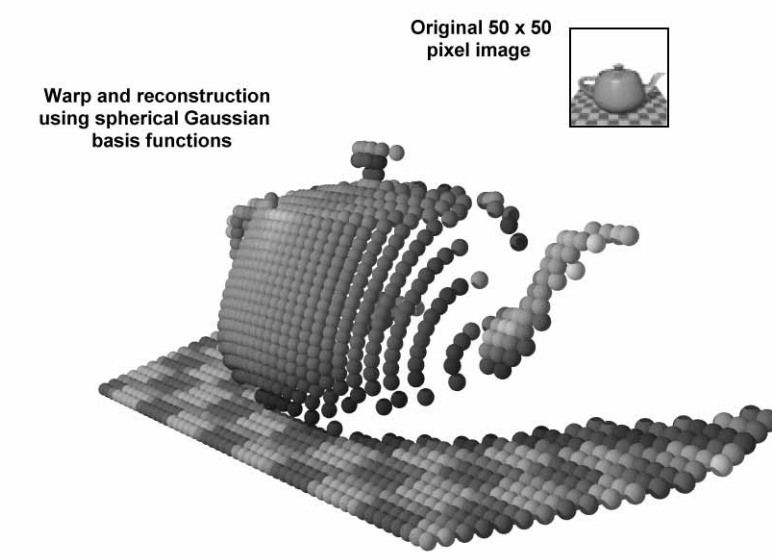

Figure 3-15: A Gaussian cloud representation of image-space points

The first reconstruction approach uses a spherical Gaussian basis function to represent each sample point. It assumes that every visible point in a reference image represents a three-

[10] The use of a sinc or Gaussian basis is complicated by the infinite extents of their kernels.

dimensional spherical cloud density located somewhere along the ray determined by the image point. In three-dimensions this radius could be determined by considering the solid angle represented at each sample point and the distance of the cloud's center from the image's center-of-projection. A two-dimensional equivalent of this radius calculation can, however, be computed directly from the warping equation.

The image-space Gaussian reconstruction method described here is a straightforward adaptation of Heckbert's Elliptical Weighted Average (EWA) filter [Heckbert89], but it is used in a forward-mapping algorithm, similar in spirit to the Splatting algorithm described by Westover [Westover91]. The support of the Gaussian reconstruction function is determined by computing the change in shape of differential circular regions surrounding each sample as they undergo the image warp. One useful measure of the change in shape is provided by the *Jacobian determinant* of the mapping function. The Jacobian determinant is a direct measure of the local change in area induced by a transformation. However, changes in differential area are not necessarily a good indication of the changes in differential shape[11]. The additional assumptions required to address this discrepancy will be discussed shortly. The Jacobian matrix of the planar-warping function given in Equation 3-12 is

$$\mathbf{J} = \begin{bmatrix} \frac{w_{11}(w_{32}v+w_{33}+w_{34}\delta(u,v))-w_{31}(w_{12}v+w_{13}+w_{14}\delta(u,v))}{(w_{31}u+w_{32}v+w_{33}+w_{34}\delta(u,v))^2} & \frac{w_{12}(w_{31}u+w_{33}+w_{34}\delta(u,v))-w_{32}(w_{11}u+w_{13}+w_{14}\delta(u,v))}{(w_{31}u+w_{32}v+w_{33}+w_{34}\delta(u,v))^2} \\ \frac{w_{21}(w_{32}v+w_{33}+w_{34}\delta(u,v))-w_{31}(w_{22}v+w_{23}+w_{24}\delta(u,v))}{(w_{31}u+w_{32}v+w_{33}+w_{34}\delta(u,v))^2} & \frac{w_{22}(w_{31}u+w_{33}+w_{34}\delta(u,v))-w_{32}(w_{21}u+w_{23}+w_{24}\delta(u,v))}{(w_{31}u+w_{32}v+w_{33}+w_{34}\delta(u,v))^2} \end{bmatrix}$$

Equation 3-19: Jacobian of the warping equation

The determinant of the Jacobian matrix simplifies to

$$\frac{\partial(u',v')}{\partial(u,v)} = \frac{\det(\mathbf{H}) + \delta(u,v)\det(\mathbf{G})}{t(u,v,\delta(u,v))^3}$$

Equation 3-20: Jacobian determinant of the warping equation

where

---

[11] For instance, consider the mapping $\phi:\{x = 10u, y = 0.1v\}$ with $\frac{\partial(x,y)}{\partial(u,v)} = \text{Determinant}\begin{bmatrix} 10 & 0 \\ 0 & 0.1 \end{bmatrix} = 1$. The Jacobian determinant indicates that the differential area surrounding any sample remains constant; yet the mapping introduces considerable stretching along the u dimension and shrinking in the v dimension.

$$\mathbf{H} = \begin{bmatrix} w_{11} & w_{12} & w_{13} \\ w_{21} & w_{22} & w_{23} \\ w_{31} & w_{32} & w_{33} \end{bmatrix} \text{ and } \mathbf{G} = \begin{bmatrix} w_{11} & w_{12} & w_{14} \\ w_{21} & w_{22} & w_{24} \\ w_{31} & w_{32} & w_{34} \end{bmatrix}$$

Equation 3-21: Camera-model matrix, H, and the structure matrix, G

The **H** component of the Jacobian determinant represents the change in projected area of an infinitesimal region of the reference image due entirely to the changes in the pinhole-camera model since $\mathbf{H} \doteq \mathbf{P}_2^{-1}\mathbf{P}_1$ and $\det(\text{Jacobian}(\mathbf{H}\bar{x})) = \det(\mathbf{H})/t(u,v,0)^3$. The **G** component represents the change in projected area due to the three-dimensional structure of the observed image point. This can be seen by letting $\mathbf{H} = \mathbf{I}$, denoting no change in the pinhole camera model between the reference and desired image. This gives

$$\frac{\partial(u',v')}{\partial(u,v)} = \frac{1}{(1+\delta(u,v)w_{34})^2}$$

indicating that the change in projected area is independent of the point's coordinate on the image plane, but instead it depends entirely on the generalized disparity value at that point. Since the matrices **H** and **G** are constant for a given pair of reference and desired views, they need only be calculated once per warp.

If we make the assumption that the warping function is well represented by a local linear approximation centered at each sample in the reference image with a constant generalized disparity value, then the Jacobian matrix can also be used to estimate the change in shape of a rotationally symmetric reconstruction kernel as follows. An infinitesimal circular region with a radius of dr is described by the expression

$$dr^2 = \begin{bmatrix} du & dv \end{bmatrix} \begin{bmatrix} du \\ dv \end{bmatrix}$$

Equation 3-22: Radius of differential region

When that region undergoes an arbitrary mapping, $\phi:(u,v) \rightarrow (u',v')$, the best linear approximation to the differential mapping is given by the Jacobian matrix

$$\begin{bmatrix} du' \\ dv' \end{bmatrix} = \mathbf{J} \begin{bmatrix} du \\ dv \end{bmatrix}$$

Equation 3-23: Differential change induced by mapping

By substituting Equation 3-23 into Equation 3-22, the mapping of the differential circular region can be determined as follows:

$$dr^2 = \begin{bmatrix} du' & dv' \end{bmatrix} (\mathbf{J}^{-1})^T \mathbf{J}^{-1} \begin{bmatrix} du' \\ dv' \end{bmatrix}$$

Equation 3-24: Projection of differential circular disk

which expands to the following conic expression:

$$dr^2 = \frac{(j_{21}^2 + j_{22}^2)du'^2 - 2(j_{11}j_{21} + j_{12}j_{22})du'dv' + (j_{11}^2 + j_{12}^2)dv'^2}{(j_{11}j_{22} - j_{12}j_{21})^2}$$

Equation 3-25: Expanded expression for differential circular disk

This equation describes an ellipse if the Jacobian determinant is positive. Therefore, any circular region centered about a reference image sample will project as an ellipse in the desired image. This property can be used to reconstruct a continuous representation of the reference image prior to resampling. The spatial domain response of any rotationally symmetric filter, such as a Gaussian, can be computed at a sample point in the desired image by evaluating Equation 3-25 at that point to determine the radius value in the undistorted filter's kernel. The resampling process can be optimized by first computing the extents of the ellipse in the desired image space. In terms of the Jacobian these extents are given by the following expressions:

$$\Delta u' = \pm \sqrt{\frac{dr^2 (j_{11}j_{22} - j_{12}j_{21})^2}{(j_{21}^2 + j_{22}^2) - \frac{(j_{11}j_{21} + j_{21}j_{22})^2}{(j_{11}^2 + j_{12}^2)}}} \qquad \Delta v' = \pm \sqrt{\frac{dr^2 (j_{11}j_{22} - j_{12}j_{21})^2}{(j_{11}^2 + j_{12}^2) - \frac{(j_{11}j_{21} + j_{21}j_{22})^2}{(j_{21}^2 + j_{22}^2)}}}$$

Equation 3-26: Screen-space extent for projected circular disk

Another approach to reconstructing a continuous representation of the reference image attempts to fit a bilinear surface patch between any four neighboring grid samples. This representation also has C^0 continuity, but it uses a polynomial basis. First, the individual sample points of the reference image are mapped to the desire image's coordinate system. These warped points will generally not correspond to sample grid positions. The connectivity of the eight-connected neighborhood of each reference sample-point is maintained after the warp. This can be managed by maintaining a buffer of two scan lines while enumerating the reference image in a visibility compatible order. The warped sample points stored in these two buffers can be considered a single strip of patches at the completion of each scan line. A

standard polygonal rasterizer can be used to scan convert each patch in the strip. Therefore, this technique can easily take advantage of specialized rasterization hardware if it is available. Once a strip is rasterized, one of the scanline buffers becomes available for storing the mapped values of the next scan line.

Shown below is an example of the same warp using each of the two reconstruction methods discussed.

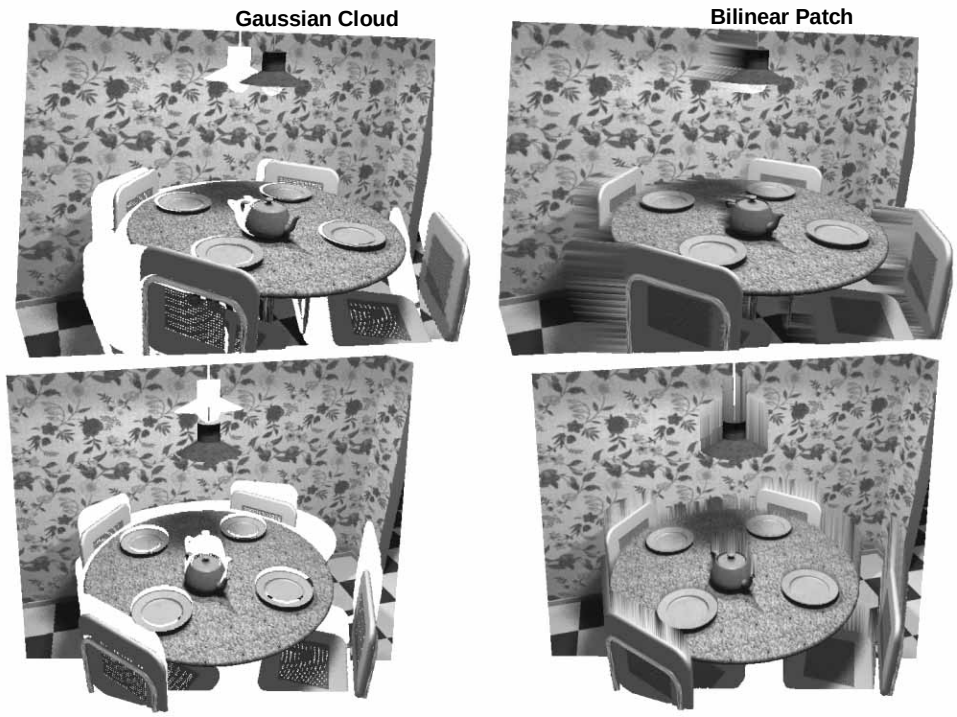

Figure 3-16:**Example image warps using different reconstruction methods**

3.7 Occlusion and Exposure Errors

Only those scene points that are visible in the reference image can be correctly reprojected by the image warp. In some cases, even the visibility of a point does not guarantee its proper reconstruction. These are not weaknesses of either the image-warping or visibility methods described; they are, instead, inherent limitations of an image-based representation.

The major visual artifacts resulting from these limitations can be classified as one of two cases, *exposure errors* or *occlusion errors.* Exposure errors occur when a background region that should have been occluded is visible in a desired image because of the absence of some foreground element from the reference image. On the other hand, occlusion errors occur in a desired image when an interpolation error in the reconstruction process introduces a false

foreground element that covers background regions visible in the actual scene. The choice of reconstruction methods plays a significant role in either amplifying or reducing these errors. However, a reduction in one class of artifact often causes an increase in the other.

Many exposures and occlusions are correct. For instance, when a viewpoint moves toward a foreground object the projection of the object will enlarge in the field-of-view such that it covers adjacent background points. As the viewpoint moves even closer to the foreground object, more of the background is occluded.

Exposure errors and occlusion errors take place either when the underlying assumptions of the reconstruction method are violated, or when there is insufficient information in the image to properly reconstruct the correct surface. These two error sources are closely related. The role of reconstruction kernel is to interpolate the missing gaps between samples. Often the information needed to correctly fill a missing image region is unavailable from the reference image.

Exposure errors are the more subtle visual artifact. The region uncovered by a legitimate exposure lends itself to interpretation as a shadow produced by a light source placed at the reference image's center-of-projection. This is particularly noticeable when the exposure occurs along object boundaries. An exposure error occurs when a ray in the desired image passes through this shadow region, allowing some background element to be erroneously seen. Both exposure errors and actual exposures are illustrated below.

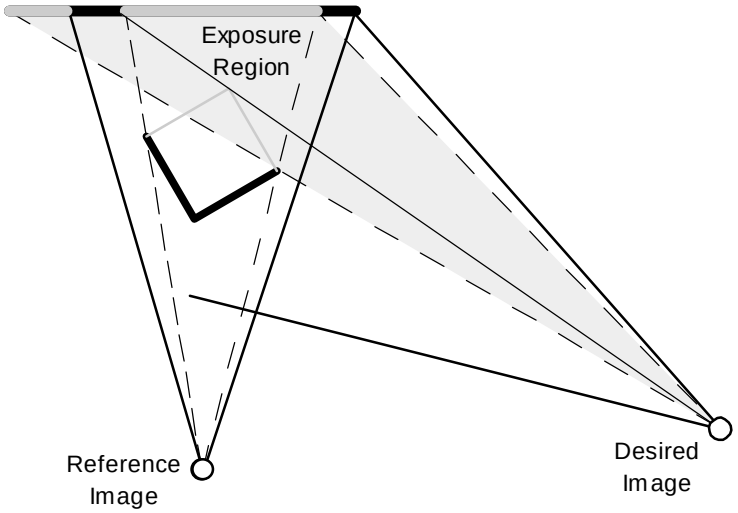

Figure 3-17:Exposures at occluding boundaries

The actual scene points that are visible from the reference image are shown darkened. The shaded region indicates where an exposure occurs in the desired image. The solid dividing line through the exposure region indicates the boundary between an actual exposure to the right and an exposure error to the left. However, without external information the difference between valid and invalid exposures cannot be resolved.

Exposure errors are most likely to occur at object silhouettes. They occur on smooth surfaces as well as along sharp depth discontinuities. This situation is depicted in Figure 3-18. Exposure errors occur immediately adjacent to those image points who's ray lies in the observed object's tangent plane. Therefore, as an observer moves to see around an object boundary, she should generally expect to see more of the object rather than any component of the background.

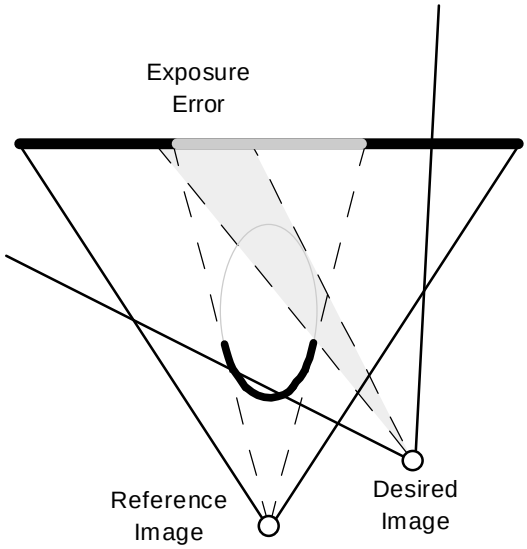

Figure 3-18:Exposure error on a smooth surface boundary

Merely changing the basis function used in the reconstruction of the reference image can eliminate exposure errors, but it introduces occlusion errors. Consider the example shown in Figure 3-19 when a polynomial basis, instead of the Gaussian cloud model, is used to approximate the underlying surface.

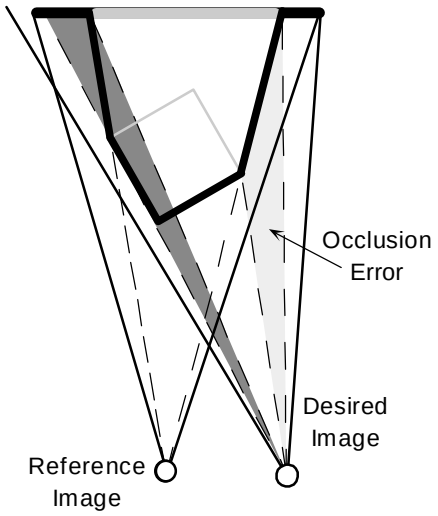

Figure 3-19: Occlusion errors introduced by polynomial reconstruction

The lighter shaded area indicates the extent of an occlusion error, whereas the darker shaded area represents an actual occlusion. The surface seen along the occlusion error corresponds to an extension of the foreground object's tangent plane. This surface will always enclose the actual surface. However, it is unlikely that any part of this extension will actually represent a point in the environment. The occlusion error will usually hide valid exposures. Furthermore, since occlusion errors are not adjacent to an actual occlusion, they appear more unnatural than exposure errors.

The continuity of the polynomial interpolation basis causes an excessive estimation of the number of points in the scene. The polynomial interpolation model reconstructs images that are indistinguishable from a model that assumes that all of the points beyond each ray's observed point are occupied. Such a model will not miss any actual scene points, but it will erroneously include scene points that do not exist. The polynomial reconstruction method will, therefore, introduce a disproportionate number of occlusion errors. This can greatly hinder the usefulness of such a model.

In contrast, the Gaussian reconstruction method represents a vacuous estimate of a scene's contents. It assumes that the visible image point is the only scene point located along the ray's extent. Therefore, a Gaussian reconstruction basis will correctly represent all empty regions of an environment, while missing all scene points that are not visible in the reference image. It is, therefore, conservative in its estimate of the occupied volume of space, whereas the

polynomial reconstruction makes a conservative estimate of the space's emptiness. Exposure errors should be expected when the Gaussian reconstruction model is used.

Valid occlusions are generally handled by the visibility algorithm. One exception is the case when a scene point from outside the viewing frustum comes into view as a result of the change in the center-of-projection. This situation results in an *invisible occluder error*. A simple example of this case is shown in Figure 3-20. This problem is a direct result of the limited field-of-view available to a planar-pinhole camera. The use of panoramic pinhole-camera models, such as the ones discussed in the next chapter, will remedy this problem.

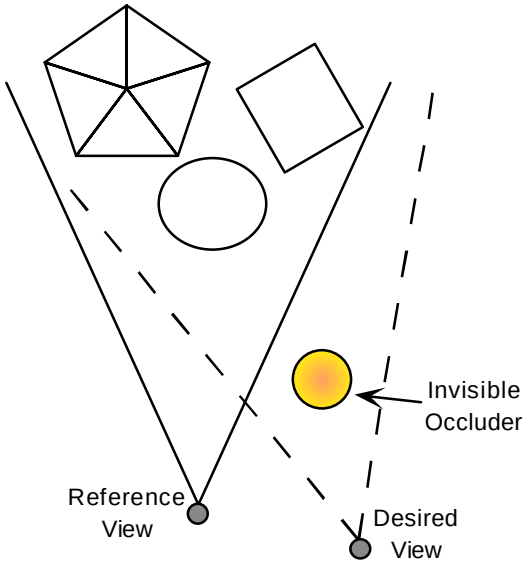

Figure 3-20: An external exposure error

The two reconstruction methods discussed previously represent two extreme assumptions concerning the structure of space. The use of either of these extreme positions introduces artifacts in the final rendering. A more accurate reconstruction should combine elements of both methods. However, this might require additional information beyond that which is deducible from the reference image alone. This is an interesting area for future research.

3.8 Summary

This chapter has presented a complete example of an image-based method for synthesizing computer graphics. Special mapping functions, called image warps, were derived that enabled arbitrary views of a scene to be generated. This scene was represented by a reference image that was augmented by a scalar value defined at each point, called generalized

disparity. An algorithm was presented to resolve the visibility of the mapped reference points at each coordinate in the desired image. Two methods were presented for reconstructing continuous representations of the warped reference image from these warped points. In subsequent chapters, aspects of this image-warping approach will be generalized and developed further.

Chapter 4

OTHER PINHOLE CAMERAS

In Chapter 3 a general model of a planar pinhole camera was introduced in order to derive and explore the warping equation. This model was particularly well suited to the task because it lent itself to easy manipulation using linear algebra. Unfortunately, real-world cameras are not usually specified in this general form. Even if they were, there are disadvantages in limiting ourselves to image-to-ray mapping functions defined on a plane. In this chapter I will compare the general model of Chapter 3 to common pinhole-camera specifications used in other applications. I will also describe a canonical pinhole-camera model that embodies only those intrinsic properties of a camera that are independent of the coordinate system in which the camera is specified. The remainder of the chapter discusses non-planar pinhole cameras that are useful both as representation formats and as distortion models for real-world imaging systems. I also present specific non-planar extensions to the warping equation, plus a general methodology for extending the warping equation to any non-planar camera model.

4.1 Alternative Planar Pinhole-Camera Models

In other application domains the mapping of points on the image plane to rays in space is described in terms other than the 3×3 matrix model used by the general pinhole model of Chapter 3. The goal of these alternate specifications is to describe the pinhole-camera model with some minimal set of physically meaningful quantities. Typically, such models are either nongeneric, admitting only a subset of the mappings achievable with a more general pinhole-camera model, or overly general, admitting different parameter choices that result in the same mapping functions. In truth, the 3×3 matrix formulation of a pinhole camera is also overly general because, while it is determined by nine parameters, any scalar multiple describes the same mapping. Thus, it can have at most 8 true degrees of freedom. In the remainder of this section several of these application-specific models will be explored and related to the general

model. I will also point out the degrees of freedom in each specification and how each parameterization affects the potential camera geometries that can be expressed.

4.1.1 Application-specific planar pinhole-camera models

The first model considered is one commonly used in computer graphics. It reflects a viewing plane parallel to two of the given basis vectors. Three parameters are used to specify the field-of-view, the width, and the height of the viewing plane. The image-space-to-ray mapping of this simple camera model is

$$\begin{bmatrix} d_i \\ d_j \\ d_k \end{bmatrix} = \begin{bmatrix} 1 & 0 & -\left({}^{width}/_{2}\right) \\ 0 & 1 & -\left({}^{height}/_{2}\right) \\ 0 & 0 & \left({}^{width}/_{2}\right)\cot\left({}^{fov}/_{2}\right) \end{bmatrix} \begin{bmatrix} u \\ v \\ 1 \end{bmatrix}$$

Equation 4-1: A simple pinhole-camera model

where the horizontal field-of-view is given by *fov*. The terms *width* and *height* give the dimensions of the viewing plane. It can be seen by inspection that this parameterization is a special case of the general pinhole-camera model. This formulation is only capable of describing viewing frustums shaped like right pyramids with rectangular bases perpendicular to the basis vector indexed by *k*.

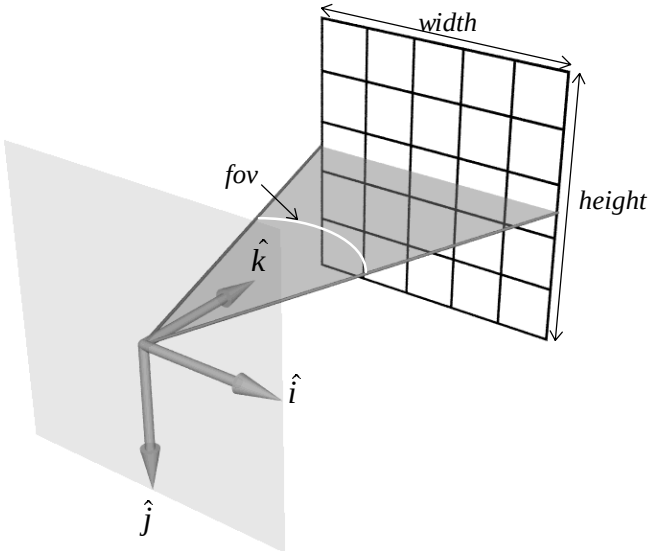

Figure 4-1: Illustration of a simple pinhole-camera model

The flexibility of this simple three-parameter model is comparable to an ideal photographer's camera[12]. The horizontal field-of-view of such a camera is determined by the focal length of the lens, *f*, and the dimensions of the film plane, as shown in Equation 4-2. For example, the film plane of a typical 35 mm camera in a landscape orientation is 36 mm wide and 24 mm high. Therefore, a 50mm lens would provide a 39.6° horizontal field-of-view for use in Equation 4-1.

$$fov = 2\text{Arctan}\left(\frac{w}{2f}\right) \quad \rightarrow \quad \begin{bmatrix} d_i \\ d_j \\ d_k \end{bmatrix} = \begin{bmatrix} 1 & 0 & -\left({}^{width}/_{2}\right) \\ 0 & 1 & -\left({}^{height}/_{2}\right) \\ 0 & 0 & f \end{bmatrix} \begin{bmatrix} u \\ v \\ 1 \end{bmatrix}$$

Equation 4-2: Finding an ideal camera's field-of-view from its focal length

A second pinhole-camera description frequently used in computer graphics is tailored to a direct specification of the viewing frustum. Its image-space-to-ray mapping function is given by

$$\begin{bmatrix} d_i \\ d_j \\ d_k \end{bmatrix} = \begin{bmatrix} \frac{right-left}{width} & 0 & left \\ 0 & \frac{bottom-top}{height} & right \\ 0 & 0 & near \end{bmatrix} \begin{bmatrix} u \\ v \\ 1 \end{bmatrix}$$

Equation 4-3: Frustum model of a pinhole camera

In this *frustum model* the viewing plane is parallel to the first two basis vectors and has a distance from the origin of *near*. The boundaries of this viewing plane are determined by the parameters *left*, *right*, *top*, and *bottom*, given in image-space units.

[12] In all likelihood, a real camera will have a slightly skewed viewing frustum. In addition, it is also likely to exhibit the angular distortion and finite aperture effects discussed later in this chapter.

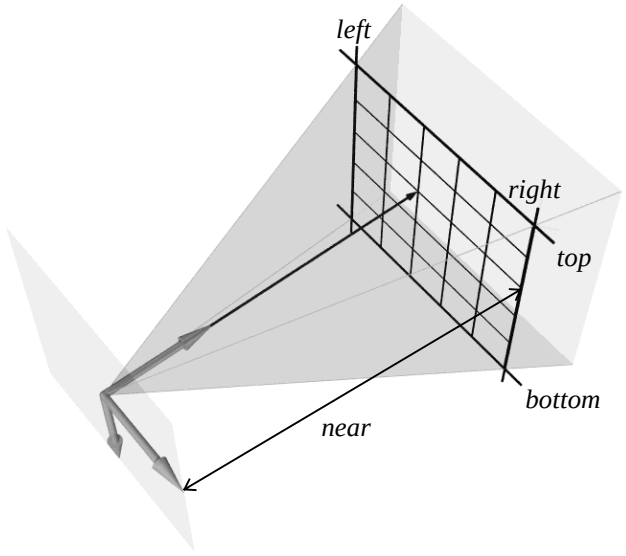

Figure 4-2: Illustration of the frustum model

This model allows non-symmetric viewing frustums to be specified, permitting off-axis projections such as those commonly used for multiplexed stereo display. Despite it's formulation in terms of five parameters, the frustum model has only four degrees of freedom since any uniform scaling of all five terms results in the same mapping.

Two real-world examples make use of the frustum model. When a bellows is used, a photographer's camera achieves projections similar to the frustum model. Also, the projection of a cropped photograph must be modeled using the frustum model.

The computer-vision community uses a model of a planar pinhole camera that utilizes several physically-based quantities in its description. These include the camera's focal length, *f*, the lengths of the image-plane basis vectors, k_u and k_v, the angle separating these basis vectors, θ, and the point on the image plane where the optical axis intersects the image plane, (c_x, c_y).

$$\begin{bmatrix} d_i \\ d_j \\ d_k \end{bmatrix} = \begin{bmatrix} k_u & k_v \cos(\theta) & -c_x \\ 0 & k_v \sin(\theta) & -c_y \\ 0 & 0 & f \end{bmatrix} \begin{bmatrix} u \\ v \\ 1 \end{bmatrix}$$

Equation 4-4: Computer-vision pinhole-camera model

This six-parameter model has more flexibility than either of the two computer-graphics models. It incorporates all of the capabilities of the frustum model with the addition of skewed *spanning vectors* in the image plane.

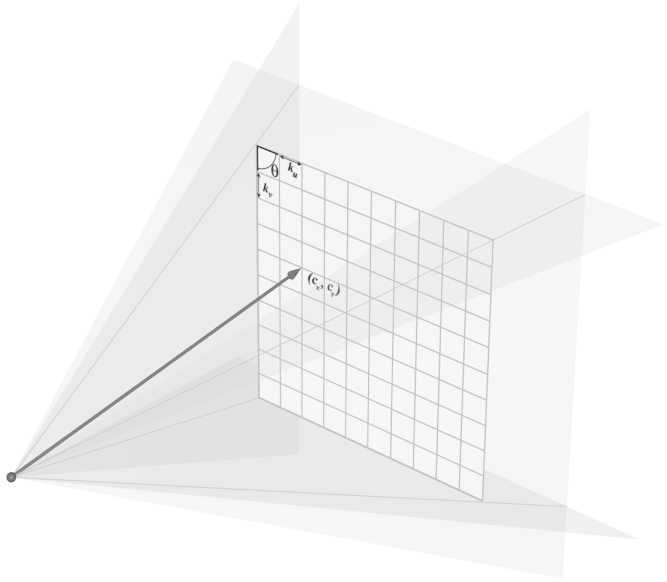

Figure 4-3: Illustration of computer-vision model

In the previous two models the first two columns, which correspond to the $\vec{a}$ and $\vec{b}$ vectors of the general model, were orthogonal and therefore independent. In the computer-vision model the angle θ determines how skewed these spanning vectors are. However, the computer-vision model is still overly general because different combinations of the f, k_u, and k_v terms can give rise to the same camera.

All three alternative planar models make the common assumption that the viewing plane is parallel to the *x*-*y* plane. This family of planes is distinguished by a vector from the origin toward the viewing plane and perpendicular to both the *x*-*y* plane and the viewing plane. This direction is called the *optical axis.* In the general planar pinhole model the optical axis is given by the vector, $\vec{a} \times \vec{b}$. In the computer-graphics and computer-vision pinhole-camera models the optical axis is the *z*-axis.

The assumption that the viewing plane is parallel to the *x*-*y* plane does not limit the generality of the planar pinhole-camera model, since this condition can always be achieved by an appropriate choice of coordinate systems. Ideally, one would like to decompose a general

pinhole-camera specification into two parts: those characteristics determined by the choice of a coordinate frame, and the intrinsic properties of the camera.

4.1.2 A canonical pinhole model

In the computer-graphics and computer-vision pinhole-camera models discussed in the previous section, the coordinate system was conveniently selected in order to simplify the model's formulation. This can be accomplished for the general pinhole camera using a **QR** decomposition that factors a matrix into the product of an orthonormal matrix, **R,** and an upper triangular matrix, **U**. Geometrically, the orthonormal matrix can be considered a rotation that aligns the pinhole model to the desirable coordinate frame. The upper-triangular matrix determines the field-of-view, focal length, optical center, and any other parameters that influence the shape of the viewing frustum. The elements of **U** constitute the so called *intrinsic properties* of the camera.

The upper triangular matrix, **U**, of a **QR** decomposition of the general pinhole-camera model can be expressed in terms of the three column vectors of **P**. This results in the expression given in Equation 4-5, in which **R** is a three-dimensional rotation matrix, and the vectors $\bar{a}$, $\bar{b}$, and $\bar{c}$ are the columns vectors from the general pinhole-camera-model matrix. Notice that the rotated pin-hole-camera matrix, **U**, has the same upper diagonal form as all the previously discussed pinhole-camera models from computer graphics and computer vision.

$$\begin{bmatrix} d_i \\ d_j \\ d_k \end{bmatrix} = \mathbf{R} \begin{bmatrix} a_1' = \sqrt{\bar{a} \cdot \bar{a}} & b_1' = \dfrac{\bar{a} \cdot \bar{b}}{a_1'} & c_1' = \dfrac{\bar{a} \cdot \bar{c}}{a_1'} \\ a_2' = 0 & b_2' = \sqrt{\bar{b} \cdot \bar{b} - b_1'^2} & c_2' = \dfrac{\bar{b} \cdot \bar{c} - b_1' c_1'}{b_2'} \\ a_3' = 0 & b_3' = 0 & c_3' = \sqrt{\bar{c} \cdot \bar{c} - c_1'^2 - c_2'^2} \end{bmatrix} \begin{bmatrix} u \\ v \\ 1 \end{bmatrix} = \mathbf{RU}\bar{u}$$

Equation 4-5: Deriving a canonical-pinhole camera from a general one

QR decompositions are not unique. In general they come in eight varieties according to the signs of the square roots appearing on the upper diagonal. If the orthonormal matrix, **R**, is limited to rotations, then the number of solutions is reduced to four: those where the signs of the determinants of the mapping matrix, **P,** and **U** agree. From this set of four, there exists only one decomposition where the two matrix entries, a_1' and b_2', are positive. I will consider this solution as the canonical representation of **U**.

This transformation has a straightforward physical interpretation. Given the general configuration depicted in Figure 3-2 there exists a family of rotations that aligns the vector $\bar{a}$ with the $\hat{i}$ basis vector. For each rotation, there also exists a second rotation about the $\hat{i}$ basis vector which makes the image plane parallel to the plane containing the $\hat{i}$ and $\hat{j}$ basis vectors. The composition of these two rotations gives the **R** matrix, and the resulting coordinates of the transformed vectors $\bar{a}'$, $\bar{b}'$, and $\bar{c}'$ are the columns of the upper-triangular **U** matrix.

Previously, I have stated that scalar multiples of the general pinhole-camera model result in the same image-space-to-ray mapping function. This is also true of the canonical pinhole-camera representation. Thus, a scaling factor can be selected so that the vector $\bar{a}$ is of unit length. The resulting **U** will have the form

$$U = \begin{bmatrix} 1 & \frac{b_1'}{a_1'} & \frac{c_1'}{a_1'} \\ 0 & \frac{b_2'}{a_1'} & \frac{c_2'}{a_1'} \\ 0 & 0 & \frac{c_3'}{a_1'} \end{bmatrix}$$

Equation 4-6: A normalization of the canonical pinhole-camera model

The resulting normalized planar pinhole model is determined by five independent parameters whose values uniquely determine the solid angle of rays captured by the particular camera. This model can be interpreted physically using the same visualization as the general pinhole model, **P**. We can also develop an intuition for reasonable parameter values by comparing the five parameters to those of the simple pinhole-camera model (Equation 4-1). For example, one might expect that the b_1'/a_1' term would be nearly 0 and that the b_2'/a_1' term would be almost 1 for all but the most unusual of cameras.

4.1.3 Planar calibration

The process of off-line camera calibration can be viewed as the determination of the five unknown parameters of **U** using observations of known points. In addition an online camera calibration process also attempts to determine the six parameters of the camera's pose (its position and orientation). These pose parameters are often called the extrinsic camera parameters, and their unambiguous assignment is dependent on the choice of coordinate frames. In addition to the simple planar pinhole model's parameters, most calibration procedures usually attempt to characterize the nonlinearities of the image-space-to-ray mapping function not described by this simplified model. In the next section I will address this problem and its impact on the warping equation developed using only the ideal planar model.

4.2 Nonlinear Pinhole-Camera Models

The planar pinhole-camera model has some shortcomings which limit its practical use and make it an inconvenient representation for image-based computer graphics. First, a planar pinhole camera is only capable of representing a subset of those rays visible from a particular viewing position. This results from the fact that even an infinite plane subtends only half of the 4π solid angle visible from a given point. Second, the idealized and mathematically elegant planar pinhole-camera model does not reflect the true nature of real-world image acquisition devices.

In this section a series of more general pinhole-camera models will be characterized which address the problems of the ideal planar model. The first set of generalizations overcomes the problem of the limited solid angle visible by a planar pinhole camera by describing the mathematical structure of several panoramic cameras. Next, a series of modified pinhole models will be discussed that account for the geometric distortions present in real-world cameras.

The essence of the pinhole camera is the mapping function from image-space coordinates to rays in a viewing space. In the case of a planar pinhole camera this mapping function is a linear rational function, easily described by a matrix. The more complicated models described in this section are algebraic in nature and more difficult to manipulate in general. However, much of the intuition developed for the linear case can be readily adapted to these more complicated models.

4.3 Panoramic Pinhole Cameras

I have described image-based computer graphics as a process in which a set of reference images is used to interpolate, extrapolate, and otherwise model the plenoptic function of a given visual environment. By fixing both the time and viewpoint, the plenoptic function reduces to a form that is equivalent to our typical notion of an image. Furthermore, any reference image used to model a scene represents some subset of such an image.

Our practical experience with images, however, is limited to a surprisingly small fraction of the visual sphere. The typical 50 mm lens on a 35 mm camera captures less than 3% of the available solid angle. Even a relatively wide angle 28 mm lens on the same camera captures just over 7% of the visual sphere. Our visual system, however, incorporates

information over a very large visual angle, estimated at about 43% of the visual sphere on average [Slater93].

The term *panoramic* is commonly used to describe images with large aspect ratios. However, its proper definition is "an unobstructed view of an extensive area". I will use the term panoramic to describe any image whose field-of-view covers a significant fraction of the visual sphere. In particular I will consider cameras that cover the full range of at least one of the two angle parameters of a properly oriented spherical coordinate system to be panoramic. Thus, an image captured through a fisheye lens would be considered more panoramic than a cropped aerial image of a city skyline. Unlike a cropped image, a true panoramic image, like any wide-angle view, usually exhibits significant perspective distortions unless viewed from the appropriate position.

The motivation for developing warping equations for wide-field-of-view images is that they are particularly well suited for use as reference images. Their use also provides many useful simplifications by eliminating boundary cases. The pinhole-camera models described first in this section are characterized by mapping functions capable of describing larger portions of the visual sphere than possible with the planar pinhole-camera model. However, like the planar pinhole model, these wide-field-of-view pinhole-camera models are ideal mathematical constructions. Thus, in the context of an image-based graphics system, they are perhaps most useful as an intermediate model representation, rather than as a description for either acquired source images or synthesized results.

In each of the models that follows all of image-space is considered to be parameterized over the domain of a unit square. These models map image points to a ray direction in a Euclidean three-space. If required, an auxiliary pre-warp can be applied to the image-space coordinates to map the pixel coordinates onto the unit square. Usually, this pre-warp is nothing more than a scaling of the two pixel coordinates by their extreme values.

Just as the canonical representation of the planar pinhole model provides for the most compact representation of the camera's intrinsic properties, similar simplifications can be applied to non-planar models. The relationship of the canonical model to an arbitrary representation was merely a choice of an appropriate coordinate system. The coordinate systems of the non-planar mapping functions can also be selected such that their expression is in terms of some minimal number of parameters. A post-warp rotation can be applied to orient

the canonical frame to any desired orientation. All of the following pinhole-camera models are presented in their canonical forms and defined over the domain of a unit square.

4.3.1 Cylindrical pinhole-camera model

In a cylindrical imaging geometry only one of the two image-space dimensions is sampled over the full range of possible angles. Thus, a cylindrical camera, like the planar model, is also only capable of representing a subset of the visual sphere. However, the solid angle subset that can be represented by cylindrical geometry does asymptotically approach the full 4π range, whereas a planar geometry can, at best, represent only 2π. The following three-parameter model can be used to specify a canonical cylindrical mapping:

$$\bar{d} = \mathbf{C}(\bar{x}) = \begin{bmatrix} \sin\left(2\pi u + k_{cylinder} v\right) \\ y_o + \left(y_1 - y_0\right) v \\ \cos\left(2\pi u + k_{cylinder} v\right) \end{bmatrix} \qquad u, v \in [0,1]$$

Equation 4-7: Canonical cylindrical mapping function

The panoramic nature of the cylindrical pinhole-camera model actually reduces the number of intrinsic camera parameters required for its concise specification, as illustrated in Figure 4-4. Two of the parameters, and y_1, control the vertical field of view. The remaining parameter, $k_{cylinder}$, behaves similarly to the skew parameter of the planar model.

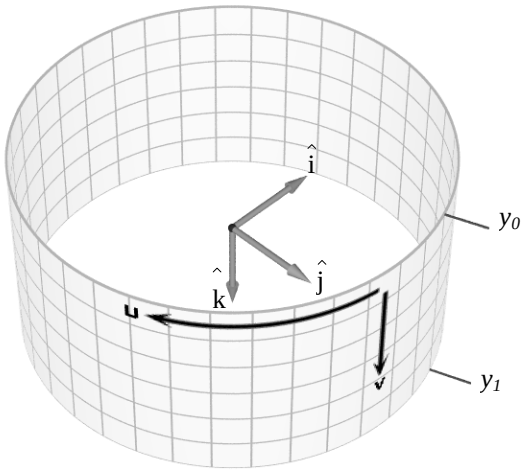

Figure 4-4: The canonical cylindrical pinhole-camera viewing surface

In this canonical representation the cylinder's axis is aligned with the $\hat{k}$ basis vector. The skew parameter in the figure shown is nearly zero, as reflected by the perpendicular orientation of the isoparametric lines shown on the viewing surface. Unlike the planar pinhole-camera case, the skew parameter has no effect on the shape of the solid angle acquired by the camera. Therefore, for each cylindrical-pinhole camera, there exists an equivalent camera, in terms of the solid angle sampled, for which the value of $k_{cylinder}$ is 0. Such a camera configuration can be achieved with an appropriate linear prewarp as shown below:

$$\begin{bmatrix} u' \\ v' \end{bmatrix} = \begin{bmatrix} 1 & \frac{-k_{cylinder}}{2\pi} \\ 0 & 1 \end{bmatrix} \begin{bmatrix} u \\ v \end{bmatrix}$$

Equation 4-8: Prewarp to remove skew parameter from a cylindrical mapping function

The inverse of the cylindrical mapping function maps a given ray's direction to an image-space coordinate. The expression for this mapping function is given in Equation 4-9[13].

$$\bar{x} = \mathbf{C}^{-1}(\bar{d}) = \begin{bmatrix} \frac{\text{Arctan}(d_x / d_z) - k_{cylinder} \frac{\frac{d_y}{\sqrt{d_x^2 + d_z^2}} - y_0}{y_1 - y_0}}{2\pi} \\ \frac{\frac{d_y}{\sqrt{d_x^2 + d_z^2}} - y_0}{y_1 - y_0} \\ 1 \end{bmatrix}$$

Equation 4-9: Inverse of the cylindrical mapping function

A cylindrical viewing surface has several practical advantages when used as a plenoptic sample representation. Since a cylinder is a developable surface it can easily be represented in a computer's memory using a two-dimensional array. Also, since the angular sampling density is constant around the cylinder's circumference it is a slightly more efficient representation than a planar projection. But the most significant advantage of the cylindrical viewing surface is that it is relatively simple to acquire such projections by reprojecting planar images acquired when a camera that is rotated on a tripod [Mann94], [Chen95], [McMillan95c]. The following figures represent projections acquired from cylindrical pinhole cameras:

[13] I am choosing to maintain the homogeneous representation of image-space points so that subsequent projective transforms might be applied.

Figure 4-5: A cylindrical pinhole model of an operating room scene

Figure 4-6: A cylindrical pinhole model of Sitterson Hall

Figure 4-7: A wide-angle cylindrical pinhole model of the old well

The image-warping equation can easily be adapted to use the cylindrical pinhole-camera model. The relationship of the image-space coordinates of a point that is seen in two images is given by

$$\mathbf{C}_1(\bar{x}_1) = \delta(\bar{x}_0)(\dot{C}_0 - \dot{C}_1) + \mathbf{C}_0(\bar{x}_0)$$

Equation 4-10: Cylinder-to-cylinder correspondence

Note the similarities between Equation 4-10 and the planar mapping of Equation 3-4. The derivation of the warping equation for the cylindrical camera is more complicated than in the planar case, since the mapping functions are nonlinear and must be manipulated as algebraic expressions instead of linear algebra. The resulting cylinder-to-cylinder warping equation is given by

$$\bar{x}_1 = \mathbf{C}_1^{-1}\left(\delta(\bar{x}_0)(\dot{C}_0 - \dot{C}_1) + \mathbf{C}_0(\bar{x}_0)\right)$$

Equation 4-11: Special cylinder-to-cylinder warping equation

In this expression the two pinhole cameras are defined independently; however, their basis vectors are assumed to be parallel. A more general version of the warping equation is required when the basis vectors are not aligned.

$$\bar{x}_1 = \mathbf{C}_1^{-1}\left(\delta(\bar{x}_0)(\dot{C}_0 - \dot{C}_1) + \mathbf{R}(\dot{a},\theta)\mathbf{C}_0(\bar{x}_0)\right)$$

Equation 4-12: General cylinder-to-cylinder warping equation

In the equation above $\mathbf{R}(\dot{a},\theta)$ is a three-dimensional rotation matrix about the axis $\dot{a}$ by an angle of θ, defined in the coordinate system of the reference image with an origin of $\dot{C}_0$. Any other parameterization of a three-dimensional rotation can also be used.

When both cylindrical pinhole-camera models are known to have the same intrinsic parameters and are defined with parallel basis vectors, the warping equation can be simplified to

$$\bar{x}_1 = \mathbf{C}^{-1}(\delta(\bar{x}_0)(\dot{C}_0 - \dot{C}_1) + C(\bar{x}_0))$$

$$\bar{x}_1 = \begin{bmatrix} \frac{1}{2\pi}\left(\text{Arctan}\left(\frac{\sin(2\pi u + k_{cylinder}v) + \delta(u,v)(C_{0x} - C_{1x})}{\cos(2\pi u + k_{cylinder}v) + \delta(u,v)(C_{0z} - C_{1z})}\right) - k_{cylinder}\left(\frac{\delta(u,v)(C_{0y} - C_{1y})}{y_1 - y_0} + v\right)\right) \\ \frac{\delta(u,v)(C_{0y} - C_{1y})}{y_1 - y_0} + v \\ 1 \end{bmatrix}$$

Equation 4-13: Aligned cylinder-to-cylinder warping equation

If the cylinder's skew parameter is zero, the warping equation further simplifies to

$$\bar{x}_1 = \begin{bmatrix} \frac{1}{2\pi}\left(\text{Arctan}\left(\frac{\sin(2\pi u) + \delta(u,v)(C_{0x} - C_{1x})}{\cos(2\pi u) + \delta(u,v)(C_{0z} - C_{1z})}\right)\right) \\ \frac{\delta(u,v)(C_{0y} - C_{1y})}{y_1 - y_0} + v \\ 1 \end{bmatrix}$$

Equation 4-14: Aligned cylinder-to-cylinder warping equation without skew

Just as in the planar-warping equation, the cylindrical-warping equation specifies a mapping of points from the reference image to their positions in a desired image. The warp is controlled by a generalized-disparity parameter that is specified at each point of the reference image. When the center-of-projection of the desired image coincides with the center-of-

projection of the reference image, the warping equation reduces to the reprojection case as follows:

$$\bar{x}_1 = \mathbf{C}_1^{-1}\left(\mathbf{R}(\dot{a},\theta)\mathbf{C}_0(\bar{x}_0)\right)$$

Equation 4-15: Cylinder-to-cylinder reprojection

As mentioned previously, panoramic images are particularly useful as reference image representations. The cylinder-to-cylinder warping function described above can be used to accomplish such mapping. Typically, though, the desired image will be a planar projection. It is possible to re-project the results of the cylinder-to-cylinder mapping onto the desired viewing plane directly.

$$\bar{x}_1 \doteq \mathbf{P}_1^{-1}\left(\delta(\bar{x}_0)(\dot{C}_0 - \dot{C}_1) + \mathbf{C}_0(\bar{x}_0)\right)$$

Since the inverse of the planar-mapping function is linear, it can be distributed across the sum as shown in the following equation:

$$\bar{x}_1 \doteq \delta(\bar{x}_0)\mathbf{P}_1^{-1}(\dot{C}_0 - \dot{C}_1) + \mathbf{P}_1^{-1}\mathbf{C}_0(\bar{x}_0)$$

Equation 4-16: Cylinder-to-plane warping equation

This expands to the following rational expressions:

$$u_1 = \frac{(b_y c_z - b_z c_y)\sin(2\pi u_0 + k v_0) + (b_x c_y - b_y c_x)\cos(2\pi u_0 + k v_0) + (b_z c_x - b_x c_z)\left(y_0 + (y_1 - y_0)v_0\right) + \left(\dot{C}_0 - \dot{C}_1\right)\cdot\left(\bar{b}\times\bar{c}\right)\delta(u_0, v_0)}{(a_y b_z - a_z b_y)\sin(2\pi u_0 + k v_0) + (a_x b_y - a_y b_x)\cos(2\pi u_0 + k v_0) + (a_z b_x - a_x b_z)\left(y_0 + (y_1 - y_0)v_0\right) + \left(\dot{C}_0 - \dot{C}_1\right)\cdot\left(\bar{a}\times\bar{b}\right)\delta(u_0, v_0)}$$

$$v_1 = \frac{(c_y a_z - c_z a_y)\sin(2\pi u_0 + k v_0) + (c_x a_y - c_y a_x)\cos(2\pi u_0 + k v_0) + (c_z a_x - c_x a_z)\left(y_0 + (y_1 - y_0)v_0\right) + \left(\dot{C}_0 - \dot{C}_1\right)\cdot(\bar{c}\times\bar{a})\delta(u_0, v_0)}{(a_y b_z - a_z b_y)\sin(2\pi u_0 + k v_0) + (a_x b_y - a_y b_x)\cos(2\pi u_0 + k v_0) + (a_z b_x - a_x b_z)\left(y_0 + (y_1 - y_0)v_0\right) + \left(\dot{C}_0 - \dot{C}_1\right)\cdot\left(\bar{a}\times\bar{b}\right)\delta(u_0, v_0)}$$

Equation 4-17: Expanded cylinder-to-plane warping equation

This equation can be used to map the points of a cylindrical pinhole-camera model to any viewing plane. Consider the following example of a cylindrical projection.

Figure 4-8: A cylindrical projection

The cylindrical projection shown above was assembled by first registering 12 planar projections and then reprojecting them onto a cylindrical viewing surface using Equation 4-14 [McMillan95c]. These planar projections were themselves reprojections of acquired images that were captured using a fish-eye lens and reprojected using a nonlinear pinhole-camera model discussed in the next subsection. The following projections demonstrates the use of the cylinder-to-plane warping equation given in Equation 4-17.

Figure 4-9: Desired images from a cylinder-to-plane warp

Each of the four images shown in Figure 4-9 result from a cylinder-to-plane warp of Figure 4-8. The lower boundary of the cylindrical viewing surface is clearly visible in the lower-left image.

4.3.2 Spherical model

A spherical imaging geometry spans the full range of both angle parameters. It therefore represents the entire 4π visual angle and a complete pencil of rays. The spherical pinhole-camera model has fewer intrinsic parameters than any other model. The following one intrinsic-parameter mapping function describes the canonical spherical pinhole camera:

$$\hat{d} = \mathbf{S}(\bar{x}) = \begin{bmatrix} \sin(2\pi u + k_{sphere} v)\sin\pi v \\ \cos\pi v \\ \cos(2\pi u + k_{sphere} v)\sin\pi v \end{bmatrix} \qquad u, v \in [0,1]$$

Equation 4-18: Spherical mapping function

Once more, the intrinsic spherical skew parameter, k_{sphere}, is similar to the planar skew factor; when it is zero, the isoparametric curves intersect at right angles. The intrinsic skew parameter does not, however, have any effect on the solid angle represented by the mapping function. Therefore, it can also be made zero with a suitable prewarp.

$$\begin{bmatrix} u' \\ v' \end{bmatrix} = \begin{bmatrix} 1 & \frac{-k_{sphere}}{2\pi} \\ 0 & 1 \end{bmatrix} \begin{bmatrix} u \\ v \end{bmatrix}$$

Equation 4-19: Prewarp to remove spherical skew

The viewing surface of the canonical spherical mapping function is shown below with a skew value of zero.

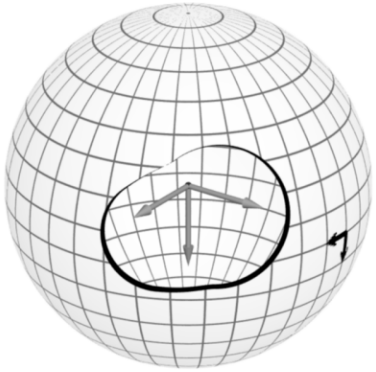

Figure 4-10: The viewing surface of the canonical spherical pinhole-camera model

The cutout allows the basis frame of the ray-space, as well as the image-space basis frame, to be seen. The image-space parameterization of the spherical camera model is non-uniform in its solid angle coverage. While none of the pinhole cameras discussed thus far (planar or cylindrical) realize a uniform sampling of the solid angle, the spherical geometry is notable in its deviation. A side effect of this nonuniform coverage is that any image-space presentation of a spherical projection appears geometrically distorted. This is especially noticeable around the poles of the projection. Furthermore, the lack of uniformity is somewhat surprising since the image-space parameters are directly related to planar angle values.

The inverse of the spherical mapping function is given by the following expression:

$$\bar{x} = \mathbf{S}^{-1}(\hat{d}) = \begin{bmatrix} \dfrac{\text{Arctan}\left(\frac{d_x}{d_z}\right)}{2\pi} - k_{sphere}\dfrac{\text{Arctan}\left(\frac{\sqrt{d_x^2+d_z^2}}{d_y}\right)}{(2\pi)^2} \\ \dfrac{\text{Arctan}\left(\frac{\sqrt{d_x^2+d_z^2}}{d_y}\right)}{2\pi} \\ 1 \end{bmatrix}$$

Equation 4-20: Inverse spherical pinhole-camera model

The spherical pinhole-camera model can also be used as a mapping function in the warping equation. A general treatment of the process for modifying the warping equation will be discussed at the end of this section.

4.4 Distorted Pinhole-Camera Models

The second group of nonlinear pinhole cameras discussed are significant because they characterize realizable imaging systems rather than mathematical abstractions. A researcher is likely to run into one of these camera models when capturing wide-angle images for use in an image-based graphics system. They can even be considered for use as reference image representations in real-time systems [VTV96].

The pinhole-camera models explained in this section are often associated with geometric distortion models. In optics, computer vision, or computer graphics the term *geometric distortion* is used to indicate deviations from a standard projection model that are manifested as shape discrepancies of the depicted object. The difficulty in defining distortions comes in the selection

of a standard projection model. The most common choice is a planar pinhole model. The advantages of the planar pinhole model include a precise mathematical description and the model's preservation of certain geometric invariants, such as collineation (the preservation of lines). However, even planar pinhole images captured at extremely wide angles exhibit perspective distortions when viewed from a point other than the original center-of-projection. This phenomenon is largely perceptual. One hypothesis [Zorin95] suggests that the visual system attempts to interpret uniform spacing in the image plane as a constant angular variation. Regardless of the perceptual ramifications, the planar model's non-uniform sampling of solid angles leads to shortcomings in its use for representation.

Planar projections are sampled more densely, in the angular sense, around the periphery of an image than in the image's center. This leads to a wasteful representation when used as a reference image because, as the field-of-view is extended, the number of additional samples grows faster than the solid angle covered by those samples. The nonuniformity of this sampling pattern and its associated distortion pattern is illustrated in Figure 4-11.

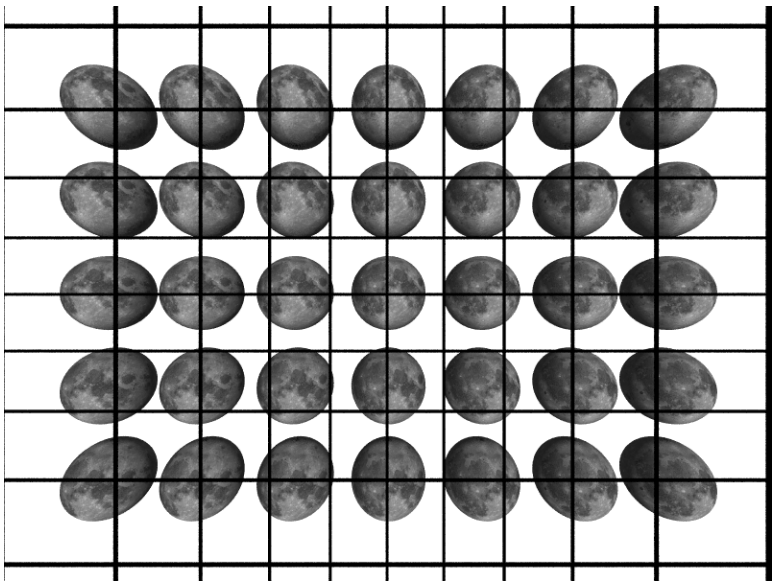

Figure 4-11: Wide-angle distortion from a 100° field-of-view planar projection

Figure 4-11 depicts a 7×5 grid of regularly spaced spheres as seen through a planar pinhole camera with a 100º field-of-view. The superimposed grid indicates an angular spacing of 10º. In general only the spheres nearest the center appear spherical. This perceptual artifact can be eliminated by viewing the figure at a distance of approximately 1.68 inches with a single

eye. The increased grid size near the periphery of the image indicates that those regions are over-sampled.

Nonlinear pinhole-camera models can come closer to a uniform sampling of solid angles. The cylindrical pinhole model achieves uniform sampling along one of the angular dimensions, as illustrated in Figure 4-12. In this figure the same 7×5 grid of spheres is shown viewed through a 100º field-of-view cylindrical projection whose axis is aligned with the vertical axis of the page. The even spacing of the horizontal grid reflects a uniform angular sampling in the horizontal direction.

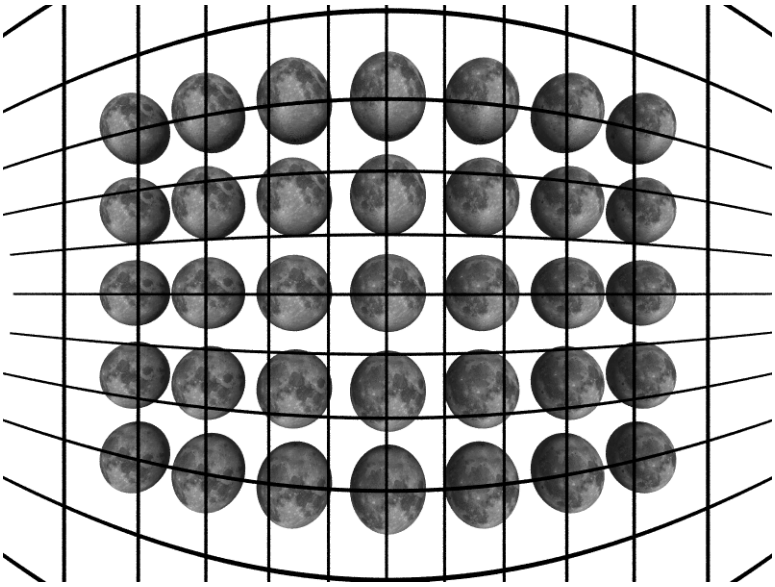

Figure 4-12: A cylindrical projection with a 100° field-of-view

The apparent curvature of the vertical grid is indicative of the fact that a cylindrical pinhole camera does not preserve lines, except those parallel to the cylinder axis. The shape of the center row of spheres in this image appears less distorted than the planar case; however, distortion is still visible along vertical columns.

Figure 4-13 shows the projection of the same scene through the fisheye pinhole-camera model discussed in the next subsection.

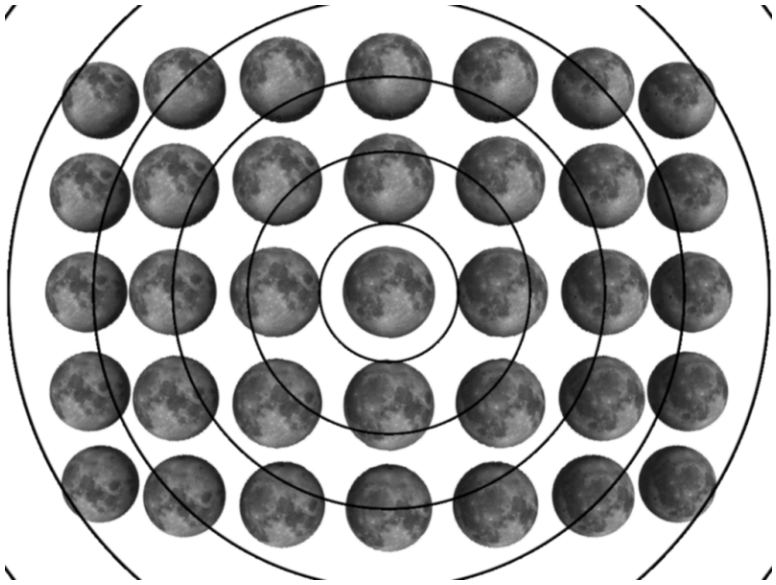

Figure 4-13: A fisheye projection with a 100° field-of-view

In a fisheye projection the angle varies linearly along the radius from the image center (the point where the optical axis intersects the viewing surface). The superimposed circles illustrate 10º increments from this image center. This angular sampling pattern is locally uniform. The uniform sampling angle comes at the loss of uniform scaling and preservation of lines. Thus, while the shape of the spheres in the fisheye projection appear undistorted, their sizes appear non-uniform, and both the rows and columns appear bent. Because of this nearly uniform angular sampling pattern, a fisheye pinhole-camera model has advantages when used as a reference image representation in an image-based computer graphics system.

4.4.1 Fisheye pinhole-camera model

Fisheye lenses are often used for very wide-angle photography. These lenses are also notable for their distinctive geometric distortion pattern. Fisheye lenses are a real-world example of a lens capable of mapping a panoramic image onto a film plane or other imager. Fisheye lenses have been designed to capture significantly more than half of the visual sphere. The picture below was taken with a fisheye lens having a diagonal field of view of nearly 180°.

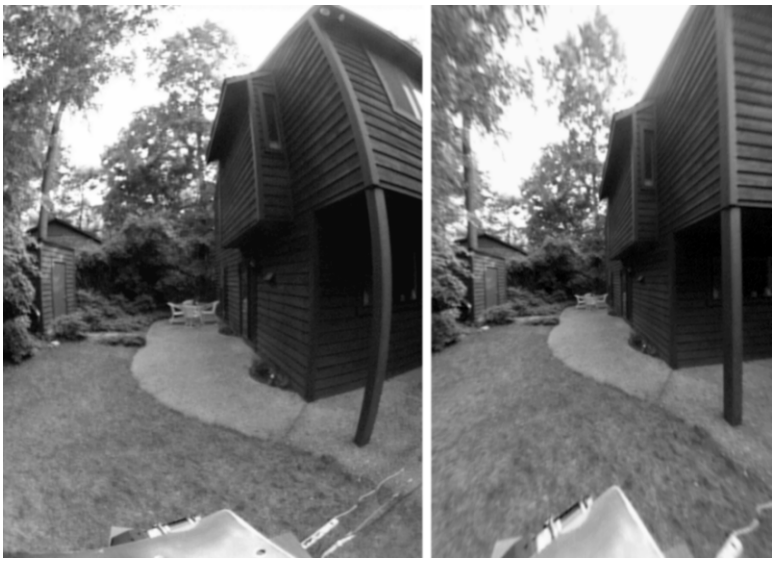

Figure 4-14: A fisheye (left) and planar (right) projection of a yard scene

The mapping of a point on the fisheye imaging surface to a ray direction vector is nonlinear in terms of image-space coordinates. However, this fisheye mapping function is linear with respect to the angle between the ray and the optical axis[14]. An ideal fisheye pinhole-camera model is described by the following mapping function:

$$\hat{d} = F(\bar{x}) = \begin{bmatrix} u_0 - u \\ v_0 - v \\ \dfrac{\kappa\sqrt{(u_0-u)^2 + (v_0-v)^2}}{\tan\left(\kappa\sqrt{(u_0-u)^2 + (v_0-v)^2}\right)} \end{bmatrix} \qquad u, v \in [0,1]$$

Equation 4-21: Fisheye distortion mapping function

A fisheye pinhole camera maps half of the visual sphere (the equivalent to an infinite plane) onto a disk of radius $\pi/2\kappa$. If appropriately designed, the imaged angle may even extend outside of this disk. The viewing surface of a fisheye pinhole camera is shown below with isoparametric lines overlaid.

[14] Fisheye projections are often confused with *spherical central projections* where, at most, a single hemisphere of solid angle is mapped to a plane, and the angular sampling density is proportional to sin θ rather than linear with θ.

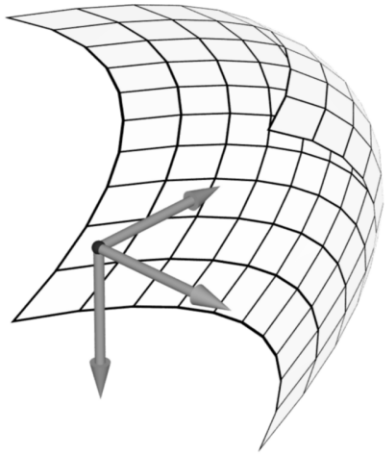

Figure 4-15: View surface of a fisheye pinhole model

Note that this viewing surface would appear as a unit square when orthographically projected onto the *x*-*y* plane. The inverse of the fisheye mapping function is given below.

$$\bar{x} = \mathbf{F}^{-1}\left(\hat{d}\right) = \begin{bmatrix} u_0 - d_x \\ v_0 - d_y \\ \dfrac{1}{\kappa\sqrt{d_x^2 + d_y^2}} \operatorname{Arctan}\left(\dfrac{\kappa\sqrt{d_x^2 + d_y^2}}{d_z}\right) \end{bmatrix}$$

Equation 4-22: Inverse fisheye distortion mapping function

4.4.2 Radial distortion pinhole-camera model

Fisheye lenses are designed so that a linear variation on the image plane corresponds to a linear change in the incident angle of an incoming ray. The apparent geometric distortions seen through a fisheye lens, such as the apparent curving of lines, are artifacts of this mapping. In most other lens designs geometric distortions relative to the planar pinhole-camera model are undesirable. These distortions arise because the design of real-world lenses involves a complex series of tradeoffs between design parameters; geometric distortions are only one consideration. In this section I will develop a pinhole camera model that is capable of approximating most of the common geometric distortions seen in real-world lenses.

Rotational symmetry is common to all of the elements in a typical compound lens design. This symmetry dictates that the pattern of geometric distortion, as well as most other lens attributes, will vary radially from the point that the system's central axis projects onto the image plane. The variations from an ideal pinhole camera seen in the image plane are usually modeled in terms of their spatial frequency using Fourier analysis. Because of the lens-system's symmetry, only the odd (sine) terms are involved in these models. It is common to consider only the first three terms of a Taylor series expansion in the summation of these additive effects [Smith92]. This results in a simple cubic radial-distortion model of the form $r' = r(1+\kappa r^2)$. This simple model can be used to accurately model the common pincushion ($\kappa > 0$) and barrel ($\kappa < 0$) geometric distortions that are frequently seen in real-lens systems [Tsai87].

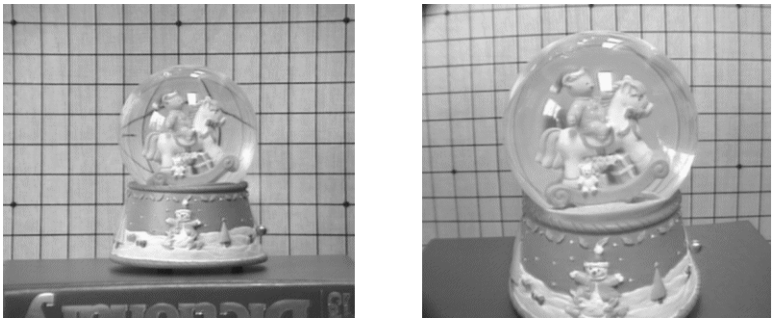

Figure 4-16:Two images exhibiting radial distortion.

In the figure above a slight pincushion distortion is visible in the telephoto (narrow field-of-view) projection shown in left image. The wide-angle projection shown in the right image exhibits noticeable barrel distortion.

The following image-space-to-ray mapping function (a.k.a. pinhole-camera model) can be used to model a radial cubic distortion:

$$\hat{d} = \mathbf{R}(\bar{x}) = \begin{bmatrix} u_0 - u \\ v_0 - v \\ \dfrac{1}{1+\kappa((u_o-u)^2+(v_0-v)^2)} \end{bmatrix} \quad u,v \in [0,1]$$

Equation 4-23: Cubic distortion mapping function

Viewing surfaces for a cubic distortion pinhole-camera model that is capable of representing both barrel and pincushion distortions are illustrated in Figure 4-17. The concave surface relative to the center-of-projection will produce a barrel distortion pattern. The convex surface produces a pincushion distortion.

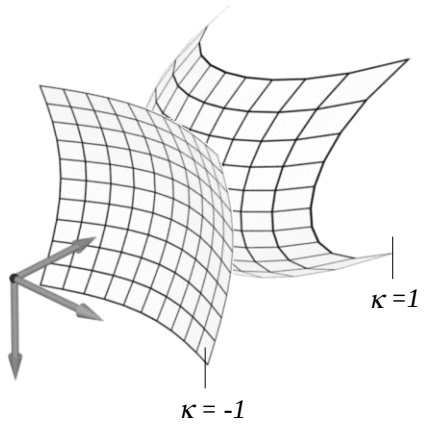

Figure 4-17: Mapping onto cubic radial distortion surfaces

The inverse mapping function from a ray direction to an image-space coordinate is

$$\bar{x} = \mathbf{R}^{-1}\left(\hat{d}\right) = \begin{bmatrix} u_0 - d_x \\ v_0 - d_y \\ d_z\left(1 + \kappa\left(d_x^2 + d_y^2\right)\right) \end{bmatrix} \quad u, v \in [0,1]$$

Equation 4-24: Inverse cubic distortion mapping function

Many more pinhole-camera models are possible. In general any one-to-one mapping from a two-dimensional parameter space to a space of rays can be considered a pinhole-camera model. In this chapter I have focused primarily on camera models that provide representational advantages because of their panoramic nature and on models that are good approximations to real-world imaging systems.

4.5 Modifying Warping Equations

To this point, warping equations have been derived for the following pinhole camera configurations:

- plane-to-plane
- cylinder-to-cylinder
- cylinder-to-plane

In this section a general methodology is developed that allows a disparity-augmented reference image with its associated pinhole-camera model to be warped to a desired image using any other pinhole-camera model. The only requirements on these pinhole-camera models are that their mapping functions be one-to-one (each image-space point maps to a unique ray and vice-versa), and that both a forward projection (image-space to ray) and an inverse projection (ray to image-space) mapping can be specified. These conditions are satisfied by all of the pinhole cameras discussed to this point.

The coordinate of a point, $\dot{X}$, in a Euclidean three space is

$$\dot{X} = \dot{C}_0 + \alpha M_0(\bar{x}_0) = \dot{C}_1 + \beta M_1(\bar{x}_1)$$

where $M_0(\bar{x})$ and $M_1(\bar{x})$ are the mapping functions from image coordinates to ray directions. These mapping functions may, or may not, use the same pinhole-camera model. As in the planar case, the terms $\dot{C}_0$ and $\dot{C}_1$ represent the three-space coordinates of the respective cameras' centers-of-projection. Isolating the projective mapping function about $\dot{C}_1$ gives

$$\mathbf{M}_1(\bar{x}_1) = \tfrac{1}{\beta}(\dot{C}_0 - \dot{C}_1) + \tfrac{\alpha}{\beta}\mathbf{M}_0(\bar{x}_0)$$

By scaling both sides by β/α, which takes advantage of the fact that a ray's direction is independent of its scale, and then defining $\delta(\bar{x}_0) = 1/\alpha$, to indicate α's dependence on the parametric coordinate $\bar{x}_0$, and computing the inverse-projective mapping of both sides, the following warping equation results:

$$\bar{x}_1 = \mathbf{M}_1^{-1}(\delta(\bar{x}_0)(\dot{C}_0 - \dot{C}_1) + \mathbf{M}_0(\bar{x}_0))$$

Equation 4-25: General geometrically consistent warp

This general equation can be used to map points specified in one image-space to any other. This includes the process of reprojection where both the source and destination images share a common center-of-projection.

4.6 Real cameras

The projection and warping approaches used in this chapter, while more general than a planar pinhole-camera model, are still only approximations to real-world imaging systems. Parametric mappings onto viewing surfaces, via nonlinear pinhole cameras, are adequate models for geometric distortions in the image plane. However, pinhole models are still unable to describe many of the artifacts commonly found in images.

The assumption that all rays collected on the viewing surface originate (or pass through) a single point in space is the most obvious simplification made in the pinhole-camera model. It is this property that gives a pinhole camera its name. In real imaging systems the rays pass through a finite aperture stop. Points on the viewing plane correspond to a weighted average of all of the rays passing through this aperture. Therefore, there is no single mapping of points on the image plane to rays in space. It is this property of real lenses that creates depth-of-field (i.e., objects at different ranges appear in various degrees of focus). In a true pinhole camera all points are in sharp focus.

Another deviation between real cameras and ideal pinhole models is the existence of a lens for the purpose of bending and focusing light. The light-bending ability of a lens is a result of its refractive properties. Refraction results from the fact that the speed at which light propagates through non-conductive materials varies depending on the materials' properties. The propagation speed through a material also depends on the wavelength of the incident light energy. Since the various colors of the spectrum are distinguished by their difference in wavelengths, the refraction of light by lenses introduces color shifts on the viewing surface. This phenomenon is called *chromatic aberration*. Optical designers go to great lengths to select lens materials and designs in order to minimize this effect. In an ideal pinhole camera, variations due to wavelength are completely ignored, whereas in reality diffraction would come into play.

4.6.1 Nonlinear camera calibration

As discussed earlier, the problem of determining either or both the intrinsic and extrinsic parameters of a pinhole-camera model from a set of image-space observations is called

camera calibration. By extending the definition of pinhole cameras to include nonlinear models, distortion parameters can also be determined in the calibration process. There are many different approaches to calibration.

One of the most popular approaches includes global optimizations based on an all encompassing model in which distortion and intrinsic parameters are simultaneously solved for [Tsai87]. A second approach involves a series of reprojections in which distortion parameters are first computed based on the preservation of known projective invariants (for example, the preservation of lines or quadrics curves). Once the distortion parameters are found, the rectified image is then reprojected to a planar viewing surface, and the intrinsic planar parameters are found [Lenz87]. The third approach involves a tabular mapping from image-space to rays. This approach is data intensive yet very flexible. Table-based calibration approaches usually require interpolation from a non-uniform sparse collection of data points. An additional difficulty of this approach arises when an inverse mapping is required.

4.7 Summary

This chapter presented several generalizations of the image-to-ray mapping functions that were assumed in Chapter 3. The general planar pinhole camera that was presumed when deriving the warping equation was first related to planar pinhole-camera models used in other applications. A canonical planar pinhole-camera model was then introduced that isolates the distinguishing characteristics of a camera from the coordinate frame in which the camera is defined. Among these characteristics are five parameters that describe a viewing frustum and the skew and aspect ratio of the viewing plane.

A series of nonlinear pinhole cameras were next defined. These had practical advantages over the planar pinhole models because they represented a larger portion of the rays seen at a given point. The panoramic nature of these camera models reduces the number of intrinsic parameters required for the pinhole camera's description, resulting in fewer parameters to be estimated in the calibration process. Another family of nonlinear pinhole cameras was defined that emulates the geometric distortions typical of real-world imaging systems. The general image-based computer graphics approach was extended to incorporate these nonlinear models.

Chapter 5

WARPING WITHOUT CALIBRATION

Previously, I have discussed how an image that has been augmented with generalized-disparity information can be warped to produce projections from different viewpoints. Initially, these warps were developed for images projected onto planar viewing surfaces, and subsequently this result was generalized to arbitrary viewing surfaces. All of these warps required the specification of both the reference and the desired centers-of-projection. In addition, the pinhole-camera models for both images were needed. In this chapter, I will discuss how to perform these warps when knowledge about the centers-of-projection and the camera models (i.e., the calibration information) is unavailable. I begin by introducing a geometric structure called an epipolar geometry which establishes image-to-image relationships that are constrained by an underlying three-dimensional geometry. Then, I relate this epipolar geometry to the planar-warping equation, and I demonstrate how an epipolar geometry can be used to determine image warps in the absence of predefined calibration information.

I consider only the planar-pinhole camera model. This greatly simplifies the discussion and allows for the simple manipulation of expressions using linear algebra. However, most of the developments presented can be generalized to nonlinear camera models, although the math is more complicated. Moreover, the intuitions developed are directly transferable between the various cases.

5.1 Epipolar Geometries and the Fundamental Matrix

The rays of one perspective image are seen as a family of lines that intersect at a common image-space point when viewed from the center-of-projection of a second image. Likewise, the rays of this second view define a similar structure in the first image. As illustrated in Figure 2-4, any two centers-of-projection and a ray from either one of them defines a planar subspace. The projection of such a plane forms a line on each image. If the two centers-of-

projection are fixed and every ray from one source is considered, an entire family of planes is defined. This set of planes, which is given the formal name *axial pencil*, will project onto each image as a family of lines called a *linear pencil*. The set of all planes sharing a line passing through two centers-of-projection is called the *epipolar geometry* of the camera configuration.

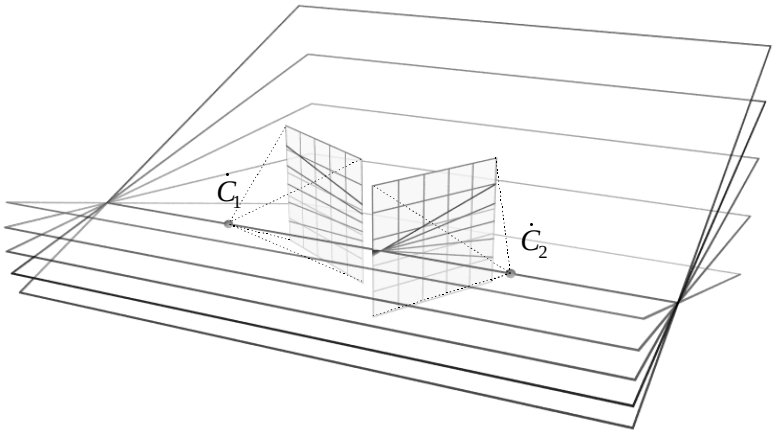

Figure 5-1: An epipolar geometry

The existence of this geometric structure has significant ramifications. For example, any general point in an image will determine a line in a second image. Also, the three-space point visible at a selected image-space point will lie on a specific line in the second image. In other words, a point in one image determines a ray in space along which a three-space point can be seen. Generally, that ray will project elsewhere as a line intersecting the projection of this visible point. The exception to this relationship occurs when the image-point's ray lies on the line connecting the two centers-of-projection. This ray will project to a point in both images. Such points are called *epipoles*. There are exactly two antipodal rays on the line connecting the centers-of-projection, each defining two epipoles. In a planar projection, only one of these two epipoles can be visible because the solid angle subtended by a plane is limited to 2π steradians. When the epipole's direction is toward the second camera's center-of-projection, it represents the origin of the ray bundle. If the epipole's direction is away from the second camera's center-of-projection, it represents a vanishing point of the ray bundle. The type of the epipole (origin vs. vanishing point) can be determined from correspondence information.

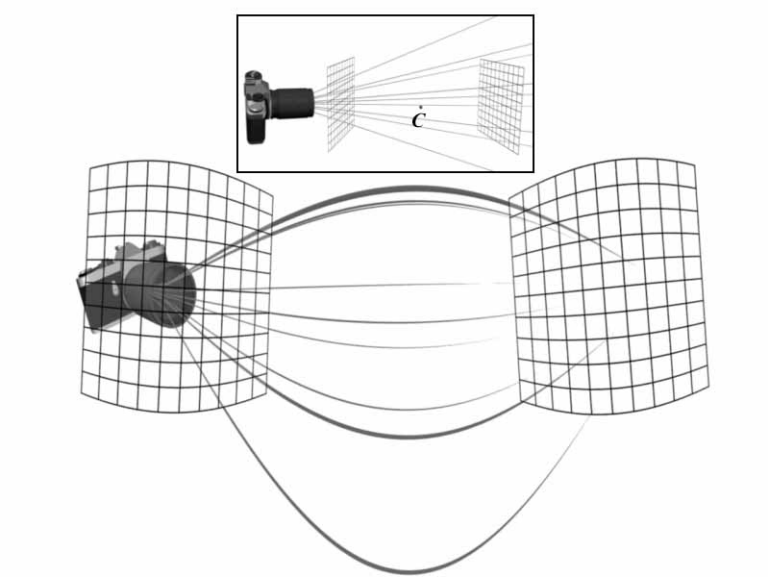

Figure 5-2: A camera shown with rays converging towards a vanishing point.

The figure above illustrates both types of epipoles. The left and right grids, as well as the overall image, are computed from a common center-of-projection projected onto a cylindrical viewing surface with a 270° horizontal field-of-view. The inset image shows these grids, the center-of-projection, $\dot{C}$, and the camera from a distance using a planar viewing surface. The image indicated by the left grid sees the rays of the camera as emerging from the camera's center-of-projection. The image represented by the right grid shows the same set of rays converging towards a common vanishing point. The rays only tend toward this point of convergence; they will never actually reach it.

5.1.1 The Fundamental Matrix

In this subsection, I present an analytical description of an epipolar geometry called the *fundamental matrix*. I will also discuss the properties of this fundamental matrix and methods for determining it. Most of the results presented here are well known within the computer-vision community. They are presented here primarily for completeness and as background for readers who are unaware of the work in this area.

An image-space equation of a line is given by an expression of the form

$$\bar{l}^T \bar{x} = Au + Bv + C = 0$$

Equation 5-1: The equation of a line in image space

Any 3×3 linear transformation can be used to map image points to lines defined on the same or some other image plane. Such a mapping is called a *correlation*[15], and it has the form

$$\bar{l} = \mathbf{R}\bar{x} \quad \text{or} \quad \begin{bmatrix} A \\ B \\ C \end{bmatrix} = \begin{bmatrix} r_{11} & r_{12} & r_{13} \\ r_{21} & r_{22} & r_{23} \\ r_{31} & r_{32} & r_{33} \end{bmatrix} \begin{bmatrix} u \\ v \\ 1 \end{bmatrix}$$

Equation 5-2: A correlation mapping points to lines

Like projective maps, which are called *collineations*, correlations are only defined down to a non-zero scale factor. This can be proven by showing that the points of a given line are not changed when the line's coefficients are multiplied by a non-zero scale factor. Since the coefficients of the line result from a product of a point and a correlation, any scaling of the correlation merely scales the line's coefficients. Therefore, a correlation has no more than eight degrees of freedom rather than the nine suggested by its matrix formulation.

An epipolar geometry is a special form of a correlation. Since all of the lines produced by an epipolar geometry intersect at a single point called the epipole, $\bar{e}$, the transpose of the correlation matrix will have the epipole's coordinate in its null space[16]. Therefore, the correlation will be singular and, in general, it will have a rank of two. This linear relationship describing epipolar geometries has been studied extensively by Faugeras [Faugeras92a] and Hartley [Hartley92]. They have given the name *fundamental matrix* to those correlations that describe epipolar geometries. The rank requirement of the fundamental matrix reduces the number of degrees of freedom from eight to, at most, seven.

Fundamental matrices map points from one image space to lines in another. This mathematical tool is consistent with our application in which points on one image plane represent rays whose projection onto other viewing planes are lines. I will use the following notation for representing fundamental matrices: $\mathbf{F}_{ba}$ will represent the mapping of points defined on image plane *a*, $\bar{x}_a$, to lines on image plane *b*, $\bar{l}_b$.

---

[15] Formally, a correlation is a mapping of an *n*-dimensional projective point to a hyperplane of dimension *n-1*. In the case of an image plane, *n = 2*, the hyperplane has 1 dimension and is, therefore, a line.

[16] $(\mathbf{R}\bar{x})^T \bar{e} = \bar{x}^T \mathbf{R}^T \bar{e} = 0$ for all $\bar{x}$. Thus, $\mathbf{R}^T \bar{e} = \bar{0}$.

$$\bar{l}_b = \mathbf{F}_{ba}\bar{x}_a$$

Equation 5-3: Fundamental matrix mapping a point to a line

In the geometric description of epipolar geometries at the beginning of this section, I mentioned that the rays in one image plane, in conjunction with a second center-of-projection, determine a set of planes as illustrated in Figure 5-1. The epipolar geometries between these two images are, therefore, not independent but related by this set of planes (i.e., there is a one-to-one mapping of epipolar lines in one image to the epipolar lines in the second). The fundamental matrices between any two image planes are related by the following expression:

$$\mathbf{F}_{ab} = \mathbf{F}_{ba}^T$$

Equation 5-4: Reversing the fundamental matrix mapping

This is easily proven since, for any two corresponding points $\bar{x}_a$ and $\bar{x}_b$,

$$(F_{ba}\bar{x}_a)^T\bar{x}_b = \bar{x}_a^T F_{ba}^T\bar{x}_b = 0$$

and taking the transpose gives

$$\left(\bar{x}_a^T F_{ba}^T\bar{x}_b\right)^T = \bar{x}_b^T F_{ba}\bar{x}_a = (F_{ba}^T\bar{x}_b)^T\bar{x}_a = 0$$

Therefore, $\mathbf{F}_{ab} = \mathbf{F}_{ba}^T$.

A more constrained formulation of the fundamental matrix that represents the 7 available degrees of freedom, rather than the 9 degrees of freedom available in a 3×3 matrix, is frequently useful. The coordinates of the epipoles from the two images are a natural way of specifying four of the seven parameters of a fundamental matrix. The coordinates of the epipoles can be found by solving for the point contained in the null space of the original fundamental matrix and for the null-space point in its transpose. The following parameterization can be used to describe any fundamental matrix that has been scaled such that $f_{11}f_{22} - f_{12}f_{21} = 1$.

$$F_{21}\left(\begin{bmatrix} e_{1u} \\ e_{1v} \\ 1 \end{bmatrix}, \begin{bmatrix} e_{2u} \\ e_{2v} \\ 1 \end{bmatrix}, q, r, \theta\right) = \begin{bmatrix} 1 & 0 \\ 0 & 1 \\ -e_{2u} & -e_{2v} \end{bmatrix} \begin{bmatrix} \cos\theta & -\sin\theta \\ \sin\theta & \cos\theta \end{bmatrix} \begin{bmatrix} q & r \\ 0 & 1/q \end{bmatrix} \begin{bmatrix} 1 & 0 & -e_{1u} \\ 0 & 1 & -e_{1v} \end{bmatrix}$$

Equation 5-5: Parameterization for a general fundamental matrix

where q, r, and θ are the remaining three parameters of the fundamental matrix.

Any matrix of the form given in Equation 5-5 will satisfy the requirements of a fundamental matrix. In addition, any general fundamental matrix can be decomposed into this form by first solving for the epipoles. Then, the upper-left 2×2 submatrix is scaled by the reciprocal of the square-root of its determinant, and, finally, the **QR** decomposition of this submatrix is computed.

This 7-parameter model serves as a useful symbolic representation of fundamental matrices in derivations because it maintains the proper number of degrees of freedom while retaining a form that can be managed with linear algebra. This model can also be used to solve for a particular instance of a fundamental matrix using any global optimization method, like the approach discussed in [Luong93b], without any external constraints.

5.1.2 Determining a Fundamental Matrix from Point Correspondences

An epipolar geometry describes image-space relationships that are implicitly coupled to a three-dimensional geometric structure (i.e., the axial pencil of planes through the line connecting the centers-of-projection of two images). This subsection describes how a general fundamental matrix can be derived based entirely on image-space relationships. In this way, three-dimensional geometric constraints can be implicitly placed upon image-space quantities.

A fundamental matrix can be found using linear methods when the coordinates for eight corresponding points on two different image planes are given (A closely related result was first presented by Longuet-Higgins [Longuet-Higgins81]). Each pair of points specifies one equation as shown below.

$$\bar{x}_2^T \mathbf{F}_{21} \bar{x}_1 = 0$$

$$u_2 u_1 f_{11} + u_2 v_1 f_{12} + u_2 f_{13} + v_2 u_1 f_{21} + v_2 v_1 f_{22} + v_2 f_{23} + u_1 f_{31} + v_1 f_{32} + f_{33} = 0$$

Equation 5-6: Linear equation in the coefficients of a fundamental matrix

This equation is linear in terms of the coefficients, f_{ij}, of the fundamental matrix, $\mathbf{F}$. An 8×8 system of linear equations with nine unknowns can be established by considering the equations generated by all eight corresponding points.

$$\mathbf{Af} = 0$$

Equation 5-7: Linear homogeneous system

A fundamental matrix can be scaled such that any one of its nine coefficients is exactly equal to one. This allows the column of $\mathbf{A}$ to be moved to the right side of the expression. The resulting matrix, $\mathbf{A}'$, will be square, and the equation will, in general, be nonhomogeneous. An element could be chosen at random and a solution could then be found for all cases except when the selected element is actually zero. Alternatively, the nonlinear constraint on the general fundamental matrix, $f_{11} f_{22} - f_{12} f_{21} = 1$, could be added as a ninth equation. However, the resulting system would require a nonlinear optimization method.

Hartley [Hartley95a] suggested another approach for solving the system of equations given in Equation 5-7 in which the constraint $\mathbf{f}^T\mathbf{f} = 1$ was introduced. It is well known that solutions to problems of the form, $\mathbf{Af} = 0$, subject to the constraint that $\mathbf{f}^T\mathbf{f} = 1$, can be found by computing the unit eigenvector associated with the smallest eigenvalue of the matrix $\mathbf{A}^T\mathbf{A}$ [Golub89] (i.e., by a singular value decomposition of $\mathbf{A}$). Also, numerically stable computation methods for solving eigensystems are well known [Press88]. Note that $\mathbf{A}^T\mathbf{A}$ is symmetric and positive definite, so its eigenvalues will all be real and positive, and its eigenvectors will be real as long as $\mathbf{A}$ is real. This eigenvector, like the fundamental matrix that it represents, is also only defined to within a scale factor. When more than eight points are given, the same system can be solved using least-squares methods.

Unfortunately, the linear-solution method described does not guarantee the rank constraint of the fundamental matrix. Given exact correspondences, this condition will be met because of the implicit constraints of the problem's definitions (that is, the image points represent rays emerging from one of two centers-of-projection). In practice, however, these point correspondences will be contaminated with noise. Therefore, we would not expect that $\det(\mathbf{F}) = 0$.

In order to find a fundamental matrix that satisfies the rank constraint, the following procedure can be used. First, a singular-value decomposition of the approximate fundamental matrix, $\tilde{\mathbf{F}}$, is determined from the eigenvector, as follows:

$$\tilde{\mathbf{F}} = \mathbf{UDV}^T$$

Equation 5-8: Singular-value decomposition of an approximate fundamental matrix

where $\mathbf{U}$ and $\mathbf{V}^T$ are orthogonal and $\mathbf{D} = diag(d_1, d_2, d_3)$ is diagonal with $d_1 \geq d_2 \geq d_3$. Then, the matrix, $\mathbf{F} = \mathbf{U}diag(d_1, d_2, 0)\mathbf{V}^T$, will be the closest singular matrix to $\tilde{\mathbf{F}}$, measured according to the Frobenius norm[17]. The image-space coordinates of the epipole in the first image are found by normalizing the third column of the matrix $\mathbf{U}$ so that its third element is one, if possible. Otherwise, one of the nongeneric fundamental matrix configurations, discussed in Appendix A, is indicated. The epipole of the second image can be found by a similar normalization of the third row of the matrix $\mathbf{V}^T$.

When using the linear method for computing the fundamental matrix, great care must be taken to avoid numerical-conditioning problems. Luong [Luong93b] has suggested several nonlinear methods to avoid these numerical instabilities. His methods are iterative, but they generally converge in relatively few steps if the initial estimate of the fundamental matrix is close to the actual solution. He recommends using the linear method as an initial guess.

Hartley [Hartley95a], on the other hand, has suggested a method that eliminates most of these conditioning problems while still allowing the closed-form linear-solution method to be used. He has shown that applying an affine transformation to both image planes, which prewarps point correspondences such that the centroids of the points in each image are at the origin and their average radius is $\sqrt{2}$, will dramatically reduce the conditioning number of the **A** matrix. This warping acts as a normalization of the image coordinates so that the resolution and distribution of corresponding image points has little influence on the fundamental matrix calculation. Hartley has shown that by using linear methods alone, accuracies comparable to those of Luong can be achieved.

5.2 Relating the Fundamental Matrix to the Image-Warping Equation

An epipolar geometry, which is represented by a fundamental matrix, determines a line of possible points that a given reference-image point might map onto. The planar-warping equation derived in Chapter 3 determines an exact mapping of reference-image points onto any other viewing plane. But, if the generalized disparity is unknown for an image-space point in the reference image, then the warping equation would also specify a line whose interpretation

[17] Taking the elements of the matrix $\tilde{\mathbf{F}}$ as a vector $\tilde{\mathbf{f}}$, and the elements of the matrix $\mathbf{F}$ as a vector $\mathbf{f}$, then the distance between matrices according to the Frobenius norm is the Euclidean distance between these vectors $\tilde{\mathbf{f}}$ and $\mathbf{f}$, $\left\|\tilde{\mathbf{f}} - \mathbf{f}\right\|$.

would be identical to that of the epipolar line given by the fundamental matrix[18]. Therefore, the planar-warping equation must also determine an epipolar geometry. In this section, this relationship is derived.

I begin with the general planar-warping equation (Equation 3-10) shown below.

$$\bar{x}_2 \doteq \delta(\bar{x}_1)\mathbf{P}_2^{-1}\left(\dot{C}_1 - \dot{C}_2\right) + \mathbf{P}_2^{-1}\mathbf{P}_1\bar{x}_1$$

The three-space vector connecting the two centers-of-projection will project onto the image planes of both pinhole cameras as a single point. All other rays will originate from this point. Therefore, the vector connecting the two centers-of-projection, $\dot{C}_1 - \dot{C}_2$, determines the epipoles in both image-space domains, $\bar{x}_1$ and $\bar{x}_2$. The image-space coordinate of the epipole on the second image plane is given by

$$\bar{e}_2 \doteq P_2^{-1}(\dot{C}_1 - \dot{C}_2)$$

Equation 5-9: Coordinate of the epipole in the second image

The planar-warping equation can now be rewritten as follows:

$$\bar{x}_2 \doteq \delta(\bar{x}_1)\varphi\bar{e}_2 + \mathbf{P}_2^{-1}\mathbf{P}_1\bar{x}_1$$

where φ is an unknown scaling factor. If both sides of this equation are multiplied by the skew-symmetric matrix $\mathbf{E}$ of the vector $\bar{e}_2$[19], the following equation results:

$$\mathbf{E}\bar{x}_2 \doteq \delta(\bar{x}_1)\varphi\mathbf{E}\bar{e}_2 + \mathbf{E}P_2^{-1}P_1\bar{x}_1$$

Since $\mathbf{E}\bar{e}_2 = \bar{0}$, the equation above simplifies to

$$\mathbf{E}\bar{x}_2 \doteq \mathbf{E}P_2^{-1}P_1\bar{x}_1.$$

---

[18] The fundamental matrix gives the line's equation in implicit form, while the warping equation produces the line's equation in a parametric form.

[19] The skew-symmetric matrix, $\mathbf{K}$, of the vector $\bar{v}$ is defined so that $\mathbf{K}\bar{x} = \bar{v} \times \bar{x}$.

$$\mathbf{K} = \begin{bmatrix} 0 & -v_z & v_y \\ v_z & 0 & -v_x \\ -v_y & v_x & 0 \end{bmatrix}$$

Now, if both sides are multiplied by $\bar{x}_2^T$, then

$$\bar{x}_2^T \mathbf{E} \bar{x}_2 = 0 = \bar{x}_2^T \mathbf{E} P_2^{-1} P_1 \bar{x}_1,$$

which means that

$$\mathbf{F}_{21} = \mathbf{E}\mathbf{P}_2^{-1}\mathbf{P}_1.$$

Thus, a fundamental matrix can be expressed in terms of the planar-warping equation. The matrix $\mathbf{E}$ is singular and of rank 2, assuring that the product $\mathbf{E}\mathbf{P}_2^{-1}\mathbf{P}_1$ has the proper form. As discussed in Chapter 3, the projective map $\mathbf{P}_2^{-1}\mathbf{P}_1$ describes a reprojection (i.e., a mapping of reference-image points to desired-image points in which the center-of-projection does not change). This mapping is invertible and, therefore, of full rank. The application of the skew-symmetric matrix, $\mathbf{E}$, removes a dimension from this mapping in the direction of the vector connecting the two centers-of-projection as illustrated below:

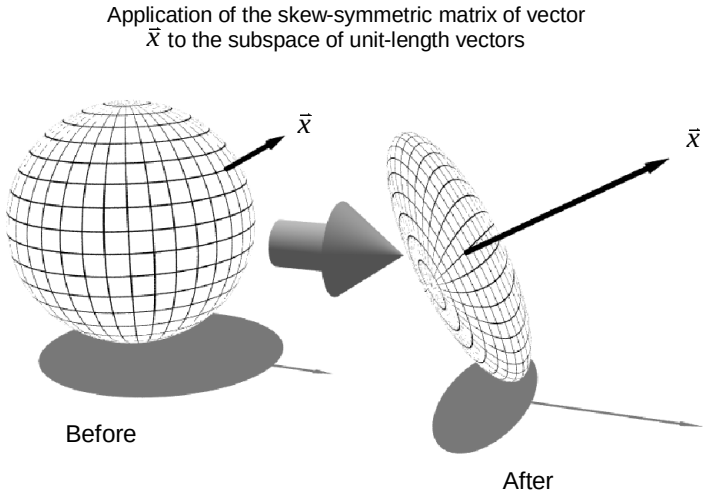

Figure 5-3: Mapping of a unit sphere before and after a skew-symmetric matrix

Thus, given a warping equation, it is straightforward to compute the corresponding fundamental matrix.

$$\mathbf{F}_{21} = skew(\mathbf{P}_2^{-1}(\dot{C}_1 - \dot{C}_2))\mathbf{P}_2^{-1}\mathbf{P}_1$$

Equation 5-10: Fundamental matrix in terms of the planar-warping equation

Since it is possible to determine a fundamental matrix from a set of image-space correspondences between two images, as shown in section 5.1.2, the remainder of this chapter explores to what extent a warping equation can be determined from a fundamental matrix.

5.2.1 Image Warps Compatible with a Fundamental Matrix

I have already shown, in Equation 5-9, that knowledge of the epipoles is equivalent to knowing the first term of the planar-warping equation shown below.

$$\bar{x}_2 \doteq \delta(\bar{x}_1)\varphi\bar{e}_2 + \mathbf{P}_2^{-1}\mathbf{P}_1\bar{x}_1$$

The epipole coordinates are readily determined from a fundamental matrix as follows. Since all epipolar lines intersect at the epipole, the following relationship must hold:

$$0 = \left(\mathbf{F}_{21}\bar{x}_1\right)^T \bar{e}_2 = \bar{x}_1^T \mathbf{F}_{21}^T \bar{e}_2 \quad \text{for all } \bar{x}_1$$

This can only be satisfied if $\mathbf{F}_{21}^T\bar{e}_2 = \bar{0}$. This establishes the following homogeneous system of three equations in three variables[20]:

$$\begin{aligned} f_{11}e_{21} + f_{21}e_{22} + f_{31}e_{23} &= 0 \\ f_{12}e_{21} + f_{22}e_{22} + f_{32}e_{23} &= 0 \\ f_{13}e_{21} + f_{23}e_{22} + f_{33}e_{23} &= 0 \end{aligned}$$

Equation 5-11: Homogeneous system to find the second image's epipole

In Equation 5-11, and in the next few derivations, I represent the epipole's coordinate as a projective point using the following notation: $\bar{e}_2 = \begin{bmatrix} e_{21} & e_{22} & e_{23} \end{bmatrix}^T$, where the first subscript indicates the epipole's image-space and the second indicates the vector element. All other double-subscripted variables indicate a matrix element.

Since the linear system of Equation 5-11 is homogeneous and the fundamental matrix is singular, any one of the unknowns can remain unassigned and the remaining two variables can

[20] At this point I will drop the subscripts on both the fundamental matrix and the epipole so that subscripts can be used for identifying the matrix and vector elements. Throughout the remainder of this section, the epipole's coordinates can be assumed to be specified in the desired image's space unless stated otherwise. Likewise, the fundamental matrix can be assumed to map reference image points to epipolar lines on the desired image.

be solved for in terms of the third. Here I will solve for e_{21} and e_{22} of the epipole's coordinate in terms of e_{23} using the first two equations[21].

$$e_{21} = \frac{e_{23}\left(f_{21}f_{32} - f_{22}f_{31}\right)}{f_{11}f_{22} - f_{12}f_{21}}$$

$$e_{22} = \frac{e_{23}\left(f_{12}f_{31} - f_{11}f_{32}\right)}{f_{11}f_{22} - f_{12}f_{21}}$$

Equation 5-12

This allows the epipole to be re-expressed as the projective (homogeneous) coordinate

$$\begin{bmatrix} e_{21} \\ e_{22} \\ e_{23} \end{bmatrix} = \begin{bmatrix} f_{21}f_{32} - f_{22}f_{31} \\ f_{12}f_{31} - f_{11}f_{32} \\ f_{11}f_{22} - f_{12}f_{21} \end{bmatrix}$$

Equation 5-13: Homogeneous coordinate of an epipole

Thus, the first term of the planar-warping equation can be found without prior knowledge of the planar-pinhole camera models or the centers-of-projection of the reference and desired images. The unknown scale factor, φ, remains in the equation, but, we can assume that any subsequent normalizations of the epipole's coordinate will cancel out this constant.

Next, we attempt to express the reprojection mapping, $\mathbf{H} = \mathbf{P}_2^{-1}\mathbf{P}_1$, in terms of the fundamental matrix. We have shown previously that $\mathbf{F} = \mathbf{EH}$. Since the matrix $\mathbf{E}$ is singular, we cannot solve for $\mathbf{H}$ directly. However, it is possible to define a family of matrices that, when multiplied by $\mathbf{E}$, will give $\mathbf{F}$. The derivation of this family follows.

I begin with the matrix equation $\mathbf{F} = \mathbf{EH}$ expressed in matrix form below.

$$\begin{bmatrix} f_{11} & f_{12} & f_{13} \\ f_{21} & f_{22} & f_{23} \\ f_{31} & f_{32} & f_{33} \end{bmatrix} = \begin{bmatrix} 0 & -e_{23} & e_{22} \\ e_{23} & 0 & -e_{21} \\ -e_{22} & e_{21} & 0 \end{bmatrix} \begin{bmatrix} h_{11} & h_{12} & h_{13} \\ h_{21} & h_{22} & h_{23} \\ h_{31} & h_{32} & h_{33} \end{bmatrix}$$

Equation 5-14: Fundamental matrix in terms of an epipole and a projective transform

[21] In practice a singular value decomposition of **F** would be used to find the eigenvector associated with the smallest eigenvalue.

This expression can be expressed as a linear system of 9 equations in 9 unknowns as follows:

$$\begin{array}{lll} f_{11} = e_{22}h_{31} - e_{23}h_{21} & f_{12} = e_{22}h_{32} - e_{23}h_{22} & f_{13} = e_{22}h_{33} - e_{23}h_{23} \\ f_{21} = e_{23}h_{11} - e_{21}h_{31} & f_{22} = e_{23}h_{12} - e_{21}h_{32} & f_{23} = e_{23}h_{13} - e_{21}h_{33} \\ f_{31} = e_{21}h_{21} - e_{22}h_{11} & f_{32} = e_{21}h_{22} - e_{22}h_{12} & f_{33} = e_{21}h_{23} - e_{22}h_{13} \end{array}$$

Equation 5-15: Equations for the elements of the fundamental matrix

Six of the nine unknown elements of $\mathbf{H}$ can be found in terms of the known values and the three elements in the last row of $\mathbf{H}$.

$$\begin{array}{lll} e_{23}h_{21} = e_{22}h_{31} - f_{11} & e_{23}h_{22} = e_{22}h_{32} - f_{12} & e_{23}h_{23} = e_{22}h_{33} - f_{13} \\ e_{23}h_{11} = e_{21}h_{31} + f_{21} & e_{23}h_{12} = e_{21}h_{32} + f_{22} & e_{23}h_{13} = e_{21}h_{33} + f_{23} \end{array}$$

Equation 5-16: Projective transform's elements in terms of the fundamental matrix

In matrix form, this expression becomes

$$e_{23}\mathbf{H} = \begin{bmatrix} f_{21} & f_{22} & f_{23} \\ -f_{11} & -f_{12} & -f_{13} \\ 0 & 0 & 0 \end{bmatrix} + \begin{bmatrix} e_{21} \\ e_{22} \\ e_{23} \end{bmatrix} \begin{bmatrix} h_{31} & h_{32} & h_{33} \end{bmatrix},$$

where h_{31}, h_{32}, and h_{33} are three free parameters that define a family of projective maps which produce the desired fundamental matrix. If the fundamental matrix is normalized so that $f_{11}f_{22} - f_{12}f_{21} = 1$, as in the general seven-parameter form given in Equation 5-5, the following simplification results:

$$\mathbf{H} = \begin{bmatrix} f_{21} & f_{22} & f_{23} \\ -f_{11} & -f_{12} & -f_{13} \\ 0 & 0 & 0 \end{bmatrix} + \begin{bmatrix} e_{2u} \\ e_{2v} \\ 1 \end{bmatrix} \begin{bmatrix} h_{31} & h_{32} & h_{33} \end{bmatrix}$$

Equation 5-17: Family of projective transformations compatible with a fundamental matrix

The normalization of the fundamental matrix yields a normalized the epipole coordinate.

This representation of the projective transformations that are compatible with a given fundamental matrix lends itself to a geometric interpretation. The first term of Equation 5-17 represents the mapping of the desired family of projective transformations onto a plane parallel to the image plane but passing through the center-of-projection[22]. The second term represents

[22] The projective points on this constitute the projective *line at infinity*.

the components of the projective transform that are lost by such a mapping. Thus, when given only the fundamental matrix associated with an image pair only the first term and the direction of the displacement out of the plane of , the projective transformation component of the associated image warp can be identified. The three parameters, h_{31}, h_{32}, and h_{33} represent the components of projective transformation's basis vectors that cannot be unambiguously determined from the fundamental matrix alone. These relationships are illustrated in the following figure:

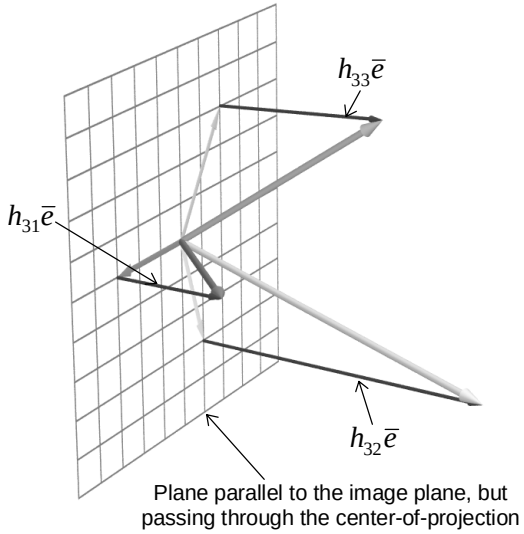

Figure 5-4: The projective transformations compatible with a given fundamental matrix

The coordinates of the epipole in the first image can be determined using a derivation similar to the one shown in Equation 5-11, where the fundamental matrix is replaced with its transpose. When the fundamental matrix is normalized so that $f_{11}f_{22} - f_{12}f_{21} = 1$ these expressions simplify to $f_{13} = -(f_{11}e_{1u} + f_{12}e_{1v})$ and $f_{23} = -(f_{21}e_{1u} + f_{22}e_{1v})$. Substituting these equalities into the three-parameter family of projective transformations defined in Equation 5-17 results in the following expression:

$$\mathbf{H} = \begin{bmatrix} f_{21} & f_{22} & -(f_{21}e_{1u} + f_{22}e_{1v}) \\ -f_{11} & -f_{12} & f_{11}e_{1u} + f_{12}e_{1v} \\ 0 & 0 & 0 \end{bmatrix} + \begin{bmatrix} e_{2u} \\ e_{2v} \\ 1 \end{bmatrix} \begin{bmatrix} h_{31} & h_{32} & h_{33} \end{bmatrix}$$

Equation 5-18: Family of projective maps in terms of epipoles

Consequently, a fundamental matrix determines the projective mapping component of a planar-warping equation to within a three-dimensional subspace. This relationship can be expressed without any explicit knowledge of the intrinsic pinhole-camera parameters, using

only information available from the fundamental matrix. The next section explains another important special class of projective transformations which will eventually be used to further constrain the family of projective maps that are compatible with a given fundamental matrix.

5.3 Physical Constraints on Projective Maps

The general projective transformation, $\mathbf{H} = \mathbf{P}_2^{-1}\mathbf{P}_1$, that appears in the warping equation has eight degrees of freedom. The additional knowledge of an epipolar geometry, as determined by a fundamental matrix, reduces the available degrees of freedom to three. In this section, I will introduce additional constraints on the pinhole-camera model which will further reduce the space of compatible projective transformations. I will also argue that these additional constraints are reasonable assumptions for a large class of images, including those acquired by real-world cameras.

5.3.1 Same-Camera Transformations

Consider a canonical planar-pinhole camera that is free to rotate in any direction about its center-of-projection, which is restricted to the origin (see section 3.4). The image-to-image mappings that can be represented by such a camera configuration define the family of *same-camera transformations*. These transformations have the following algebraic form:

$$\mathbf{C} = \mathbf{H}_{samecamera} = \mathbf{U}^{-1}\mathbf{R}\mathbf{U}$$

Equation 5-19: Same-camera transformation

The projective transformation, **C,** determines an image-to-image mapping via the composition of three transforms. The first is an image-to-ray mapping specified by a canonical pinhole-camera model, **U**; the second is a rotation, **R**, of the camera's coordinate system; and, the third is a ray-to-image mapping determined by the canonical pinhole-camera's inverse, $\mathbf{U}^{-1}$. The same-camera family of projective mappings is determined by the five intrinsic camera parameters (defined in Section 4.1.2) of the canonical pinhole-camera model, **U**, and the three rotational parameters of **R**. Three-dimensional rotations, like **R**, can be parameterized in terms of a unit vector, $\bar{r}$, specifying an axis of rotation and an angle, θ, specifying the amount of rotation. Restricting the axis of rotation to be of unit-length does not reduce the generality of this parameterization, and it allows for a minimal specification using only three-parameters.

Same-camera transformations are *similarity transforms* of rotation matrices, which means that both **C** and **R** will have the same eigenvalues and, hence, the same characteristic

polynomials. The characteristic polynomial and the eigenvalues of a general rotation matrix, such as **R,** are

$$\lambda^3 - (1+2\cos\theta)\lambda^2 + (1+2\cos\theta)\lambda - 1 = (\lambda-1)(\lambda^2 - 2\cos\theta\lambda + 1) = 0$$
$$\lambda = \{1, \cos\theta \pm i\sin\theta\}$$

Equation 5-20: Characteristic polynomial and eigenvalues of a rotation matrix

where θ is the rotation angle about the axis.

The family of matrices equivalent to a given projective transform, **C**, can be represented by $\sigma\mathbf{C}$, where σ is a non-zero scalar, since projective transformations scaled by a non-zero scale factor are equivalent. The same-camera transformations, $\sigma\mathbf{C}$, have the following characteristic polynomial:

$$\lambda^3 - \sigma\text{Trace}(C)\lambda^2 + \sigma^2\sum_{i=1}^{3}\text{Minor}(C,i,i)\lambda - \sigma^3\text{Determinant}(C) = 0$$

Equation 5-21: Characteristic polynomial of scaled same-camera warp

The individual terms of Equation 5-20 and Equation 5-21 are equal since the transformations are similar. The constant terms of the two polynomials can be made equal by selecting an appropriate scale factor, σ, such that the determinant of $\sigma\mathbf{C}$ is one. The expression for this scale factor is

$$\sigma = \frac{1}{\sqrt[3]{\text{Determinant}(\mathbf{C})}}$$

Equation 5-22: Scale factor that makes the determinant of σC equal one

The characteristic polynomial of a rotation has the property that the coefficients of the first and second degree terms have equal magnitudes and a restricted range. This relationship can be used to establish constraints on the trace and the sum of the diagonal minors of a same-camera transformation. By equating the remaining terms in Equation 5-20 and Equation 5-21, subject to the scaling constraint given in Equation 5-22, the following relationships can be established:

$$\frac{\text{Trace}(\mathbf{C})}{\text{Determinant}(\mathbf{C})^{\frac{1}{3}}} = \frac{\sum_{i=1}^{3} \text{Minor}(\mathbf{C}, i, i)}{\text{Determinant}(\mathbf{C})^{\frac{2}{3}}} = 1 + 2\cos\theta$$

This yields the following two constraints on a same-camera transformation, $\mathbf{C}$:

$$\text{Determinant}(\mathbf{C}) = \left(\frac{\sum_{i=1}^{3} \text{Minor}(\mathbf{C}, i, i)}{\text{Trace}(\mathbf{C})} \right)^{3}$$

$$-1 \le \frac{\text{Trace}(\mathbf{C})}{\text{Determinant}(\mathbf{C})^{\frac{1}{3}}} \le 3$$

Equation 5-23: Constraints on a same-camera transformation

These two constraints can be used to verify if a given projective transformation is of the same-camera class[23]. Since they depend entirely on the characteristic polynomials of the given projective transformation, they will be invariant to any transformation of the pinhole-camera matrix, and are, therefore, independent of the pinhole-camera model $\mathbf{U}$. For example, the system

$$\mathbf{C}_1 = \mathbf{U}_1^{-1}\mathbf{R}_1\mathbf{U}_1$$

has the same characteristic polynomial as

$$\mathbf{C}_2 = \mathbf{U}_1^{-1}\mathbf{U}_2^{-1}\mathbf{R}_1\mathbf{U}_2\mathbf{U}_1$$

Since the upper triangular matrices are a subgroup under matrix composition, the product $\mathbf{U}_2\mathbf{U}_1$ can produce a mapping from a given pinhole-camera model to any other. Therefore, the constraints induced by the characteristic polynomial do not provide any information about the canonical camera model. Instead they only provide information about the rotation component of the transformation. For this application, the primary purpose of these constraints is to assure

[23] Clearly, there exist matrices outside of this class. For example, consider the class of upper-triangular projective matrices. In order for $\mathbf{U}_2 = \mathbf{U}_1^{-1}\mathbf{R}\mathbf{U}_1$ then $\mathbf{U}_1\mathbf{U}_2\mathbf{U}_1^{-1} = \mathbf{R}$. Since the class of upper-triangular matrices is a subgroup of linear transformations under composition the matrix $\mathbf{R}$ must be a member of that subgroup. But, the only rotation matrices in this subgroup are the identity and the other valid rotations with ± 1 along the diagonal. Thus, upper-triangular matrices are not generally a same camera transformation.

that a given transformation will fall within the same-camera subspace of projective transformation. In the next subsection, I will determine the conditions under which a unique canonical-pinhole-camera model can be determined from a same-camera transformation.

5.3.2 Determining a Camera Model from a Same-Camera Transformation

Projective transformations that satisfy the same-camera constraints described in the previous subsection can be used to determine a one-parameter family of pinhole-camera models. Any one of these pinhole-camera models will be consistent with the given matrix. The associated rotation matrix can also be derived for any selected camera from this one-parameter family.

$$\mathbf{R}_\rho = \mathbf{U}_\rho \mathbf{C} \mathbf{U}_\rho^{-1}$$

The one parameter family of pinhole camera models can be determined as follows. Rewriting $\mathbf{C} = \mathbf{U}^{-1}\mathbf{R}\mathbf{U}$ gives $\mathbf{U}\mathbf{C} = \mathbf{R}\mathbf{U}$. Consider that a rotation of a vector space preserves both the distances and the angles between vectors[24]. Therefore, if the columns of **U** are considered as vectors, the given expression can be interpreted as follows:

$$\begin{bmatrix} \bar{a}' & \bar{b}' & \bar{c}' \end{bmatrix} = \begin{bmatrix} \bar{a} & \bar{b} & \bar{c} \end{bmatrix} \mathbf{C} = \mathbf{R} \begin{bmatrix} \bar{a} & \bar{b} & \bar{c} \end{bmatrix}$$

The following rotational invariants will provide six equations in terms of the nine known elements from **C** and the six unknowns from **U**:

$$\begin{array}{lll} \bar{a}' \cdot \bar{a}' = \bar{a} \cdot \bar{a} & \bar{b}' \cdot \bar{b}' = \bar{b} \cdot \bar{b} & \bar{c}' \cdot \bar{c}' = \bar{c} \cdot \bar{c} \\ \bar{a}' \cdot \bar{b}' = \bar{a} \cdot \bar{b} & \bar{a}' \cdot \bar{c}' = \bar{a} \cdot \bar{c} & \bar{b}' \cdot \bar{c}' = \bar{b} \cdot \bar{c} \end{array}$$

Equation 5-24: Rotational invariants of a same-camera transformation

An equivalent set of equations can be found algebraically by multiplying $\mathbf{U}\mathbf{C} = \mathbf{R}\mathbf{U}$ by its transpose, $\mathbf{C}^T\mathbf{U}^T = \mathbf{U}^T\mathbf{R}^T$, which gives $\mathbf{C}^T\mathbf{U}^T\mathbf{U}\mathbf{C} = \mathbf{U}^T\mathbf{U}$. The symmetric matrix $\mathbf{S} = \mathbf{U}^T\mathbf{U}$ has the six invariant quantities as its elements.

[24] The so-called Euclidean metrics.

$$C^T \begin{bmatrix} \bar{a}\cdot\bar{a} & \bar{a}\cdot\bar{b} & \bar{a}\cdot\bar{c} \\ \bar{a}\cdot\bar{b} & \bar{b}\cdot\bar{b} & \bar{b}\cdot\bar{c} \\ \bar{a}\cdot\bar{c} & \bar{b}\cdot\bar{c} & \bar{c}\cdot\bar{c} \end{bmatrix} C = \begin{bmatrix} \bar{a}\cdot\bar{a} & \bar{a}\cdot\bar{b} & \bar{a}\cdot\bar{c} \\ \bar{a}\cdot\bar{b} & \bar{b}\cdot\bar{b} & \bar{b}\cdot\bar{c} \\ \bar{a}\cdot\bar{c} & \bar{b}\cdot\bar{c} & \bar{c}\cdot\bar{c} \end{bmatrix}$$

Equation 5-25: Rotational invariants expressed as a matrix product

Equating the matrices on an element-by-element basis yields six unique equations that are identical to those derived earlier using the geometric argument. In the case where the same-camera transformation is known, this system of equations will be linear in the six unknown elements of the symmetric matrix **S.** The resulting homogenous system of linear equations is shown below.

$$\begin{bmatrix} c_{11}^2-1 & 2c_{11}c_{21} & 2c_{11}c_{31} & c_{21}^2 & 2c_{21}c_{31} & c_{31}^2 \\ c_{11}c_{12} & c_{11}c_{22}+c_{12}c_{21}-1 & c_{11}c_{32}+c_{12}c_{31} & c_{21}c_{22} & c_{21}c_{32}+c_{22}c_{31} & c_{31}c_{32} \\ c_{11}c_{13} & c_{11}c_{23}+c_{13}c_{21} & c_{11}c_{33}+c_{13}c_{31}-1 & c_{21}c_{23} & c_{21}c_{33}+c_{23}c_{31} & c_{31}c_{33} \\ c_{12}^2 & 2c_{12}c_{22} & 2c_{12}c_{32} & c_{22}^2-1 & 2c_{22}c_{32} & c_{32}^2 \\ c_{12}c_{13} & c_{12}c_{23}+c_{13}c_{22} & c_{12}c_{33}+c_{13}c_{32} & c_{22}c_{23} & c_{22}c_{33}+c_{23}c_{32}-1 & c_{32}c_{33} \\ c_{13}^2 & 2c_{13}c_{23} & 2c_{13}c_{33} & c_{23}^2 & 2c_{23}c_{33} & c_{33}^2-1 \end{bmatrix} \begin{bmatrix} \bar{a}\cdot\bar{a} \\ \bar{a}\cdot\bar{b} \\ \bar{a}\cdot\bar{c} \\ \bar{b}\cdot\bar{b} \\ \bar{b}\cdot\bar{c} \\ \bar{c}\cdot\bar{c} \end{bmatrix} = \begin{bmatrix} 0 \\ 0 \\ 0 \\ 0 \\ 0 \\ 0 \end{bmatrix}$$

Equation 5-26: Homogenous linear system determined by C

This linear system only has a rank of 4, and, therefore, has a two-parameter family of solutions[25]. One of these parameters can be established by fixing any one of the three vector lengths to 1. Since the pinhole-camera model, **C,** is only defined to within a scale factor, choosing one vector's length does not affect the solution.

The constraints, $\bar{a}\cdot\bar{a}=1$ and $\bar{a}\cdot\bar{b}=s$, provide a convenient parameterization that also has a useful geometric interpretation. It also results in a pinhole-camera model in the normalized canonical form of Equation 4-6. The angle $\bar{a}\cdot\bar{b}$ is a measure of the skew between the image-space basis vectors, discussed in Chapter 4. In most real-world image-acquisition systems, this skew factor is nearly 0 because typical solid-state sensors, such as charge-coupled devices, are manufactured to precise standards in which the orthogonality of the two-dimensional array of photosites is nearly guaranteed. Thus, we can limit our consideration of viable same-camera transformations to those where the *s* component of the associated pinhole camera is nearly 0. Since *s* is physically linked to the inner products of two vectors (one

[25] The lower-right 4×4 submatrix will, in general, have a non-zero determinant. Any larger submatrix will always have a determinant of zero, when the determinant and trace constraints of the same-camera transform are considered. Thus the linear system has a rank of four.

constrained to a unit length and the other of a computed length), our interpretation of *s* can easily be mapped to an angle, and, therefore, made independent of an external scale. This is important because it allows us to consider the smallness of *s* within a fixed context. In general, we also expect $\bar{b} \cdot \bar{b} / \bar{a} \cdot \bar{a} \approx r^2$, since the ratio of the lengths is indicative of the aspect ratio, *r*, of the sampling grid, and this value is usually known in most real imaging systems.

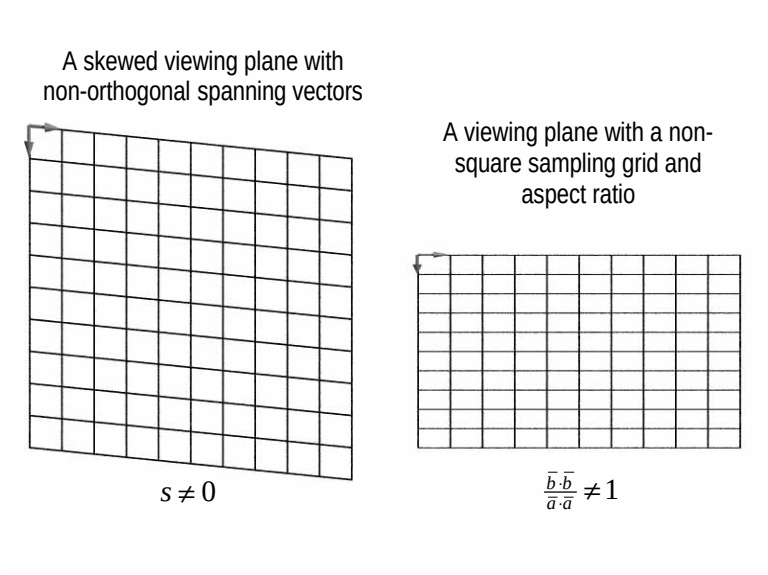

Figure 5-5: The skew and aspect ratio properties of a planar-pinhole camera

A canonical planar-pinhole camera model can be determined by substituting the elements of the solution vector from Equation 5-26 into the expression given in Equation 4-5 and choosing the positive-valued square roots for the diagonal elements. When the parmeterization, $\bar{a} \cdot \bar{a} = 1$ and $\bar{a} \cdot \bar{b} = s$, is chosen for the homogenous linear system, the following planar-pinhole camera model results:

$$\mathbf{P_C} = \begin{bmatrix} 1 & s & \bar{a} \cdot \bar{c} \\ 0 & \sqrt{(\bar{b} \cdot \bar{b}) - s} & \chi = \dfrac{(\bar{b} \cdot \bar{c}) - s(\bar{a} \cdot \bar{c})}{\sqrt{(\bar{b} \cdot \bar{b}) - s}} \\ 0 & 0 & \sqrt{(\bar{c} \cdot \bar{c}) - (\bar{a} \cdot \bar{c})^2 - \chi^2} \end{bmatrix}$$

Equation 5-27: Planar-pinhole camera model of a same-camera transform

Ordinarily, we would expect that $s \approx 0$ and the term $\sqrt{(\bar{b} \cdot \bar{b}) - s}$ to be approximately the height-to-width aspect ratio of the sampling grid. Under typical conditions, we would also expect $\bar{a} \cdot \bar{c} < 0$ and $\chi < 0$ if the image-space origin is considered to be the upper-left corner of the image.

5.3.3 Closed-form solutions for the intrinsic camera-parameters

Given a specific instance of a projective transformation, which satisfies the same-camera constraints of Equation 5-23, the homogeneous linear system of Equation 5-26 can be solved using either a global optimization method or a singular-value decomposition if sufficient constraints are imposed such that there is a unique solution. Hartley has shown that when given three or more images taken from a common center-of-projection a solution can be found using a global optimization method, with the exception of a few degenerate the camera configurations [Hartley94]. By using multiple images he was able to avoid imposing any external constraints. However, the non-linear optimization method that he employed required an initial estimate of the intrinsic parameters that are being solved for.

Here, I will propose an alternate approach to this problem that provides a closed-form solution. Closed-form solutions are useful because they can be computed without an initial estimate of the final solution, they require a constant time to compute, and they can be further analyzed. Since the solution-space of intrinsic-camera parameters that are consistent with a same-camera transformation are a two-dimensional subspace within the six-dimensional space of upper-diagonal matrices, additional constraints are required to guarantee that the solution is unique. I will assume a unit-length spanning vector and zero-skew constraint on the solution space, which is a reasonable assumption for most camera configurations, as discussed previously. When these constraints are substituted into Equation 5-25 the following rotational invariants result:

$$\begin{bmatrix} c_{11} & c_{12} & c_{13} \\ c_{21} & c_{22} & c_{23} \\ c_{31} & c_{32} & c_{33} \end{bmatrix}^T \begin{bmatrix} 1 & 0 & \bar{a}\cdot\bar{c} \\ 0 & \bar{b}\cdot\bar{b} & \bar{b}\cdot\bar{c} \\ \bar{a}\cdot\bar{c} & \bar{b}\cdot\bar{c} & \bar{c}\cdot\bar{c} \end{bmatrix} \begin{bmatrix} c_{11} & c_{12} & c_{13} \\ c_{21} & c_{22} & c_{23} \\ c_{31} & c_{32} & c_{33} \end{bmatrix} = \begin{bmatrix} 1 & 0 & \bar{a}\cdot\bar{c} \\ 0 & \bar{b}\cdot\bar{b} & \bar{b}\cdot\bar{c} \\ \bar{a}\cdot\bar{c} & \bar{b}\cdot\bar{c} & \bar{c}\cdot\bar{c} \end{bmatrix}$$

Equation 5-28: Constrained rotational-invariant matrix

In order to simplify subsequent derivations I will introduce the following elements of **C**'s adjoint matrix as constants:

$$\mathbf{Z} = \begin{bmatrix} c_{22}c_{33} - c_{23}c_{32} & c_{13}c_{32} - c_{12}c_{33} & c_{12}c_{23} - c_{13}c_{22} \\ c_{23}c_{31} - c_{21}c_{33} & c_{11}c_{33} - c_{13}c_{31} & c_{13}c_{21} - c_{11}c_{23} \\ c_{21}c_{32} - c_{22}c_{31} & c_{12}c_{31} - c_{11}c_{32} & c_{11}c_{22} - c_{12}c_{21} \end{bmatrix}$$

Note that $\mathbf{C}$'s adjoint matrix, $\mathbf{Z}$, is also $\mathbf{C}$'s inverse since $\mathbf{C}$ has a determinant of 1. In addition, the trace of this adjoint matrix is equivalent to the sum of $\mathbf{C}$'s diagonal minors. Thus, by the same camera constraints, $\text{Trace}(\mathbf{C}) = \text{Trace}(\mathbf{Z})$.

Arbitrary equations in the remaining four unknowns of the symmetric matrix can be generated by multiplying Equation 5-28 by any column vector on the right and any row vector on the left, $\bar{u}^T\mathbf{C}^T\mathbf{S}\mathbf{C}\bar{v} = \bar{u}^T\mathbf{S}\bar{v}$. Some care must be exercised to assure that the resulting equations are linearly independent. Generally three choices of vectors $\bar{v}_1 = \bar{u}_1$, $\bar{v}_2 = \bar{u}_2$, and $\bar{v}_3 = \bar{u}_3$, such that $\det\begin{bmatrix}\bar{v}_1 & \bar{v}_2 & \bar{v}_3\end{bmatrix} \neq 0$ (i.e., the three vectors are not collinear) along with a fourth vector, $\bar{v}_4 \neq \bar{u}_4$, will suffice. Furthermore, if the vectors are selected appropriately, very simple expressions can result. For example, the vector $\bar{u} = \bar{v} = \begin{bmatrix} c_{32} & -c_{31} & 0 \end{bmatrix}^T$ gives the following expression:

$$\bar{b} \cdot \bar{b}_{General} = \frac{c_{32}^2 - z_{32}^{\ 2}}{z_{31}^{\ 2} - c_{31}^2}$$

Equation 5-29: Closed-form solution for the quantity $\bar{b} \cdot \bar{b}$ in the general case

This equation will hold unless either or both of the c_{31} or c_{32} elements of $\mathbf{C}$ are zero. These special cases, which include the affine subset of same-camera transformations, are treated separately in Appendix B. A similar application of the vectors $\bar{u} = \bar{v} = \begin{bmatrix} 0 & 0 & 1 \end{bmatrix}^T$ in conjunction with various substitutions will give the following expression for $\bar{c} \cdot \bar{c}$ in terms of $\bar{b} \cdot \bar{b}$:

$$\bar{c} \cdot \bar{c}_{General} = \frac{(\bar{b} \cdot \bar{b})(c_{13}c_{32}z_{21}^2 - c_{23}c_{31}(c_{23}c_{32} + c_{33}^2 - z_{11}^2)) + (c_{31}c_{23}z_{12}^2 - c_{32}c_{13}(c_{13}c_{31} + c_{33}^2 - z_{22}^2))}{c_{31}c_{32}(c_{13}c_{31} + c_{23}c_{32} + c_{33}^2 - 1)}$$

Equation 5-30: Closed-form solution for the quantity $\bar{c} \cdot \bar{c}$ in the general case

Using a similar approach the following expressions for the two remaining components of $\mathbf{S}$ can be found:

$$\bar{a}\cdot\bar{c}_{General}=\frac{(\bar{c}\cdot\bar{c})c_{31}^2-(\bar{b}\cdot\bar{b})z_{21}^2+c_{33}^2-z_{22}^2}{2c_{31}c_{33}}$$

$$\bar{b}\cdot\bar{c}_{General}=\frac{(\bar{c}\cdot\bar{c})c_{32}^2+(\bar{b}\cdot\bar{b})(c_{33}^2-z_{11}^2)-z_{12}^2}{2c_{32}c_{33}}$$

Equation 5-31: Closed-form solution for the quantities $\bar{a}\cdot\bar{c}$ and $\bar{b}\cdot\bar{c}$ in the general case

These four quantities can be substituted into Equation 5-27 to compute the canonical pinhole camera model. Therefore, a closed-form solution for the planar pinhole-camera model can be determined for any projective mapping satisfying the constraints of a same-camera transformation given the prior knowledge that the imager has an orthogonal sampling grid. This result can be used to determine the calibration any of such a camera given only two images taken from a common center of projection. The only limitation of the given equations is that both of the c_{31} or c_{32} elements of $\mathbf{C}$ are required to be nonzero. However, equivalent solutions for these four unknowns can be derived for all these cases with the notable exception of the affine case in which both c_{31} and c_{32} are zero. Only three of these four parameters can be found in the affine transformation case; a detailed discussion of this case is given in Appendix B.

Consider the following example. Given the following rotation matrix and pinhole-camera model, which represents a 512 × 512 image with a 45° horizontal field-of-view symmetric frustum:

$$\mathbf{R}\left(\begin{bmatrix}\frac{-3}{7} & \frac{6}{7} & \frac{2}{7}\end{bmatrix}^T,\frac{\pi}{9}\right)\approx\begin{bmatrix}0.950769 & -0.119873 & 0.285775\\ 0.0755662 & 0.984000 & 0.161349\\ -0.300544 & -0.131810 & 0.944615\end{bmatrix}\qquad \mathbf{P}=\begin{bmatrix}1 & 0 & -256\\ 0 & 0.98 & -256\\ 0 & 0 & 618\end{bmatrix}$$

a same-camera transformation and its inverse can be computed as

$$\mathbf{C}=\begin{bmatrix}0.826271 & -0.170985 & 251.570\\ -0.0499298 & 0.929398 & 118.505\\ -0.000486318 & -0.000209020 & 1.12371\end{bmatrix}\qquad \mathbf{Z}=\begin{bmatrix}1.06914 & 0.139555 & -254.072\\ -0.00152468 & 1.05083 & -110.479\\ 0.000462419 & 0.000255861 & 0.759398\end{bmatrix}$$

The rotationally invariant quantities of the same camera transformation can be determined using the closed-form equations as follows (six-significant digits were maintained throughout all calculations):

$$\bar{b} \cdot \bar{b} \approx 0.960382$$
$$\bar{c} \cdot \bar{c} \approx 5.13098 \times 10^5$$
$$\bar{a} \cdot \bar{c} \approx -256.027$$
$$\bar{b} \cdot \bar{c} \approx -250.905$$

Finally, the pinhole-camera's intrinsic parameters can be determined from Equation 5-27.

$$\tilde{\mathbf{P}} = \begin{bmatrix} 1 & 0 & -256.027 \\ 0 & 0.979990 & -256.027 \\ 0 & 0 & 618.059 \end{bmatrix}$$

This technique could be used as a calibration process for computing intrinsic-camera parameters based solely on image observations. The camera, whose sampling grid is assumed to be orthogonal, must first be placed on a tripod or rotational stage and adjusted so that its panning motion is about the camera's center-of-projection. This can be accomplished by translating the camera in the plane perpendicular to the rotational axis until there is no apparent change in parallax. Any pair of images taken with this configuration are related by a same-camera transformation. The actual transformation can be determined using a well-known linear method described by both [Heckbert89] and [Wolberg90] which requires the identification of a minimum of four corresponding points in each image. Typically, many more points would be used in conjunction with a least-squares solution method. Once the transform was found it should be verified that it satisfies the same-camera constraints of Equation 5-23. If these constraints are not satisfied, the matrix must somehow be minimally perturbed such that it has a valid characteristic polynomial. Once this is completed, the closed-form solution method demonstrated in the previous examples can be used to find the camera's intrinsic parameters. In addition, the extrinsic parameters representing the rotation between the two images can be determined as follows:

$$\mathbf{R} = \mathbf{PCP}^{-1}$$

Equation 5-32: The rotation between the camera models of a same-camera transform

5.4 Deriving a Planar Pinhole-Camera Model from Images

Next, I consider the problem of establishing a warping equation for a reference image whose extrinsic and intrinsic pinhole-camera parameters are unknown. In order to establish the generalized-disparity values for the reference image, at least one other image is required in order to determine correspondences. I will require that both the reference image and the second

image used for correspondence be acquired using the same camera. In such a case, the relationship between the second image's planar pinhole-camera model to the pinhole model of the reference image is given by $\mathbf{P}_2 = \mathbf{R}_2\mathbf{P}_1$, and the corresponding warping equation has the following form:

$$\bar{x}_2 = \delta(\bar{x}_1)\mathbf{P}_1^{-1}\mathbf{R}_2^{-1}(\dot{C}_1 - \dot{C}_2) + \mathbf{P}_1^{-1}\mathbf{R}_2^{-1}\mathbf{P}\bar{x}_1$$

Equation 5-33: Planar warps resulting from the same camera

As one would expect, the matrix product in the second term of Equation 5-33 is a same-camera transformation.

Once eight or more corresponding image-space points are identified in the two images, a fundamental matrix can be determined using the methods outlined in subsection 5.1.2. This fundamental matrix establishes the epipolar geometry between the two images. The determinant of the upper-left 2×2 submatrix of this fundamental matrix can then be tested for generality. If this determinant is nonzero (both epipoles are finite), the fundamental matrix can then be normalized by scaling it by the reciprocal of the determinant's square-root. In this typical situation a three-parameter family of projective transformations compatible with the computed fundamental matrix can be identified using Equation 5-18. We can further limit this three-parameter space of projective transforms to those that also satisfy the same-camera transform constraints derived in section 5.3.1. Equations for the scalar-matrix quantities used to determine these constraints for this three-parameter family of projective transforms are given in the following subsection.

5.4.1 Scalar matrix quantities of transforms with known epipolar geometries

In this subsection I define the matrix relationships necessary to determine if a projective transformation that is compatible with a given fundamental matrix is also in the same-camera family. I will refer to an instance of a projective transformation that is compatible with the given fundamental matrix **F,** as specified in Equation 5-18, as $\sigma\mathbf{H}_\mathbf{F}$. Recall that the fundamental matrix of Equation 5-18 has been normalized so that it is of the form given in Equation 5-5. The non-zero scale factor, σ, is included because all such projective transformations are equivalent. The same-camera transformation constraints, derived in Equation 5-23, are specified in terms of three scalar matrix quantities: the determinant, the trace, and the sum of the diagonal minors.

The determinant of $\sigma\mathbf{H_F}$ is

$$\text{Determinant}(\sigma\mathbf{H_F}) = \sigma^3(h_{31}(f_{12}f_{23} - f_{22}f_{13}) + h_{32}(f_{21}f_{13} - f_{11}f_{23}) + h_{33})$$

The coefficients of h_{31}, h_{32}, and h_{33} are the coordinates of the null-space vector in the fundamental matrix's transpose. This can be seen by comparing the coefficients to Equation 5-13. Therefore, these coordinates identify the epipole of the reference image (i.e., the projection of the second image's center-of-projection in the reference image). I will refer to the screen-space coordinate of the reference image's epipole as $\bar{e}_1 = \begin{bmatrix} e_{1u} & e_{1v} & 1 \end{bmatrix}^T$ [26]. Substituting the epipole's coordinates into the equation above gives

$$\text{Determinant}(\sigma\mathbf{H_F}) = \sigma^3(h_{31}e_{1u} + h_{32}e_{1v} + h_{33}).$$

Equation 5-34: Determinant of a transform compatible with a given fundamental matrix

The trace of $\sigma\mathbf{H_F}$ is

$$\text{Trace}(\sigma\mathbf{H_F}) = \sigma(h_{31}e_{2u} + h_{32}e_{2v} + h_{33} + f_{21} - f_{12})$$

Equation 5-35: Trace of a transform compatible with a given fundamental matrix

The sum of the diagonal minors of $\sigma\mathbf{H_F}$ is

$$\sum_{i=1}^{3} \text{Minor}(\sigma\mathbf{H_F}, i, i) = \sigma^2(-h_{31}(f_{12}e_{2u} + f_{22}e_{2v} + f_{23}) + h_{32}(f_{11}e_{2u} + f_{21}e_{2v} + f_{13}) + h_{33}(f_{21} - f_{12}) + 1)$$

The expression for $\bar{e}_2$'s coordinates given in Equation 5-11 can be used to simplify this expression. Note that in the assumed normalization, the term $e_{23} = f_{11}f_{22} - f_{12}f_{21} = 1$. This gives the expressions $f_{11}e_{2u} + f_{21}e_{2v} + f_{31} = 0$ and $f_{12}e_{2u} + f_{22}e_{2v} + f_{32} = 0$. Rearranging and substituting these terms into the expression for the sum of the diagonal minors shown above gives

[26] The coordinates of the epipole in the first image, $\bar{e}_1$, are generally different from the coordinates of the epipole in the second image, $\bar{e}_2$. Even when they have the same coordinate values, they are still defined in different screen spaces.

$$\sum_{i=1}^{3} \text{Minor}(\sigma \mathbf{H_F}, i, i) = \sigma^2 (h_{31}(f_{32} - f_{23}) + h_{32}(f_{13} - f_{31}) + h_{33}(f_{21} - f_{12}) + 1)$$

I will introduce the following notation in order to simplify later expressions:

$$\tilde{m} = \begin{bmatrix} m_1 \\ m_2 \\ m_3 \end{bmatrix} = \begin{bmatrix} f_{32} - f_{23} \\ f_{13} - f_{31} \\ f_{21} - f_{12} \end{bmatrix}$$

Equation 5-36: Vector of minor coefficients

This substitution gives the following simplified expression:

$$\sum_{i=1}^{3} \text{Minor}(\sigma \mathbf{H_F}, i, i) = \sigma^2 (h_{31} m_1 + h_{32} m_2 + h_{33} m_3 + 1)$$

Equation 5-37: Sum of the diagonal minors of compatible transforms

5.4.2 Finding a Camera Solution

In order for a given transformation to be a member of the same-camera class, the scale factor of the transform, σ, must be selected so that its determinant is equal to one. This constraint gives the following expression:

$$h_{31} e_{1u} + h_{32} e_{1v} + h_{33} = \frac{1}{\sigma^3}$$

Equation 5-38: Unit-determinant constraint

The second constraint on a same-camera transformation is that its trace must equal the sum of its diagonal minors. The equivalence of the trace and the sum of the diagonal minors can be expressed by subtracting Equation 5-37 from Equation 5-35. The following equation results:

$$\sigma(h_{31}(e_{2u} - \sigma m_1) + h_{32}(e_{2v} - \sigma m_2) + h_{33}(1 - \sigma m_3) - (\sigma - m_3)) = 0$$

If σ is zero, the resulting transformation cannot have a determinant of one as required by Equation 5-38. Thus, σ is non-zero and it can, therefore, be factored out giving

$$h_{31}(e_{2u} - \sigma m_1) + h_{32}(e_{2v} - \sigma m_2) + h_{33}(1 - \sigma m_3) = (\sigma - m_3)$$

Equation 5-39: Trace-equals-sum-of-minors constraint

Both Equation 5-38 and Equation 5-39 are of degree one in terms of h_{31}, h_{32}, and h_{33}. Therefore, for any fixed value of σ the locus of points in the parameter space which satisfy the unit-determinant constraint is a plane. Likewise, the locus of parameter-space points that satisfy the trace-equals-the-sum-of-minors constraint is also a plane. The intersection of these two planes represents the set of transformations where both constraints are satisfied. Generally, the intersection of two planes will be a line. As the parameter σ is varied, a family of lines is swept out in the parameter space. These lines define a two-dimensional subspace of projective transformations that are compatible with the given fundamental matrix and are potentially same-camera transformations. An example of this two-parameter surface is illustrated below.

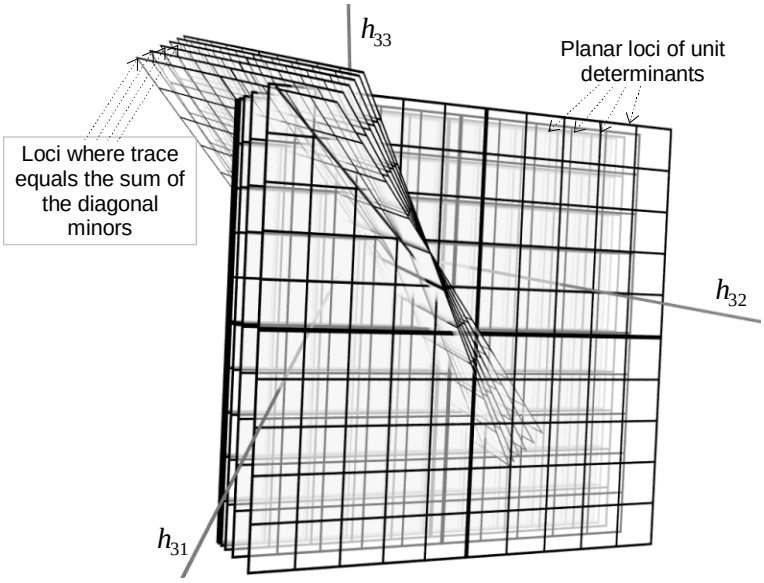

Figure 5-6: Surface of potentially compatible projective transformations

Next, I will reformulate the surface description in terms of two parameters to facilitate searching for a valid camera model. The first parameter will be the scale factor σ. The second is the trace of the projective transform prior to scaling, which will be represented by the symbol τ.

$$\tau = h_{31}e_{2u} + h_{32}e_{2v} + h_{33} + m_3$$

Equation 5-40: The trace of the desired transform prior to scaling

The three parameters h_{31}, h_{32}, and h_{33}, which define the subspace of projective transformations compatible with a given fundamental matrix, can be expressed in terms of σ and τ as follows:

$$h_{31} = \frac{\sigma^3((m_2 - e_{1v}m_3)(\tau - m_3) - (e_{1v} - e_{2v})) + \sigma^2\tau(e_{1v} - e_{2v}) + e_{2v}m_3 - m_2}{\sigma^3(m_1(e_{1v} - e_{2v}) - m_2(e_{1u} - e_{2u}) + m_3(e_{1u}e_{2v} - e_{1v}e_{2u}))}$$

$$h_{32} = \frac{1}{\sigma^3(e_{1v} - e_{2v})} - \frac{h_{31}(e_{1u} - e_{2u}) - m_3 + \tau}{(e_{1v} - e_{2v})}$$

$$h_{33} = \frac{1}{\sigma^3} - h_{31}e_{1u} - h_{32}e_{1v}$$

Equation 5-41: Expressions for $h_{31,}$ h_{32}, and h_{33} in terms of σ and τ

The parameterization of the compatible same-camera surface given in Equation 5-41 is suitable for all cases except when the epipoles of both images have the same coordinate. This special case is discussed further in Appendix C.

The final identification of the projective transformation, which is both a same-camera transformation and is compatible with the given fundamental matrix, requires that three additional relational constraints be satisfied. These constraints are listed below.

$$\begin{aligned} &1) \quad -1 \le \sigma\tau \le 3 \\ &2) \quad \bar{b} \cdot \bar{b} \ge 0 \\ &3) \quad \bar{r} \cdot \bar{r} \ge 0 \end{aligned}$$

Equation 5-42: Three relational constraints on a same-camera transformation

The last two relationships can be tested using Equation 5-29 and Equation 5-30 on the parametric surface described by Equation 5-41. The elements of the matrices $\mathbf{C}$ and $\mathbf{Z}$ in terms of h_{31}, h_{32}, and h_{33}, are given below. It is assumed that these terms result from Equation 5-41.

$$\mathbf{C}_F = \sigma \begin{bmatrix} h_{31}e_{2u} + f_{21} & h_{32}e_{2u} + f_{22} & h_{33}e_{2u} + f_{23} \\ h_{31}e_{2v} - f_{11} & h_{32}e_{2v} - f_{12} & h_{33}e_{2v} - f_{13} \\ h_{31} & h_{32} & h_{33} \end{bmatrix}$$

$$\mathbf{Z}_F = \sigma^2 \begin{bmatrix} h_{32}f_{13} - h_{33}f_{12} & h_{32}f_{23} - h_{33}f_{22} & h_{32}f_{33} - h_{33}f_{32} + e_{1u} \\ h_{33}f_{11} - h_{31}f_{13} & h_{33}f_{21} - h_{31}f_{23} & h_{33}f_{31} - h_{31}f_{33} + e_{1v} \\ h_{31}f_{12} - h_{32}f_{11} & h_{31}f_{22} - h_{32}f_{21} & h_{31}f_{32} - h_{32}f_{31} + 1 \end{bmatrix}$$

Equation 5-43: Same-camera transform and adjoint compatible with F

The matrix elements from Equation 5-43 allows Equation 5-29 and Equation 5-30 to be evaluated for arbitrary points on the surface of potentially compatible transforms. Using these results, the second two relationships of Equation 5-42 can be tested. Figure 5-8 illustrates the subspace of potentially compatible transforms satisfying the conditions of Equation 5-42.

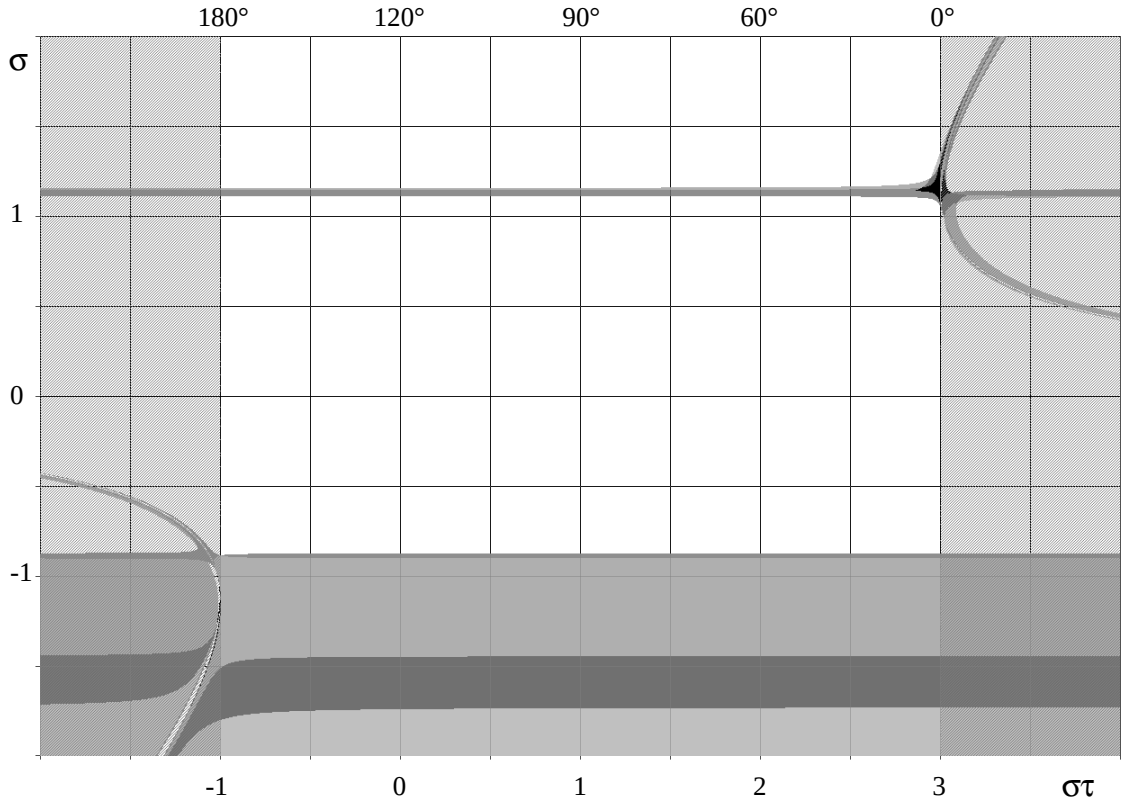

Figure 5-7: The solution space of compatible same-camera transformations

Figure 5-8 shows a solution space for a particular same-camera model. The scale-factor parameter, σ, is shown in a range of -2 to 2. The horizontal axis represents the product of the two parameters, $\sigma\tau$, in the range from -2 to 4. In this parameter space the first relational constraint of Equation 5-42 defines the vertical band the range from $-1 \leq \sigma\tau \leq -3$. The rotation angle of the same-camera corresponding to the $\sigma\tau$ value is shown across the top of the figure. The darkened curve indicates regions of the parameter space where one or both of the two remaining relational constraints of Equation 5-42 are satisfied. Only within the black region are all three conditions satisfied.

The fundamental matrix used to illustrate the solution-space in Figure 5-8 was determined by 28 corresponding points selected from two images with resolutions of 768×512 pixels. This fundamental matrix was found using the methods described in section 5.1.2. The error in a fundamental matrix can be quantified by computing the average distance of all identified points from the line produced by their corresponding point in the other image. In this example, this average error is 0.3894 of a pixel. The values of this matrix and its associated epipoles, shown to six significant figures, are

$$\mathbf{F}_{21} = \begin{bmatrix} -0.0836038 & -0.981640 & -305.318 \\ 1.03385 & 0.177880 & 207.391 \\ 472.261 & -363.335 & -37892.4 \end{bmatrix} \quad \bar{e}_1 = \begin{bmatrix} -149.273 \\ -298.315 \\ 1 \end{bmatrix} \quad \bar{e}_2 = \begin{bmatrix} -459.641 \\ -493.967 \\ 1 \end{bmatrix}$$

Equation 5-44: Fundamental matrix used in Figure 5-8

The valid same-camera solutions are restricted to a compact region of the solutions space. While it might be possible to derive a closed-form solution for a camera model within this enclosed region, the high-degree of the polynomial expressions involved would likely lead to numerical instabilities in computing such a solution. Furthermore, it is well known that such high-order rational systems are extremely sensitive to any noise in the input. Instead of seeking a closed-form solution, a global-optimization method can be used to identify a specific camera model within this region. This requires the selection of an appropriate penalty function based on a reasonable set of assumptions concerning the camera model. I have employed the following penalty function for this purpose:

$$E(\sigma,\tau) = \kappa_1(\bar{b}\cdot\bar{b} - \alpha^2)^2 + \kappa_2 e^{-\bar{c}\cdot\bar{c}} + \kappa_3\left(1 - e^{\frac{-(\bar{a}\cdot\bar{c}+w/2)^2}{w}} + 1 - e^{\frac{-(\bar{b}\cdot\bar{c}+\alpha h/2)^2}{\alpha h}}\right)$$

Equation 5-45: Error function used in the global optimization

The first term of the penalty function biases the solution toward the estimated aspect-ratio, α, of the image sampling grid (in the absence of other information, a value of $\alpha = 1$ is usually safe unless there is noticeable aspect-ratio distortions in the image). The second term drives the solution away from negative values of $\bar{c}\cdot\bar{c}$, and the third term of the error function, where w and h represent the image's width and height in pixels, causes the solution to prefer nearly symmetric viewing frustums. The weighting factors κ_1, κ_2, and κ_3 control the relative importance of each penalty term. Values of $\kappa_1 = 1$, $\kappa_2 = 1$, and $\kappa_3 = 0.1$ have given reasonable results, and variations in these weighting factors have very little influence on the final camera model.

A Levenberg-Marquardt global optimization method was used to solve for the final camera model [Press88]. This optimization method generally converges rapidly if the initial estimates of σ and τ are near the actual solution. Such an initial estimate can usually be made when the solution space is contained in a compact region like that shown in Figure 5.8[27].

[27] While the possibility of multiple solutions within this region exists, the variations in the resulting camera models are minimal. However, it has been observed that this variation increases

The final camera model derived from the fundamental matrix of Equation 5-44 is

$$\mathbf{P}_1 = \mathbf{P}_2 = \begin{bmatrix} 1 & 0 & -381.504 \\ 0 & 0.999951 & -191.141 \\ 0 & 0 & 643.787 \end{bmatrix}$$

Equation 5-46: Estimated camera model

where $\sigma = 1.14196$ and $\tau = 2.59207$. This model can be compared to a simple pinhole-camera model using manufacturer's lens specifications. Both images were taken using a 28mm focal-length lens and captured on a 36mm by 24mm image plane focused at a distance of approximately 1.5m. The image plane dimensions and effective focal length[28] must be scaled by $^{768\text{pixels}}/_{36\text{mm}}$ to be in the same units as Equation 5-46. The resulting simple pinhole-camera model using the manufacturer's specification is

$$\mathbf{P}_{Simple} = \begin{bmatrix} 1 & 0 & -384 \\ 0 & 1 & -256 \\ 0 & 0 & 608.696 \end{bmatrix}$$

Equation 5-47: Simple pinhole-camera model using manufacturer's specs

5.5 An Example

The following example illustrates the entire process of building an image-based model without a priori knowledge of the camera calibration. The images shown below were taken with the same camera using a fixed focal-length lens with constant shutter and aperture settings. A total of 48 corresponding points are identified in each image, and they are shown as crosses. The original contrast of the image has been reduced so that the annotations are visible.

---

dramatically as the rotation angle approaches 0. Appendices C and D address these numerically difficult situations.

[28] The effective focal length is computed using the thin lens law $\frac{1}{f_{effective}} = \frac{1}{f_l} - \frac{1}{d_{object}}$, where f_l is the focal length and $d_{effective}$ is the distance to the object in focus.

Figure 5-8:

The fundamental matrix was then computed using the linear method described by [Hartley92]. Next a Levenberg-Marquardt nonlinear optimization similar to the one described by [Luong93b] was used to minimize the error in the fundamental matrix. The 7-parameter model given in Equation 5-5 was used to describe the fundamental matrix in the optimization process, and the linear-solution was used as an initial guess. The resulting epipolar lines are shown below superimposed over the image and the given correspondences.

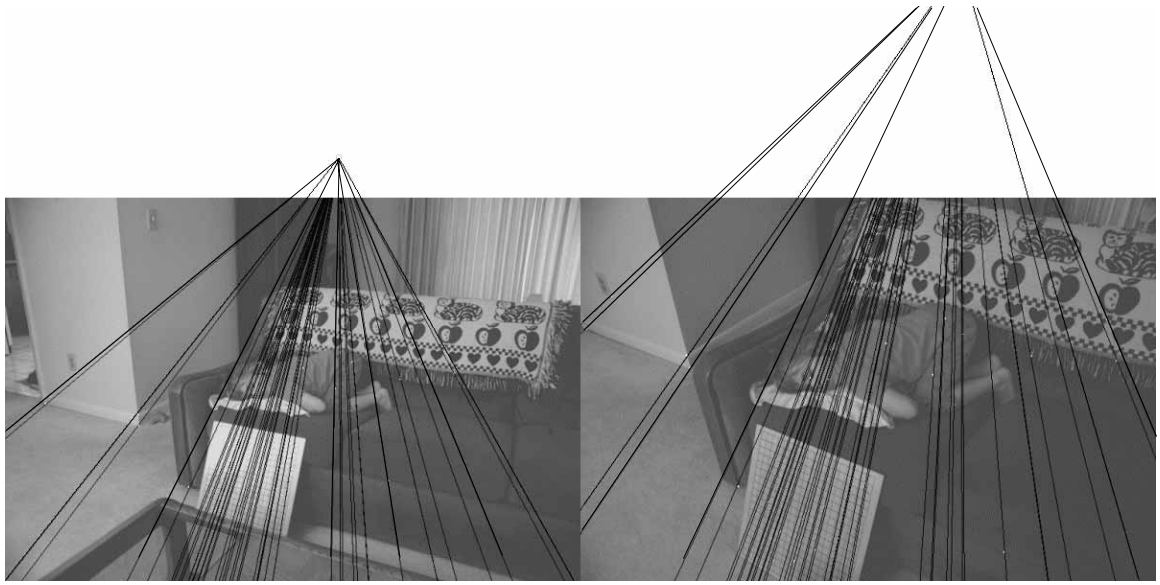

Figure 5-9

The image was then rectified, using a method similar to the one described by [Seitz96], by transforming the epipole in each image to $[0,1,0]^T$ using a three-dimensional rotation and an affine transformation. In this configuration, the epipolar lines are aligned with the vertical columns of the image. A correlation-based method using a 5×5 sliding window was then used to compute the disparity value at each pixel in the right image, which will be the reference. The

inverse of the rectification transform was then applied to the right image to provide the final disparity values. These generalized-disparity values are shown below.

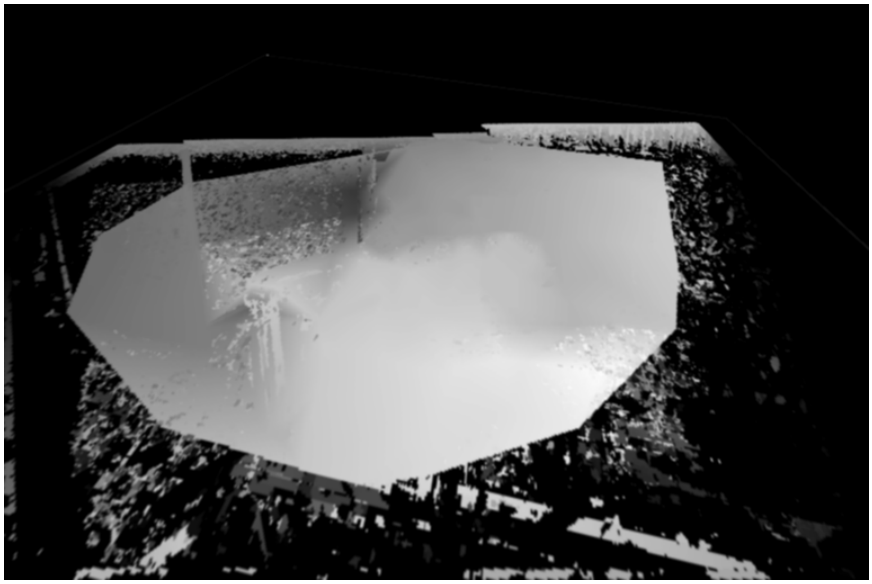

Figure 5-10

The fundamental matrix was then used to estimate a same-camera model. The results of several image warps based on this model are shown below.

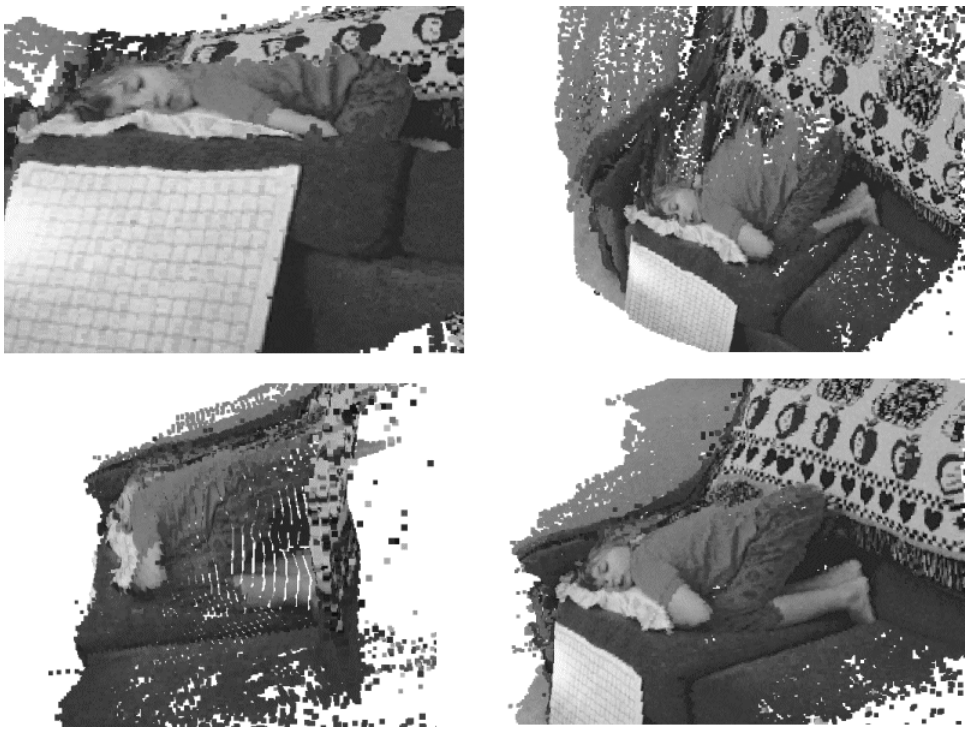

Figure 5-11

5.6 Discussion

This chapter has addressed the problem of determining a planar image-warping equation when the center-of-projection and the pinhole-camera model of the reference image are unavailable. This allows for the generation of image-based computer graphics with no external information beyond a reference image and a second image from the same camera for establishing correspondences. Alternatively, these results might be used to find the calibration of a pinhole-camera model based on the epipolar geometry determined from image observations[29].

Maybank [Maybank92], Faugeras [Faugeras92a], and Luong [Luong93a] have described a similar method for determining a pinhole-camera model from an epipolar geometry. Their method requires three camera displacements (i.e., four images with associated correspondences) and is able to determine all five intrinsic camera parameters without any assumptions. [Maybank92] provides a formal proof for the uniqueness of their solution.

Maybank's, Faugeras', and Luong's self-calibration method establishes two conic expressions from each epipolar geometry, whereas the approach described here derives four equations from a rank-deficient 6×6 system describing the rotational geometric invariants (Equation 5-26). In such a system, four of the unknowns can be solved for in terms of the remaining two. The values of these remaining two unknowns can be established under two assumptions. The first assumption, limiting the length of one of the spanning vectors, is equivalent to a scaling of the pinhole-camera model and therefore does not limit the solution space. The second assumption limits the solution space to pinhole-cameras with orthogonal sampling grids. This is reasonable for most real-world cameras. Both self-calibration methods suffer from numerical sensitivities.

Hartley [Hartley94] has described another self-calibration method based on a rotating camera. Since all of the images in his method are required to have the same center-of-projection, no epipolar geometry is defined. His approach is similar to determining a camera model from a same-camera transformation as described in section 5.3.2. Hartley's method determines all 5 pinhole-camera parameters and uses a global optimization to find the desired camera model.

---

[29] In the approach described, only 4 of the 5 intrinsic camera parameters (the fifth skew parameter is assumed to be zero) and 5 of the 6 extrinsic parameters (all three rotation parameters and a vector in the translation direction) can be found.

The same-camera method that I described can only determine four parameters within a restricted subspace. However, it does provide a closed-form solution for that case.

There are still several open issues concerning the self-calibration method that I have put forth. For practical use, the numerical stability and special-case handling of this solution method are important concerns that need to be addressed. A complete analysis of the problem's numerical sensitivity, along with the development of a computation strategy for maintaining the greatest possible accuracy in the solution, would be a valuable addition to this work. Furthermore, an interesting open question is whether the described approach leads to a unique solution in all cases.

Algebraic curve theory might provide an answer to the uniqueness question. By determining the rank of each constraint curve, it is possible to determine the number of times that a general line will intersect the curve. An examination of the degree and rank of the algebraic expression's denominator allows the number of unique components to be determined. Careful analysis of the curve components that are intersected by vertical lines through the region of the solution space between $-1 \leq \sigma t \leq 3$ might provide an upper-bound on the number of regions in which the remaining two relationships of Equation 5-42 can be simultaneously satisfied.

Alternatively, a visualization of the solution space of potential same-camera transforms that are compatible with a given epipolar geometry can be used to establish an initial guess for a global optimization method. In this chapter I have also provided a suitable error function for use in this global optimization process.

Chapter 6

COMPUTING VISIBILITY WITHOUT DEPTH

Recall that in Chapter 3 an algorithm was presented for computing a correct visibility solution for a warped image. This algorithm establishes an ordering for the warping that back-to-front. In this chapter I will prove the correctness of this visibility algorithm. I will adopt a spherical pinhole-camera model instead of the planar pinhole-camera model used in the original algorithm. Because a spherical pinhole-camera model is panoramic, as described in Chapter 4, all the rays originating from its center-of-projection have a unique description. Using a spherical model has two benefits. First, there will always be an image of the desired center-of-projection on a spherical viewing surface of the reference image; this halves the number of enumeration cases. Second, since the projected image of the desired center-of-projection will always fall within the parameter domain, the nine cases described in section 3.5.1 all reduce into one case. Once the algorithm is proven correct for the spherical case, it is straightforward to extend it to the planar model.

In this chapter I provide a formal proof for the visibility algorithm's correctness in the case of a spherical viewing plane. I then extend this result to planar-viewing surfaces. Finally, I present a summary of how to extend the algorithm to any other viewing surface. In the following chapter I will return to more general discussions of the image-based approach.

6.1 Definitions

A perspective-projected image is defined by a central point and a single-valued range function specified over a bundle of rays emanating from that point. Coordinates are assigned to rays using a parameter space defined on some viewing surface. This central point of the perspective-projected image is its center-of-projection. Any perspective-projected surface has a dual representation - the mapping of the ray bundle onto a spherical viewing plane having the same center-of-projection. Within such a framework, all rays have a unique coordinate.

In this derivation I will consider a set of spherical coordinate frames, $\{S_1, S_2, \ldots, S_n\}$, embedded within a global Cartesian coordinate system, W. An example is shown in the following figure:

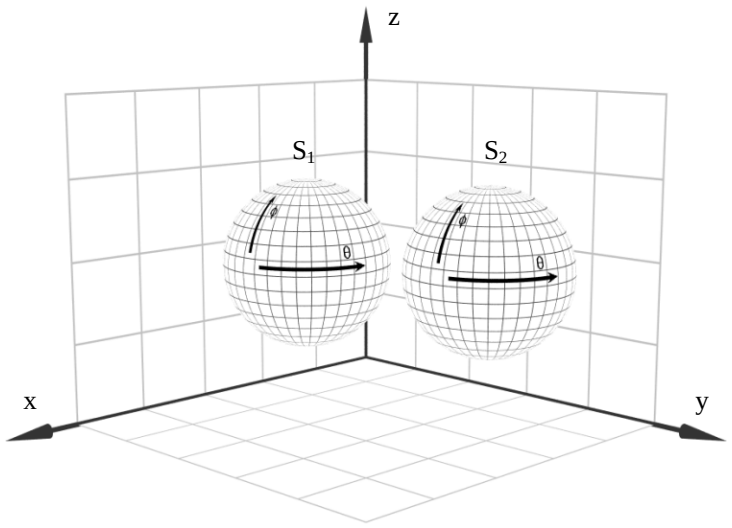

Figure 6-1: Spherical coordinate frames embedded in a Cartesian coordinate system

The origin of a spherical frame represents a center-of-projection with a unit sphere as a viewing surface.

This analysis assumes the existence of scene points somewhere within the global coordinate frame, W. For each scene point there exists a mapping from the global coordinate frame to the coordinate frame of any spherical domain.

This mapping of points from W to S_i is not necessarily one-to-one. I will consider a particular subset of this mapping that assigns coordinates to only those points closest to the frame's center-of-projection along each ray. This particular mapping is called an *occlusion-compatible mapping*, and it is consistent with a proper visibility solution for opaque surfaces.

Chapters 3 and 4 described image warping equations that mapped the visible points seen from one center-of-projection to their correct coordinate in any other projective image. However, these two-dimensional image-warping functions might map several points from the original image's domain to a single point in the final image. Such a point in the final image will be referred to as a *multiplicity* of the mapping. The specific claim of this proof is that an

occlusion- compatible mapping can also be established independent of the scene points' distances from either the original or final centers-of-projection.

6.2 Proof

In this discussion the initial projective image is assumed to be the S_i frame, and the desired image's frame is S_j. In general all possible reprojections of a point, $\bar{x}$, that fall along a given ray, (θ_x, ϕ_x), of S_i are constrained to lie within a plane. This plane is defined by the line segment, l, connecting the initial and desired centers-of-projection and the ray itself. There are two exceptions to this. On a spherical viewing surface there exists one ray in the direction of the line segment connecting the two centers-of-projection. This ray, (θ_+, ϕ_+), which is called the *positive epipole*, is the virtual image of the desired center-of-projection on the original surface. The ray in the opposite direction is called the *negative epipole*, (θ_-, ϕ_-). It corresponds to the vanishing point for all rays originating from S_j in the direction of S_j when projected onto S_j's viewing surface. Points along either of these epipolar rays are constrained to lie on the line that has l as a segment. This line is also common to all the planes associated with a ray, as discussed previously. These constraint planes are called *epipolar planes*. The projections of these epipolar planes onto the viewing surface lie along longitudinal lines of a sphere having the epipoles as poles. This relationship is shown in the following figure:

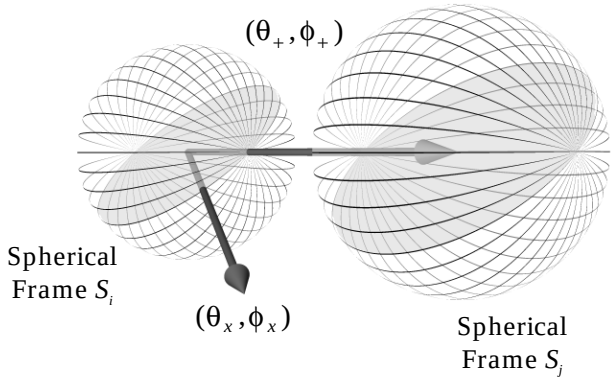

Figure 6-2: An epipolar plane defined by a ray and two centers-of-projection

Next, consider an isolated multiplicity on the projective mapping from S_i to S_j, as shown in the following figure:

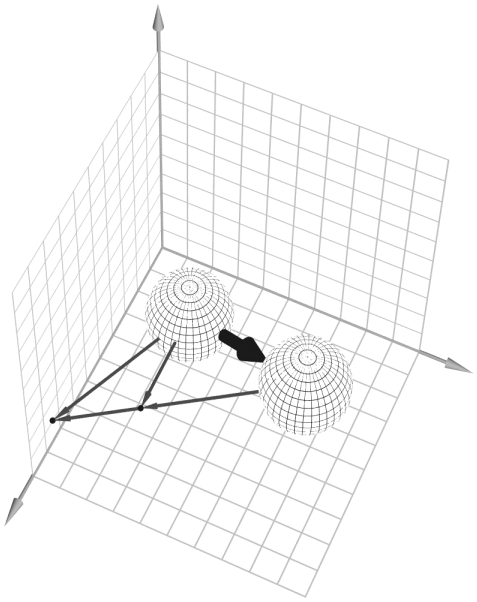

Figure 6-3: A multiplicity induced by translation of coordinate frames

Theorem 1. *The points of a multiplicity and the centers of* S_i *and* S_j *are coplanar, except when the multiplicity lies along an epipole.*

Proof: The points of the multiplicity are collinear with the origin of S_j since they share the same coordinates. A second line segment connects the frame origins, S_i and S_j. In general these lines are distinct and, since they share a common point, they must be coplanar. If the points of the multiplicity happen to fall along the line containing the segment connecting S_i and S_j, then no unique plane is determined.

It follows from the definition that the plane of a multiplicity is also an epipolar plane. This plane is common to all of those rays in the original image whose points map onto the multiplicity. Thus, from Theorem 1, we can conclude that all of the multiplicities that are introduced by projective mappings occur entirely within epipolar planes.

Having established the importance of epipolar planes, it is now only necessary to consider points within a particular epipolar plane throughout the remainder of the proof. Assume that a Euclidean or rigid-body transformation is applied to the global coordinate frame, W, that simultaneously aligns the epipolar ray with the x-axis and the epipolar plane of interest with the x-y plane. Then consider a uniform scaling of the global coordinates such that the distance between the centers-of-projection is 1. This transformation can also be thought of as a re-parameterization of three-dimensional space. This situation is shown in the following figure:

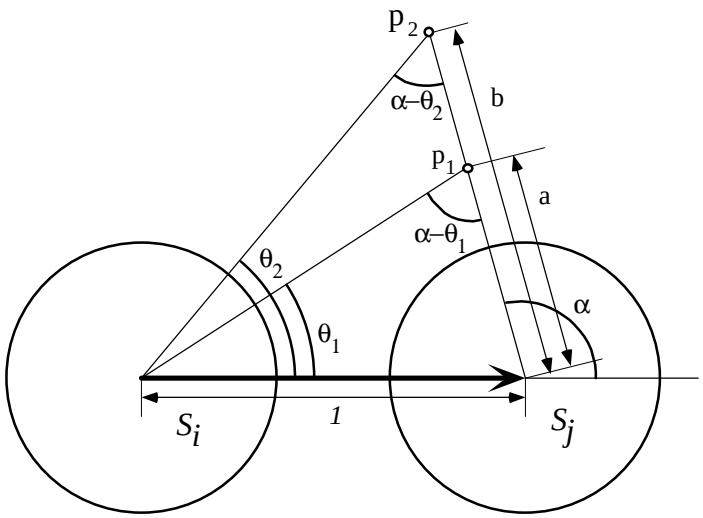

Figure 6-4: A multiplicity illustrated in an epipolar plane

Theorem 2. *If* $\cos\theta_1 > \cos\theta_2$ *and* $0 < \theta_1, \theta_2, \alpha < \pi$, then a < b.

Proof: The length of sides a and b can be found in terms of the angles θ_1, θ_2, and α using the law of sines as follows:

$$\frac{a}{\sin\theta_1} = \frac{1}{\sin(\alpha - \theta_1)} \qquad \frac{b}{\sin\theta_2} = \frac{1}{\sin(\alpha - \theta_2)}$$

Thus,

$$a = \frac{\sin\theta_1}{\sin(\alpha - \theta_1)} \quad \text{and} \quad b = \frac{\sin\theta_2}{\sin(\alpha - \theta_2)}$$

$$a = \frac{\sin\theta_1}{\sin\alpha\cos\theta_1 - \cos\alpha\sin\theta_1} \qquad b = \frac{\sin\theta_2}{\sin\alpha\cos\theta_2 - \cos\alpha\sin\theta_2}$$

$$a = \frac{1}{\sin\alpha\cot\theta_1 - \cos\alpha} \qquad b = \frac{1}{\sin\alpha\cot\theta_2 - \cos\alpha}$$

The denominators in the expressions of a and b must be strictly positive, since the lengths of a and b are positive over the range of angles defined. The ratio of a to b can be expressed as

$$\frac{a}{b} = \frac{\sin\alpha\cot\theta_2 - \cos\alpha}{\sin\alpha\cot\theta_1 - \cos\alpha}$$

The given relationship

$$\cos\theta_1 > \cos\theta_2$$

implies

$\cot\theta_1 > \cot\theta_2$, (since cos θ and cot θ are monotonically decreasing)

$\sin\alpha\cot\theta_1 > \sin\alpha\cot\theta_2$, (sin α is always positive over the interval)

$\sin\alpha\cot\theta_1 - \cos\alpha > \sin\alpha\cot\theta_2 - \cos\alpha$, (subtraction from both sides)

$1 > \dfrac{\sin\alpha\cot\theta_2 - \cos\alpha}{\sin\alpha\cot\theta_1 - \cos\alpha}$, (since both sides are strictly positive)

Therefore, $\frac{a}{b} < 1$ and $a < b$. For angles θ_1 and θ_2 within the interval $[0, \pi]$, the relationship $\cos\theta_1 > \cos\theta_2$ also implies that $\theta_1 > \theta_2$.

Consider all of the points visible from S_i whose rays lie on a common epipolar plane. If, during the mapping of points from S_i to S_j, each point is mapped in order of decreasing θ, then, by Theorem 2, when a multiplicity occurs along a given ray defined on S_j, the most recently mapped point will always have a closer range value than any previously mapped point. Therefore, it is possible to compute an occlusion-compatible mapping by traversing the point set in order of decreasing angle toward the epipole. In this approach later surface points will overwrite previous ones. Notice that this mapping procedure only considers the coordinates of the unmapped points in the initial frame, S_i, and the vector toward the desired center-of-projection. It does not use any range information.

Since all interactions between points are constrained to take place along epipolar planes, each epipolar plane can be treated independently. This method can be used as an algorithm for computing occlusion-compatible surfaces via the reprojection of any projective image. The resulting surface will also be a projective image since only a single surface element along each ray is retained. The resulting reprojection order is depicted in the figure shown below.

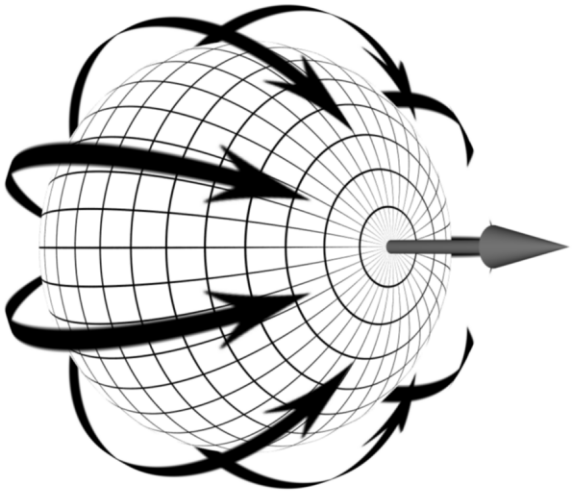

Figure 6-5: A reprojection order that guarantees an occlusion-compatible result

6.3 Mapping to a Planar Viewing Surface

Next, I apply the implications of this result to a planar projected surface. The bundle of rays described by a center-of-projection and a planar viewing surface are a subset of those rays given by a spherical viewing surface with the same center-of-projection.

The solid angle of a planar ray bundle can never be more than 2π, and this maximum solid angle occurs when the projection plane is unbounded. We can, therefore, map any planar projective image onto a subset of a spherical domain with a re-parameterization of the plane. Once the planar projected surface is so mapped, the reprojection to a desired center-of-projection can proceed along epipolar planes in order of decreasing θ from the negative epipole towards the positive epipole, as described previously. The resulting spherical mapping can then be re-parameterized to match the desired planar viewing surface.

Many of these re-parameterization and reprojection steps can be combined. In the figure shown below the initial surface of projection is overlaid onto an equivalent spherical viewing surface. The enumeration direction along decreasing angles of the epipolar planes as implied by the change in center-of-projection is depicted by arrows on both surfaces. Notice that the field lines which correspond to epipolar planes map onto lines in their planar image. This is to be expected since the intersection of any two planes is generally a line.

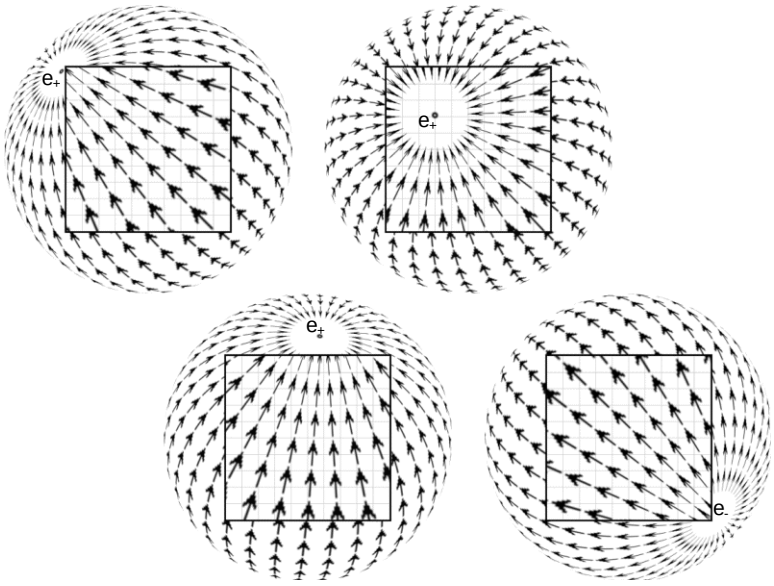

Figure 6-6: Occlusion-compatible traversals mapped onto planar viewing surfaces

In the following figure the enumeration directions are shown without the underlying spherical map. Isoparametric lines of the planar domain are also shown for each of the planar viewing surfaces.

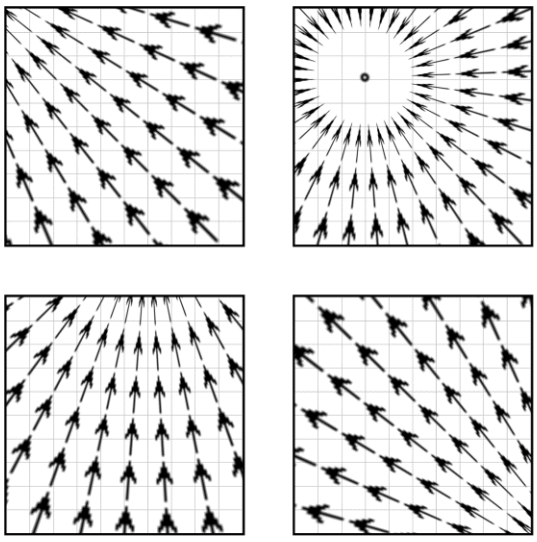

Figure 6-7: Occlusion-compatible planar traversal orders

Consider the relationship of these images to the visibility algorithm given in Chapter 3. The first step of the visibility algorithm is to compute the projection of the desired viewpoint onto the reference image. This projection is either the positive or negative epipole. Observe that one of these epipoles is the common intersection point of the vector field. An image's epipoles may fall outside of the projected image. Nonetheless, a valid enumeration order always

converges to the image of the positive epipole and diverges away from the negative epipole. There are only three possible configurations of the epipole relative to a planar viewing surface. The infinite extension of the viewing plane is intersected by either the positive or the negative epipole, or it is parallel to both. Therefore, the set of epipolar planes, whose spherical images correspond to the longitudinal lines of the sphere, will, on a planar viewing surface, map to a pencil of directed lines that either converge, diverge, or are parallel as determined by the positive epipole's relation to the plane. These three cases are illustrated below.

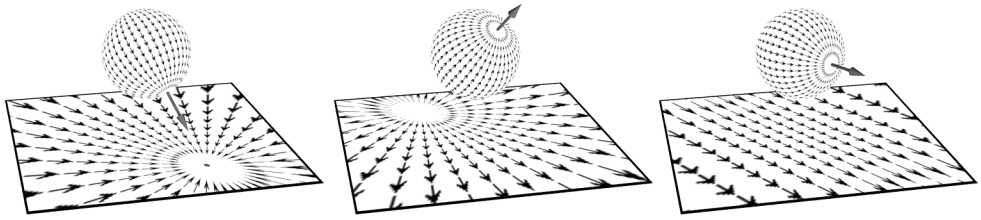

Figure 6-8: Spherical enumeration directions projected onto a plane

The second step of the visibility algorithm divides the viewing plane along the row and column defined by the coordinates of the epipole. If the epipole's coordinates fall within the planar image, this subdivision step partitions the viewing plane into four parts. When the epipolar planes converge or diverge, there exists exactly one epipolar plane that is parallel to the rows of the reference image. Likewise, there is exactly one epipolar plane parallel to the reference image's columns. These planes define the boundaries across which the enumeration direction's slope changes sign in the image's parameter space as illustrated below.

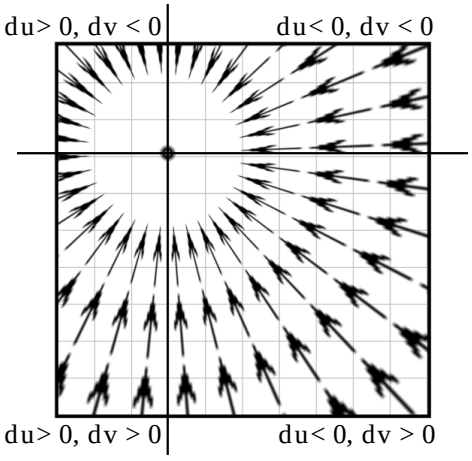

Figure 6-9: Subdivision of the image plane into four sheets

The various enumeration orders of the visibility algorithm can be derived by considering the signs of the directed lines' slopes in each subregion. If one coordinate of the epipole falls outside of the parameter domain, then the region is divided into two subregions. If both coordinates fall outside of the parameter domain, then all of the enumeration directions along the epipolar planes will have a common direction. This last condition corresponds to the single-sheet case of the algorithm.

The final step in mapping the spherical-viewing-surface algorithm onto a planar viewing plane is determining the order of enumeration. It is clear that points on the planar surface can be reprojected along the epipolar planes and that the result would be consistent with the spherical reprojection. This result would correspond to mapping the original planar image onto a spherical projected image with the same center-of-projection, and then reprojecting the result onto a new spherical frame. While this approach works, it is inconvenient since it involves extra mapping steps. These steps can be avoided if the enumeration order is specified in the planar parameter space. Next, I will show how enumeration along rows and columns of the viewing plane used in the visibility algorithm presented in Chapter 3 is equivalent to enumeration along the epipolar planes of the spherical viewing surface.

In the spherical case each longitudinal line, which corresponds to an epipolar plane, was considered independently. In the modified planar case I will consider several epipolar planes simultaneously. In the following figure a single subregion of the image plane is shown with two directed isoparametric lines overlaid.

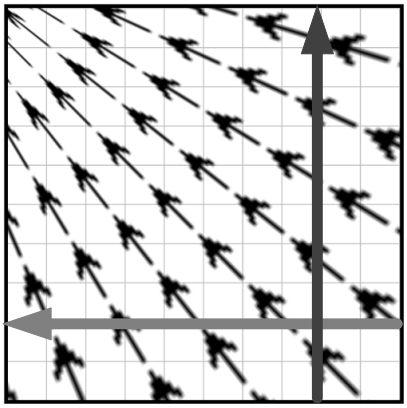

Figure 6-10: An equivalent enumeration along the rows and columns of a planar image

The overlaid vectors have the following properties. Each vector's direction is consistent with the spherical flow field's projection onto the corresponding parameter axis. This direction will be the same for all isoparametric lines in a given sheet since both components of the flow field's slope have a constant sign. A given isoparametric line will cross the projected image of each epipolar plane in the subregion exactly once. If a series of these isoparametric lines are enumerated in the direction of the flow field's remaining component, then the overall image of the spherical flow field is preserved. Furthermore, the relative ordering of the two parameters is arbitrary.

By Theorem 1, multiplicities are constrained to occur only within epipolar planes. The projected-spherical flow field is the image of these epipolar planes. If a series of isoparametric lines are mapped in the transverse direction in the order determined by the sheet's slope component, then each point along the epipolar plane will be reprojected in order of decreasing θ. This relative ordering is independent of the u or v parameter choice. Theorem 2 proves that such an ordering is occlusion compatible. Therefore, the resulting planar enumeration is equivalent to mapping the planar viewing surface onto a spherical viewing surface and performing the reprojection there. Thus, the planar algorithm given is also occlusion compatible.

The various partitions and enumeration orders of the planar visibility algorithm all arise from parameterization on a planar viewing surface. The choice of a desired center-of-projection determines both the subdivision boundaries as well as the number of sheets. The enumeration direction relative to the epipolar ray's image is determined by whether the image is of the positive or negative epipole.

Now I will consider the case where the projection plane is parallel to the epipole. Since the projections of all epipolar planes onto the planar viewing surface are parallel, these projections can be considered a special partitioning case in which there is only a single sheet. The parameterization still determines the enumeration order along isoparametric lines based on the slope of the flow field induced by the image of the spherical frames' lines of longitude. Even though both of the epipoles project to infinity on the planar viewing surface, the direction from the negative to the positive epipole is still well defined. The visibility algorithm will handle this case correctly.

6.4 Discussion

Special cases of the visibility algorithm presented in this paper have been developed by Anderson [Anderson82] and Adelson and Hodges [Adelson93b]. Anderson's hidden-line algorithm considered the case of height-fields rather than projective images. In a height-field the surface's range values are measured by their projection onto a basis vector that is orthogonal to the parameter-space dimensions. In a perspective-projected image range values are measured from the center-of-projection. A height-field is a useful representation for bivariate functions. It is also notable that Anderson's algorithm enumerates the surface in an order opposite of the presented algorithm. This requires a representation of the periphery of the surface being drawn. Anderson's painting rule, which requires that a surface can never overwrite a surface point which has already been written, is the opposite of maintaining only the last surface written at each point. Anderson's enumeration order has the advantage of never generating points that are subsequently overwritten. This is reasonable considering that his algorithm was developed for line-plotter applications where, unlike computer-graphics displays, once ink is drawn on the paper it cannot be satisfactorily overwritten. This reduction in the number of writes, however, comes at the cost of maintaining the auxiliary data structure representing the drawn surface's boundary. Depending on the implementation, the representation of the boundary buffer can itself introduce problems. If the extents of the boundaries are represented using a sampled representation, then quantization artifacts can introduce precision problems in future comparisons. If the boundary curves are represented explicitly as line segments, the storage requirement are potentially large.

Adelson and Hodges proposed a method for generating stereo pairs from a single planar ray-traced image by reprojecting the right eye's image to the left eye's view. The algorithm they describe is equivalent to the special case of the given visibility algorithm where the epipolar ray is both parallel to the view plane and is oriented along an isoparametric line of the planar projection. This unique geometry allows for the right eye's image to be generated by enumerating and reprojecting the left eye's image along all scan lines from left to right.

The given visibility algorithm can also be extended to other viewing surfaces by using the same procedure of mapping the problem from the original viewing surface to a spherical viewing surface, reprojecting it, and then mapping it back onto the original surface. The following figure shows this progression of mappings on a cylindrical viewing surface.

Once more the longitudinal lines of the spherical projection correspond to the projected images of the epipolar planes that are induced by a change in center-of-projection in the direction of the epipolar ray. Images of these epipolar planes can be mapped onto a cylindrical viewing surface that shares the same center-of-projection. The cylindrical projected surface can then be reprojected along these lines of longitude in an order progressing from the negative to the positive epipolar rays. The resulting enumeration would be equivalent to the spherical reprojection which has been proven to be occlusion compatible.

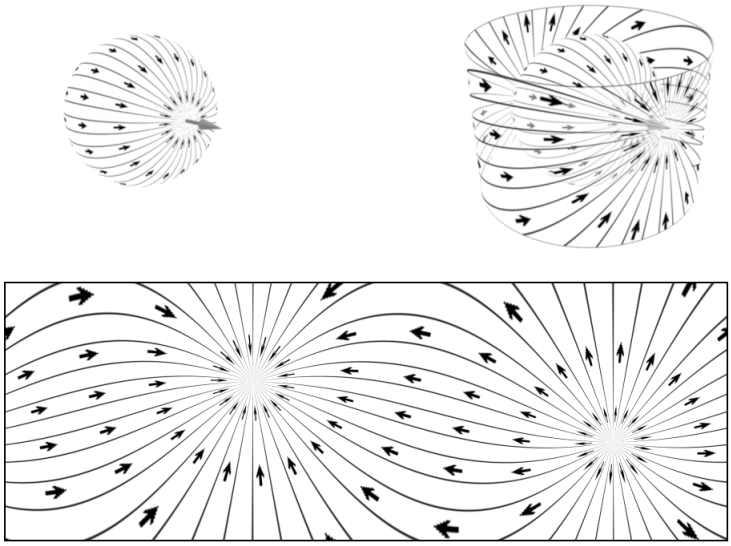

Figure 6-11: A mapping of epipolar planes onto a cylindrical viewing surface

Using the method outlined above, visibility algorithms can be established for any viewing surface that is topologically equivalent to a sphere (i.e., its range function is strictly single valued). While this is the case for all perspective-projected images, it does not easily extend to more general surface representations.

Chapter 7

COMPARING IMAGE-BASED AND GEOMETRIC METHODS

Despite the differences in scene representation, there are surprising similarities between the rendering methods used for geometry-based and image-based computer graphics. Many of these are a natural consequence of the common result shared by both approaches— an image. However, the parallels between the two methods extend much further. In this chapter I examine these two approaches side by side, with a focus on these similarities and differences.

There are tremendous advantages in leveraging the past twenty-five years of accumulated expertise in graphics architectures as a starting point for image-based systems. Recently, hardware architectures supporting geometry-based three-dimensional computer graphics have made the difficult transition from a highly specialized add-on for high-end computer systems to a commodity item for personal computers. In the near future there may be considerable interest in adapting these built-in graphics capabilities for use in image-based rendering. In the longer term the greatest potential for image-based computer graphics may lie in hybrid systems capable of merging both modeling approaches.

The success of geometry-based computer graphics has, to a large degree, resulted from breaking down the three-dimensional rendering problem into smaller manageable pieces. This modular approach provides an invaluable organization for the rather daunting list of chores required to convert a geometric specification into an image. It has also facilitated the application of parallelism in the design of graphics systems and has therefore played a significant role in enhancing performance.

While there is no single rendering approach used by all geometry-based computer graphics systems, most can be classified as either *primitive driven* or *display driven*. Primitive-driven methods traverse the list of scene elements, computing each primitive's contribution to the final image before proceeding to the next element. A display-driven approach progresses

through all of the sample points of the output image seeking those scene elements that determine the sample's value. Either of these techniques is applicable to the image-based computer graphics method described here. The next two sections discuss these distinct approaches and give analogous image-based methods.

7.1 The Image-Based Graphics Pipeline

In the primitive-driven approach to geometric computer graphics, model elements are processed sequentially and, to a large extent, independently as they are converted from their three-dimensional definitions into a sampled two-dimensional image. This transformation takes place in several steps. The geometric elements are first tessellated into planar facets. Then, the facets are transformed from the canonical modeling coordinate system of the geometric primitive to the desired scene position. The color of the facet can be resolved once its position relative to the viewing point and the illumination sources is known. If some part of the facet lies within the field-of-view of a simulated camera, the three-dimensional coordinates of the facet's vertices can be projected onto the simulated camera's viewing plane. With the image-space coordinates of the facet's vertices known, an image is computed by sampling the interior of the facet at integer grid points. This list of operations makes up the standard graphics pipeline, as illustrated below[Foley90].

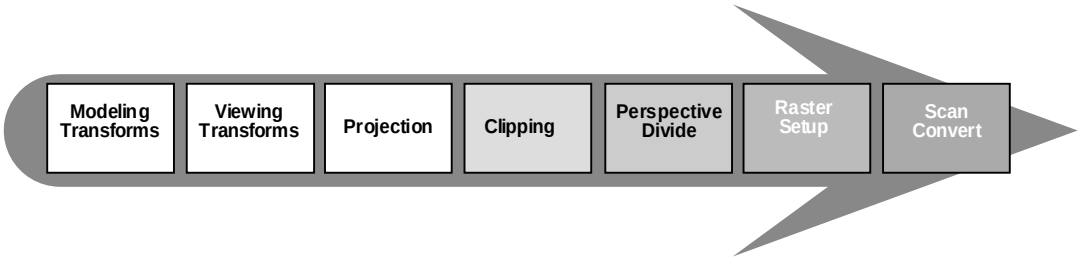

Figure 7-1: Standard geometry-based graphics pipeline

The first stages of the graphics pipeline process geometric primitives. The operations performed at these stages are primarily three-dimensional coordinate transformations that map canonical geometric models to desired positions. The latter stages of the graphics pipeline operate on image-space quantities. It is at this point that the minimal representation of the geometry given by its vertex coordinates is converted into image-space samples representing actual three-dimensional points.

The warping phase of the image-based rendering method bears a close resemblance to a three-dimensional transformation. In fact the standard 4×4 matrix multiplier of the graphics pipeline could be used to compute the linear terms of the image warp given in Equation 3-16 as follows:

$$\begin{bmatrix} x \\ y \\ 1 \\ w \end{bmatrix} = \begin{bmatrix} w_{11} & w_{12} & w_{14} & w_{13} \\ w_{21} & w_{22} & w_{24} & w_{23} \\ 0 & 0 & 0 & 1 \\ w_{31} & w_{32} & w_{34} & w_{33} \end{bmatrix} \begin{bmatrix} u_1 \\ v_1 \\ \delta(u_1, v_1) \\ 1 \end{bmatrix}$$

Equation 7-1: Using a 4×4 matrix multiplier to compute the image warp

The use of a matrix multiplier would not, however, take advantage of the coherence available due to the sequential processing of reference image coordinates. In general only the third column of the matrix needs to be computed for each pixel. The remaining terms can be replaced with additions using the method of forward differences.

Following the linear-expression computations, an image-based rendering system would test whether the *w* component of the transformed image point is positive, indicating that it is in front of the pinhole camera. Once this is established, the remaining terms can be tested to see if they fall into the valid range of image coordinates.

$$0 \geq x > w \times width \quad \text{and} \quad 0 \geq y > w \times height$$

Equation 7-2: Image-based view port clipping

This series of tests is reminiscent of the clipping step in the traditional geometry-based pipeline.

The next stage of the image-based rendering approach divides both the *x* and *y* components by *w*, just like in the projection stage of the geometry-based approach. The final reconstruction and resampling processes of the image-based method are comparable to the rasterization phase of the graphics pipeline. Standard rasterization hardware might even be used to approximate the bilinear surface reconstructed when a C^0 polynomial basis is used[30].

Thus, a graphics pipeline can be defined for the image-based approach to computer graphics as illustrated below.

[30] This is only an approximation since a bilinear surface is not planar.

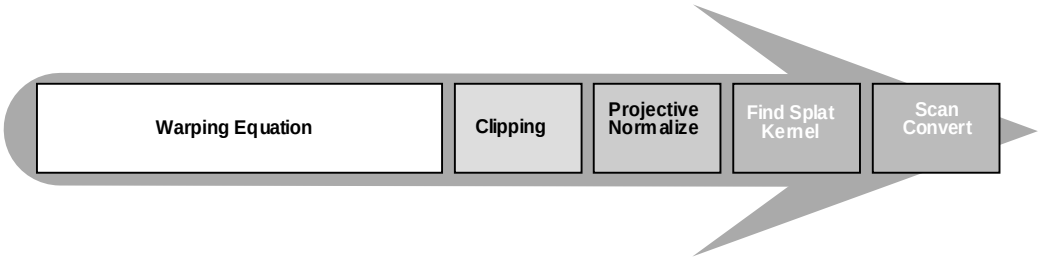

Figure 7-2: A image-based graphics pipeline

In the geometry-based graphics pipeline, visibility is usually determined at one of two stages. Either the geometric primitives are presorted according to their distance from the viewing position prior to the viewing transformation, or visibility is resolved on a sample-by-sample basis during the rasterization process using the z-buffer algorithm.

The benefits of presorting-visibility methods are that they can take advantage of fast sorting algorithms, they can be computed incrementally for animated sequences, and the visibility solution is computed at a relatively high level of geometric representation. However, a strict depth ordering on the basis of objects is difficult to define when scene elements interpenetrate. Solving this problem usually requires significant geometric processing, including the subdivision of scene elements. In general, presorting methods for computing visibility are only considered for scenes with very few surfaces.

On the other hand, the z-buffer method for computing visibility generally works for any configuration of objects because it considers geometry at the low level of points. Thus, the z-buffering algorithm is tightly coupled with the sampling process. The major disadvantages of the z-buffer method result from breakdowns in the underlying assumptions made during the sampling process. For instance, most z-buffering algorithms consider the entire sampling region to be represented by a single depth value. Yet, it is possible that several actual surfaces at various depths might be represented within a sampling region. This is particularly noticeable along object silhouettes and along curves where surfaces interpenetrate. Z-buffering methods are the most common method used for resolving visibility in scenes composed of a large number of surface elements.

The image-based method of resolving visibility most closely resembles the geometry-based presorting approach. However, in the image-based case, this sorting is trivially computed

since it can be determined without any geometric knowledge of the elements being rendered. The resulting drawing order of the reference image is simply a function of the pinhole camera model and the change in the center-of-projection between the reference and desired images. Furthermore, the scene representation used in image-based rendering does not allow interpenetrating scene elements. Thus, both the computational expense of computing an object ordering and the special case handling of the geometry-based representation are absent from the image-based approach.

7.2 An Inverse-Mapped Approach to Image-Based Rendering

The classical display-driven approach to geometry-based computer graphics is the ray-casting method described by Appel [Appel67] and enhanced by Whitted [Whitted80]. From the standpoint of a system architecture, the identification of distinct processing steps in the display-driven computer graphics approach is not nearly as developed as in the primitive-driven approach. Most systems, however, share the common algorithmic structure shown in Figure 7-3.

A significant step in the display-driven approach to geometry-based computer graphics is the mapping of a pixel coordinate to a three-dimensional ray. This ray is used in the geometric calculations necessary for determining the visible scene primitives. A similar step can be identified for the image-based approach. The fundamental matrix relating points in the desired image to lines in the reference image can be determined using either pinhole camera parameters (i.e., by taking the transpose of Equation 5-10, $\mathbf{F}_{21} = (skew(\mathbf{P}_2^{-1}(\dot{C}_1 - \dot{C}_2))\mathbf{P}_2^{-1}\mathbf{P}_1)^T$), or by using image correspondences and Hartley's method [Hartley95a] as discussed in Chapter 5. Alternatively, the nonlinear methods of Luong [Luong93b] could be used.

```
1)  foreach pixel of the desired image
2)      determine the ray specified by the pixel
3)      set distance  to closest intersection = large value
4)      set visible point = background
5)      foreach scene primitive
6)          if the ray intersects the primitive then
7)              compute distance along ray of intersection
8)              if distance to intersection < closest  and
9)                 distance to intersection > 0 then
10)                set visible point = point of intersection
11)                set closest = distance
12)             endif
13)         endif
14)     endfor
15)     Illuminate visible point
16)     set pixel = intensity of illumination at point
17) endfor
```

Figure 7-3: Algorithm for a display-driven rendering approach

The product of a fundamental matrix with a desired pixel coordinate gives the equation of a line through the reference image, as illustrated below.

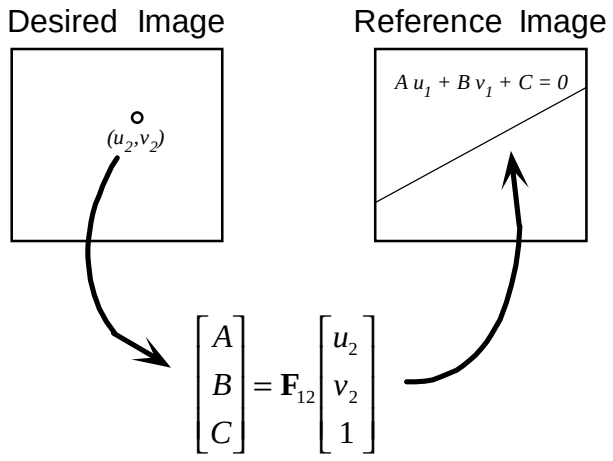

Figure 7-4: Projection of a desired ray onto a reference image

This line is the projection onto the reference image of the ray emerging from the desired image's center-of-projection and passing through the identified point.

The precise segment along this line can be computed by examining the limits of the warping equation given in Equation 3-10[31]. The maximum image-space extent along the ray corresponds to the case when the generalized disparity value approaches zero since generalized disparity is inversely related to range. Thus,

$$ {}_{\infty}\bar{x} = \mathbf{P}_1^{-1}\mathbf{P}_2\bar{x}_2 $$

Equation 7-3: Maximum extent of epipolar line segment

Similarly, the minimum extent along the line segment occurs when the generalized disparity value approaches infinity. The coordinate of this point in the reference image is given by

$$ {}_{0}\bar{x} = \mathbf{P}_1^{-1}(\dot{C}_2 - \dot{C}_1) $$

Equation 7-4: Minimum extent of epipolar line segment

The coordinate of the minimum extent is independent of the selected sampling point from the desired image. This point is the epipole of the desired image as seen by the reference. In other words it is the projection onto the reference image of the desired image's center-of-projection. The identification of the ray's extents is analogous to setting the maximum ray distance in Step 3 of the ray-tracing algorithm and testing for the positive ray length in Step 9. This process is shown in the following figure.

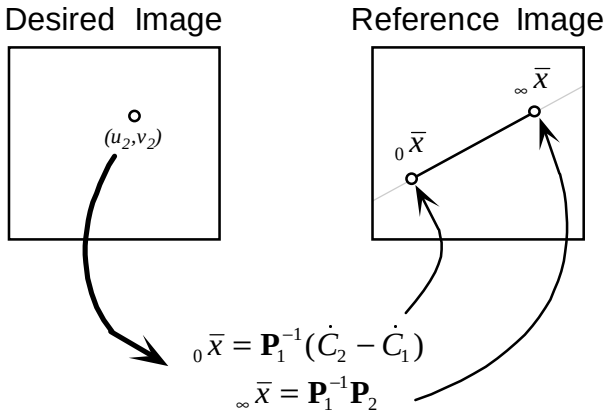

[31] In order to preserve the notions of the reference image and the desired image in this case, the sense of the warping equation is inverted.

Figure 7-5: Endpoints of a ray in a reference image

Either or both of the ray's endpoints might lie outside of the reference image's coordinate range. Furthermore, the sign of the third component of the two endpoints, ${}_0\bar{x} = [{}_0x_1, {}_0x_2, {}_0x_3]^T$ and ${}_\infty\bar{x} = [{}_\infty x_1, {}_\infty x_2, {}_\infty x_3]^T$, must be examined in order to properly determine the ray's direction of propagation within the image. The following cases can occur:

1) If both ${}_0x_3$ and ${}_\infty x_3$ are positive, the desired center-of-projection falls in front of the reference image, and the ray intersects an extended image plane[32] propagating from ${}_0\bar{x}$ to ${}_\infty\bar{x}$. The valid extent of the epipolar line is the segment connecting ${}_0\bar{x}$ to ${}_\infty\bar{x}$ in the reference image.

2) If ${}_0x_3$ is positive and ${}_\infty x_3$ is negative, the desired center-of-projection also falls in front of the reference image, but the ray does not intersect an extended image plane. In this case the ray propagates from ${}_0\bar{x}$ to a point out of view. The valid extent of the epipolar line is the half-line from ${}_0\bar{x}$ in the direction opposite of ${}_\infty\bar{x}$.

3) If ${}_0x_3$ is negative and ${}_\infty x_3$ is positive, the desired center-of-projection lies behind the reference image, and the ray intersects the extended image plane. In this case the ray propagates from some point out of view to ${}_\infty\bar{x}$. The valid extent of the epipolar line is the half-line ending at ${}_\infty\bar{x}$ in the direction opposite ${}_0\bar{x}$.

4) If both ${}_0x_3$ and ${}_\infty x_3$ are negative, the desired center-of-projection lies behind the reference image, and the ray does not intersect the extended image plane. All such rays can be ignored since no point visible in the reference image falls along their extent.

The intersection of the projected ray's valid extent with the segment of the epipolar line visible within the image gives the actual ray's extent within the reference image.

Having identified two points on an epipolar line in the reference image, ${}_0\bar{x}$ and ${}_\infty\bar{x}$, we can always find any other point on the line by

[32] The extended image plane is an unbounded plane that is both parallel to the actual viewing plane and an infinite distance from the origin. Exactly half of the rays emerging from any point intersect a given extended plane.

$$\bar{p}(t) = {}_0\bar{x}t + {}_\infty\bar{x}(1-t)$$

Equation 7-5: A parametric form of a line

where the parameter t is allowed to vary from -∞ to +∞. This represents the points on the line as a linear combination of the two endpoints. If we substitute $t = \frac{\tau}{1+\tau}$, the following alternative representation results:

$$\bar{p}(\tau) = {}_0\bar{x}\frac{\tau}{1+\tau} + {}_\infty\bar{x}\frac{1}{1+\tau}$$

Equation 7-6: The tau form of a line

The new interpolation variable, τ, is consistent with the generalized disparity values $\delta(\bar{x}_1)$ at the two extremes (i.e., when $\tau = \delta(\bar{x}_1) = 0$ then $\bar{p}(0) = {}_\infty\bar{x}$, and when $\tau = \delta(\bar{x}_1) = \infty$ then $\bar{p}(\infty) = {}_0\bar{x}$). Therefore, if the reference image point ${}_\infty\bar{x}$ is visible at our desired image point, it is must have a disparity value of 0. Likewise, for the reference image point ${}_0\bar{x}$ to be visible at our desired image point, it is must have a disparity value of +∞. The necessary value of $\delta(\bar{p}(\tau))$ can be found for all points on the line by first solving either expression in Equation 3-Z for $\delta(u,v)$.

$$\delta(u_1, v_1) = \frac{w_{11}u_1 + w_{12}v_1 + w_{13} - u_2(w_{31}u_1 + w_{32}v_1 + w_{33})}{w_{34}u_2 - w_{14}}$$

$$\delta(u_1, v_1) = \frac{w_{21}u_1 + w_{22}v_1 + w_{23} - v_2(w_{31}u_1 + w_{32}v_1 + w_{33})}{w_{34}v_2 - w_{24}}$$

Equation 7-7: Disparity required to map a reference point to a desired point

Then, solve Equation 7-6 for τ.

$$\tau(u_1, v_1) = \frac{w_{34}(w_{11}u_1 + w_{12}v_1 + w_{13} - u_2(w_{31}u_1 + w_{32}v_1 + w_{33}))}{(w_{34}u_2 - w_{14})(w_{31}u_1 + w_{32}v_1 + w_{33})}$$

$$\tau(u_1, v_1) = \frac{w_{34}(w_{21}u_1 + w_{22}v_1 + w_{23} - v_2(w_{31}u_1 + w_{32}v_1 + w_{33}))}{(w_{34}v_2 - w_{24})(w_{31}u_1 + w_{32}v_1 + w_{33})}$$

Equation 7-8: Theta value at a point on the ray's extent

Clearly, the relationship of $\delta(u,v)$ to τ is

$$\delta(u_1, v_1) = \frac{\tau(u_1, v_1)(w_{31}u_1 + w_{32}v_1 + w_{33})}{w_{34}}$$

Equation 7-9: Minimum disparity required for a given tau value

Therefore, given any point on the actual ray's extent within a reference image, the value of τ for that point can be computed using either expression of Equation 7-8. For the best results, the first expression should be used when the epipolar line's slope has an absolute value less than 1, and the second expression should be used otherwise. The value of the generalized disparity which would make this same point visible along the ray is given by solving Equation 7-9 with the value of τ computed for the point. The full desired image can be computed as follows:

```
1)  foreach pixel of the desired image
2)      compute the epipolar line in reference image
3)      determine the projected ray's actual extent
4)          foreach point along the propagation direction
5)              find τ at point
6)              find δ needed to see point
7)              if (δ at point) ≥ δ needed
8)                  break;
9)          endfor
10)     set pixel = intensity at point
11) endfor
```

Figure 7-6: Display-driven image-based rendering

Determining the generalized disparity value (Step 7) and the intensity value (Step 10) at an arbitrary point in the reference image requires interpolation. This algorithm is analogous to the ray-tracing algorithm given in Figure 7-6. It has an advantage over geometry-based ray-tracing in that it traverses only a small fraction of the potentially visible points for a given ray. It also traverses the reference image in such a way that the first intersection found is guaranteed to represent the closest point.

7.3 Discussion

There are significant parallels between the rendering algorithms used for geometry-based computer graphics and image-based computer graphics. In this chapter I have shown an image-based rendering approach that has many similarities to the traditional three-dimensional rendering pipeline. Likewise, I described an image-based approach that is similar to ray tracing.

In both cases when analogous functions were compared side-by-side, the image-based approach was generally found to require fewer operations. Thus, as the number of geometric primitives used to describe a scene approaches the number of pixels represented in an image of that scene, we might expect that an image-based approach will outperform a geometry-based approach.

Chapter 8

CONCLUSIONS AND FUTURE WORK

The notion of a *model* is one of the most important concepts in computer graphics. It is the job of a model to capture the essence of the concrete entity that it represents. While it is important that a model remain true to the original, it is even more significant for a model to be both simple and elegant. Geometric models are a perfect example of this assertion. We are taught early on that geometry is but an abstraction. In our world, there are no dimensionless points, no infinitely long and immeasurably thin lines, and no perfectly flat planes. Yet, we have chosen geometry, with its simplicity and elegance, to represent those models that we hope to visualize.

In the formative stages of computer graphics, the choice of geometric models was indeed a clever optimization, because it allowed an uncountable number of surface points to be specified using only a compact list of coordinates. But, as the field of computer graphics advances, we are witnessing the erosion of this economy. Most practitioners would agree that we are rapidly approaching the day when scenes composed of multiple millions of primitives will be commonplace. In fact, one proposed measure of scene complexity is the ratio of modeling primitives to the number of pixels rendered. In view of this, one might question the logic of using three points to enclose a region of space whose projection is less than one pixel.

There are, however, other ways to represent objects for the purposes of visualization. Images are particularly appealing because their visual source helps to form our expectation. Most of us would agree that an image captures, from a single viewpoint, the visual essence of a scene. Thus, all that is required is a method for transforming this essence to new viewpoints. This research has presented just such a method.

8.1 Synopsis

In this thesis, I have contributed methods for transforming an image of a scene captured from one point to an approximation of the scene as it would be viewed from some other point. I have provided a framework for defining this approximation in the form of a plenoptic function. I discussed a method for determining which of the transformed points would be visible in the final image, along with techniques for representing a continuum of points when given only a set of samples. Then, the notion of a camera was explored, and I explained how these rendering techniques could be easily adapted to camera models which were either more flexible or more realistic than the original planar-pinhole camera. The relationship of the rendering method to the camera's geometry was then explored, and I found that, in some cases, very little geometric knowledge is required to synthesize reasonable images from others. Finally, the similarities between geometry-based and image-based computer graphic systems were investigated. At the system level many parallels between the two methods became apparent, and it was found that image-based techniques often surpass the geometric methods. This is particularly true when the number of primitives is comparable to the number of pixels in a reference image.

In the remainder of this chapter, I will concentrate on the specific advantages and disadvantages of the image-based computer graphics approach presented here. I will then cover limitations of the proposed methods. Finally, a wide range of open problems suitable for future research are presented.

8.1.1 Advantages of image-based computer graphics

Overall performance of geometry-based computer graphics systems continues to depend on the number elements composing a scene. Techniques for avoiding the unnecessary processing of scene primitives that are either occluded or outside a desired image's field-of-view are an active area of research in geometry-based computer graphics. These techniques are particularly useful in scenes with significant depth complexity. On the other hand, an image, by definition, represents only a visible subset of a scene and has a depth complexity of exactly one. For viewing positions nearby an image's center-of-projection, it is reasonable to expect that there will be only moderate changes in the visible scene elements.

The performance of an ideal image-based computer graphics system would be proportional to number of pixels rendered rather than the number of primitives used in the representation. In the forward-mapping case of image-based rendering, the computation

required is actually proportional to the number of reference image pixels used by the image warp. When the resolution of the reference image is comparable to the desired image, and the viewing positions are suitably close, then the performance is nearly ideal. However, the performance of the forward mapping case cannot be considered independent of the model's representation, since surely we must consider the samples of a reference image as modeling primitives. So, in the case of a forward-mapping image-based system, the primary performance advantage results from the visibility preprocessing inherent in the image representation.

An inverse-mapping image-based system, though, can nearly approximate the performance of an ideal system. Consider a reference image sampled at $R \times R$ resolution, and a desired image with resolution of $D \times D$. The computation required in the naïve algorithm explained in Chapter 7 is proportional to $D^2 \alpha R$, where D^2 is the number of pixels in the image and α is a constant that is generally less than one[33]. If a simple pyramid representation is used for the reference image, it appears possible that this performance can be made proportional to $D^2 \log(\alpha R)$. Additionally, the pyramid might be used to address aliasing problems that are common to display-driven methods.

Another computational advantage of image-based computer graphics methods is derived from the spatial coherence of images. Many of the calculations involved in image warping can be made incremental by using forward-difference techniques, since the underlying representation is regular when compared to the nearly random configurations that geometric primitives assume. A good example is the coordinate transformation used in both cases discussed in Chapter 7. A geometry-based system uses a 4×4 matrix transformation to realize a mapping of a three-dimensional point to an image-space coordinate (requiring at least 12 multiplies and 12 additions for the transform, plus 1 divide and 3 more multiplies for the projective normalization). All of these operations are required because any point might occur during the mapping. In contrast, the analogous mapping of two-dimensional reference image points to image-space coordinates described in Chapter 3 requires, in the general case[34], only 5 multiplies, 6 additions, and 1 divide. If we assume that three-dimensional triangles specified by three vertices are used as primitives, then each will require 3×(15 multiplies + 12 adds + 1 division) operations per rendered pixel compared to the (5 multiplies + 6 adds + 1 division)

---

[33] This assumes that some fraction of the projected ray's extent will be clipped. In the case of a stereo camera configuration (Chapter 3) α will exactly equal one. Note that it is also likely that a given ray will terminate early, thus further reducing the constant α.

[34] Ignoring initial set up.

operations required for the image-based case[35]. Thus, even ignoring the advantage of a reduced depth complexity, an image-based approach should outperform a geometry-based system when each primitive contributes fewer than 3 pixels to the final rendered image.

A final advantage of image-based rendering is that photorealism is achieved with no additional operations, since the photometric properties of a scene are determined entirely by pre-computed values of the reference images (The inability of image-based systems to properly represent view-dependent illumination artifacts, such as specular reflection, will be discussed in the future work section). In modern geometry-based systems, the computational effort dedicated to shading overshadows the geometric computations. In an image-based system, shading can be considered as a preprocess that has no effect on the interactive performance. This is similar to radiosity methods that are commonly used for geometry-based techniques. However, radiosity methods will generally involve significantly more computation than image acquisition.

8.1.2 Disadvantages of image-based computer graphics

In this section I will discuss many of the inherent drawbacks of the image-based approach when compared with geometric methods. Other shortcomings are also identified and considered in the future work section. However, I consider the problems discussed here nearly insurmountable without major revisions in the approach.

Image-based models are non-metric representations; thus, while they are well suited for the purpose of visualization, they not particularly useful as computational models. The fundamental difficulty of this problem has long vexed the computer vision community. The central goal of the classic structure-from-images problem has been to extract a model whose validity is then judged against the standard of an abstract geometric representation[36]. My approach, admittedly, uses many results that are generally well known among computer vision researchers. However, it is my application of these results to the problem of mapping images to images, rather than attempting to extract geometric models, that distinguishes my work. The significance of a centimeter's accuracy when either *visualizing* or *analyzing* a scene strongly depends on where that centimeter falls relative to the viewer's pose. This dependence,

---

[35] The advantage of the image-based case increases if the reference pixel projects to more than one pixel.

[36] Like those used in traditional three-dimensional computer graphics.

however, is lost when accuracy is defined in terms of Euclidean measurements, rather than in terms of the projective domain where the visualizations and the analyses occur.

Throughout this presentation I have ignored the temporal dimension of the plenoptic function. The cost of considering time is particularly significant because it adds an entire dimension to the plenoptic representation. Unfortunately, since this dimension is not geometric, it is difficult to tailor the approximation process in terms of geometric constraints as was done in the static geometry case. In contrast, it is relatively simple to define temporal behaviors for geometric models. In the absence of some significant innovation it seems that image-based methods are doomed to treat the time dimension as a database query problem.

Another disadvantage of using images as a representation for three-dimensional computer graphics is that, unlike geometry, images constrain where a scene can be viewed from. This problem is related to the lack of a metric representation, mentioned previously, but it also encompasses the issue of visibility. An image does not represent points that cannot be seen, and visible points are not represented equally. In contrast, a geometric representation of a rotationally symmetric closed object represents more invisible points than visible ones[37]. Furthermore, unless some view-dependent simplification method is used, all the points of a geometric model are represented with comparable accuracy. These shortcomings appear to be intrinsic to the image format.

8.1.3 Limitations of image-based methods

In this section I will discuss some of the limitations of image-based computer graphics methods that arise in practice. Several aspects of the image-based approach, while theoretically correct, suffer from sensitivities to errant inputs and singularities under certain geometric configurations.

The image-synthesis methods discussed here depend on a generalized disparity defined at every point on the image plane. While it is possible to obtain this disparity information from correspondence information between images, the automated extraction of such correspondence information is well known to be a difficult problem. An ideal system must also be able to automatically determine this exact correspondence information. In practice the resolution

[37] Due to perspective projection, generally, more than half of a closed surface will be obscured by the remainder.

obtainable is limited by the sampling densities of the source images. Some of these problems can be overcome with the appropriate technologies. For instance, the ambiguity problems of the general correspondence problem can be minimized using structured light [Besl89]; the recovery of disparities in occluded image regions can be overcome by considering multiple images [Bolles87]; and approximate geometric models can be used to guide the correspondence process [Debevec96]. The image-based approach is not bound to any particular method for establishing correspondence, and therefore, it is well suited for hybrid combinations of methods. The apparent quality of a scene's representation is closely related to the accuracy of the disparity information available. The quest for the accurate disparity information used in image-based representations is akin to the difficulty of acquiring accurate three-dimensional geometric models. Both problems have shown potential for automated solutions, but in practice, the intervention of a human is generally required before satisfactory results can be attained.

The image-based approaches described are also subject to certain numerical computation problems when confronted with noisy data. Most of these problems occur when extracting information from sampled images. The computation of the fundamental matrix, as described in Chapter 5, is known to be susceptible to noise [Luong93b]. It is also known that there exist particular non-generic configurations of image points in which the solution is singular [Torr95]. A similar situation occurs when solving the same-camera constraints. The best approach to dealing with the singular configurations is to overspecify the system and use a least-squares approach. This has the combined benefits of reducing the effects of noise, in the case where it is uniformly distributed, and reducing the probability that a singular configuration of points will arise. Unfortunately, an overspecification requires additional correspondence information.

8.2 Future work

In this last section I will discuss future research directions and potential derivations from the work presented in this thesis.

8.2.1 Sampling an environment

A principled approach for selecting a set of reference images is desperately needed. In my opinion, there are at least three avenues worthy of exploration. The first approach would involve searching for a *global solution* that attempts to assure that every point in a scene is well represented. Such an approach might also consider external constraints on potential viewing positions. For example, consider a game where the user is not allowed to crawl on the floor to

look at the undersides of furniture. Such a priori information might considerably reduce the size of the image set needed to represent a scene. A second approach might focus on a *local solution* that assures that some specific object or region of interest is well represented. This approach appears to be closely related to the specification of an aspect graph [Plantinga90]. A third potentially useful approach involves determining incremental solutions. Such an approach can be summarized as follows: given N reference images, what single additional image would most increase the usefulness of the model? This last approach appears similar to the way that a human might approach the problem.

8.2.2 Reconstruction and resampling

Another interesting area for future research involves enhancing the reconstruction of a continuous image representation prior to the resampling of the desired image, as discussed in Chapter 3. One simple improvement would be to incorporate higher degrees of continuity (estimates of the tangent space and curvatures at each point).

Another approach to this problem would be to devise a family of basis functions that allows for varying degrees of connectivity throughout the image, permitting the selective use of sparse (Gaussian-like) and dense (Polynomial-like) representations at various image regions. Such an approach might be similar to the regularization techniques suggested by [Grimson81] and [Terzopolous84]. These techniques employ multiconstraint optimizations to minimize some energy function that is expressed as a weighted sum of different penalty and stabilizing forces. Anisotropic diffusion models might also be applied to the reconstruction problem where the local diffusion coefficient might be based on some estimate of a given point's connectivity to its surrounding neighborhood [Perona90] [Whitaker93].

8.2.3 Incorporating information from multiple reference images

In the ideal image-based computer graphics system, information missing from a warped image would be filled in by warping some fraction of another image. The difficulty lies in identifying what reference-image subregion will supply the missing data without actually warping the entire reference image. Some preliminary work has been done by [Mark97] who has found effective clipping algorithms that minimize the cost of subsequent warps. Also, the inverse-mapping approach that is currently being explored by me and Bishop shows particular promise in this area. The primary difficulty is to establish a good confidence estimate for any reconstructed point. The confidence estimate in Mark's approach requires additional geometric information beyond a purely image-based representation. The method used in the inverse-

mapping case estimates the disparity gradient at each pixel to establish the confidence in a given reconstruction. It is easy to construct examples where this measure is invalid (i.e., when actual surfaces are nearly tangent to the visual ray). However, most of these errors result in a false negative. Thus, there is still hope that a better reconstruction might be found in another reference image if the surface is represented redundantly.

8.2.4 Image-based computer graphics systems

Identifying how systems might be built specifically for rendering image-based computer graphics, or how existing geometry-based systems might be augmented to support image-based methods is another interesting area for future research. An ideal system would need access to a large database of reference images. Interesting problems include strategies for accessing and caching images. Alternatively, image-based methods might be best served by accessing and caching rays. Developing specialized hardware architectures for use in image warping and reconstruction is one more promising area for additional research. Furthermore, there is significant potential for parallelism when warping since only the image points on the same epipolar line can possibly interact.

8.2.5 View dependence

The image-based computer graphics methods described in this thesis map the photometric observations from one viewing position to any other viewing position. However, the intensity of light reflected from a surface point generally varies according to the direction of observation. This view-dependent distribution of the outgoing light that is reflected from a surface is called a surface's *radiance function*. The approach taken in this research makes the assumption that the radiance function of all surfaces is well represented by a uniform distribution over the hemisphere surrounding a point. Such a surface model is called an ideal Lambertian reflector.

It might be possible, however, to incorporate a surface's radiance function into the plenoptic model. Furthermore, it appears likely that such an extension might be accomplished with only slight modifications of the plenoptic function's representation. Consider the following: the subspace of a plenoptic function defined at any point in space describes the set of impinging rays, whereas the radiance function describes the rays emanating from a point. Both functions can be parameterized using two angles to indicate each ray's direction. Moreover, the useful regions of the plenoptic function, for the purpose of visualization, are the empty points of the represented environment. In contrast, a radiance function is only defined at occupied points

within the space (assuming that there is no participating medium such as smoke). Consequently, there is no practical overlap of these two functions. Therefore, any general representation of a plenoptic (radiance) function can be potentially extended to incorporate radiance (plenoptic) information without increasing the dimension of the representation. It also seems likely that an interpolation method could be developed to incorporate information from both function types.

An alternative approach for incorporating view-dependent effects into an image-based computer graphics system involves replacing the photometric values of a reference image with a complete material specification. Such an approach might use the warping equation to map reference image points to their position in the desired image, while deferring the shading calculations until the final visibility is resolved. The primary difficulty of this type of approach appears to be the acquisition of suitable models.

8.2.6 Plenoptic approximation methods other than warping

Image warping is just one possible approach for reconstructing a plenoptic function from a series of images. Other researchers [Levoy96] [Gortler96] have suggested alternatives that depend largely upon queries to a database of rays in order to reconstruct the desired images. The disadvantage of the warping approach is that it requires the image to be augmented with additional information that represents the projective structure of the actual points within the space. The database approach, on the other hand, is data intensive. It has been argued that there is tremendous potential for compression in the database approach. I would suggest that this potential is maximized only when the algorithm used for the compression is cognizant of the geometric structure of the scene being represented. This leads back to a more image-warping-like approach. It also seems likely that a hybrid of the warping and database systems could be built to take advantage of each approach's strengths.

There may also be tremendous potential in exploring alternate interpolation bases for the plenoptic reconstruction problem. Since the function is naturally represented as a field of spherical subspaces, a spherical wavelet representation appears to be a particularly promising area for future exploration.

Appendix A

NONGENERIC FORMS OF THE FUNDAMENTAL MATRIX

Usually a fundamental matrix can be described using Equation 5-5. However, there exist nongeneric camera configurations that cannot be expressed in this form. These exceptional cases correspond to having at least one of the two image planes parallel to the line connecting the centers-of-projection. This condition can be recognized when the determinant of the upper submatrix is zero ($f_{11} f_{22} - f_{12} f_{21} = 0$). In real-world applications, it is unlikely that such configurations will occur. These exceptional cases are presented here primarily for completeness and so that suitable tests for detecting these configurations can be identified[38].

In the general case of a fundamental matrix, the epipoles of each image have a proper projection onto the other image. Such epipoles are considered *finite*, and their homogeneous representations can be projectively normalized. In the exceptional cases of the fundamental matrix, one or both of the epipoles are *infinite.* Thus, they are represented by a projective vector with a zero-valued projective component. These points lie on the so-called *line at infinity* defined for the projective plane. When these points are interpreted using the *planar* or *flat* model of projective space, they are considered as pure directions rather than actual points [Coxeter74] [Stofi91]. The implication of such configurations on the epipolar geometry is that the rays from one center-of-projection project onto the other image as parallel lines. The slope of these lines is given by the ratio of the two nonzero projective coordinates, and, in the projective sense, they are considered to intersect at infinity.

The first parameterization for a nongeneric fundamental matrix considers the case when only one of the two epipoles is infinite and the f_{11} element is non-zero. The canonical form of this

[38] It should also be noted that the nongeneric epipolar geometries described by the special forms of the fundamental matrix are artifacts of a planar viewing surface. Most of these cases are eliminated, and certainly less likely to occur, when a panoramic viewing surface is considered.

representation assumes that the fundamental matrix has been scaled so that its f_{11} element is one. The following six-parameter model results:

$$F_{2\tilde{1}}\left(\begin{bmatrix} e_{1u} \\ e_{1v} \\ 0 \end{bmatrix}, \begin{bmatrix} e_{2u} \\ e_{2v} \\ 1 \end{bmatrix}, q, r, s\right) = \begin{bmatrix} 1 & 0 \\ 0 & 1 \\ -e_{2u} & -e_{2v} \end{bmatrix} \begin{bmatrix} 1 & \frac{-e_{1u}}{e_{1v}} & q \\ r & \frac{-be_{1u}}{e_{1v}} & s \end{bmatrix}$$

Equation A-1: Model for a fundamental matrix with one finite and one infinite epipole

The curved circumflex symbol indicates which image-space contains the infinite epipole. The case of a single infinite epipole in the first image with epipolar lines having a nonzero slope is indicated when $f_{11}f_{22} - f_{12}f_{21} = 0$ and $f_{21}f_{32} - f_{22}f_{31} = 0$[39]. An infinite epipole in the second image that also has epipolar lines with a nonzero slope is indicated when the same set of conditions occurs in the fundamental matrix's transpose. Equation A-1 describes a six-dimensional subspace of linear transforms because any scalar multiple of the infinite epipole will result in the same fundamental matrix. This is consistent with a geometric interpretation of an infinite epipole as a pure direction, which can be specified by a single angle.

A five-parameter model of the fundamental matrix arises when the slopes of the epipolar lines are equal to zero. A model for this case is given below:

$$F_{2\tilde{1}}\left(\begin{bmatrix} e_{1u} \\ 0 \\ 0 \end{bmatrix}, \begin{bmatrix} e_{2u} \\ e_{2v} \\ 1 \end{bmatrix}, q, r, \theta\right) = \begin{bmatrix} 1 & 0 \\ 0 & 1 \\ -e_{2u} & -e_{2v} \end{bmatrix} \begin{bmatrix} \cos\theta & -\sin\theta \\ \sin\theta & \cos\theta \end{bmatrix} \begin{bmatrix} q & r \\ 0 & 1/q \end{bmatrix} \begin{bmatrix} 0 & 1 & 0 \\ 0 & 0 & 1 \end{bmatrix}$$

Equation A-2: Fundamental matrix with one finite and one zero-slope infinite epipole

The breve symbol is used to indicate an image-space that contains a zero-slope infinite epipole. The zero-slope case of a single infinite epipole in the first image is indicated when the single-infinite-epipole condition ($f_{11}f_{22} - f_{12}f_{21} = 0$ and $f_{21}f_{32} - f_{22}f_{31} = 0$) is caused by zeros in the leftmost column of the fundamental matrix. In such a configuration, the f_{11} element cannot be normalized by scaling. A zero-slope infinite epipole in the second image is indicated by a topmost row of zeros.

[39] Equivalently, this condition is indicated when the right-side vector associated with the singular value of the fundamental matrix's singular-value decomposition has a third element of zero.

When the epipoles of both images are infinite and have nonzero slopes, the following 5-parameter model can be used for the fundamental matrix:

$$F_{\hat{2}\hat{1}}\left(\begin{bmatrix} e_{1u} \\ e_{1v} \\ 0 \end{bmatrix}, \begin{bmatrix} e_{2u} \\ e_{2v} \\ 0 \end{bmatrix}, q, r, s\right) = \begin{bmatrix} 1 & 0 \\ \frac{-e_{2u}}{e_{2v}} & 0 \\ q & r \end{bmatrix} \begin{bmatrix} 1 & \frac{-e_{1u}}{e_{1v}} & s \\ 0 & 0 & 1 \end{bmatrix}$$

Equation A-3: Fundamental matrix with two non-zero-slope infinite epipoles

This nongeneric condition is indicated by a fundamental matrix with a nonzero f_{11} value in which $f_{11}f_{22} - f_{12}f_{21} = 0$, $f_{21}f_{32} - f_{22}f_{31} = 0$, and $f_{12}f_{23} - f_{22}f_{31} = 0$.

The following four-parameter model can be used to represent an epipolar geometry with two infinite epipoles in which the epipolar lines of the first image have a zero slope.

$$F_{\hat{2}\hat{1}}\left(\begin{bmatrix} e_{1u} \\ 0 \\ 0 \end{bmatrix}, \begin{bmatrix} e_{2u} \\ e_{2v} \\ 0 \end{bmatrix}, q, r, s\right) = \begin{bmatrix} 1 & r \\ \frac{-e_{2u}}{e_{2v}} & \frac{-be_{2u}}{e_{2v}} \\ q & s \end{bmatrix} \begin{bmatrix} 0 & 1 & 0 \\ 0 & 0 & 1 \end{bmatrix}$$

Equation A-4: Fundamental matrix with a non-zero slope and a zero-slope infinite epipole

This condition is indicated by a fundamental matrix with a leftmost zero-column and a nonzero f_{12} value. Two infinite epipoles with zero-slope epipolar lines in the second image are indicated by the same conditions applied to the given fundamental matrix's transpose.

A final three-parameter model of the fundamental matrix can be used to characterize the case when the epipolar lines of both images have a zero slope and both epipoles are infinite. Such a matrix is indicated when both the leftmost column and topmost row of the fundamental matrix are zero. Such a fundamental matrix can be normalized by scaling the matrix by the reciprocal of the squareroot of the determinant of the lower-right submatrix (causing the resulting submatrix to have a determinant of one). A model for this nongeneric situation is given below:

$$F_{\hat{2}\hat{1}}\left(\begin{bmatrix} e_{1u} \\ 0 \\ 0 \end{bmatrix}, \begin{bmatrix} e_{2u} \\ 0 \\ 0 \end{bmatrix}, q, r, \theta\right) = \begin{bmatrix} 0 & 0 \\ 1 & 0 \\ 0 & 1 \end{bmatrix} \begin{bmatrix} \cos\theta & -\sin\theta \\ \sin\theta & \cos\theta \end{bmatrix} \begin{bmatrix} q & r \\ 0 & 1/q \end{bmatrix} \begin{bmatrix} 0 & 1 & 0 \\ 0 & 0 & 1 \end{bmatrix}$$

Equation A-5: Fundamental matrix with two zero-slope infinite epipoles

In such a configuration, the epipolar lines of both images will correspond to the scan lines (i.e., isophotes of constant *v*) of both images. Notice that this arrangement is identical to the stereo-camera condition depicted in Figure 3-4. Therefore, depth-from-stereo methods, which depend on mechanical calibration, rely upon a particularly nongeneric camera configuration (a 3-dimensional subspace of a generally 7-dimensional problem). As a result, they should be expected to be very sensitive to any external system noise.

Appendix B

SPECIAL CASES OF THE CLOSED-FORM SAME-CAMERA SOLUTION

In Chapter 5 a method was derived for computing the intrinsic parameters of a non-skewed planar-pinhole camera from a projective transformation, $\mathbf{C}$, that satisfies the same-camera constraints given by Equation 5-23. A closed-form solution for the camera's intrinsic parameters was presented for all cases except when $c_{31} = 0$ and $c_{32} = 0$. Generally, these conditions are unlikely because they comprise a two-dimensional subspace within the seven dimensional space of same-camera transforms. For completeness, however, these special cases of the projective transform, $\mathbf{C}$, are addressed in this Appendix.

The various special cases of $\mathbf{C}$ are depicted in the following diagram:

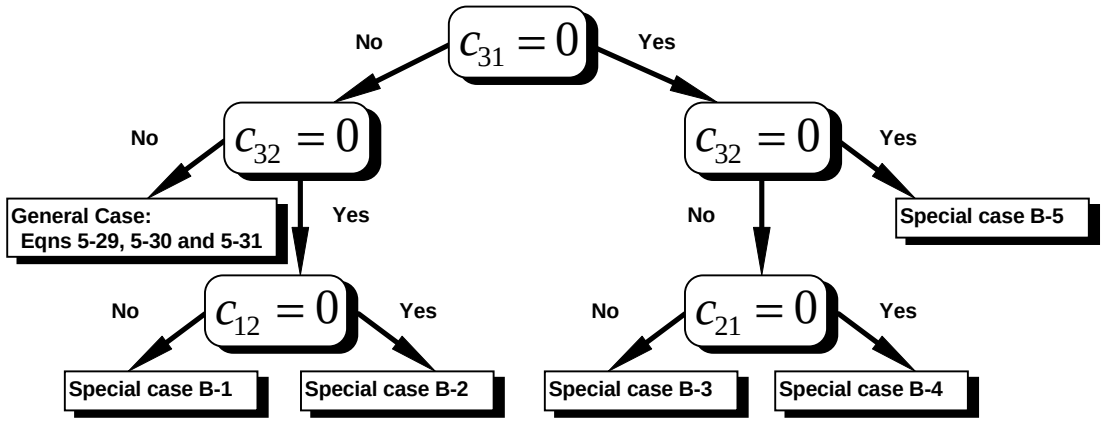

Figure A-1: Diagram of the special case solutions

First, I will consider the special case of same-camera projective transformation where $c_{31} \neq 0$, $c_{32} = 0$, and $c_{12} \neq 0$. The Euclidean metrics of such a camera can be expressed as follows:

$$\bar{b}\cdot\bar{b}=\frac{c_{12}^2}{1-c_{22}^2}$$

$$\bar{a}\cdot\bar{c}=\frac{c_{12}(z_{22}c_{22}-c_{11})-c_{22}(\bar{b}\cdot\bar{b})(z_{21}c_{22}+c_{21})}{c_{12}c_{31}}$$

$$\bar{b}\cdot\bar{c}=\frac{(\bar{b}\cdot\bar{b})z_{21}c_{22}-z_{22}c_{21}}{c_{31}}$$

$$\bar{c}\cdot\bar{c}=\frac{(\bar{b}\cdot\bar{b})c_{23}^2+2c_{33}((\bar{a}\cdot\bar{c})c_{13}+(\bar{b}\cdot\bar{c})c_{23})+c_{13}^2}{1-c_{33}^2}$$

Equation B-1: Solution for camera metrics when $c_{31}\neq 0$, $c_{32}=0$, and $c_{12}\neq 0$

When $c_{31}\neq 0$, $c_{32}=0$, and $c_{12}=0$ the vector $\bar{b}\cdot\bar{b}$ cannot be determined; however, the remaining Euclidean metrics can be solved for as follows:

$$\bar{a}\cdot\bar{c}=\frac{c_{33}-z_{22}c_{11}}{c_{31}(z_{22}+1)}$$

$$\bar{b}\cdot\bar{c}=\frac{2(\bar{a}\cdot\bar{c})c_{31}(c_{11}(c_{33}^2-1)-c_{13}c_{31}c_{33})+(c_{33}^2-1)(c_{11}-1)-c_{13}^2c_{31}^2}{c_{31}(c_{21}+z_{21})(c_{33}+1)}$$

$$\bar{c}\cdot\bar{c}=\frac{2(\bar{a}\cdot\bar{c})c_{31}(c_{11}c_{23}(c_{33}+1)-c_{13}c_{21}c_{33})+(c_{33}+1)(c_{11}^2c_{23}-c_{23})-c_{13}^2c_{21}c_{31}}{c_{31}(c_{21}+z_{21})(c_{33}+1)}$$

Equation B-2: Solution for camera metrics when $c_{31}\neq 0$, $c_{32}=0$, and $c_{12}=0$

This situation arises when the camera's axis of rotation is aligned with one of the basis vectors of the image plane.

The next special case considered occurs when $c_{31}=0$, $c_{32}\neq 0$, and $c_{21}\neq 0$.

$$\bar{b}\cdot\bar{b}=\frac{1-c_{11}^2}{c_{21}^2}$$

$$\bar{a}\cdot\bar{c}=\frac{c_{11}z_{12}-(\bar{b}\cdot\bar{b})c_{21}z_{11}}{c_{32}}$$

$$\bar{b}\cdot\bar{c}=\frac{(\bar{b}\cdot\bar{b})(c_{11}z_{11}-c_{22})-c_{11}^2z_{12}-c_{11}c_{12}}{c_{21}c_{32}}$$

$$\bar{c}\cdot\bar{c}=\frac{(\bar{b}\cdot\bar{b})(1-c_{22}^2)-2c_{32}((\bar{a}\cdot\bar{c})c_{12}+(\bar{b}\cdot\bar{c})c_{22})-c_{12}^2}{c_{32}^2}$$

Equation B-3: Solution for camera metrics when $c_{31}=0$, $c_{32}\neq 0$, and $c_{21}\neq 0$

The condition when $c_{31}=0$, $c_{32}\neq 0$, and $c_{21}=0$ can also occur when the camera's rotation axis is aligned with one of the image-space basis vectors. In this case the following solution arises:

$$\bar{b}\cdot\bar{b}=\frac{2z_{13}(\bar{a}\cdot\bar{c})c_{32}c_{33}+(\bar{c}\cdot\bar{c})c_{32}(c_{22}-c_{33}z_{11})+c_{12}^2c_{23}c_{33}-c_{13}^2c_{22}c_{32}}{c_{23}(c_{33}-z_{11}c_{22})}$$

$$\bar{a}\cdot\bar{c}=-\frac{c_{12}}{c_{32}}$$

$$\bar{b}\cdot\bar{c}=\frac{2(\bar{a}\cdot\bar{c})\left(c_{12}c_{23}^2c_{32}+c_{13}c_{33}\left(1-c_{22}^2\right)\right)-(\bar{c}\cdot\bar{c})\left(c_{22}^2\left(c_{33}^2-1\right)-c_{23}^2c_{32}^2-c_{33}^2+1\right)+c_{12}^2c_{23}^2+c_{13}^2\left(1-c_{22}^2\right)}{2c_{23}\left(z_{11}c_{22}-c_{33}\right)}$$

$$\bar{c}\cdot\bar{c}=\frac{(\bar{b}\cdot\bar{b})\left(1-c_{22}^2\right)-2c_{32}\left((\bar{a}\cdot\bar{c})c_{12}+(\bar{b}\cdot\bar{c})c_{22}\right)-c_{12}^2}{c_{32}^2}$$

Equation B-3: Solution for camera metrics when $c_{31}=0$, $c_{32}\neq 0$, and $c_{21}=0$

When $c_{31}=0$ and $c_{32}=0$ the resulting projective transformation is affine. In this case the vector $\bar{c}\cdot\bar{c}$ cannot be determined; however, the remaining camera metrics can be solved for as follows:

$$\bar{b}\cdot\bar{b}=-\frac{c_{11}c_{12}}{c_{21}c_{22}}$$

$$\bar{a}\cdot\bar{c}=\frac{(\bar{b}\cdot\bar{b})c_{21}c_{23}-c_{13}(1-c_{11})}{2-c_{11}-c_{22}}$$

$$\bar{b}\cdot\bar{c}=\frac{c_{12}c_{13}-c_{23}(\bar{b}\cdot\bar{b})(1-c_{22})}{2-c_{11}-c_{22}}$$

Equation B-5: Solution for camera metrics when $c_{31}=0$ and $c_{32}=0$

Appendix C

FINDING CAMERA MODELS IN IMAGES WITH COMMON EPIPOLES

The typical case in which a pair of images have the same epipole coordinate arises when a camera is translated without rotation, as depicted in the following figure:

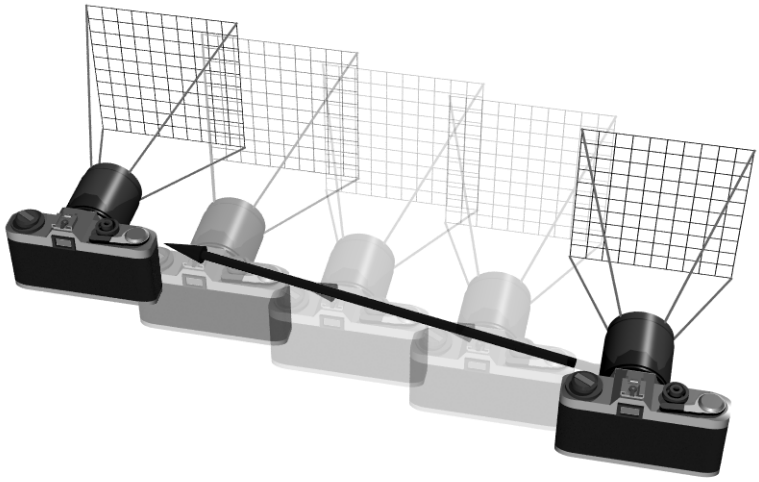

Figure C-1: A typical camera configuration leading to common epipole coordinates

The same-camera surface parameterizations given by Equations 5-34, 5-35, and 5-37 are degenerate in this case. Such configurations are common enough, however, to deserve special treatment. A second less likely case of a pair of images having the same epipolar coordinate occurs when the rotational axis and the translation direction are coincident. This situation is shown in Figure C-2. The methods developed in this Appendix apply to both of these cases.

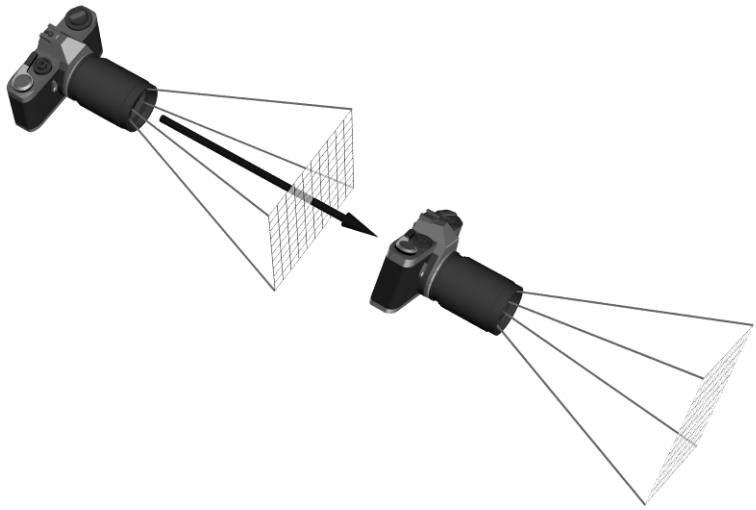

Figure C-2: A second configuration leading to common epipole coordinates

When an image pair has common epipole coordinates (a state that can be determined by a fundamental matrix and its transpose having the same point in their null spaces), the trace of the compatible matrix can be expressed in terms of its determinant as follows :

$$\text{Trace}(\sigma\mathbf{H_F}) = \frac{\text{Determinant}(\sigma\mathbf{H_F})}{\sigma^2} + \sigma m_3 = \frac{1}{\sigma^2} + \sigma m_3$$

Equation C-1: Value of trace when the epipole coordinates are the same in both images

This can easily be seen by equating the epipoles in Equation 5-34 and Equation 5-35.

Furthermore, if Equation 5-34 is solved for the parameter h_{33} and substituted into the trace-equals-the-sum-of minors equation, all dependence on the remaining two parameters, h_{31} and h_{32}, cancels out and the following expression results:

$$\frac{(\sigma-1)(\sigma+1)(\sigma^2-\sigma m_3+1)}{\sigma^2} = 0$$

Equation C-2: Values of σ that potentially satisfy the same-camera constraints

Since a non-zero value of σ is required for the projective transformation to have a unit determinant, we need only consider the four roots of the numerator as potential scaling factors. Substituting these values into Equation C-1 and verifying the remaining relational constraint of the same-camera transformation gives

$$-1 \le 1 \pm m_3 \le 3$$
$$-1 \le -1 \pm m_3\sqrt{m_3^2 - 4} \le 3$$

Equation C-3: Valid ranges for the trace of the projective transform

With the exception of the points $m_3 = \pm 2$ there is no common overlap between these two solution sets. The first relationship applies when $|m_3| \le 2$, while the second relationship applies when $2 \le |m_3| \le \sqrt{2\sqrt{5}+2} \approx 2.54403$. All other values for m_3 do not allow for a valid same-camera solution. Thus, frequently only two of these four solutions need be considered.

The angle of the camera's rotation can be directly determined from the trace, which in this case has one of four possible values:

$$\theta \in \left\{ \text{Arccos}(\tfrac{m_3}{2}), \text{Arccos}(\tfrac{-m_3}{2}), \text{Arccos}\left(-1+\tfrac{m_3\sqrt{m_3^2-4}}{2}\right), \text{Arccos}\left(-1-\tfrac{m_3\sqrt{m_3^2-4}}{2}\right) \right\}$$

Equation C-4: Rotation angles

In the typical translation-only case depicted in Figure C-1 $m_3 = 2$ (recall that $m_3 = f_{21} - f_{12}$ and, in the case of no rotation, $\mathbf{F} = \text{Skew}(\bar{e}_2)\mathbf{I}$). In this situation the rotation angles reduce to $\theta = \{0, \pi\}$. In most applications, only the rotation angle θ needs to be considered since generally a pair of translated cameras whose orientation varies by π radians will see no points in common, with an exception occurring when the epipole is within the field-of-view.

Appendix D

AN EXAMPLE IMAGE-BASED SYSTEM

D.1 Overview

This Appendix provides source code for an example image-based computer graphics system written in the Java programming language. This image-warping implementation assumes a planar-pinhole camera model for both the reference and desired images. It also supports multiple reference images. Each reference image is stored in JPEG compressed format while the associated disparity data is stored as a gray scale GIF image that has been scaled and quantized to 256 levels. An example HTML file for invoking the image warper is shown below.

```
<HTML>
<HEAD>
<!-- created: 04/03/96 by Leonard McMillan -->
<TITLE> Image-Based Computer Graphics Applet</TITLE>
</HEAD>
<BODY>
<H1> Image-Based Computer Graphics Applet </H1>
<HR>
<CENTER>
<APPLET code="Vwarp.class" width=400 height = 400>
<param name="numrefs" value=4>
<param name="reference0" value="proja.jpg,proja.gif,0,-36,36, -22.745,45.2376,4.78461,
0.142156,0,0, 0,-0.057735,-0.129904, 0.529088,1.31943">
<param name="reference1" value="projb.jpg,projb.gif,-23.1403,-27.5776,36,
11.6545,49.2742,4.78459, 0.108898,-0.0913759,0, -0.0371113,-0.0442276,-0.129904,
0.000615401,1.32566">
<param name="reference2" value="projc.jpg,projc.gif,-9.98,-27.44,41.71, -5.4776,46.3995,-
4.85222, 0.123386,-0.0448759,0, -0.0267762,-0.0736211,-0.105361, 0.398979,1.30172">
<param name="reference3" value="projd.jpg,projd.gif,40,6,32, -43.2382,-31.1167,11.3524, -
0.0225834,0.150556,0, 0.0428222,0.00642333,-0.145952, 0.366496,1.43569">
<param name="move" value=2>
<param name="fov" value=60>
</APPLET>
</CENTER>
<HR>
</BODY>
</HTML>
```

Each reference image is specified by a parameter string with a name of the form “referenceX," where X is the index of the reference image. The first two arguments of the parameter’s value specify the names of the image and disparity files. The following three numbers of the comma separated string define the coordinates of the image’s center-of-

projection. The next nine numbers define the projection matrix for the planar image-space to ray mapping function in row-major order. The last two numbers specify the minimum and maximum disparity values represented by the 256 levels of the disparity image.

D.2 Modules and Classes

The example planar image warper is partitioned into five files with the following contents:

Vwarp.java contains the central applet which implements separate threads for the image warper and the user interface.
Reference.java defines a generic interface for a reference image.
PlanarReference.java contains an implementation of a planar reference image with warping methods. It also implements a PlanarView which encapsulates all of the pinhole-camera information associated with a planar reference image.
Vector3D.java provides general vector and matrix objects.
Raster.java defines an interface to an image that allows pixels to be accessed randomly.

D.3 Source

The source code for each file is provided below.

D.3.1 Vwarp.java

```
import java.applet.*;
import java.awt.*;
import java.util.*;
import java.awt.image.*;
import PlanarReference;
import Vector3D;


public class Vwarp extends Applet implements Runnable {
    final static float DEFAULT_FOV = 40;
    final static float DEFAULT_MOVE = 1;

    int curRef;           // index of current reference image
    int numRefs;          // number of reference images available
    PlanarReference reference[ ]; // array of reference images
    Vector3D eyePoint;        // desired center-of-projection
    Vector3D lookAt;          // optical axis
    Vector3D up;          // three-space vector that projects up
    float hfov;           // horizontal field-of-view
    float moveScale;          // size of step
    PlanarView currentView;       // desired view point and projection
    Raster window;        // display window
    Image output;         // working image


// The init method is the first one executed when the applet is loaded
    public void init()
    {
        // Get the number of reference images
        try {
            numRefs = Integer.parseInt(getParameter("numrefs"));
        } catch (NumberFormatException e) {
            numRefs = 0;
        }

        // read in the reference images
        reference = new PlanarReference[numRefs];
        for (int i = 0; i < numRefs; i++) {
```

```
            String refInfo = getParameter("reference"+i);
            if (refInfo == null) continue;
            StringTokenizer parser = new StringTokenizer(refInfo, " ,");
            // get viewing parameters
            try {
                Image image = getImage(getDocumentBase(), parser.nextToken());
                Image disparity = getImage(getDocumentBase(), parser.nextToken());
                Vector3D O  = new Vector3D(parser);     // center-of-projection
                Vector3D Vp = new Vector3D(parser);     // vector to image origin
                Vector3D Du = new Vector3D(parser);     // x spanning vector
                Vector3D Dv = new Vector3D(parser);     // y spanning vector
                float mind, maxd;
                mind = Float.valueOf(parser.nextToken()).floatValue( );
                maxd = Float.valueOf(parser.nextToken()).floatValue( );
                Matrix3x3 P = new Matrix3x3(Du, Dv, Vp);
                PlanarView view = new PlanarView(O, P);
                reference[i] =
                    new PlanarReference(this, image, disparity, maxd, mind, view);
            } catch (NumberFormatException e) {
                System.err.println("Error: Invalid float value");
                System.exit(1);
            }
            showStatus("Image["+i+"] size = " + reference[0].width
                       + " x " + reference[0].height);
        }

        // set default view
        curRef = 0;
        eyePoint = reference[curRef].getOrigin();
        lookAt = reference[curRef].getCenter();
        up = new Vector3D(0, 0, 1);
        hfov = DEFAULT_FOV;
        String fovval = getParameter("fov");
        if (fovval != null) {
            try {
                hfov = Float.valueOf(fovval).floatValue();
            } catch (NumberFormatException e) {
                hfov = DEFAULT_FOV;
            }
        }
        hfov *= Math.PI / 180;

        moveScale = DEFAULT_MOVE;
        String moveval = getParameter("move");
        if (moveval != null) {
            try {
                moveScale = Float.valueOf(moveval).floatValue();
            } catch (NumberFormatException e) {
                moveScale = DEFAULT_MOVE;
            }
        }

        window = new Raster(size().width, size().height);
        window.fill(Color.blue);
        output = window.toImage(this);

        currentView = new PlanarView(eyePoint, lookAt, up, hfov, size( ));
        warpInfo(ENQUEUE, currentView);
    }


// the following variables permit the warper and
// user interface to operate asynchronously
    protected final static int ENQUEUE = 0;
    protected final static int DEQUEUE = 1;
    protected int warpCount = 0;
    protected boolean warpOutstanding = false;
    protected PlanarView warpView, nextView;
    Thread warper;
```

```
// this method passes *recent* events to the warper thread
protected synchronized boolean warpInfo(int action, PlanarView view)
{
    boolean rval = true;
    if (action == ENQUEUE) {
        nextView = new PlanarView(view);
        warpOutstanding = true;
        warpCount += 1;
    } else
    if (action == DEQUEUE) {
        if (warpOutstanding) {
            warpView = new PlanarView(nextView);
            warpOutstanding = false;
        } else {
            rval = false;
        }
    }
    return rval;
}


// spawn a separate thread for the warper
public void start()
{
    warper = new Thread(this);
    warper.start();
}


public void stop()
{
    warper.stop();
}


// performs a warp if an event is pending
public void run()
{
    long time = 0;
    while (true) {
        if (warpInfo(DEQUEUE, null)) {
            window.fill(getBackground());
            time = System.currentTimeMillis();
            reference[curRef].Warp(warpView, window);
            time = System.currentTimeMillis() - time;
            output = window.toImage(this);
            paint(this.getGraphics());
        } else {
            showStatus(time+"ms  Waiting for input ["+warpCount+"]");
            try {
                System.gc();
                Thread.sleep(100);
            } catch (InterruptedException e) {
                break;
            }
        }
    }
}


// copys the image to the display
public void paint(Graphics g)
{
    g.drawImage(output, 0, 0, this);
}


// simplify redraws
public void update(Graphics g)
{
    g.setColor(getForeground());
    paint(g);
}

Vector3D V0;              // vector in the direction
```

```
                                        // of the initial mouse button press

// handle the pressing of a mouse button
public boolean mouseDown(Event e, int x, int y)
{
    V0 = Vector3D.normalize(currentView.map(x, y));
    return true;
}


// handle drags of the mouse while a button is held down
public boolean mouseDrag(Event e, int x, int y)
{
    Vector3D V1 = Vector3D.normalize(currentView.map(x, y));
    Vector3D Axis = V1.cross(V0);
    Vector3D newLook = new Vector3D(lookAt);

    // rotate the current look-at direction
    if (Axis.length() > 0.0001) {
        float angle = (float) Math.asin(Vector3D.length(Axis));
        newLook = newLook.rotate(Axis, angle);
    }

    // translate along the look-at direction if either
    // shift or control is pressed during the drag
    if (e.shiftDown()) {
        eyePoint = eyePoint.plus(V0.scale(moveScale));
    } else
    if (e.controlDown()) {
        eyePoint = eyePoint.plus(V0.scale(-moveScale));
    }

    // update the current viewing matrix
    PlanarView view = new PlanarView(eyePoint, newLook, up, hfov, size( ));
    warpInfo(ENQUEUE, view);
    return true;
}


// handle releases of mouse button
public boolean mouseUp(Event e, int x, int y)
{
    Vector3D V1 = Vector3D.normalize(currentView.map(x, y));
    Vector3D Axis = V1.cross(V0);

    // rotate the look-at vector
    if (Axis.length() > 0.0001) {
        float angle = (float) Math.asin(Vector3D.length(Axis));
        lookAt = lookAt.rotate(Axis, angle);
    }

    // translate if either the shift or control key was pressed
    if (e.shiftDown()) {
        eyePoint = eyePoint.plus(V0.scale(moveScale));
    } else
    if (e.controlDown()) {
        eyePoint = eyePoint.plus(V0.scale(-moveScale));
    }

    // update the current view
    currentView = new PlanarView(eyePoint, lookAt, up, hfov, size( ));
    warpInfo(ENQUEUE, currentView);
    return true;
}


// handle keyboard events
public boolean keyDown(Event e, int key)
{
    if (key == 'n') {         // go to next reference image
        curRef += 1;
        if (curRef == numRefs)
            curRef = 0;
        warpInfo(ENQUEUE, currentView);
    } else
```

```
        if (key == 'r') {         // reset viewing parameters
            eyePoint = reference[curRef].getOrigin();
            lookAt = reference[curRef].getCenter();
            up = new Vector3D(0, 0, 1);
            currentView = new PlanarView(eyePoint, lookAt, up, hfov, size( ));
            warpInfo(ENQUEUE, currentView);
        } else
        if (key == 'w') {         // display a wider field-of-view
            hfov *= 1.125f;
            currentView = new PlanarView(eyePoint, lookAt, up, hfov, size( ));
            warpInfo(ENQUEUE, currentView);
        } else
        if (key == 'z') {         // zoom into the current field-of-view
            hfov *= 0.88888888f;
            currentView = new PlanarView(eyePoint, lookAt, up, hfov, size( ));
            warpInfo(ENQUEUE, currentView);
        }
        return true;
    }
}
```

D.3.2 Reference.java

```
import java.awt.*;
import java.awt.image.*;
import java.util.*;
import Raster;

public class Reference extends Raster {
    protected float maxDisparity, minDisparity;

    // Constructor
    public Reference(Component root, Image img, Image dsp, float maxd, float mind)
    {
        super(img);                          // get the image pixels
        Raster dspras = new Raster(dsp);     // get the disparity values

        // determine the pixel buffer's width and height
        if ((dspras.width != width) || (dspras.height != height)) {
            System.err.println("Error: image and disparity are of different sizes");
            return;
        }

        // copy the disparity information into the pixel array

        for (int p = 0; p < pixel.length; p++) {
            int rgb = pixel[p] & 0x00ffffff;
            int d = dspras.pixel[p] & 0x0000ff00;
            pixel[p] = (d << 16) | rgb;
        }

        maxDisparity = maxd;
        minDisparity = mind;
    }
}
```

D.3.3 PlanarReference.java

```
import java.awt.*;
import java.awt.image.*;
import java.util.*;
import Reference;
import Vector3D;
import Raster;

public class PlanarReference extends Reference {
    protected Vector3D Du, Dv, L;
    protected PlanarView view;
    protected float K[][];
    protected float splat;
```

```
// Constructor
public PlanarReference(Component root, Image img, Image dsp, float maxd, float mind,
                       PlanarView v)
{
    super(root, img, dsp, maxd, mind);
    view = v;
    K = new float[256][3];
}

// Methods
public Vector3D getOrigin( )
{
    return view.origin( );
}

public Vector3D getCenter( )
{
    return view.map(width/2, height/2);
}

// the actual warping is done in this method
private protected void
sheet(PlanarView outView, Raster output, int u0, int u1, int v0, int v1)
{
    int du, dv;
    float dr, ds, dt;
    float drdu, dsdu, dtdu;
    float drdv, dsdv, dtdv;
    float lr, ls, lt;
    float kr, ks, kt;
    float dblW, dblH;

    dblW = (float) output.width;
    dblH = (float) output.height;

    if (v1 >= v0) {
        dv = 1;
        drdv = Dv.x;
        dsdv = Dv.y;
        dtdv = Dv.z;
    } else {
        dv = -1;
        drdv = -Dv.x;
        dsdv = -Dv.y;
        dtdv = -Dv.z;
    }

    drdu = Du.x;
    dsdu = Du.y;
    dtdu = Du.z;
    dr = drdv - (u1 - u0)*drdu;
    ds = dsdv - (u1 - u0)*dsdu;
    dt = dtdv - (u1 - u0)*dtdu;

    if (u1 >= u0) {
        du = 1;
    } else {
        du = -1;
        drdu = -drdu;
        dsdu = -dsdu;
        dtdu = -dtdu;
    }

    lr = L.x;
    ls = L.y;
    lt = L.z;
    for (int v = v0; v != v1; v += dv) {
        for (int u = u0; u != u1; u += du, lr += drdu, ls += dsdu, lt += dtdu) {
            int x, y, d;
            float r, s, t;
            int color = pixel[v*width + u];
            float ktable[] = K[color >>> 24];
            t = ktable[0] + lt;
            if (t <= 0) continue;
            r = ktable[1] + lr;
```

```
            if (r < 0 || r >= dblW*t) continue;
            s = ktable[2] + ls;
            if (s < 0 || s >= dblH*t) continue;
            t = 1f / t;
            r *= t;
            s *= t;
            x = (int)r;
            y = (int)s;
            color |= 0xff000000;
            d = (int)(t*splat*(outView.map(x,y).length()/view.map(u,v).length()) + 1);

            if (d >= 2) {
                int dx, dy;
                x -= (d >> 1);
                dx = d;
                if (x < 0) {
                    dx += x;
                    x = 0;
                } else
                if (x + d >= output.width) {
                    dx += x - output.width;
                }

                y -= (d >> 1);
                dy = d;
                if (y < 0) {
                    dy += y;
                    y = 0;
                 } else
                if (y + d >= output.height) {
                    dy += y - output.height;
                }


                y = y*output.width;
                for (int j = 0; j < dy; j++) {
                    for (int i = 0; i < dx; i++) {
                       output.pixel[y+x+i] = color;
                    }
                    y += output.width;
                }
            } else {
                output.pixel[y*output.width + x] = color;
            }
        }
        lr += dr;
        ls += ds;
        lt += dt;
    }
}


float detP1, detP2, a1xb1, a2xb2, units;

public void Warp(PlanarView outView, Raster output)
{
    int eyeu, eyev;         // desired eye's projection in new view
    Vector3D Deye;          // baseline vector
    Vector3D T;             // temporary vector
    float t;

    // project the new eye's position
    // to reference image coordinates
    Deye = view.baseline(outView);
    T = view.inverseMap(Deye);


    detP1 = view.P.determinant();
    detP2 = outView.P.determinant();
    a1xb1 = view.Du( ).cross(view.Dv( )).length();
    a2xb2 = outView.Du( ).cross(outView.Dv( )).length();
    splat = (float)(detP1*a2xb2*Math.sqrt(a1xb1))/(detP2*a1xb1);
    System.out.println("P1 =" + view.P);
    System.out.println("P2 =" + outView.P);
```

```
System.out.println("detP1 = "+ detP1);
System.out.println("detP2 = "+ detP2);
System.out.println("a1xb1 = "+ a1xb1);
System.out.println("a2xb2 = "+ a2xb2);
System.out.println("splat = "+ splat);

// handle the cases of a zero-length baseline or
// a baseline direction tangent to the viewplane
if (T.z == 0) {
    t = -1;
    eyeu = (T.x >= 0) ? width : -1;
    eyev = (T.y >= 0) ? height : -1;
} else {
    t = 1 / T.z;
    eyeu = (int) (t*T.x);
    eyev = (int) (t*T.y);
}

// compute subspace of projected eye's position
//
//          4 | 3 | 5         13| 12|14
//         ---+-V-+---       ---+-^-+---
//          1 |>0<| 2         10|<9>|11
//         ---+-^-+---       ---+-V-+---
//          7 | 6 | 8         16| 15|17
//
int subspace = 0;
if (eyeu < 0) subspace += 1; else if (eyeu >= width) subspace += 2;
if (eyev < 0) subspace += 3; else if (eyev >= height) subspace += 6;
if (t > 0) subspace += 9;

// project reference's eye position and view
// plane to the coordinates in desired view
//
// Warp Eqn:
//     y = P[1]^-1 (C[0] - C[1]) d(x) + P[1]^-1 P[0] x
//         --------- K ---------         -[Du|Dv|L]-
T = outView.inverseMap(Deye);

// initialize perturbation table
K[0][0] = T.z*minDisparity;
K[0][1] = T.x*minDisparity;
K[0][2] = T.y*minDisparity;
t = (maxDisparity - minDisparity) / 255;
T.z *= t;
T.x *= t;
T.y *= t;
for (int i = 1; i < 256; i++) {
    K[i][0] = K[i-1][0] + T.z;
    K[i][1] = K[i-1][1] + T.x;
    K[i][2] = K[i-1][2] + T.y;
}

Du = outView.inverseMap(view.Du( ));
Dv = outView.inverseMap(view.Dv( ));

int xmax = width - 1;
int ymax = height - 1;
// Warp sheets
switch (subspace) {
  case 0:
    L = outView.inverseMap(view.map(xmax, 0));
    sheet(outView, output, xmax, eyeu, 0, eyev);
    L = outView.inverseMap(view.map(xmax, ymax));
    sheet(outView, output, xmax, eyeu, ymax, eyev - 1);
    L = outView.inverseMap(view.map(0, ymax));
    sheet(outView, output, 0, eyeu + 1, ymax, eyev);
    L = outView.inverseMap(view.map(0, 0));
    sheet(outView, output, 0, eyeu + 1, 0, eyev + 1);
    break;
  case 1:
    L = outView.inverseMap(view.map(xmax, 0));
    sheet(outView, output, xmax, -1, 0, eyev);
    L = outView.inverseMap(view.map(xmax, ymax));
    sheet(outView, output, xmax, -1, ymax, eyev - 1);
```

```
  break;
case 2:
  L = outView.inverseMap(view.map(0, ymax));
  sheet(outView, output, 0, width, ymax, eyev);
  L = outView.inverseMap(view.map(0, 0));
  sheet(outView, output, 0, width, 0, eyev + 1);
  break;
case 3:
  L = outView.inverseMap(view.map(xmax, ymax));
  sheet(outView, output, xmax, eyeu, ymax, -1);
  L = outView.inverseMap(view.map(0, ymax));
  sheet(outView, output, 0, eyeu + 1, ymax, -1);
  break;
case 4:
  L = outView.inverseMap(view.map(xmax, ymax));
  sheet(outView, output, xmax, -1, ymax, -1);
  break;
case 5:
  L = outView.inverseMap(view.map(0, ymax));
  sheet(outView, output, 0, width, ymax, -1);
  break;
case 6:
  L = outView.inverseMap(view.map(xmax, 0));
  sheet(outView, output, xmax, eyeu, 0, height);
  L = outView.inverseMap(view.map(0, 0));
  sheet(outView, output, 0, eyeu + 1, 0, height);
  break;
case 7:
  L = outView.inverseMap(view.map(xmax, 0));
  sheet(outView, output, xmax, -1, 0, height);
  break;
case 8:
  L = outView.inverseMap(view.map(0, 0));
  sheet(outView, output, 0, width, 0, height);
  break;
case 9:
  L = outView.inverseMap(view.map(eyeu, eyev));
  sheet(outView, output, eyeu, width, eyev, -1);
  L = outView.inverseMap(view.map(eyeu, eyev + 1));
  sheet(outView, output, eyeu, width, eyev+1, height);
  L = outView.inverseMap(view.map(eyeu - 1, eyev + 1));
  sheet(outView, output, eyeu - 1, -1, eyev + 1, height);
  L = outView.inverseMap(view.map(eyeu - 1, eyev));
  sheet(outView, output, eyeu - 1, -1, eyev, -1);
  break;
case 10:
  L = outView.inverseMap(view.map(0, eyev));
  sheet(outView, output, 0, width, eyev, -1);
  L = outView.inverseMap(view.map(0, eyev + 1));
  sheet(outView, output, 0, width, eyev + 1, height);
  break;
case 11:
  L = outView.inverseMap(view.map(xmax, eyev));
  sheet(outView, output, xmax, -1, eyev, -1);
  L = outView.inverseMap(view.map(xmax, eyev + 1));
  sheet(outView, output, xmax, -1, eyev + 1, height);
  break;
case 12:
  L = outView.inverseMap(view.map(eyeu, 0));
  sheet(outView, output, eyeu, width, 0, height);
  L = outView.inverseMap(view.map(eyeu - 1, 0));
  sheet(outView, output, eyeu - 1, -1, 0, height);
  break;
case 13:
  L = outView.inverseMap(view.map(0, 0));
  sheet(outView, output, 0, width, 0, height);
  break;
case 14:
  L = outView.inverseMap(view.map(xmax, 0));
  sheet(outView, output, xmax, -1, 0, height);
  break;
case 15:
  L = outView.inverseMap(view.map(eyeu, ymax));
  sheet(outView, output, eyeu, width, ymax, -1);
  L = outView.inverseMap(view.map(eyeu-1, ymax));
```

```
            sheet(outView, output, eyeu - 1, -1, ymax, -1);
            break;
          case 16:
            L = outView.inverseMap(view.map(0, ymax));
            sheet(outView, output, 0, width, ymax, -1);
            break;
          case 17:
            L = outView.inverseMap(view.map(xmax, ymax));
            sheet(outView, output, xmax, -1, ymax, -1);
            break;
        }
    }
}


class PlanarView {
    protected Vector3D O;              // center of projection
    protected Matrix3x3 P;             // projection manifold matrix
    protected boolean invFlag;
    protected Matrix3x3 iP;

    // constructors
    public PlanarView()
    {
        O = new Vector3D(0, 0, 0);
        P = new Matrix3x3();
        invFlag = false;
    }

    public PlanarView(Vector3D O, Matrix3x3 P)
    {
        this.O = O;
        this.P = P;
        invFlag = false;
    }

    public PlanarView(PlanarView v)
    {
        O = v.O;
        P = v.P;
        invFlag = false;
    }

    public PlanarView(Vector3D eye, Vector3D look, Vector3D up, float hfov, Dimension win)
    {
        O = new Vector3D(eye);
        Vector3D Du = Vector3D.normalize(look.cross(up));
        Vector3D Dv = Vector3D.normalize(look.cross(Du));
        float fl = (float)(win.width / (2*Math.tan(0.5*hfov)));
        Vector3D Vp = Vector3D.normalize(look);
        Vp.x = Vp.x*fl - 0.5f*(win.width*Du.x + win.height*Dv.x);
        Vp.y = Vp.y*fl - 0.5f*(win.width*Du.y + win.height*Dv.y);
        Vp.z = Vp.z*fl - 0.5f*(win.width*Du.z + win.height*Dv.z);
        P = new Matrix3x3(Du, Dv, Vp);
        invFlag = false;
    }

    // member functions
    public PlanarView clone(PlanarView original)
    {
        return new PlanarView(new Vector3D(original.O), new Matrix3x3(original.P));
    }

    public final Vector3D baseline(PlanarView V)
    {
        return new Vector3D(O.x - V.O.x, O.y - V.O.y, O.z - V.O.z);
    }

    public final Vector3D inverseMap(Vector3D V)
    {
        if (invFlag == false) {
            iP = P.inverse();
            invFlag = true;
        }
        return iP.times(V);
```

```
    }

    public final Vector3D origin( )
    {
        return new Vector3D(O.x, O.y, O.z);
    }

    public final Vector3D Du( )
    {
        return new Vector3D(P.element(0,0), P.element(1,0), P.element(2,0));
    }

    public final Vector3D Dv( )
    {
        return new Vector3D(P.element(0,1), P.element(1,1), P.element(2,1));
    }

    public final Vector3D Vp( )
    {
        return new Vector3D(P.element(0,2), P.element(1,2), P.element(2,2));
    }

    public final Vector3D map(int u, int v)
    {
        return new Vector3D(P.M[0]*u + P.M[1]*v + P.M[2],
                            P.M[3]*u + P.M[4]*v + P.M[5],
                            P.M[6]*u + P.M[7]*v + P.M[8]);
    }
}
```

D.3.4 Vector3D.java

```
import java.util.*;

class Vector3D {
    public float x, y, z;

    // constructors
    public Vector3D( )
    {
    }

    public Vector3D(float x, float y, float z)
    {
        this.x = x; this.y = y; this.z = z;
    }

    public Vector3D(StringTokenizer parser) throws NumberFormatException
    {
        x = Float.valueOf(parser.nextToken()).floatValue( );
        y = Float.valueOf(parser.nextToken()).floatValue( );
        z = Float.valueOf(parser.nextToken()).floatValue( );
    }

    public Vector3D(Vector3D v)
    {
        x = v.x;
        y = v.y;
        z = v.z;
    }

    // methods
    public final float dot(Vector3D B)
    {
        return (x*B.x + y*B.y + z*B.z);
    }

    public final float dot(float Bx, float By, float Bz)
    {
        return (x*Bx + y*By + z*Bz);
    }
```

```
    public static final float dot(Vector3D A, Vector3D B)
    {
        return (A.x*B.x + A.y*B.y + A.z*B.z);
    }

    public final Vector3D cross(Vector3D B)
    {
        return new Vector3D(y*B.z - z*B.y, z*B.x - x*B.z, x*B.y - y*B.x);
    }

    public final Vector3D cross(float Bx, float By, float Bz)
    {
        return new Vector3D(y*Bz - z*By, z*Bx - x*Bz, x*By - y*Bx);
    }

    public final static Vector3D cross(Vector3D A, Vector3D B)
    {
        return new Vector3D(A.y*B.z - A.z*B.y, A.z*B.x - A.x*B.z, A.x*B.y - A.y*B.x);
    }

    public final float length( )
    {
        return (float) Math.sqrt(x*x + y*y + z*z);
    }

    public final static float length(Vector3D A)
    {
        return (float) Math.sqrt(A.x*A.x + A.y*A.y + A.z*A.z);
    }

    public final Vector3D normalize( )
    {
        float t = x*x + y*y + z*z;
        if (t != 0 && t != 1) t = (float) (1 / Math.sqrt(t));
        return new Vector3D(x*t, y*t, z*t);
    }

    public final static Vector3D normalize(Vector3D A)
    {
        float t = A.x*A.x + A.y*A.y + A.z*A.z;
        if (t != 0 && t != 1) t = (float)(1 / Math.sqrt(t));
        return new Vector3D(A.x*t, A.y*t, A.z*t);
    }

    public final Vector3D rotate(Vector3D Axis, float angle)
    {
        Matrix3x3 R = Matrix3x3.rotation(Axis, angle);
        return R.times(this);
    }

    public final Vector3D scale(float s)
    {
        return new Vector3D(s*x, s*y, s*z);
    }

    public final Vector3D plus(Vector3D A)
    {
        return new Vector3D(x+A.x, y+A.y, z+A.z);
    }

    public String toString()
    {
        return new String("["+x+", "+y+", "+z+"]");
    }
}


class Matrix3x3 {
    public float M[ ];

    // constructors
    public Matrix3x3( )
    {
        M = new float[9];
    }
```

```
public Matrix3x3(Vector3D c1, Vector3D c2, Vector3D c3)
{
    M = new float[9];
    M[0] = c1.x;    M[1] = c2.x;    M[2] = c3.x;
    M[3] = c1.y;    M[4] = c2.y;    M[5] = c3.y;
    M[6] = c1.z;    M[7] = c2.z;    M[8] = c3.z;
}

public Matrix3x3(float m11, float m12, float m13,
                 float m21, float m22, float m23,
                 float m31, float m32, float m33)
{
    M = new float[9];
    M[0] = m11;     M[1] = m12;     M[2] = m13;
    M[3] = m21;     M[4] = m22;     M[5] = m23;
    M[6] = m31;     M[7] = m32;     M[8] = m33;
}

public Matrix3x3(Matrix3x3 m)
{
    M = new float[9];
    M[0] = m.M[0];  M[1] = m.M[1];  M[2] = m.M[2];
    M[3] = m.M[3];  M[4] = m.M[4];  M[5] = m.M[5];
    M[6] = m.M[6];  M[7] = m.M[7];  M[8] = m.M[8];
}

// instance methods
public final float element(int row, int col)
{
    return M[row*3+col];
}

public final void setElement(int row, int col, float v)
{
    M[row*3+col] = v;
}

public final Matrix3x3 scale(float d)
{
    return new Matrix3x3(
                d*M[0], d*M[1], d*M[2],
                d*M[3], d*M[4], d*M[5],
                d*M[6], d*M[7], d*M[8]
            );
}

public final Matrix3x3 plusScaled(Matrix3x3 A, float s)
{
    return new Matrix3x3(
                M[0]+s*A.M[0], M[1]+s*A.M[1], M[2]+s*A.M[2],
                M[3]+s*A.M[3], M[4]+s*A.M[4], M[5]+s*A.M[5],
                M[6]+s*A.M[6], M[7]+s*A.M[7], M[8]+s*A.M[8]
            );
}

public final Vector3D times(Vector3D X)
{
    return new Vector3D(M[0]*X.x + M[1]*X.y + M[2]*X.z,
                        M[3]*X.x + M[4]*X.y + M[5]*X.z,
                        M[6]*X.x + M[7]*X.y + M[8]*X.z);
}

public final Matrix3x3 transpose( )
{
    return new Matrix3x3(M[0], M[3], M[6],
                         M[1], M[4], M[7],
                         M[2], M[5], M[8]);
}

public final float determinant( )
{
    return (M[0]*(M[4]*M[8] - M[5]*M[7]) +
            M[1]*(M[5]*M[6] - M[3]*M[8]) +
            M[2]*(M[3]*M[7] - M[4]*M[6]));
```

```
}

public final Matrix3x3 adjoint( )
{
    return new Matrix3x3(M[4]*M[8] - M[5]*M[7],
                         M[2]*M[7] - M[1]*M[8],
                         M[1]*M[5] - M[2]*M[4],
                         M[5]*M[6] - M[3]*M[8],
                         M[0]*M[8] - M[2]*M[6],
                         M[2]*M[3] - M[0]*M[5],
                         M[3]*M[7] - M[4]*M[6],
                         M[1]*M[6] - M[0]*M[7],
                         M[0]*M[4] - M[1]*M[3]);
}

public final Matrix3x3 inverse( )
{
    float m11 = M[4]*M[8] - M[5]*M[7];
    float m12 = M[2]*M[7] - M[1]*M[8];
    float m13 = M[1]*M[5] - M[2]*M[4];
    float d = M[0]*m11 + M[3]*m12 + M[6]*m13;
    if (d == 0)
        return null;
    else {
        d = 1/d;
        return new Matrix3x3(d*m11, d*m12, d*m13,
                         d*(M[5]*M[6] - M[3]*M[8]),
                         d*(M[0]*M[8] - M[2]*M[6]),
                         d*(M[2]*M[3] - M[0]*M[5]),
                         d*(M[3]*M[7] - M[4]*M[6]),
                         d*(M[1]*M[6] - M[0]*M[7]),
                         d*(M[0]*M[4] - M[1]*M[3]));
    }
}

// class methods
public final static Matrix3x3 diag(float d)
{
    return new Matrix3x3(d, 0, 0, 0, d, 0, 0, 0, d);
}

public final static Matrix3x3 identity()
{
    return diag(1);
}

public final static Matrix3x3 skewSymmetric(Vector3D V)
{
    return new Matrix3x3(
                       0, -V.z,  V.y,
                    V.z,    0, -V.x,
                   -V.y,  V.x,    0
                );
}

public final static Matrix3x3 quadSymmetric(Vector3D V)
{
    float xy = V.x*V.y;
    float xz = V.x*V.z;
    float yz = V.y*V.z;

    return new Matrix3x3(
                   V.x*V.x,      xy,     xz,
                        xy, V.y*V.y,     yz,
                        xz,      yz, V.z*V.z
                );
}

public final static Matrix3x3 rotation(Vector3D Axis, float angle)
{
    float cosx = (float) Math.cos(angle);
    float sinx = (float) Math.sin(angle);
    Axis = Axis.normalize( );
    Matrix3x3 R;
    R = diag(cosx);
```

```
        R = R.plusScaled(skewSymmetric(Axis), sinx);
        R = R.plusScaled(quadSymmetric(Axis), 1-sinx);
        return R;
    }

    public String toString()
    {
        return "[["+M[0]+", "+M[1]+", "+M[2]+"],"+
               " ["+M[3]+", "+M[4]+", "+M[5]+"],"+
               " ["+M[6]+", "+M[7]+", "+M[8]+"]]";
    }
}
```

D.3.5 Raster.java

```
import java.awt.*;
import java.awt.image.*;
import java.util.*;

class Raster implements ImageObserver {
    public int width, height;
    public int pixel[];
    private ImageProducer producer;

    ////////////////////////// Constructors //////////////////////

    /**
     *  This constructor which takes no arguments
     *  allows for future extension.
     */
    public Raster()
    {
    }

    /**
     *  This constructor creates an uninitialized
     *  Raster Object of a given size (w x h).
     */
    public Raster(int w, int h)
    {
        width = w;
        height = h;
        pixel = new int[w*h];
    }

    /**
     *  This constructor creates an Raster initialized
     *  with the contents of an image.
     */
    public Raster(Image img)
    {
        width = -1;
        height = -1;
        int w = img.getWidth(this);
        int h = img.getHeight(this);
        if (w >= 0) width = w;
        if (h >= 0) height = h;

        try {
            while ((width < 0) || (height < 0)) {
                Thread.sleep((long) 100);
            }
            if (width*height == 0) return;
            pixel = new int[width*height];
            PixelGrabber  pg = new PixelGrabber(img,0,0,width,height,pixel,0,width);
            pg.grabPixels();
        } catch (InterruptedException e) {
            width = 0;
            height = 0;
            pixel = null;
            return;
        }
```

```
    }

    public boolean imageUpdate(Image img, int flags, int x, int y, int w, int h)
    {
        if ((flags & WIDTH) != 0) width = w;
        if ((flags & HEIGHT) != 0) height = h;
        if ((flags & ABORT) != 0) { width = 0; height = 0; }
        if ((flags & ERROR) != 0) { width = 0; height = 0; }
        return ((flags & ALLBITS) != 0);
    }

    ////////////////////////// Methods //////////////////////////

    /**
     *  Returns the number of pixels in the Raster
     */
    public final int size( )
    {
        return width*height;
    }

    /**
     *  Fills a Raster with a solid color
     */
    public final void fill(Color c)
    {
        int s = size();
        int rgb = c.getRGB();
        for (int i = 0; i < s; i++)
            pixel[i] = rgb;
    }

    /**
     *  Converts Rasters to Images
     *      9/2/96 : removed final from method definiton
     */
    public Image toImage(Component root)
    {
        return root.createImage(new MemoryImageSource(width, height, pixel, 0, width));
    }

    /**
     *  Gets a pixel from a Raster
     */
    public final int getPixel(int x, int y)
    {
        return pixel[y*width+x];
    }

    /**
     *  Gets a color from a Raster
     */
    public final Color getColor(int x, int y)
    {
        return new Color(pixel[y*width+x]);
    }

    /**
     *  Sets a pixel to a given value
     */
    public final boolean setPixel(int pix, int x, int y)
    {
        pixel[y*width+x] = pix;
        return true;
    }

    /**
     *  Sets a pixel to a given color
     */
     public final boolean setColor(Color c, int x, int y)
     {
        pixel[y*width+x] = c.getRGB();
        return true;
     }
}
```

BIBLIOGRAPHY

[Adelson91] Adelson, E. H. and J. R. Bergen, *"The Plenoptic Function and the Elements of Early Vision,"* **Computational Models of Visual Processing**, Chapter 1, Edited by Michael Landy and J. Anthony Movshon, The MIT Press, Cambridge, Massachusetts, 1991.

[Adelson93a] Adelson, S.J. and L.F. Hodges, *"Stereoscopic Ray-Tracing,"* **The Visual Computer**, Springer-Verlag, 1993, pp. 127-144.

[Adelson93b] Adelson, S. J. and L. F. Hodges, *"Exact Ray-Traced Animation Frames Generated by Reprojection,"* Technical Report GIT-GVU-93-30, Georgia Institute of Technology, Atlanta, GA, July 1993.

[Aliaga96] Aliaga, D., "*Visualization of Complex Models Using Dynamic Texture-Based Simplification*", **IEEE Visualization '96**, Oct 27-Nov 1, 1996, pp. 101-106.

[Anderson82] Anderson, D., *"Hidden Line Elimination in Projected Grid Surfaces,"* **ACM Transactions on Graphics**, October 1982.

[Appel67] Appel, A., *"The notion of quantitative invisibility and the machine rendering of solids,"* **Proceedings of the ACM National Conference**, ACM, New York, October, 1967, pp. 387-393.

[Azarbayejani93] Azarbayejani, A., B. Horowitz, and A. Pentland, *"Recursive Estimation of Structure and Motion using Relative Orientation Constraints,"* **Proceedings of the 1993 IEEE Conference on Computer Vision and Pattern Recognition**, 1993, pp. 294-299.

[Barnard86] Barnard, S.T. *"A Stochastic Approach to Stereo Vision,"* SRI International, Technical Note 373, April 4, 1986.

[Beier92] Beier, T. and S. Neely, *"Feature-Based Image Metamorphosis,"* **Computer Graphics** (SIGGRAPH'92 Conference Proceedings), Vol. 26, No. 2, July 1992, pp. 35-42.

[Beymer93] Beymer, D., A. Shashua, and T. Poggio, *"Example Based Image Analysis and Synthesis,"* MIT, Artificial Intelligence Laboratory, A.I. Memo No. 1431, C.B.C.L. Paper No. 80, November 1993.

[Besl89] Besl, P.J., *"Active Optical Range Imaging Sensors,"* **Advances in Machine Vision**, ed. Jorge L.C. Sanz, Springer-Verlag, 1989, pp. 1-63.

[Blinn76] Blinn, J. F. and M. E. Newell, *"Texture and Reflection in Computer Generated Images,"* **Communications of the ACM**, Vol. 19, No. 10, October 1976, pp. 542-547.

[Bolles87] Bolles, R. C., H. H. Baker, and D. H. Marimont, "*Epipolar-Plane Image Analysis: An Approach to Determining Structure from Motion*," **International Journal of Computer Vision**, Vol. 1, 1987.

[Catmull74] Catmull, E., "*A Subdivision Algorithm for Computer Display of Curved Surfaces*," Ph.D. Thesis, Department of Computer Science, University of Utah, Tech. Report UTEC-CSc-74-133, December 1974.

[Chen93] Chen, S. E. and L. Williams. "*View Interpolation for Image Synthesis*," **Computer Graphics** (SIGGRAPH'93 Conference Proceedings), July 1993, pp. 279-288.

[Chen95] Chen, S.E., "*QuickTime VR - An Image-Based Approach to Virtual Environment Navigation*," **Computer Graphics** (SIGGRAPH '95 Conference Proceedings), August 6-11, 1995, pp. 29-38.

[Coxeter74] Coxeter, H. S. M., **Projective Geometry,** Second Edition, University of Toronto Press, Toronto, Canada, 1974.

[Crow84] Crow, F. C., "*Summed-Area Tables for Texture Mapping*," **Computer Graphics** (SIGGRAPH'84 Conference Proceedings), Vol. 18, No. 3, July 1984, pp. 207-212.

[Debevec96] Debevec, P. E., C. J. Taylor and J. Malik, "*Modeling and Rendering Architecture from Photographs: A Hybrid Geometry- and Image-Based Approach*," **Computer Graphics** (SIGGRAPH'96 Conference Proceedings), August 4-9, 1996, pp. 11-20.

[Faugeras92a] Faugeras, O. D., Q.-T. Luong, and S.J. Maybank, "*Camera Self-Calibration: Theory and Experiments*," **Proceedings of the 2nd European Conference on Computer Vision**, Springer-Verlag, 1992, pp. 321-334.

[Faugeras92b] Faugeras, O. D., "*What can be seen in three dimensions with an uncalibrated stereo rig?*," **Proceedings of the 2nd European Conference on Computer Vision**, Springer-Verlag, 1992, pp. 563-578.

[Faugeras93a] Faugeras, O., **Three-dimensional Computer Vision: A Geometric Viewpoint**, The MIT Press, Cambridge, Massachusetts, 1993.

[Faugeras93b] Faugeras, O., "*What Can Two Images Tell Us About a Third One?*," INRIA, Technical Report No. 2014, July 1993.

[Franke82] Franke, R., "*Scattered Data Interpolation: Tests of Some Methods*," **Mathematics of Computation**, Vol. 38, No. 157, January 1982, pp. 181-200.

[Foley90] Foley, J. D., A. van Dam, S.K. Feiner, and J.F. Hughes, **Computer Graphics - Principles and Practice**, 2nd Edition, Addison-Wesley Publishing Company, Reading, MA, 1990.

[Glassner86] Glassner, A., "*Adaptive Precision in Texture Mapping*," **Computer Graphics** (SIGGRAPH'86 Conference Proceedings), Vol. 20, No. 4, July 1996, pp. 297-306.

[Golub89] Golub, G. H. and C. F. Van Loan, **Matrix Computations**, John Hopkins Press, 2nd Edition, Baltimore, MD, 1989.

[Gortler96] Gortler, S.J., R. Grzeszczuk, R. Szeliski, and M.F. Cohen, "*The Lumigraph*," **Computer Graphics** (SIGGRAPH'96 Conference Proceedings), August 4-9, 1996, pp. 43-54.

[Greene86] Greene, N., "*Environment Mapping and Other Applications of World Projections,*" **IEEE Computer Graphics and Applications**, November 1986.

[Hartley92] Hartley, R., R. Gupta, and T. Chang, "*Stereo from uncalibrated cameras,*" **Proceedings of the IEEE Conference on Computer Vision and Pattern Recognition**, 1992, pp. 761-764.

[Hartley94] Hartley, R.I., "*Self-Calibration from Multiple Views with a Rotating Camera,*" **Proceedings of the European Conference on Computer Vision**, May 1994, pp. 471-478.

[Hartley95a] Hartley, R.I., "*In Defence of the 8-point Algorithm,*" **Proceedings of the IEEE International Conference on Computer Vision**, 1995, pp. 1064-1070.

[Hartley95b] Hartley, R.I., "*A linear method for reconstruction from lines and points*," **Proceedings of the IEEE International Conference on Computer Vision**, 1995, pp. 882-887.

[Heckbert86] Heckbert, P. S., "*Survey of Texture Mapping,*" **IEEE Computer Graphics and Applications**, Vol. 6, No. 11, Nov. 1986, pp. 56-67.

[Heckbert89] Heckbert, P. S., "*Fundamentals of Texture Mapping and Image Warping,*" Masters Thesis, Department of EECS, UCB, Technical Report No. UCB/CSD 89/516, June 1989.

[Horn81] Horn, B., and B.G. Schunck, "*Determining Optical Flow,*" **Artificial Intelligence**, Vol. 17, 1981.

[Horn89] Horn, B.K.P., "*Obtaining Shape from Shading Information,*" **Shape From Shading**, Chapter 6, Edited by Berthold K. Horn and Michael J. Brooks, The MIT Press, Cambridge, Massachusetts, 1989.

[Hsu94] Hsu, R., K. Kodama, and H. Harashima, "*View Interpolation Using Epipolar Plane Images,*" **Proceedings of the First IEEE International Conference on Image Processing**, Vol. 2, November 1994, pp. 745-749.

[Kanatani88] Kanatani, K., "*Transformation of Optical Flow by Camera Rotation,*" **IEEE Transactions on Pattern Analysis and Machine Intelligence,** Vol. 10, No. 2, March 1988.

[Kanatani89] Kanatani, K., "*3D Euclidean Versus 2D Non-Euclidean: Two Approaches to 3D Recovery from Images,*" **IEEE Transactions on Pattern Analysis and Machine Intelligence,** Vol. 11, No. 3, March 1989, pp. 329-332.

[Laveau94] Laveau, S. and O. Faugeras, "*3-D Scene Representation as a Collection of Images and Fundamental Matrices,*" INRIA, Technical Report No. 2205, February 1994.

[Lenz87] Lenz, R. K. and R. Y. Tsai, "*Techniques for Calibration of the Scale Factor and Image Center for High Accuracy 3D Machine Vision Metrology,*" **Proceedings of the IEEE International Conference on Robotics and Automation**, March 31 - April 3, 1987.

[Levoy96] Levoy, M. and P. Hanrahan, "*Light Field Rendering,*" **Computer Graphics** (SIGGRAPH'96 Conference Proceedings), August 4-9, 1996, pp. 31-42.

[Lindeberg95] Lindeberg, T., "*A Scale Selection Principle for Estimating Image Deformations,*" **Proceedings of the Fifth International Conference on Computer Vision**, June 1995, pp. 134-141.

[Lippman80] Lippman, A., "*Movie-Maps: An Application of the Optical Videodisc to Computer Graphics,*" **Computer Graphics** (SIGGRAPH '80 Conference Proceedings), 1980.

[Longuett-Higgins81] Longuet-Higgins, H. C., "*A Computer Algorithm for Reconstructing a Scene from Two Projections,*" **Nature**, Vol. 293, September 1981.

[Longuett-Higgins84] Longuet-Higgins, H. C., "*The Reconstruction of a Scene From Two Projections - Configurations That Defeat the 8-Point Algorithm,*" **Proceedings of the First IEEE Conference on Artificial Intelligence Applications**, December 1984.

[Lucas81] Lucas, B. and T. Kanade, "*An Iterative Image Registration Technique with an Application to Stereo Vision,*" **Proceedings of the Seventh International Joint Conference on Artificial Intelligence**, Vancouver, 1981.

[Luong93a] Luong, Q.-T. and O. Faugeras, "*Self-calibration of a Stereo Rig from Unknown Camera Motions and Point Correspondences,*" INRIA, Technical Report No. 2014, July 1993.

[Luong93b] Luong, Q.-T., R. Deriche, O. Faugeras, and T. Papadopoulo, "*On Determining the Fundamental Matrix: Analysis of Different Methods and Experimental Results,*" INRIA, Technical Report No. RR-1894 , 1993.

[Mann94] Mann, S. and R. W. Picard, "*Virtual Bellows: Constructing High Quality Stills from Video,*" **Proceedings of the First IEEE International Conference on Image Processing**, November 1994.

[Mark97] Mark, W. R., L. McMillan, and G. Bishop**, Proceedings of 1997 Symposium on Interactive 3D Graphics** (Providence, Rhode Island, April 27-30, 1997).

[Maybank92] Maybank, S.J. and O. D. Faugeras, "*A Theory of Self-Calibration of a Moving Camera,*" **International Journal of Computer Vision**, 8:2, Kluwer Academic Publishers, 1992, pp. 123-151.

[McMillan95a] McMillan, L., and G. Bishop, "*Head-Tracked Stereo Display Using Image Warping,*" **1995 IS&T/SPIE Symposium on Electronic Imaging Science and Technology**, SPIE Proceedings #2409A, San Jose, CA, February 5-10, 1995, pp. 21-30.

[McMillan95b] McMillan, L., "*A List-Priority Rendering Algorithm for Redisplaying Projected Surfaces,*" University of North Carolina, Department of Computer Science, UNC Technical Report TR95-005, 1995.

[McMillan95c] McMillan, L., and G. Bishop, "*Plenoptic Modeling: An Image-Based Rendering System,*" **Computer Graphics** (SIGGRAPH '95 Conference Proceedings), August 6-11, 1995, pp. 39-46.

[Mitchell88] Mitchell, D.P. and A.N. Netravali, "*Reconstruction Filters in Computer Graphics,*" **Computer Graphics** (SIGGRAPH'88 Conference Proceedings), Vol. 22, No. 4, August 1988, pp. 221-228.

[Noble96] Noble, A., D. Wilson, and J. Ponce, "*On Computing Aspect Graphs of Smooth Shapes from Volumetric Data,*" **Proceedings of IEEE MMBIA**, 1996, pp. 299-308.

[Perona90] Perona, P. and J. Malik, "*Scale-Space and Edge Detection using Anisotropic Diffusion*", **IEEE Transactions on Pattern Analysis and Machine Intelligence**, Vol. 12, December (1990), pp. 629-639.

[Plantinga90] Plantinga, H. and C. R. Dyer, "*Visibility, Occlusion, and the Aspect Graph*," **International Journal of Computer Vision**, Kluwer Academic Publishers, The Netherlands, 1990, pp. 137-160.

[Prazdny83] Prazdny, K., "*On the Information in Optical Flows*," **Computer Vision, Graphics, and Image Processing**, Vol. 22, No. 9, 1983, pp. 239-259.

[Press88] Press, W. H., B. P. Flannery, S. A. Teukolsky, and W. T. Vetterling, **Numerical Recipes in C**, Cambridge University Press, Cambridge, England, 1988, pp. 309-317.

[Regan94] Regan, M., and R. Pose, "*Priority Rendering with a Virtual Reality Address Recalculation Pipeline*," **Computer Graphics** (SIGGRAPH '94 Conference Proceedings), 1994.

[Rogers85] Rogers, D.F., **Procedural Elements for Computer Graphics**, McGraw-Hill, New York, NY, 1985.

[Schaufler96] Schaufler, G. and W. Stürzlinger, *"Three Dimensional Image Cache for Virtual Reality,"* **Computer Graphics Forum** (Eurographics '96), Vol. 15, No. 3, Aug. 1996, pp. 227-235.

[Segal92] Segal, M., C. Korobkin, R. van Widenfelt, J. Foran, and P. Haeberli, "*Fast Shadows and Lighting Effects Using Texture Mapping*," **Computer Graphics** (SIGGRAPH '92 Conference Proceedings), Vol. 26, No. 2, July 26-31, 1992, pp. 249-252.

[Seitz96] Seitz, S.M. and C. R. Dyer, "*View Morphing*," **Computer Graphics** (SIGGRAPH'96 Conference Proceedings), August 4-9, 1996, pp. 21-30.

[Semple52] Semple, J. G., and G. T. Kneebone, **Algebraic Projective Geometry**, Oxford University Press, London, England, 1952.

[Shade96] Shade, J., D. Lischinski, D. Salesin, T. DeRose, "*Hierarchical Image Caching for Accelerated Walkthroughs of Complex Environments*," **Computer Graphics** (SIGGRAPH'96 Conference Proceedings), pp. 75-82, August 4-9, 1996.

[Shantz82] Shantz, M., "*Two-pass Warp Algorithm for Hardware Implementation*," **SPIE Vol. 367 Processing and Display of Three-Dimensional Data**, 1982, pp. 160-164.

[Shashua93] Shashua, A., "*Projective Depth: A Geometric Invariant For 3D Reconstruction From Two Perspective/Orthographic Views and For Visual Recognition*," **Proceedings of the Fourth IEEE International Conference on Computer Vision,** 1993, pp. 583-590.

[Shashua94] Shashua, A., "*Projective Structure from Uncalibrated Images: Structure from Motion and Recognition*," **IEEE Transactions on Pattern Analysis and Machine Intelligence**, Vol. 16, No. 8, August 1994, pp. 778-790.

[Slater93] Slater, M., and M. Usoh, "*Simulating Peripheral Vision in Immersive Virtual Environments,*" **Computers and Graphics**, Vol. 17, No. 6, 1993, pp. 643-653.

[Smith92] Smith, W.J., and Genesee Optics Software, Inc., **Modern Lens Design: A Resource Manual**, McGraw-Hill, Inc., New York, NY, 1992.

[Stolfi91] Stolfi, J., **Oriented Projective Geometry: A Framework for Geometric Computations**, Academic Press, Inc., San Diego, CA, 1991.

[Sutherland74] Sutherland, I. E., R. F. Sproull, and R. A. Schumacker, *"A Characterization of Ten Hidden-Surface Algorithms,"* **ACM Computing Surveys**, 6(1), March 1974, pp. 1-55. (Also in J. C. Beatty and K. S. Booth, eds, **Tutorial: Computer Graphics**, Second Edition, IEEE Computer Society Press, Silver Springs, MD, 1982, pp. 384-441.)

[Szeliski94] Szeliski, R., *"Image Mosaicing for Tele-Reality Applications,"* DEC and Cambridge Research Lab Technical Report, CRL 94/2, May 1994.

[Szeliski96] Szeliski, R., "*Video Mosaics for Virtual Environments*," **IEEE Computer Graphics and Applications**, March 1996, pp. 22-30.

[Tomasi91] Tomasi, C., and T. Kanade, "*Detection and Tracking of Point Features*," Technical Report, CMU-CS-91-132, Carnegie Mellon University, April 1991.

[Tomasi92] Tomasi, C., and T. Kanade, "*Shape and Motion from Image Streams: a Factorization Method; Full Report on the Orthographic Case*," Technical Report, CMU-CS-92-104, Carnegie Mellon University, March 1992.

[Torr95] Torr, P.H.S., A. Zisserman, and S.J. Maybank, "*Robust Detection of Degenerate Configurations for the Fundamental Matrix*," **Proceedings of the IEEE International Conference on Computer Vision**, 1995, pp. 1037-1042.

[Tsai87] Tsai, R. Y., "*A Versatile Camera Calibration Technique for High-Accuracy 3D Machine Vision Metrology Using Off-the-Shelf TV Cameras and Lenses*," **IEEE Journal of Robotics and Automation**, Vol. RA-3, No. 4, August 1987.

[Upstill90] Upstill, S., **The Renderman Companion: A Programmer's Guide to Realistic Computer Graphics**, Addison Wesley, Reading, Massachusetts, 1990.

[VTV96] "*VTV® Software Development Kit: Reference Manual*," Version 2.01, Warp Ltd., P. O. Box 2910, Nuku'alofa, Kingdom of Tonga, South Pacific, `http://www.warp.com/`, August 1996.

[Wang90] Wang S.C. and J. Staudhammer, "*Visibility Determination on Projected Grid Surfaces*," **IEEE Computer Graphics and Applications**, July 1990.

[Westover90] Westover, L. A., "*Footprint Evaluation for Volume Rendering*," **Computer Graphics** (SIGGRAPH'90 Conference Proceedings), Vol. 24, No. 4, August 1990, pp. 367-376.

[Westover91] Westover, L. A., **SPLATTING: A Parallel, Feed-Forward Volume Rendering Algorithm**, Doctoral Thesis, Department of CS, University of North Carolina, Chapel Hill, NC, 1991.

[Whitaker93] Whitaker, R. T., and S. M. Pizer. *"A Multi-scale Approach to Nonuniform Diffusion,"* **Computer Vision, Graphics, and Image Processing** (Special issue on Image Understanding), Vol. 57, No. 1, Jan. 1993, pp. 99-110.

[Whitted80] Whitted, T., "*An improved illumination model for shaded display*," **Communications of the ACM**, Vol. 23, No. 6, June 1980, pp. 343-349.

[Williams83] Williams, L., "*'Pyramidal Parametrics,*" **Computer Graphics** (SIGGRAPH'83 Conference Proceedings), Vol. 17, No. 3, July 1983, pp. 1-11.

[Wolberg90] Wolberg, G., **Digital Image Warping**, IEEE Computer Society Press, Los Alamitos, California, 1990.

[Wolff94] Wolff, L. B., and E. Angelopoulou, *"3-D Stereo Using Photometric Ratios,"* **Proceedings of the European Conference on Computer Vision**, Springer-Verlag, 1994, pp. 247-257.

[Wright73] Wright, T., "*A Two-Space Solution to the Hidden Line Problem for Plotting Functions of Two Variables,*" **IEEE Transactions on Computers**, January 1973.

[Zorin95] Zorin, D. and A. H. Barr, "*Correction of Geometric Perceptual Distortions in Pictures,*" **Computer Graphics** (SIGGRAPH'95 Conference Proceedings), August 1995, pp. 257-264.